CHARACTERIZATION OF PLASTIC DEFORMATION MECHANISMS IN ULTRAFINE GRAINED FCC METALS USING MEMS BASED NANOMECHANICAL TESTING METHODS

A Dissertation
Presented to
The Academic Faculty

By

Saurabh Gupta

In Partial Fulfillment
Of the Requirements for the Degree
Doctor of Philosophy in the
George W. Woodruff School of Mechanical Engineering

Georgia Institute of Technology

May, 2019

CHARACTERIZATION OF PLASTIC DEFORMATION MECHANISMS IN ULTRAFINE GRAINED FCC METALS USING MEMS BASED NANOMECHANICAL TESTING METHODS

Approved by:

Dr. Olivier N. Pierron, Advisor
George W. Woodruff School of Mechanical Engineering
Georgia Institute of Technology

Dr. Richard W. Neu
George W. Woodruff School of Mechanical Engineering
Georgia Institute of Technology

Dr. Ting Zhu
George W. Woodruff School of Mechanical Engineering
Georgia Institute of Technology

Dr. Brad L. Boyce
Center for Integrated Nanotechnologies
Sandia National Laboratories

Dr. Josh Kacher
School of Materials Science and Engineering
Georgia Institute of Technology

Date Approved: January 17, 2019

ACKNOWLEDGEMENTS

I would like to first thank my advisor Dr. Olivier Pierron for supporting and guiding me through this arduous and exciting journey over the last four and a half years. He had a good balance between giving me the freedom to set my own timelines and pushing me at times to achieve certain objectives. I have learnt a lot from him and would try to emulate some of his qualities in my own professional career. Lastly I would thank him for all the financial support he has provided through my entire PhD.

I would like to thank my committee members Dr. Ting Zhu, Dr. Josh Kacher, Dr. Brad Boyce and Dr. Richard Neu for their time and excellent suggestions for improving my thesis. I would especially like to thank Brad for the financial support towards my visits to CINT and his insights which were crucial in carrying out the in-situ experiments at Sandia. I would also like to thank Josh for helping me with the TKD and EBSD measurements.

I would like to show my gratitude towards everyone at CINT who helped me in numerous ways. I am really grateful for very fruitful discussions with Khalid Hattar and his guidance in expanding the scope of my experiments. I am greatly obligated to Chris Barr for performing all the in-situ experiments with the Push-to-Pull and the help with PED scans. I cannot thank Bill Mook enough for all his time and support during my visits to Sandia and I will always cherish our speculative discussions. I would like to thank Katie Jungjohann for training me to use the TEM and all the great advice during my in-situ experiments. Finally, I

would like to thank Subbu, Shalini and Claire for helping me out with the day-to-day issues at Sandia and making my trips really fun.

I would like to thank my current and previous lab mates: Ehsan, Farzad, Kyungjin, Alejandro, Gabe and Sandra. My transition into the PhD program was greatly supported by Ehsan and he was a great friend and a mentor. I would also like to thank Farzad for transferring his knowledge to me effortlessly so that I could continue his work.

I would like thank all the IEN staff who have trained me on using the advanced tools without which my PhD would not be possible. I am extremely grateful for all the help I got from Eric Woods without whom I would not have able to do all the characterization. I want to thank Walter Henderson for his help with the nanoindentation experiments. I express my gratitude towards Dana Foster whose help with all the administrative matters was invaluable.

Last but not the least, I would like to thank my parents for their immense patience and support during these years and my sister who has been a constant source of motivation.

TABLE OF CONTENTS

LIST OF TABLES

LIST OF FIGURES

LIST OF SYMBOLS AND ABBREVIATIONS

$\Delta\sigma$	Amount of stress relaxation
V_a	Apparent activation volume
k	Boltzmann constant
CS_1	Capacitive Sensor 1
CS_2	Capacitive Sensor 2
α_{CS_1}	CS_1 calibration constant
α_{CS_2}	CS_2 calibration constant
v	Dislocation velocity
E	Elastic Modulus
d	Grain size
θ_0	Initial angle of rotation
f_0	Initial resonant frequency
X_{LS}	Load sensor displacement
ρ_m	Mobile Dislocation Density
V_{out}	MS3110 output voltage
$\delta\sigma$	Noise in stress
N_f	Number of cycles to failure
ε_0	Permittivity of free space
$\dot{\gamma}_p$	Plastic shear strain rate
$\dot{\varepsilon}_p$	Plastic strain rate
κ	Relative permittivity of air

X_S	Sample displacement
T	Temperature
X_A	Thermal actuator displacement
V_{in}	Thermal actuator input voltage
V^*	True activation volume
σ_y	Yield Stress
CG	Coarse-grained
FCC	Face-centered cubic
FFT	Fast Fourier Transform
FEM	Finite Element Method
FIB	Focused Ion Beam
GB	Grain Boundary
HCF	High Cycle Fatigue
LCF	Low Cycle Fatigue
MEMS	Microelectromechanical Systems
MD	Molecular Dynamics
NC	Nanocrystalline
NSR	Noise-to-signal ratio
PSB	Persistent Slip Band
PED	Precession Electron Diffraction
PTP	Push-to-Pull
SEM	Scanning Electron Microscope
SPD	Severe Plastic Deformation
SOI	Silicon-On-Insulator
TEM	Transmission Electron Microscope

TKD	Transmission Kikuchi Diffraction
UFG	Ultra-fine Grained
VHCF	Very High Cycle Fatigue

SUMMARY

A MEMS-based *in-situ* TEM nanomechanical testing technique was developed to characterize mechanisms of plastic deformation in ultrafine-grained FCC metals via transient mechanical tests. Advances were made to an existing *in-situ* TEM nanomechanical tensile testing technique which uses a MEMS device that integrates a thermal actuator and two capacitive sensors to load and measure the uniaxial stress-strain response of a sample, respectively. Several characterization tools such as SEM along with Finite Element models were used to rationalize and correct the stress-strain curves obtained with the MEMS device. This MEMS device was used to measure the signature parameters of rate-controlling mechanisms of plastic deformation, like true activation volume, of ultrafine-grained FCC microspecimens and the reliability of the measurements was quantified. In a separate study, MEMS-based microresonators were used to study the effects of an 850-nm-thick Au coating on very high cycle fatigue behavior of Ni microbeams under extreme stress gradients. FIB, SEM and EDS techniques were used to characterize cracking in the microbeams and models were developed to rationalize the observations.

Three significant improvements were made to the existing MEMS-based *in-situ* TEM nanomechanical tensile testing technique: (1) Electronic sensing scheme was modified to obtain independent measurements from the two capacitive sensors compared to the old scheme of measuring only the difference between the capacitive sensor readings. (2) The elastic compliance due to the epoxy used for clamping the microspecimens was measured and its viscoplastic

behavior was characterized. Finite Element models along *in-situ* SEM characterization were used to establish that the plastic strain in the microspecimen can be accurately measured although there are compliance issues with obtaining elastic strains. (3) LabView code was developed to filter the electronic signals to maintain a low noise-to-signal ratio required for performing transient mechanical tests. Finally, issues related to drift in the TEM imaging while performing *in-situ* TEM experiments were mitigated. This enhanced MEMS technique was used to perform transient repeated stress relaxations on UFG 100-nm-thick Au and 200-nm-thick Al microspecimens inside the TEM. For Au microspecimens the true activation volume was found to be between 2-10 b^3 while for Al microspecimens it was between 5-20 b^3. The environment (vacuum vs air) was seen to have no effect on the activation volumes. It was found that the value of the true activation volume was very sensitive to the logarithmic fits used to obtain strain rates from the relaxation segments. A value greater than 0.9 for the R^2 of the fit and a noise-to-signal ratio smaller than 0.2 were identified as thresholds for reliable true activation volume measurements. It was found that the accurate determination of the calibration constant of the capacitive sensor measuring the stress α_{CS_2} was very crucial for the accuracy of stress as well as true activation volume. It was found that the error in true activation volume was directly proportional to the error in α_{CS_2}. GB dominated dislocation plasticity was observed in the Au microspecimens during the *in-situ* stress relaxations. The Al microspecimens were tested with a PTP device in combination with Precession Enhanced Diffraction (PED). From the PED maps grain growth was observed to occur in conjunction with plastic deformation.

The effect of an 850-nm-thick electroplated Au coating on the very high cycle bending fatigue behavior of electroplated Ni microbeams tested under resonance in air at high frequencies (~9 kHz) was investigated. The S-N curves show longer fatigue lives for the coated microbeams by at least a factor of 5 compared to the uncoated ones. This beneficial effect was demonstrated to be related to the delay in oxygen-assisted void formation, and therefore in void-assisted fatigue crack nucleation and growth in Ni. The improvement in fatigue life was limited by the fatigue degradation of the Au coating, which was also controlled by the formation of nanosized voids. Once a fatigue crack in the coating reached the interface, delamination occurred, leading to exposure of the underlying Ni to air and fast, "uncoated-like", fatigue degradation thereafter. This study highlighted that thin, noble metallic coatings can significantly improve the fatigue lives of metallic microbeams whose very high cycle fatigue behavior is sensitive to the environment and controlled by void formation.

These studies have provided new insights towards our understanding of the mechanisms of plastic deformation in ultrafine-grained metals. The development of this quantitative MEMS based *in-situ* TEM tensile technique is a major step towards integrating our understanding from computer simulations, which have become powerful enough to simulate volumes as big as a cubic micrometer, to the *in-situ* TEM observations directly. The study on the very high cycle fatigue behavior highlights a radical shift needed in our understanding of the mechanisms responsible for crack nucleation and propagation under extreme stress gradients.

CHAPTER 1

BACKGROUND AND MOTIVATION

1.1. Introduction

Thin films are classified as a layer of material whose characteristic dimension, in this case thickness, ranges from fractions of a nanometer to several micrometers. Thin films have aroused interest in researchers since the early 20th century. Unusual optical and electrical properties of deposits on the walls of glass discharge tubes made researchers curious. Eventually thin films found their way into large scale industrial use during the Second World War as optical coatings (mirrors, anti-reflective coatings, etc.). Since then advances in microscopy techniques and vacuum technology have paved the way to a wide variety of applications and materials being used as thin films. The technological revolution brought about by the microelectronics industry saw an unprecedented increase in the use of thin films made from metals as conductive interconnects between different layers of the assembly. Until the late 1990s, the attractive electronic, magnetic and optical properties were the cornerstone of interest in thin films, however it was soon realized that the mechanical properties cannot be neglected.

The thin films used as interconnects experience tremendous stresses due to the high temperature processing of these devices. This can lead to failure and less reliability of these devices. It has become progressively important to understand the mechanical properties of thin film materials both for extensive

applications as non-structural elements and for use as microelectromechanical devices [1].

This chapter aims to understand two aspects of the mechanical behavior of thin films: (i) the mechanisms responsible for the plastic deformation of thin films in Section 1.2 and (ii) the very high cycle fatigue behavior of thin metallic coatings at small scale in Section 1.3. Therefore, this chapter is divided into two parts, each part discussing the prior art separately.

1.2. Part I: Mechanical behavior of metallic thin films

Thin films exhibit mechanical properties significantly different from their bulk counterparts. Our understanding of the bulk material behavior generally fails to describe the mechanical properties of thin films because of the dominance of effects of surfaces/interfaces, finite number of grains in the structure and the role played by manufacturing process. It has been shown that the manufacturing process controls the microstructure and surfaces in the material and hence plays an important role in determining the mechanical properties [2].

When the characteristic length of the microstructure become comparable to the characteristic dimensions of the structure mechanical properties tend to depend on the size of the structure and start showing size effects. In metallic thin films this translates to mechanical properties showing size effects when the film thickness approaches the micrometer and submicrometer regime. Elastic mechanical properties are determined by atomic interactions and therefore they are not expected to differ between bulk material and thin films. On the other

hand, mechanical properties such as yield stress, fracture toughness which are determined by plastic processes differ between bulk material and thin films. Plasticity, fatigue and fracture processes depend on defect generation and evolution, which are mechanisms that operate on characteristic length scales. These length scales are comparable to the thickness of thin films and size of MEMS devices. Therefore it is important to understand the basic mechanisms of plastic deformation at micrometer structural length scale to be able to design the MEMS systems for better strength and reliability.

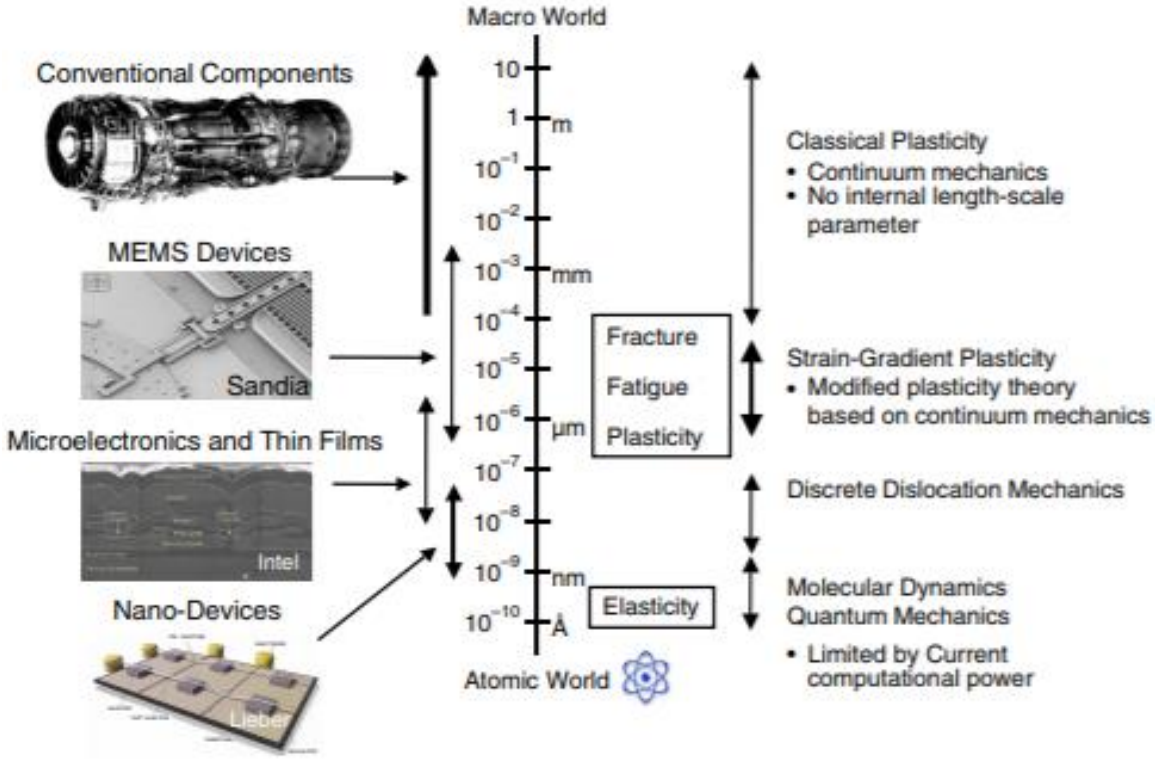

Figure 1.1 Schematic depicting the length scales at which mechanical properties start showing size effects [3].

The size effect in mechanical properties is not only observed in thin films but is a more general phenomena. The crucial idea is that whenever the geometric or microstructural length scales are comparable to the characteristic length scale of the plastic processes (i.e., submicrometer) mechanical properties

show size effect. In other words if the grain size, an important microstructural dimension, of a bulk material is reduced to submicrometer or below mechanical properties would differ from a coarse-grained bulk material. Metals with grain size less than 100nm are classified as nanocrystalline (NC) metals while those with grain sizes between 100nm to 1 μm are called ultrafine grained (UFG) metals. The average grain size of thin films is usually controlled by the thickness of the film due to something called the "specimen thickness effect" [4, 5].

1.2.1. Mechanical properties of NC and UFG FCC metals

This section reviews the elastic and plastic mechanical properties of nanocrystalline (NC) and ultrafine grained (UFG) FCC metals and the physical mechanisms responsible for the observed trends. These NC/UFG FCC metals may show reduced elastic modulus [6-12], higher yield stress [13-17], lower ductility [18-22] and higher strain rate sensitivity [23-27] compared to the corresponding coarse-grained metals. One important thing to keep in mind is that the studies presented below have been performed by different investigators on different materials using different processing techniques. Therefore, completely isolating the sole effect of grain size on the mechanical properties from the effects of processing such as defect density, porosity, etc. is not a trivial task. In order to capture the intrinsic effect of the small grain size on mechanical properties it will be desirable if a group conducts investigations on a single material using several processing routes, and it is surprising that it has not been done yet.

1.2.1.1. Yield strength

The size effect in mechanical properties can be easily observed in the yield stress of metals which is very strongly affected by the grain size. It is generally observed that the yield stress increases with decreasing grain size. In conventional grain size regime (micrometer or coarse-grained) the dependence of yield stress, σ_y, on the grain size, d, is very well captured by the Hall-Petch relation [28, 29]:

$$\sigma_y = \sigma_0 + kd^{-1/2} \quad (1\text{-}1)$$

where σ_0 is the friction stress and k is a constant. This is indeed an approximation, and a more general formulation is to use a power expression with exponent $-n$, where $0.3 \leq n \leq 0.7$.

In accordance to the Hall-Petch relation, nanostructured metals, because of their small grain sizes, are expected to be strong and hard. This has been indeed found to be the case by several studies which have measured the yield stress through uniaxial tension/compression tests and micro- or nano-indentation. It has been shown by several investigators that by decreasing the grain size by 2-3 orders of magnitude, nanostructured materials are at least 4-5 times stronger than their coarse-grained counterparts. The peak yield strength of pure nanostructured copper with grain size approaching approximately 20 nm can reach as high as 900 MPa [13-16] compared to 200 MPa for coarse-grained copper. Compressive and microhardness tests on NC-Pd have reported at least a 4-fold increase in yield stress for grain sizes ~50nm compared to coarse-grained Pd [14, 17].

However, it has been observed that the Hall-Petch relationship is not followed at the finer grain sizes and yield stresses in the UFG/NC are much lower than predicted by the Hall-Petch relation [13, 16]. In this context, it is important to remember that the strength values determined in bulk NC metals obtained by consolidating metal powders have to be considered with caution. Since the relative densities of materials produced this way were not near theoretical values, the strength values determined might have been lower than the true values. However, samples produced by severe plastic deformation methods also show similar behavior [30]. Some researchers have also reported a negative Hall-Petch slope for very small grain sizes, i.e., yield stress decreases as grain size is decreased below ~10-15 nm [13, 31, 32].

The breakdown in the Hall–Petch trend has been attributed to different deformation mechanisms that become dominant once the grain size is reduced down below a critical value [33]. Chokshi et al. [13] attributed this negative trend to diffusional creep in nanocrystalline samples at room temperature analogous to grain-boundary sliding in conventionally-grained samples at high temperature. Another common explanation for the break-down of Hall-Petch relationship is pile-up breakdown at small grain sizes. The concept of pile-ups has been at the root of the traditional explanation for the H–P effect. As the grain size is decreased, the number of dislocations piled up against a grain boundary decreases, at a fixed stress level, since this number is a function of the applied stress and of the distance to the source. Conversely, an increased stress level is needed to generate the same number of dislocations at the pile-up. At a critical grain size, we can no longer use the concept of a pile-up to explain the plastic

flow. Figure 1.3 (a) shows pile-ups for a grain size in the micrometer regime. The sources are assumed to be in the center of the grain, leading to positive and negative dislocation pile-ups generated by the activation of a Frank–Read source. As the grain size is reduced to the nanocrystalline regime, the number of dislocations at the pile-up is eventually reduced to one. Thus, the multiplying effect on the stress field is lost [34, 35]. This is shown in Figure 1.3 (b).

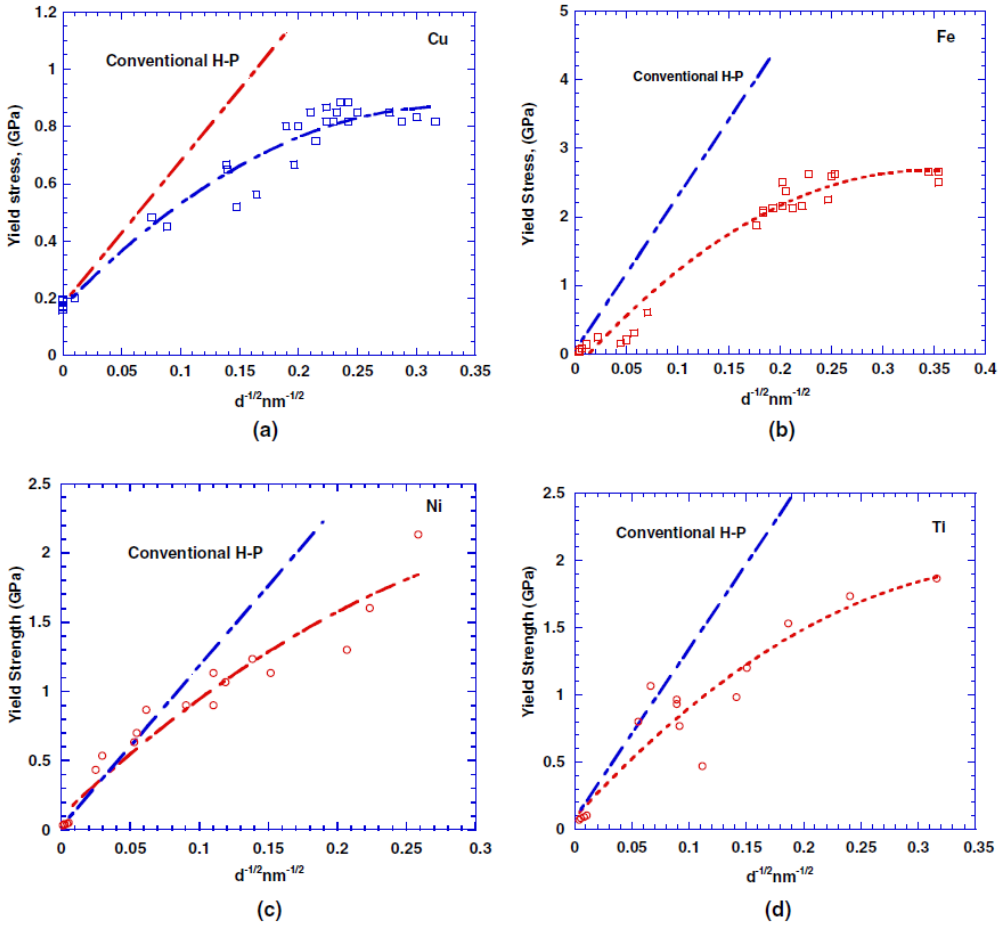

Figure 1.2 Plots showing the trend of yield stress with grain size for different metals as compared to the conventional Hall-Petch response: (a) copper, (b) iron, (c) nickel and (d) titanium [36].

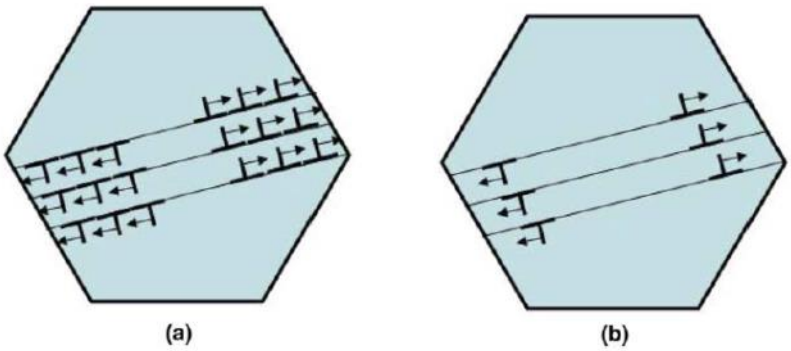

Figure 1.3 Breakup of dislocation pile ups: (a) microcrystalline regime and (b) nanocrystalline regime [36].

1.2.1.2. Ductility

Ductility is defined as the maximum amount of strain a material can endure without fracture or rupture. It is conventional wisdom that strengthening of a metal generally leads to loss of ductility. However, this depends on the mechanism of strengthening. Precipitation hardening and cold work increase the strength of metals at the expense of ductility of the metal, however grain size refinement or Hall-Petch strengthening does not lead to loss in ductility in coarse-grained metals. Hall-Petch strengthening is probably the only classical mechanism which leads to increase in both strength and ductility. But as we approach ultrafine or nanocrystalline regime the room temperature ductility is observed to decrease with reduction in grain size [18, 19] although the strength increases as discussed in Section 1.2.1.1. Most nanostructured metals fail in the elastic regime without undergoing any plastic deformation [20-22]. Further, metals that exhibit ductile behavior at conventional grain sizes show reduced ductility, sometimes brittle behavior, at the smallest nanometer grain sizes [37]. The loss of ductility in the NC/UFG regime prevents the use of these metals in

load bearing applications, to avoid catastrophic failures, even though they possess high strength.

Koch [38] identified three major sources of limited ductility in nanocrystalline materials, namely: (1) artifacts from processing (e.g., pores); (2) tensile instability; (3) crack nucleation or shear instability.

1.2.1.3. Strain hardening

NC and UFG metals cannot generally sustain uniform tensile elongation. Several reports show virtually no strain hardening after an initial stage of rapid strain hardening over a small plastic strain regime (~1-3%) which is different from the response of coarse-grained polycrystalline metals [37-41]. The conventional mechanism for the high work-hardening rates in FCC metals, including the formation of dislocation locks, formation of dipoles and significant pinning due to dislocation intersections, have yet to be experimentally confirmed for NC materials during room-temperature tensile tests [42].

That the strain hardening capacity is saturated very quickly is easy to understand for some nanostructured metals processed by severe plastic deformation (SPD) [30]. In this case, the refinement of the originally large grains into the NC or UFG regime is achieved through the accumulation and rearrangement of dislocations generated during SPD. Such NC or UFG metals usually contain a high density of dislocations in a heavy-deformation microstructure. Similar to the later stages of strain hardening of conventional metals [43], the strain hardening rate is very low because the densities of

dislocations appear to saturate due to dynamic recovery. Work hardening is observable only when very large additional strain is added. Strain hardening also remains insignificant in cases where NC/UFG bulk metals processed using SPD have undergone either dynamic recovery during SPD, or recovery through post-SPD annealing such that the dislocation density is low inside the grains [30, 41, 44].

In all dislocation models, strain hardening is a consequence of the fact that some fraction of the mobile dislocations that produce the strain do not exit through the surface, and are not absorbed in the grain boundaries, and do not annihilate each other, but are stored in the crystals or react with other dislocations to form new obstacles to continued slip [45]. The strain hardening capacity of NC metals is not expected to be very large as their extremely small grain size makes it difficult to store dislocations. Small grain size increases the image forces on dislocations and interactions with grain boundaries. Some estimates have predicted no dislocation pile-up (at least two dislocations) for d < ~ 20 nm [46]. This is shown as a schematic in Figure 1.4. Therefore, it follows from the above discussion that strain hardening in metals with grain sizes less than 20 nm is expected to be negligible.

However, even in metals with grain sizes are in the ultrafine regime strain hardening has been found to be diminishing at room temperature [27, 47-49]. This is due to the fact that dynamic recovery processes are the main reason for the inability to effectively accumulate defects, thereby saturating the defect density and therefore limiting the strain hardening.

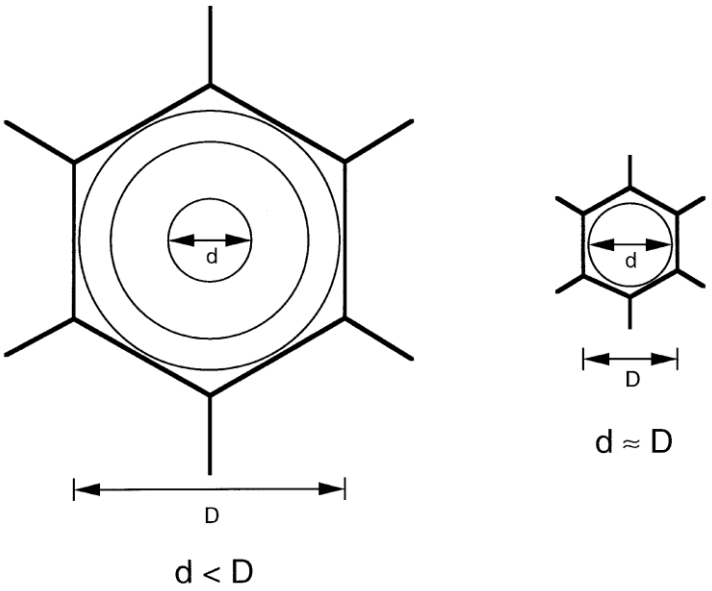

Figure 1.4 The dislocation pile-up mechanism must break down when the diameter d of the smallest dislocation loop does not fit into a grain of size D [50].

1.2.1.4. Strain rate sensitivity

Strain rate sensitivity m measures the sensitivity of the material response to the applied strain rate. When it is used to describe the effect of strain rate on the yield stress, it is defined as:

$$m = \partial \ln \sigma / \partial \ln \dot{\varepsilon} \qquad (1\text{-}2)$$

The strain rate sensitivity is found to increase in the ultrafine and nanocrystalline regime compared to the coarse-grained metals. Values as high as $m \sim 0.5$ have been reported for NC Ni [23], Au [24] and Cu [25]. But it has been argued that under very slow strain rates observed during the creep behavior, deformation can be entirely controlled by diffusional mechanisms such as Coble creep (m = 1) and grain boundary sliding (m = 0.5) [26, 27]. But nevertheless, compared to large-grained Cu, m for SPD processed UFG Cu tested in quasi-static strain rate regime

have been found to be around 0.015 [26]. Values in the range of m~0.04 have been reported for cryo-rolled UFG Cu [27]. These m values are also substantially elevated compared to large-grained FCC metals whose m values are around 0.004 [51]. Figure 1.5 shows the variation of m with grain size d as documented by several experimental studies for Cu and Ni. It can be clearly seen that strain rate sensitivity for FCC metals increases when the grain size reduces to NC and UFG regimes. Another important aspect that can be seen from Figure 1.5 is the scarcity of experimental data regarding the m values at reduced grain sizes. A systematic study from coarse-grained conventional microstructures down to UFG/NC grain sizes would therefore be particularly useful.

Strain rate sensitivity m is associated with a corresponding activation volume v by Eq. (1-3). Higher m values mean lower v, and this implies a change in the rate controlling deformation mechanisms as described in Section 1.2.3. The activation volumes associated with NC/UFG metals are in the range of 1-10 b^3, while for CG metals it is of the order of ~1000 b^3.

$$m = \frac{\sqrt{3}kT}{v\sigma} \tag{1-3}$$

where k is the Boltzmann constant, T is the absolute temperature and σ is the uniaxial flow stress.

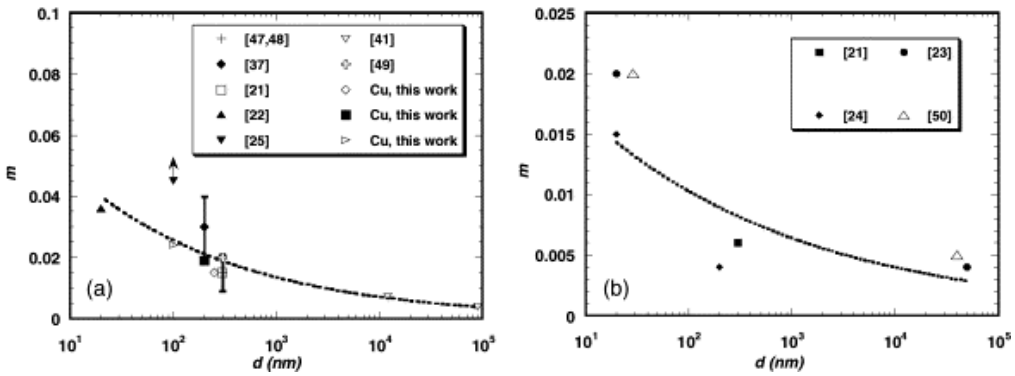

Figure 1.5 m vs d for (a) Cu and (b) Ni [26].

1.2.2. Deformation mechanisms in NC and UFG FCC metals

Most of the deformation mechanisms known to operate in coarse-grained metals are also found in NC/UFG metals. What is notable though, is the striking difference in the regimes at which these mechanisms operate in nanograin compared to a large micron-size grain, and in the intrinsic relation and competition between these mechanisms.

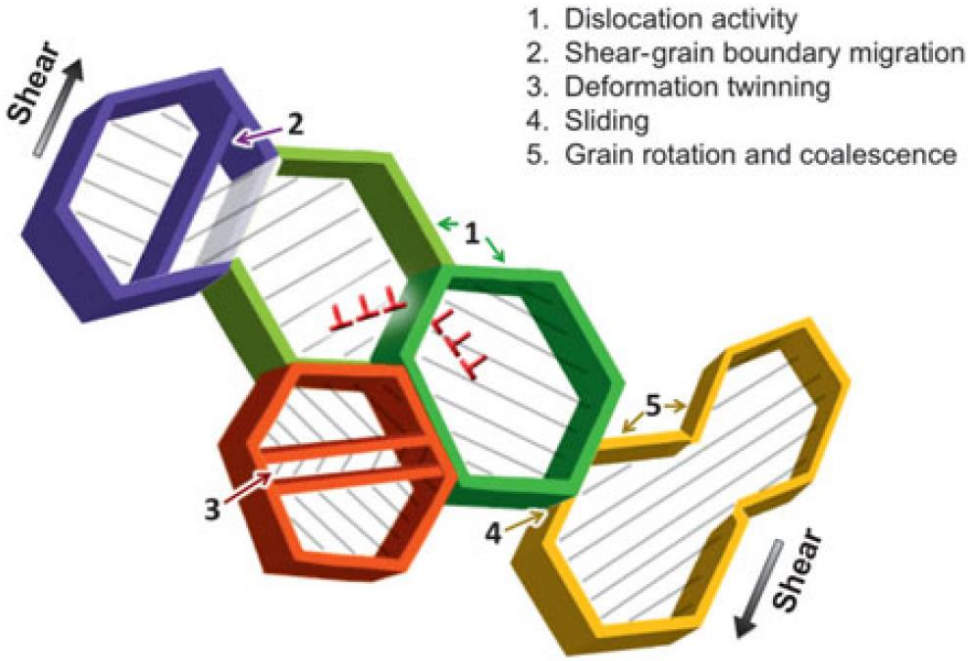

Figure 1.6 Schematic of various deformation mechanisms that can operate in NC/UFG metals [52].

1.2.2.1. Dislocation-based mechanisms

In coarse grained metals the dominant deformation mechanism is usually the slip of dislocations in the grains interior. The dislocations are generated and stored in the grains interior during plastic deformation. The dislocation based mechanisms for plastic deformation have been studied for well over 70 years. Therefore, we expect to see dislocation activity even in smaller grains. Indeed,

dislocations have been directly observed by several researchers in NC/UFG metals in the TEM, both during in-situ straining and also inferred from the post-mortem imaging of fractured samples [53-55]. There also have been several reports of the lack of observation of any kind of dislocation activity in metals with grain size smaller than 20 nm [56]. In general though, dislocation-based plasticity is observed above a critical grain size somewhere in the vicinity of 30–100 nm. This critical grain size has not been pinned down conclusively, and is undoubtedly dependent on the metal, its microstructure (e.g. texture, impurities, grain size distribution) and the processing history. Below the critical size, if dislocations are moving, they do not leave any evidence in their wake. For FCC metals, which have been the object of most of the studies, it appears that this critical grain size is around 30 nm [57].

Dislocations in coarse grained metals are believed to be generated at Frank-Read sources especially those formed due to double cross slip [58, 59]. A Frank-Read source operates at the shear stress $\tau_{F-R} \approx Gb/L$, where G denotes the shear modulus, b the magnitude of Burgers vector, and L the source size, that is, the distance between two pinning points for the initial gliding dislocation segment. For geometric reasons, the maximum size L_{max} of a conventional Frank-Read source that can operate in a grain of size d is estimated as $L_{max} \approx d/3$ [60]. Therefore, in order to activate a Frank-Read source, one needs to apply a critical minimum shear stress of:

$$\tau_{F-R} \geq 3Gb/d \tag{1-4}$$

This stress rapidly increases with decreasing grain size d. According to Eq. (1-4), the critical stress for activating a Frank- Read source can be increased to

unrealistically huge values of G/40-G/10 in NC metals with grains sizes of 10–30 nm or smaller. Therefore, dislocation generation via Frank-Read sources in metallic nanomaterials is significantly hampered, or even completely suppressed when the grain size decreases to the order of 10 nm.

These Frank-Read sources exists in the grain interior as discussed above. However, there are also arguments that Frank-Read source has not been observed experimentally [61]. Theoretically, any dislocation segment that can slip but have two ends pinned can act as a Frank-Read source. Considering that dislocations slip on different slip systems often interact with each other to form dislocation jogs and networks, it is reasonable to assume that the Frank-Reed source can easily form in the interior of coarse-grains. When grains are refined to a critical size below 100 nm, dislocations often no longer exist in the grain interior. Although trapped dislocations have been observed in grains much smaller than 100 nm, and even down to 5 nm [42, 62], these are exceptions in a small fraction of grains instead of typical cases. Shown in Figure 1.7 is hierarchy and size ranges of different structural features of nanostructured Ti, which was processed by severe plastic deformation (SPD) [63]. As shown, the interiors of grains or sub-grains smaller than 100 nm are largely dislocation free. Without dislocations in the interior of nanometer-sized grains, the conventional dislocation sources that operate in coarse-grained metals no longer work.

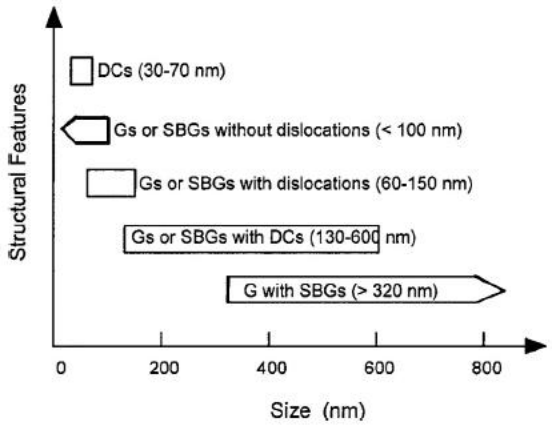

Figure 1.7 Hierarchy and size ranges of different structural features in nanostructured Ti processed by severe plastic deformation. Grains and subgrains are largely dislocation free in their interior when their sizes are reduced to below 100 nm [63]. The acronyms are G – grains, SBG – subgrains, DC – dislocation cells.

It is commonly understood that grain boundaries act as barriers to dislocation motion [58]. The microstructural constraint on the size of the Frank-Read sources limits dislocation sources in the grain interiors of NC/UFG grains and leads to intricate interplay between dislocation and grain boundary processes [64]. For grain sizes smaller than 1 μm, mobile dislocations must be nucleated from sources other than Frank-Read sources, such as the grain boundaries or grain junctions [65]. Since, the fraction of grain boundaries increases drastically at smaller grain sizes, grain boundaries can become effective dislocation sources and sinks [53, 55, 66]. Emission of dislocations from grain boundaries has been experimentally documented in UFG meals [55, 67] and NC metals [53, 68].

Dislocations emitted by GBs are not only full dislocations but they are also emitted as partial dislocations. Typically, in all of the early MD simulations for NC metals performed at grain sizes below 20nm dislocations were found only in

the form of single partial dislocations [31, 69, 70]. This was later experimentally verified under high-resolution electron microscopy (HRTEM) [71-73]. This has been justified because when the grain size is below a critical size, it becomes easier to emit partial dislocations than full dislocations [64, 74]. It is found that in nanocrystalline Ni full dislocations on the non-equilibrium GBs are often dissociated into two partials, which can readily glide into the grain interior, with a wide stacking fault in-between [75]. Another reason for the observation of partial-slip-generated stacking fault is due to the large splitting distance between the leading and trailing partials of a full dislocation [74, 76]. Due to the orientation difference between the Burgers' vectors of the leading and trailing partials, the applied stress may drive the two partials further apart. When the splitting distance is larger than the grain size, the trailing partial will not have the opportunity to be emitted from the GB and the leading partial produces a stacking fault across the grain. Since the emission and slip of partial dislocations from GBs leave behind stacking faults, this can have beneficial effect on the mechanical properties by increasing the ductility and work hardening in the metal.

1.2.2.2. Deformation twinning

Classically, the phenomenon of deformation twinning is limited to large grain sizes (>10μm) and metals with low stacking fault energy such as Cu [77], although high strain rate and low deformation temperature can significantly promote twinning. In comparison, nanocrystalline materials have a very different

behavior in the formation of stacking faults and deformation twins [64]. Deformation twinning in NC Al was found by MD simulations [65, 68] and then confirmed experimentally [78, 79]. Nanocrystalline FCC metals are found to generally deform by twinning more easily, especially in those FCC metals with medium to high stacking fault energy, although twinning may become difficult again at very small grain sizes [80].

Coarse-grained FCC metals are believed to twin via several conventional mechanisms including the pole mechanism [81], prismatic glide mechanism [82], faulted dipole mechanism [83], or other mechanisms [84, 85]. These mechanisms often require a dislocation source in the grain interior to operate. This poses a problem for NC metals and alloys since their grain interior are often free of dislocations as discussed earlier.

Twinning mechanisms observed and proposed in NC FCC metals by both MD simulations [65, 68] and HRTEM [64] include homogeneous nucleation by the coincidental overlapping of two stacking fault ribbons formed by dissociated lattice dislocations [71], grain boundary splitting and migration [79], overlapping of a stacking fault from the grain boundary with a dissociated lattice dislocation [75], partial dislocation emission from the GBs [72, 86], cross-slip of twinning partials [87, 88], the dislocation rebound at GB [87, 89], etc. The primary mechanism for the formation of deformation twins in NC FCC metals is partial dislocation emission from GBs. A partial multiplication mechanism on the GB has been proposed to explain why partials can be emitted from every slip plane to form a deformation twin [90].

1.2.2.3. Grain boundary sliding

Grain boundary sliding (GBS) means a relative shear of neighboring grains across the grain boundary as shown in Figure 1.8. It is clear that sliding alone cannot accomplish this deformation. Plastic flow is necessary to accompany sliding in order to accommodate the grains. In coarse-grained metals there are two separate, and mechanistically distinct, types of GBS [91]. The first type of GBS refers to the relative displacement of adjacent grains where the grains retain essentially their original shape but they become visibly displaced with respect to each other. This type of GBS is designated *Rachinger sliding* and it occurs in a polycrystalline matrix under creep conditions where there is a net increase in the number of grains lying within the gauge length along the direction of the tensile stress. In practice, grains have irregular shapes in polycrystalline matrices and it follows, therefore, that Rachinger sliding must be accommodated by some intragranular movement of dislocations within the adjacent grains. The second type of GBS occurs exclusively in Nabarro- Herring and Coble diffusion creep and it refers to the boundary offsets that develop as a direct consequence of the stress-directed diffusion of vacancies. This type of GBS is designated as *Lifshitz sliding* [92].

There are several studies experimentally reporting GBS at room temperature in UFG and NC metals [93-95]. However, there are new and different accommodation mechanisms in NC metals as compared to the mechanisms during superplasticity of coarse-grained metals where GBS is the dominant mechanism. GB sliding is found in large number of MD simulations of

NC metals at low temperature ($T < 0.3T_m$) [31, 96, 97]. At present there is a firm consensus among researchers that GB sliding is an important deformation mode in NC and UFG metals at room temperature but the atomistic mechanisms responsible for or accommodating GB sliding are still under debate. These mechanisms include stress-assisted free volume migration [97], GB diffusion [98], generation and motion of GB dislocations [99].

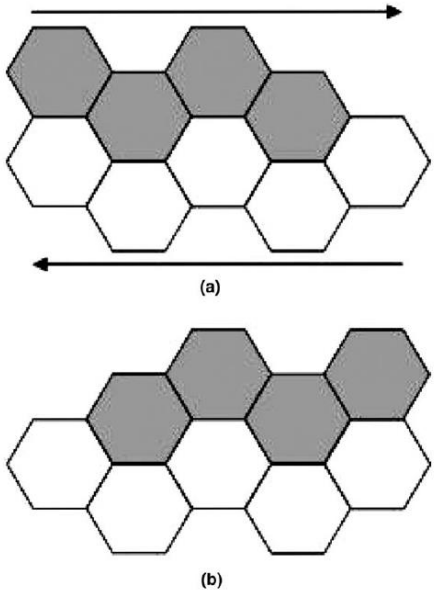

Figure 1.8 Grain boundary sliding model: (a) initial position of grains and (b) position after top layer has slid to right [36].

1.2.2.4. Grain rotation

It has been shown by post deformation and in-situ TEM experiments that plastic flow can be accommodated by the rotations of crystal lattice or grain rotation which plays an essential role in the deformation of NC metals [54, 62, 100-102]. One way by which grains can rotate is by disclination motion. A disclination is a line defect characterized by a rotation of the crystalline lattice

around its line [100]. Motion of a disclination dipole, which is a combination of two disclinations, causes plastic flow accompanied by crystal lattice rotation behind the disclinations.

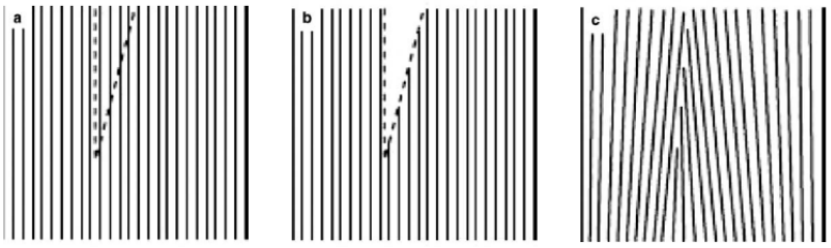

Figure 1.9 Illustration of the elastic distortion associated with a partial wedge disclination (or terminating tilt grain boundary). (a) A set of planes in a perfect crystal. A wedge shaped piece of material is removed from the crystal in (b), and the new surfaces are allowed to close in (c) to fill the wedge. The resulting crystal in (c) contains a terminating tilt grain boundary, i.e., a terminating array of edge dislocations, and considerable elastic distortion, which increases the elastic strain energy of the remaining solid [103].

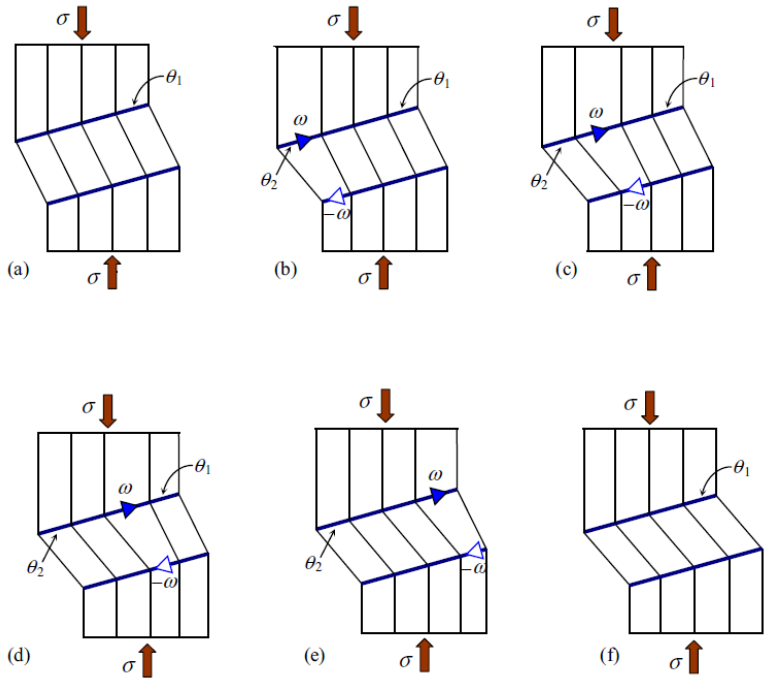

Figure 1.10 Misorientation band in a crystal under stress (schematically). Disclinations (triangles) are generated at grain boundaries and compose a dipole configuration. Their motion along grain boundaries mediates plastic flow associated with crystal lattice rotation within the misorientation band [99].

1.2.2.5. Stress driven grain boundary migration

Stress-driven migration of GBs can contribute to both plastic flow and grain growth in NC/UFG metals [104-108], as with their CG counterparts; see, e.g., [109, 110]. In particular, grain growth mediated by GBs migration can result in nano-to-CG transformation, which causes strain softening. Following experimental observations [106, 108, 111] and computer simulations [112, 113], GB migration and grain growth extensively occur in NC/UFG metals deformed at high stresses. GB migration and grain growth in UFG Al and Al-Mg films was observed under in-situ indentation under TEM at room temperature [105, 114]. Stress-driven migration of GBs was identified as an important deformation mechanism in UFG metals subjected to high stresses during indentation at room temperature. It was reported that NC Al film has significant grain growth at room temperature during tensile tests at high stresses [108]. It is important to note that substantial grain growth was observed exclusively in regions with high local stresses. Specifically, grain growth occurred in vicinities of crack tips serving as effective stress concentrators. Stress-driven GB migration is believed occurred, leading to grain growth.

1.2.2.6. Interaction between different mechanisms and deformation maps

In general, various deformation modes can concurrently operate and significantly affect each other in nanostructured metals with NC and/or UFG grains. In particular, various deformation mechanisms accommodate each other

in nanostructured metals, so that there exists effective interaction between such mechanisms [115]. There are several important examples of interacting deformation mechanisms in NC/UFG metals. Dislocation slip effectively accommodates GB sliding through emission of dislocations from triple junctions that stop GB sliding [99]. At the same time, GB sliding itself can be stimulated by slip. Dislocations that slip in the grain interior reach GB regions and undergo splitting transformations [30]. As a result of such transformations, GB dislocations are formed whose motion leads to GB sliding. Thus, the dislocation slip and GB sliding sustain/accommodate each other, providing effective concurrent operation in nanostructured metals. GB sliding can also be accommodated by grain rotations [55, 99]. Experimental data indicates occurrence of concurrent GB sliding and grain rotations in NC Pd and Ni [116, 117]. This interplay between GB sliding and rotational deformational modes plays an important role in superplastic deformation in nanostructured metals.

Along with GB sliding, GB migration under stress can occur as an effective deformation mechanism in NC/UFG metals. Following [118], stress-driven GB sliding and migration can cooperatively occur as one process mediating plastic flow in NC metals. During such a cooperative operation, mutual accommodation of defects generated owing to GB sliding and those generated owing to GB migration comes into play. The cooperative GB sliding and migration process serves as a special deformation mode that is more energetically favored then "pure" GB sliding. Theoretical results [118] are consistent with experimental observations [119, 120] of concurrent GB sliding and grain growth in plastically deformed NS materials. In a recent study concurrent GB migration and grain

rotation in thin nanocrystalline Au films with a thickness of 10 nm and average grain size of 18 nm was observed in situ at room temperature using a TEM [101].

It is also important to note that different deformation mechanisms can be dominant in a NC/UFG metal, depending on its grain size, temperature, strain rate and stress. Figure 1.11 shows the statistical distribution of the probability of different deformation mechanisms in NC Au films. It can be seen that above 20nm grain size, the dominant deformation mode is plasticity by full dislocations. On the other hand for smaller grain sizes, GB migration dominates the deformation. Figure 1.12 shows a deformation map for nanostructured FCC metals by [99]. Here also, slip by full dislocations dominates grain sizes above 100 nm. But for smaller grain sizes Coble creep dominates for slower strain rates and GB sliding and migration dominate during higher strain rates. Twinning and slip by partial dislocation occupy the region between 30-100 nm grain size and moderate to high strain rates.

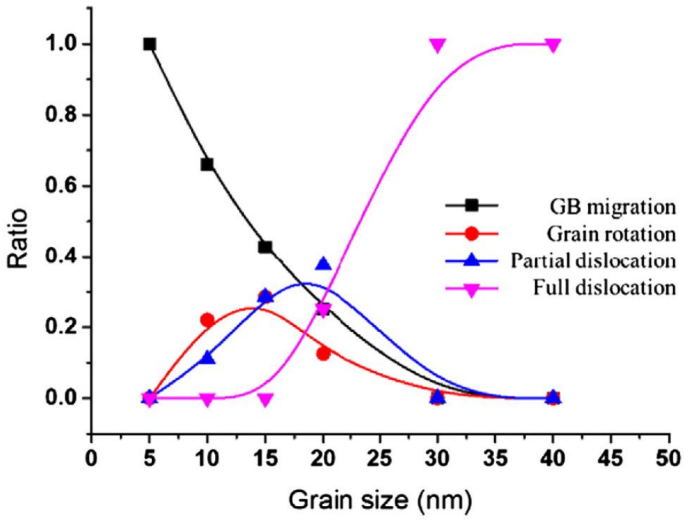

Figure 1.11 Statistical distributions of the probability for the action of deformation mechanisms in grains of NC Au films as functions of grain size [121].

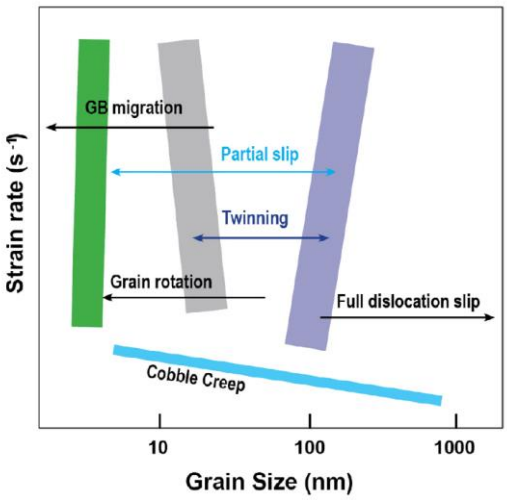

Figure 1.12 Schematic deformation mechanism map for nanostructured FCC metals with medium to high stacking fault energy at room temperature [99].

1.2.3. Activation volumes of NC and UFG FCC metals

1.2.3.1. Activation volume theory

In this section, a brief overview is provided of the classical theory behind stress-assisted, thermally activated dislocation plasticity, and of the use of transient tests to calculate the activation volume associated with the governing deformation mechanisms. More thorough treatments of these topics can be found in textbooks [122, 123], and additional overviews in [124-128]. First, the Orowan equation is invoked, highlighting the fact the plastic shear strain rate ($\dot{\gamma}_p$) is governed by both mobile dislocation density (ρ_m) and dislocation velocity (v):

$$\dot{\gamma}_p = \alpha \rho_m v b \tag{1-5}$$

where b is the Burgers vector and α is a geometric coefficient. Since the dislocation glide velocity is thermally activated, v is given by:

$$v = v_0 \exp(-\Delta G(\tau^*)/kT) \tag{1-6}$$

where v_0 is the pre-exponential factor, k is the Boltzmann constant, T is the temperature, and ΔG is the activation energy to overcome the local barrier that is associated with a specific dislocation mechanism.

Because the dislocation mechanism is also stress assisted, the magnitude of ΔG is a (decreasing) function of the local shear stress, τ^*. Here, the applied shear stress τ is assumed to be the sum of two components, highlighting the necessity for the applied stress τ to counterbalance both lattice resistance and local microstructural barriers for dislocation glide:

$$\tau = \tau_i + \tau^* \tag{1-7}$$

where τ_i is the internal stress and τ^* is the effective stress. The internal stress τ_i is the athermal contribution to the flow stress, resulting from long-range internal stresses impeding the plastic flow, the temperature dependence of which is weak in FCC metals. The effective (or local) stress τ^* is the thermal component of the total stress, and accounts for the stress needed to overcome the short-range barrier responsible for the temperature and strain-rate dependence in FCC metals. Distinct mechanisms can have similar ΔG values, hence it is useful to assess the variation of ΔG with τ^* to further identify the governing mechanism. Specifically, the true activation volume, V^*, is defined as:

$$V^* = -\frac{\partial \Delta G}{\partial \tau^*} \tag{1-8}$$

This equation highlights the fact that during thermal activation, the effective stress τ^*does work on the activation volume V^*, thereby reducing the

effective energy barrier ΔG as illustrated in Figure 1.13. Physically, V^* is proportional to the number of atoms involved in the thermally activated process responsible for the dislocation overcoming the local barrier, which is why it is considered a signature of that specific mechanism. For competing processes with the same activation energy ΔG, the operating mechanism can be determined by calculating the true activation volume, as different rate processes can have very different V^* values [128].

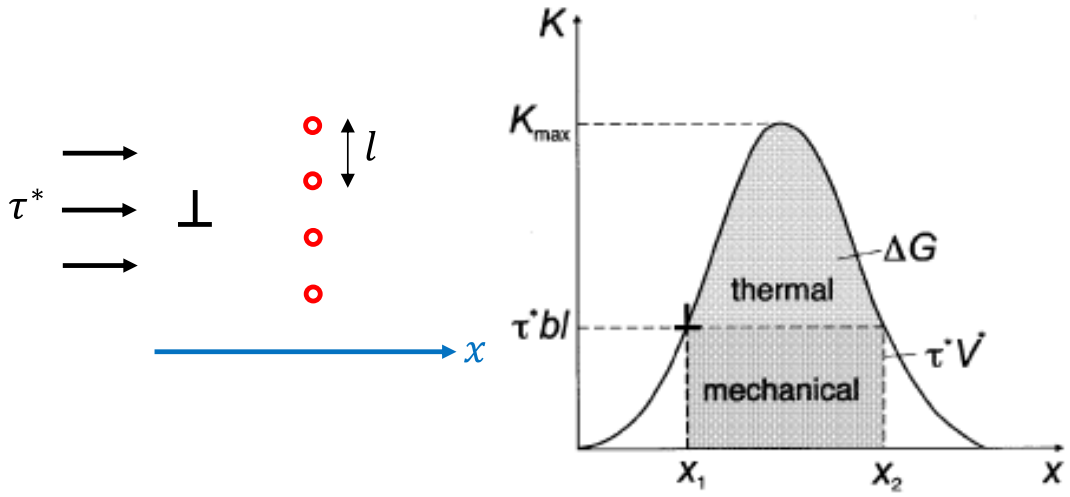

Figure 1.13 Schematic showing the contributions of thermal and mechanical driving forces to overcome an energy barrier created by an obstacle of size l for a dislocation to pass through [129].

Based on Eqs. (1-5), (1-6), and (1-8), the true activation volume is equal to:

$$V^* = kT\frac{\partial ln\dot{\gamma}_p}{\partial \tau^*} \tag{1-9}$$

given that at a given instant, ρ_m is constant and therefore $\dot{\gamma}_p$ (a measurable quantity) can be used instead of dislocation velocity v. Experimentally, the derivative in Eq. (1-9) can be calculated by measuring small finite changes, more specifically during a stress relaxation segment:

$$V^* = kT\frac{\ln(\dot{\gamma}_{p2}/\dot{\gamma}_{p1})}{\Delta\tau^*} \quad (1\text{-}10)$$

where $\dot{\gamma}_{p1}$ and $\dot{\gamma}_{p2}$ represent the plastic shear strain rate at the beginning and end of the segment, respectively, and $\Delta\tau^*$ represents the decrease in effective stress during the segment. The issue with Eq. (1-10) is that the mobile dislocation density ρ_m may not necessarily be constant during the relaxation segment, thereby invalidating the assumption of a frozen microstructure used for Eq. (1-9). Because both dislocation density and dislocation velocity change during a transient relaxation test, an apparent activation volume, V_a can be calculated as:

$$V_a = kT\frac{\ln(\dot{\gamma}_{p2}/\dot{\gamma}_{p1})}{\Delta\tau} = \sqrt{3}kT\frac{\ln(\dot{\varepsilon}_{p2}/\dot{\varepsilon}_{p1})}{\Delta\sigma} \quad (1\text{-}11)$$

where $\Delta\tau$ represents the decrease in total applied stress, since both τ_i and τ^* vary during the relaxation segment. The right-hand side term of Eq. (1-11) is used if normal stress σ and strain ε are employed instead of the shear values (we have $\sigma = \sqrt{3}\tau$). Compared to $V^*$and Eq. (1-8), V_a represents the effect of the total shear stress on the free energy:

$$V_a = -\frac{\partial\Delta G}{\partial\tau} \quad (1\text{-}12)$$

The following phenomenological equation is often employed to calculate V_a, in cases where the stress relaxation follows a logarithmic variation with time:

$$V_a = -\frac{kT\ln(1+t/c_r)}{\Delta\tau} = -\frac{\sqrt{3}kT\ln(1+t/c_r)}{\Delta\sigma} \quad (1\text{-}13)$$

In order to calculate V^*, Eq. (1-10) is employed during a repeated stress relaxation test which allows for the separation of the effects of dislocation density and dislocation mobility on the strain rate. Specifically, the specimen is reloaded

at the end of the first relaxation segment, typically to a stress value equal to the initial stress of the first relaxation segment. The critical assumption is that the reloading occurs at a constant dislocation density ρ_m, either because we can assume that the reloading is elastic, or because the reloading occurs fast enough such that there is no time for significantly increasing ρ_m. Hence, with this assumption, the observed increase in plastic shear strain rate after the reloading (initial rate of the second relaxation segment, $\dot{\gamma}_{i2}$) with respect to the rate right before the reloading (rate at the end of the first relaxation segment, $\dot{\gamma}_{f1}$) only results from an increase in v, and the true activation volume can be calculated using Eq. (1-10) for the case of the reloading [126]:

$$V^* = kT\frac{\ln\left(\dot{\gamma}_{i2}/\dot{\gamma}_{f1}\right)}{\Delta\tau_{12}} = \sqrt{3}kT\frac{\ln\left(\dot{\varepsilon}_{i2}/\dot{\varepsilon}_{f1}\right)}{\Delta\sigma_{12}} \tag{1-14}$$

where $\Delta\tau_{12}$ is the increase in stress during reloading. Here $\Delta\tau_{12}$ also represents a change in effective stress τ^* based on the assumption of a constant ρ_m.

This theory mainly concerns with the thermal activation of dislocations in a classical context of interactions of dislocations with other dislocations or obstacles. These obstacles can include grain boundaries in a process such as pinning of dislocations by grain boundaries. However, rate controlling processes involving grain boundaries such as dislocation emission through grain boundaries, grain boundary sliding, grain boundary diffusion must also be included when activation volumes of nanocrystalline materials are been considered. Therefore, this framework is extended to consider any thermally activated process and Eqs. (1-6), (1-8) and (1-12) are valid for any process that is thermally activated.

Different rate processes can have drastically different characteristic activation volumes; for example, $V^* \approx 0.1\, b^3$ for lattice diffusion versus $V^* \approx 1000\, b^3$ for the Orowan looping of a dislocation line across the pinning points in coarse-grained metals, where b is the Burgers vector length. As a result, the activation volume can serve as an effective kinetic signature of deformation mechanism. This is illustrated by the schematic in Figure 1.14, where the activation volume corresponds to the slope of an activation energy curve plotted as a function of stress. Notice that while the activation volume generally varies with stress, it is often treated as a constant when the rate or stress change is not large. Suppose the two competing processes have the same activation energy (indicated by the short-dash line in Figure 1.14) giving the same rate of transition, one can use the activation volume to identify the operative one in an experiment or a simulation. Furthermore, Figure 1.14 indicates that for the two processes with different activation volumes, the process with a higher energy barrier at low stresses may change to have a lower barrier at high stresses. This cross-over of energy barriers often underlies the switching of the rate-controlling mechanism in experiments.

1.2.3.2. Activation volumes for NC/UFG metals

Plastic flow in coarse grained FCC metals is governed by motion of dislocations and has been extensively studied [129]. As described in the previous section, dislocations interact with various types of obstacles and thermal activation can sometimes assist the dislocations to overcome obstacles with a

sufficiently low energy barrier. At room temperature, several obstacles for dislocation glide have been reported and each of them have a characteristic activation volume. A dislocation cutting forest dislocations has a very large activation volume, generally of the order of $1000b^3$ [122, 124]. However, activation volume values of the order of $40b^3$ have also been reported for cross-slip [130]. A kink-pair mechanism exhibits small activation volumes in the range of $10b^3$ [131].

Figure 1.15 shows activation volumes obtained by different investigators for NC and UFG metals at room temperature. Karanjgaokar et al. [132] report apparent activation volumes of $6.4b^3$ at room temperature which monotonically increases to $29.5b^3$ at 110° C for 850-nm-thick Au films with grain size of 64 nm tested at strain rates of 10^{-5} -10^{-2} s^{-1}. They suggest grain boundary diffusion plays an important role in the plastic deformation in this strain rate regime although the activation volume is not ~1 b^3. They propose that since these grain boundary processes occur together with other deformation mechanisms that ensure geometric compatibility, a coupling of no less than two deformation mechanisms is necessary. Thus, the activation volume for GB diffusional processes would be higher than the expected true activation volume of 1 b^3 for a purely diffusional process. Jonnalagadda et al. [10] reported a change in activation volume from 4.5 b^3 to 12.5 b^3 after a strain rate of 10^{-4} s^{-1} was reported for Au films with 30 nm grain size and was attributed to a change from grain boundary processes to dislocation plasticity.

On the other hand, several researchers do not consider Coble creep and grain boundary sliding to dominate tensile deformation in the grain size range

greater than 30 nm. Wang et al. [124] obtained true activation volume of the order of 10 b^3 in Ni thin films with average grain size of ~30nm. Although the activation volume is similar to values obtained for Au, they disregard Coble creep and grain boundary sliding to be dominant because the activation volumes are not close to 1 b^3. Instead they suggest interactions of partial dislocations with grain boundaries to control the strain rate.

Mohanty et.al [125] also report true activation volumes for NC Ni in the vicinity of ~10 b^3 but they do not attribute this value to any specific mechanisms instead they propose that multiple mechanisms like dislocation-grain boundary interactions (by dislocation propagation and/or nucleation), grain boundary diffusion and grain boundary sliding can have activation volumes in the vicinity of ~10 b^3. They further say that activation volume represents the sum total of all operative deformation mechanisms.

Gianola et al. [133] have reported activation volumes in the range of 10-55 b^3 ($m \sim 0.036$-0.14) for 300 nm thin NC aluminum films with average grain size of 104 nm. They have associated the high strain rate sensitivities to stress-assisted grain growth and MD simulations predict these high m values for GB mediated processes such as GB sliding, migration and dislocation nucleation. However, these MD simulations were carried out at very high strain rates although the experiments were conducted at much lower strain rates ranging from 10^{-5} to 10^{-3} s^{-1}.

As described in this section there is a lot of discrepancy in determining the dominant mechanisms operating in nanocrystalline metals partly arising due to the various interpretations of the meaning of activation volume itself.

Quantitative in-situ TEM experiments seem to be the way forward to better understand these mechanisms and the meaning of activation volumes associated with these mechanisms.

Further, there is no established relationship between the true and apparent activation volumes. Mohanty et al. report true activation volume is always lower than the apparent activation volume, but the difference is large at low strains and becomes almost negligible at strains $\gtrsim 8\%$ for NC Ni with average grain size 26nm [125]. Wang et al. also observe apparent activation volumes higher than the true activation volumes at low plastic strains, even at high temperatures [124, 134]. Conrad calculates that the true activation volume for dislocation glide is 1.5 times the apparent activation volume [135]. Duhamel et al. predict, using a model considering exclusively grain boundary sliding and dislocation emission from grain boundaries, that the apparent activation volume is greater than the true activation volume and it reaches a maxima at a critical effective stress [136]. Using this technique, this can also be further investigated.

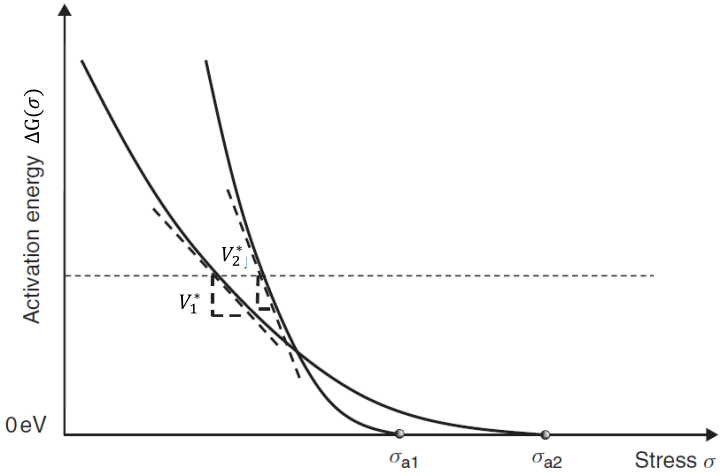

Figure 1.14 Schematic of the stress-dependent activation energy for two competing thermally activated processes. They have different activation volumes (V_1^* versus V_2^*) and athermal threshold stresses (σ_{a1} versus σ_{a2}) [137].

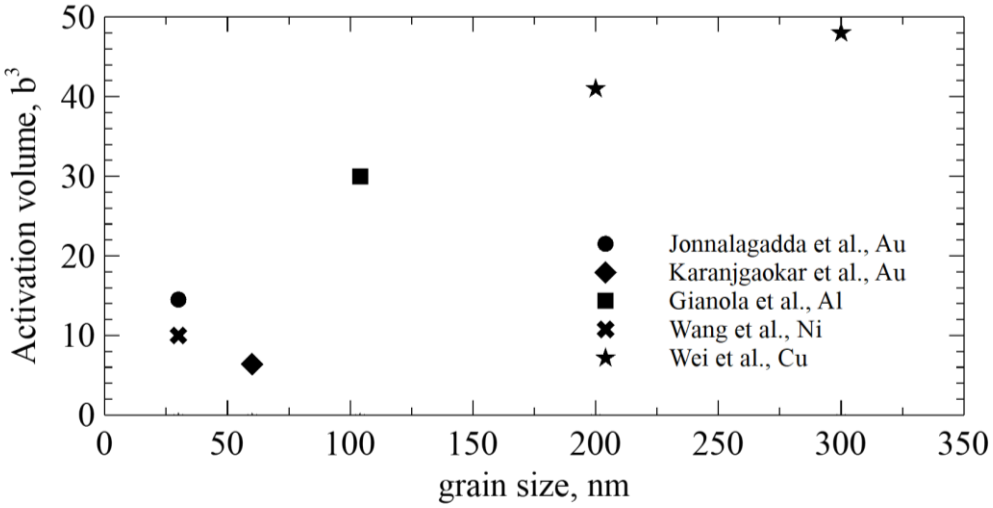

Figure 1.15 Activation volumes of NC and UFG metals at room temperature from the literature.

1.2.4. Small scale mechanical testing

It is obvious that the micro- and nano-sized structures such as thin films, nanowires, etc. require mechanical testing methods at the relevant length scales to quantitatively determine their mechanical properties such as elastic modulus, flow stress, and fracture toughness, however the same holds true for bulk materials with nano-sized microstructures. Bulk materials have undergone significant developments in the last decades to enhance their structural and functional properties often rendering them as nanomaterials from a microstructure perspective e.g., bulk nanocrystalline metals. Micro- and nano-mechanical testing methods can often shed light into the deformation mechanisms of these bulk materials. Further, the fracture of a bulk material begins with local formation and accumulation of defects, therefore any bulk material benefits from the understanding of mechanical phenomena at the

nanoscale. Mechanical testing at the micro- and nanoscales is quite challenging. Since the physical dimensions of specimens range from a few hundred micrometers down to as small as 1 nm, novel mechanical testing methods have been developed to successfully measure their properties. Specimens of such size are easily damaged through handling and it is difficult to position them to ensure uniform loading along specimen axes. They are also difficult to attach to the instrument grips. Testing has been shown to suffer from inadequate load resolution as well as having data reduction formulas that are hypersensitive to precise dimensional measurements. To minimize these effects, a variety of micro- and nanoscale testing techniques have been employed to investigate size effects on mechanical properties [1, 3, 138, 139].

Most small scale testing methods have been centered on two main geometries namely thin films and nanowires. Methods for testing thin films include using a either a sharp or flat indenter to probe a small volume of material [140-143], methods based on bending or curvature of the thin film [144, 145], tensile testing methods and MEMS-based techniques [146-149]. Methods for testing a nanowire include scan probe microscopy, AFM, SEM and TEM based methods [150, 151]. In this section the focus will be on the scope and limitations of the methods used to test thin films.

A relatively versatile method for probing the mechanical response of thin film is nanoindentation, e.g., [140-142], which allows determining the hardness and Young's modulus. Nevertheless, substrate effects are difficult to avoid when the films are very thin (typically 100–200 nm) to keep sufficient accuracy in the depth and force measurements. Furthermore, the extraction of strength and

strain hardening data in ductile films is extremely complex due to the inherent strain gradient plasticity effects [152], [153] as well as pile-up and sink-in effects [154], [155]. Fracture properties are not easily accessible either [156]. The bulge test constitutes another type of test for imposing to submicrometer material films relatively homogenous plane strain tension state of stress if sufficiently wide [144, 145]. Moderate amount of deformation can be imposed without failure at the boundaries. Boundary condition effects usually prevent cracking to occur within the homogenously deformed region. Compression methods have recently received much interest, following the pioneering work of [143]. The compression is provided by a flat punch pushing on micropillars with small aspect ratio to avoid buckling problems. This test can be performed up to very large strains to address thus not only the first instants of plasticity but also the large strain behavior and strain hardening response. The boundary conditions are difficult to control and the test does not allow probing the fracture properties. Although, these methods were significant developments in measuring the mechanical response at the small scale but their capabilities for probing into the mechanisms responsible for the mechanical behavior is severely limited.

In-situ nanomechanical testing are the current state-of-the-art techniques to understand material behavior down to the nanoscales. A few novel in-situ experimental set-ups have been developed to study NC/UFG metals. One of the first successful attempts was a set-up developed by Swygenhoven et al. [157] that uses *in situ* synchrotron x-ray-diffraction technique (Figure 1.16 (f)) which allows the measurement of diffraction profiles continuously during mechanical testing, providing an *in situ* peak profile analysis capability. This

technique although very powerful is still dwarfed by direct in-situ TEM measurements since it relies on the interpretation of the measured peak broadening. A unique in-situ tensile testing method was realized by coupling a TEM nanoindentation device with a push-to-pull (PTP) device [151, 158] shown in Figure 1.16 (e). A PI 95 TEM PicoIndenter system from Hysitron Inc. was used in displacement-controlled compression mode with a conductive diamond flat punch indenter to acquire raw load and displacement data and the motion of the flat punch indenter was converted to tensile strain via the PTP device, also developed by Hysitron Inc. This system allows for real time observations of the deformation in the sample however thermal drift of the indenter could be an issue while performing transient mechanical tests. Similar "push-to-pull" mechanisms have been realized by using a micro-mechanical device (MMD) loaded via the Nanofactory TEM-nanoindenter [159, 160].

MEMS-based methods have by far proven to be superior to any other tensile testing methods for thin films [146-149]. MEMS has the potential to impact nanomechanical characterization through controlled actuation, high-resolution force/displacement measurements, integrated multi-functions and tiny size for in situ electron microscopy testing. MEMS based testing have two essential features: a mechanism for providing the driving force or displacement and a sensor for measuring the load and displacement in the specimen [147, 161]. MEMS based testing systems have an added benefit that they can be miniaturized to be placed inside a TEM and allow in-situ testing of nanostructures to directly observe their deformation mechanisms, allowing truly quantitative in situ TEM nanomechanical testing [162-164]. The most

straightforward way to measure force and displacement with a high degree of resolution is to take advantage of the high magnification imaging inside a TEM to measure the displacement of various components of the MEMS device (load sensor, actuator, specimen) to measure force and displacement with a high degree of resolution [162-165]. Espinosa and coworkers were the first to measure the load electronically via a capacitive sensor [166-168] (shown in Figure 1.16 (b)). This was a major development since it allowed the TEM or SEM to be used for continuous observation of the specimen deformation and failure with sub-nanometer resolution, while simultaneously measuring the applied load electronically with nanonewton resolution. Therefore, the electron beam need not be frequently switched to measure load and displacement. The displacement of the sample was however still measured using displacement markers on the specimen itself or using the gap edges as the markers. This limited the magnification to a certain extent.

This limitation was overcome by Pierron and coworkers using two capacitive sensors on either side of the specimen to measure the load and displacement electronically [169, 170] as shown in Figure 1.16 (d). This MEMS device is the nanoscale equivalent of the universal testing machine in the sense that the two capacitive sensors provide a complete σ-ε response directly without the need for any kind of imaging. As shown in Figure 1.17 a fully quantitative nanomechanical technique such as this MEMS device which can perform simultaneous microstructural observations is a significant step towards a better fundamental understanding of the rate-controlling mechanisms when combined with the understanding from atomistic simulations.

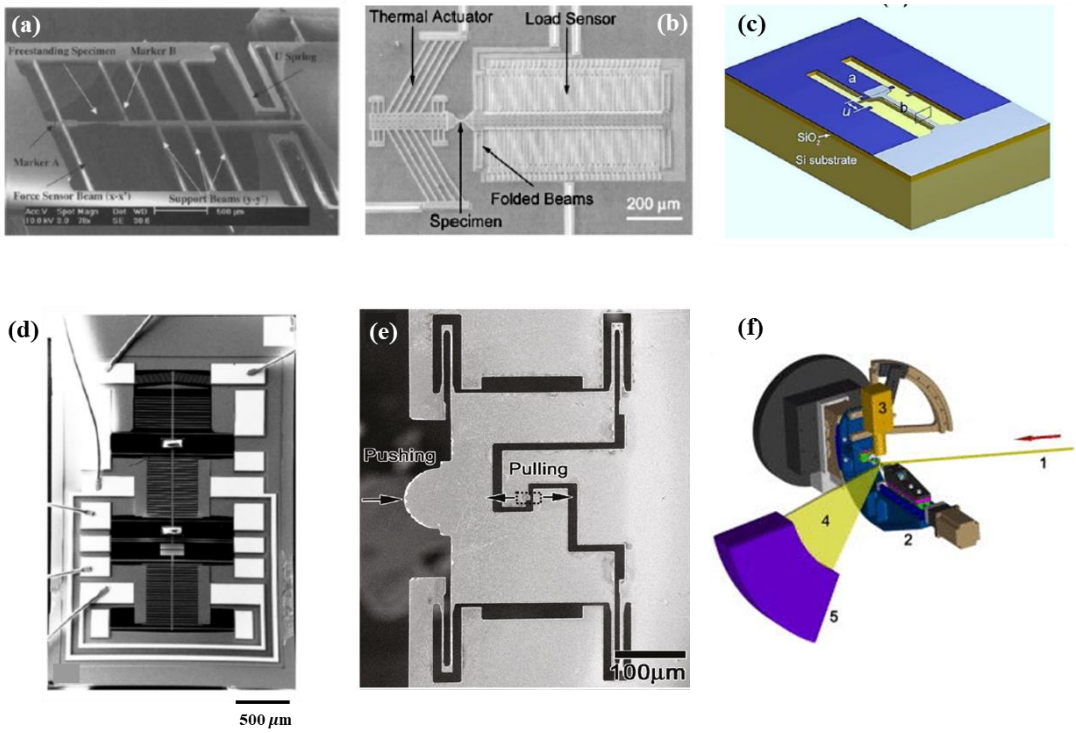

Figure 1.16 (a) A preliminary in-situ MEMS-based tensile testing set-up with markers for force and displacement sensing and a bulk piezoelectric actuator [8, 171, 172]. (b) MEMS platform consisting of a thermal actuator and a capacitive sensor [167, 168, 173]. (c) Schematic of "lab-on-chip" tensile stage [174]. (d) MEMS with capacitive sensors for load and displacement sensing and a thermal actuator [169, 175]. (e) A push-to-pull device for in-situ testing [151, 158, 176]. (f) In-situ X-ray diffraction set-up [157].

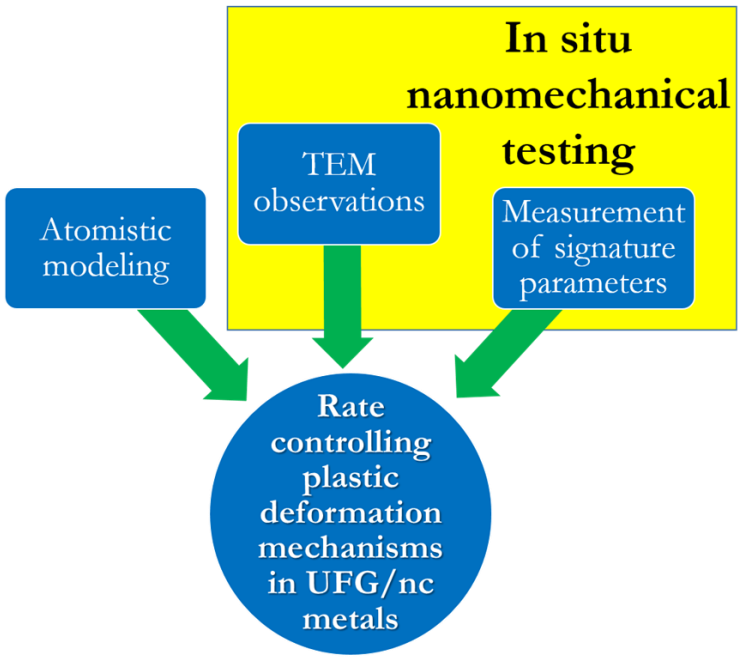

Figure 1.17 Multi-dimensional approach to identifying rate-controlling mechanisms.

1.2.5. Current state of the MEMS technique developed by Pierron and co-workers

The MEMS device has been used to characterize transient relaxation behavior in 100-nm-thick UFG Au microspecimens [177]. The *in situ* TEM results show that the transient relaxation behavior under large stresses is accommodated by sustained dislocation motion, either intergranular or transgranular, only in a few grains (the larger grains (above ~200 nm) that are favorably oriented for maximum shear (main glide plane or grain boundary orientation close to 45°)). Over time, the dislocation sources, located in or close to grain boundary and triple junctions, become less operative as a result of the decrease in applied stress, or exhausted, likely leading to a transition to a grain boundary- diffusion based mechanism. However, most of these sources are robust enough to produce additional dislocations upon increase of the applied stress, contributing to significantly larger ductility than for monotonic tests by maintaining localized shear regions.

These TEM observations have provided many insights into the transient behavior of the UFG Au microspecimens, there are several outstanding questions. What is the rate-controlling mechanism? What is the activation volume for such mechanisms? A deeper quantitative understanding is needed to answer these questions. Although these TEM observations were made using the MEMS device, the electronic sensing was not functional during these experiments. This highlights an important issue of reliability with the current state of the MEMS technique.

In order to fulfil the approach shown in Figure 1.17 for understanding the rate controlling mechanisms it is therefore important to repeat these transient relaxation experiments *in-situ* with complete quantification of the relaxation behavior such as the strain rates and stress so that signature parameters of the rate controlling mechanisms can be identified. There are several challenges in accomplishing this task. The MEMS device needs to be characterized for the accuracy of the measurements needed for such transient tests. Factors that frequently introduce errors in nanomechanical testing such as compliance of the clamps need to be quantified. In-situ experiments are always prone to drift issues and the problem is complicated even further when electronic measurements down to the nanometer resolution need to be made in the TEM. Therefore, after the characterization of the technique it ultimately needs to work inside the TEM.

1.3. Part II: Thin metallic coatings to enhance fatigue life in small scale materials

1.3.1. Classical fatigue mechanisms

It is now well-known that fatigue crack initiation in conventional coarse grain pure FCC metals is triggered by extrusion-mediated surface roughness as presented in Figure 1.18 [178, 179]. This roughness occurs at the intersection of free surface and persistent slip bands (PSBs) and is a direct consequence of cyclic microplasticity [180]. In the saturation stage of the cyclic loading, strain is highly localized near PSBs. Ultimately cyclic irreversibilities along PSBs trigger the formation of protrusions [181, 182]. The corners of protrusions, with irreversible slip-unslip, are the preferential sites for fatigue crack initiation [183]. This sequence of events is regarded as conventional for fatigue crack nucleation in pure mono-crystalline and coarse grain FCC metals. One of the most comprehensive theories of surface relief formation is based on the hypothesis that the origin of irreversibility for the motion of PSBs is dislocation pair annihilation and generation of vast number of vacancies within PSBs [184].

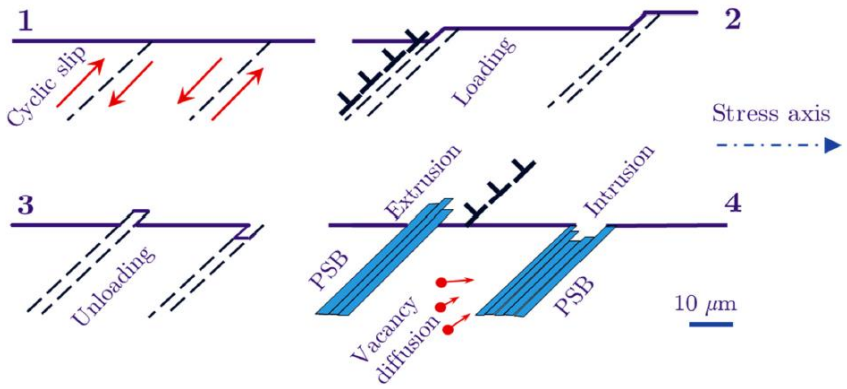

Figure 1.18 Schematic diagram of stages before crack nucleation in fatigued coarse grain FCC metals [185].

1.3.2. Metallic thin films as coatings to enhance fatigue life

The NC/UFG metals are frequently found in applications in the form of thin films. Thin hard coatings are routinely employed in structural materials, particularly metals, to protect them from corrosion and wear [186, 187]. Their use for improving fatigue life is less straightforward [188-195]. Any surface coating that could potentially delay fatigue crack nucleation at or near the surface would in principle improve the high cycle fatigue (HCF) behavior of a metal (whose life is mainly dominated by the nucleation of fatigue cracks) [193]. However, the coating may break at the location of the extrusions developing at the surface of the underlying metal due to persistent slip band (PSB) formation, thereby resulting in little benefit [194]. Alternatively, secondary cracking resulting from the presence / deposition of the coating (either due to cracking of the coating [190, 196] or cracking of the metal underneath the coating due to surface modification resulting from the coating process [197]) can also decrease the fatigue life of the component [195]. Cracking of the coating is more likely if large residual tensile stresses are present [190, 191]. Secondary cracking may not reduce fatigue life if the presence of the coating results in large compressive residual stresses that can effectively improve the fatigue life by decreasing the effective stress intensity factor range (i.e. decreasing crack growth rates) [198, 199], with the opposite effect for residual tensile stresses. Stoudt et al. argued an effective coating should exhibit the following five properties to prevent fatigue crack nucleation: "(i) hardness — to suppress the development of the characteristic PSB-induced surface morphology, (ii) toughness — to resist cracking where

subsurface PSBs intersect the film, (iii) cyclic work hardenability — to prevent slip localization, (iv) residual compressive stresses — to counter the effects of tensile stresses, and (v) adherence — to maintain surface film contact with the substrate" [195]. They demonstrated that a 5-μm-thick nanometer-scale multilayered coating, consisting of 125 40-nm-thick Cu/Ni bilayers and likely having the five aforementioned characteristics, significantly improved the fatigue life (by more than one order of magnitude) of bulk polycrystalline Cu.

1.3.3. Small-scale metallic coatings

In contrast to bulk metals, only a few studies have investigated the role of coatings on the fatigue properties of small scale materials, such as thin films and microbeams [200-203]. Additional coating characteristics may be required because of the possible size effects on fatigue mechanisms. A recent HCF study showed an order of magnitude increase in N_f due to the presence of a 10-nm-thick Ta coating on 1-μm-thick Cu films on polymer substrates [202]. For the 1-μm-thick Cu films with a mean grain size of 1.2 μm, fatigue extrusions form under reverse loading and plastic strain amplitudes up to 0.5% as a result of cell-like dislocation structures [204]. For this film thickness / grain size regime, Kraft and co-workers have shown that the dislocation structures are similar to that observed in bulk materials (thinner films / small grain size are required to transition from bulk behavior to interface-dominated behavior) [204]. Wang et al. investigated the effect of a 10-nm-thick Ta coating on the HCF regime (N_f between 10^5 and 10^6 cycles) of these 1-μm-thick Cu films [202]. They showed that the increase in N_f for the coated films results from the suppression of extrusion

formation due to the inability of the dislocations to escape at the Cu film's surface. Instead of well-defined extrusions, wrinkles form at the surface, leading to either cracking of the Ta coating (from which extrusions can eventually form), or bulging and delamination of the Cu film from the substrate (also eventually leading to film cracking).

Compared to the thin metallic films on polymer substrates, the bending fatigue behavior of the Ni microbeams studied by [205-208] is significantly different due to the presence of extreme stress gradients (η = 17%/μm) as shown in . The corresponding plastic strain gradient is ~45%/μm. In other words, at a distance of 2 μm from the sidewall's surface (~equivalent to one or twice the grain size) of the microbeam, the plastic strain is only 5% the value of the outer edge. These extreme stress gradients, which are at least one order of magnitude larger than sharp notches at the macroscopic scale, have been shown to affect significantly the *S-N* curves of the microbeams [205]. Our recent quantitative *in situ* SEM testing of these microresonators and *post-mortem* FIB cross-sections gave further insight into the environmental effects and governing fatigue mechanisms [208]. We showed that the endurance limit (at ~10^8 cycles) is related in both environments (vacuum and air) to the threshold for fatigue crack nucleation. However, the threshold *in vacuo* (σ_a = 420 MPa) is much larger than in air (σ_a = 300 MPa), with corresponding approximate plastic strain amplitudes of 10^{-4} and 10^{-5}, respectively. During a fatigue test *in vacuo* at σ_a = 420 MPa, extrusions are observed on the sidewalls, but no fatigue cracks are nucleated (even after 6.4×10^7 cycles). For σ_a > 420 MPa, fatigue cracks do nucleate at the edges of extrusions, but require about one order of magnitude more cycling

compared to air. Post-mortem FIB cross-sections highlighted the presence of nanoscale voids in the subsurface of the extrusions, whose interconnections formed fatigue cracks. Also, a larger concentration of voids was observed in air compared to vacuum. These observations suggest that the nucleation of fatigue cracks is controlled by void formation, supposedly from vacancy condensation processes that are known to be enhanced in the presence of oxygen [209-213]. Fatigue damage controlled by void formation, including the nucleation of fatigue cracks, has already been observed in VHCF studies of bulk UFG Cu at low ε_{pa} < 10^{-6} [214, 215]. It is therefore reasonable that this mechanism also govern the fatigue crack nucleation of the microbeams under extreme plastic strain gradients that may prevent the formation of cell-like dislocation structures in the HCF regime.

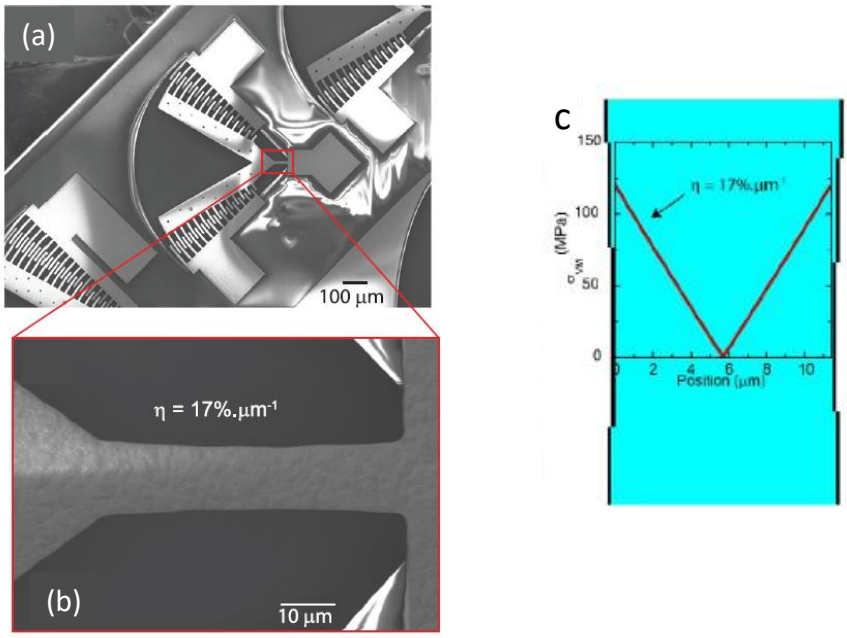

Figure 1.19 (a) SEM image of entire microresonator. (b) Microbeam characterized by η = 17%/µm (see (c) stress distribution across the beam width for an angle of rotation of 5 mrad) [205, 216].

1.4. Motivation for the thesis

It has been definitively recognized by experiments and simulations that the NC/UFG FCC metals show an order of magnitude higher strain rate sensitivity compared to their microcrystalline counterparts [23-27]. The activation volume associated with the high strain rate sensitivity of nanostructured metals is of the order of 1-10 b^3 which is two orders of magnitude lower than CG metals implying different atomistic mechanisms controlling the deformation in nanostructured metals compared to CG metals. However, the mechanisms underlying such trends are not well understood even after decades of research [217]. Several deformation mechanisms have been identified, either via experiments and/or simulations, in NC /UFG metals which are not observed in CG metals at room temperature but there is a lack of *quantitative* understanding of these mechanisms that can rationalize the observed variations in parameters as the characteristic structural length scales are altered by several orders of magnitude. MD simulations can provide deeper insights into the underlying mechanisms but they suffer from several limitations from being applicable to quasi-static strain rates [218]. Also, the results from MD simulations need to be verified experimentally. Moreover, plastic deformation in nano-grains does not leave behind any footprints in its wake unlike CG metals [219], so post-deformation analysis would not be of much help in understanding the deformation mechanisms. Therefore, there is a need for developing *in-situ* quantitative nanomechanical techniques for better quantitative understanding of the deformation mechanisms.

This thesis aims at building on top of the MEMS-based technique for in-situ TEM nanomechanical testing proposed in [169, 170, 175]. It will aim at overcoming the limitations in the capacitive sensing capabilities of the MEMS device, highlighted in Section 1.2.4. The capabilities of the technique to accurately measure stresses and strains will be assessed by characterizing the various sources of errors such as compliance in the clamps and noise-to-signal ratio of the capacitive sensing. Further, the issues related to the drift during in-situ operation of the MEMS device will have to be studied for successful experiments. After establishing the capability of the technique to measure activation volumes and performing microstructural observations at the same time, the MEMS device will be used to perform transient stress relaxations of UFG Au and Al microspecimens in the TEM.

This thesis also aims to study the use of UFG Au in thin film form as a coating to improve fatigue behavior. As emphasized in Section 1.3 recent studies by our group have highlighted strong size effects on the bending high cycle fatigue behavior of electroplated Ni microbeams tested using MEMS microresonators [208]. Ultralow fatigue crack growth rates were measured for these microbeams (average values down to ~10^{-14} m/cycle), and a discontinuous process for both fatigue crack nucleation and propagation that involved void formation, most likely based on vacancy condensation processes was proposed [208]. The environment plays a significant effect on fatigue lives that are three orders of magnitude longer *in vacuo* than in air. Studies on irradiation of metals (whereby large concentrations of vacancies are introduced) have shown that oxygen stabilizes void nucleation compared to the other vacancy cluster defects,

by decreasing the void surface energy through a chemisorption process [209-213]. It is therefore possible that the formation of voids during cyclic loading of the Ni microbeams in air is facilitated by the presence of oxygen, resulting in faster nucleation and growth of small cracks. Given the observed fatigue damage and significant environmental effects for the uncoated microbeams, an Au coating on the Ni microbeams is expected to act as a diffusion barrier to prevent oxygen from assisting void formation.

The objectives of this thesis are as follows:

- Develop a fully quantitative *in-situ* TEM MEMS-based nanomechanical testing technique which can simultaneously measure activation volume and allow microstructural observations under high magnification.
- Understand and qualify the issues related to the drift in the TEM imaging as well as electronic sensing during in-situ operation of the MEMS set-up.
- Provide measures of reliability for the signature parameters such as the true activation volume calculated from *in-situ* transient stress relaxations.
- Investigate the role of 850-nm-thick electroplated Au coatings on the fatigue behavior of Ni microbeams, particularly its effect on void-controlled fatigue crack nucleation using MEMS microresonators.

CHAPTER 2

EXPERIMENTAL METHODS

2.1. Overview

This chapter presents different nanomechanical testing methods used and developed in this study. Section 2.2 outlines the development of a MEMS based technique for in-situ TEM tensile testing. Section 2.3 presents the details of the commercial in-situ tensile testing technique based on Push-to-Pull devices. Section 2.4 presents the details of MEMS microresonators used for Very High Cycle Fatigue (VHCF) testing of microbeams under extreme stress gradients.

2.2. Development of MEMS-based in-situ TEM tensile testing

2.2.1. Geometry of the MEMS device

The MEMS device shown in Figure 2.1 (a) and schematized in Figure 2.1 (b) provides the means for the actuation and sensing via electrical signals and is central to the testing technique. It consists of a thermal actuator, two interdigitated capacitive sensors (CS_1 and CS_2), a load sensing beam and a "specimen gap" for observations in the TEM. The MEMS devices are fabricated by MEMSCAP using the SOIMUMPs process. The silicon-on-insulator (SOI) wafer consists of a 10-μm-thick n-type monocrystalline Silicon on a 1 μm thin oxide layer sitting on a 400-μm-thick substrate. The monocrystalline Si

structural layer is patterned to create the required components of the device while the substrate is patterned and etched from "bottom" side to the oxide layer to create freestanding structures for TEM imaging purposes.

The thermal actuator consists of ten pairs of beams inclined at 5° which provide the driving displacement to the device by resistive heating. The displacement of the thermal actuator can be controlled by controlling the voltage being applied across the inclined beams, however the displacement of the specimen being tested cannot be controlled as explained later in this section. A very large heat sink is provided between the thermal actuator and the nearest capacitive sensor, the distance of the actuator from the specimen gap being about 1.5 mm. This heat sink limits the temperature increase near the specimen gap to 0.07 °C/10 nm displacement of the thermal actuator which means a temperature increase of 10 °C for a typical test [175]. The capacitive sensor CS_1 is sandwiched between two air gaps filled with epoxy glue which provide a rigid and yet electrically isolated connection to the rest of the device as shown in Figure 2.1 (b). It should be noted that the SOIMUMPs Plus process offers the capability of having free-standing silicon oxide bridges underneath the Si structural layer [220], which would circumvent the need to filling the air gaps with epoxy glue. One of the air gaps connects CS_1 to the thermal actuator while the other air gap connects it to one end of the specimen gap. CS_1 therefore measures the displacement of the thermal actuator X_A. The other capacitive sensor CS_2 is rigidly connected to the load sensor and hence measures the displacement of the load sensor X_{LS}. The specimen gap lies between the two capacitive sensors and the displacement of the specimen X_S is therefore given by:

$$X_S = X_A - X_{LS} \quad (2\text{-}1)$$

It should be noted that in the absence of a specimen the load sensor does not move and therefore CS_2 measures zero displacement upon application of a voltage to the thermal actuator. It should also be noted that the test is not displacement controlled since X_S cannot be controlled. X_A can be controlled via controlling the voltage applied to the thermal actuator but X_{LS} depends on the specimen since the load sensor has to move in order to measure the load in the specimen, therefore from Eq. (2-1) X_S cannot be controlled. The load sensor is made of 4 beams (length: 500 μm) deforming in bending mode. The width of the load sensor beam primarily dictates the load sensor stiffness K_{LS}, which can either be 480 or 100 Nm^{-1} in the present study. K_{LS} should be designed such that it is less than the stiffness of the specimen (K_S) being tested. The force F measured by the load sensor can be calculated from its displacement X_{LS} as follows:

$$F = K_{LS} * X_{LS} \quad (2\text{-}2)$$

The applied stress is obtained by dividing F by the specimen's cross sectional area, and the strain by dividing X_S by the specimen's gauge length. The next section provides details on the CS_1 and CS_2 measurements which provide X_A and X_{LS}.

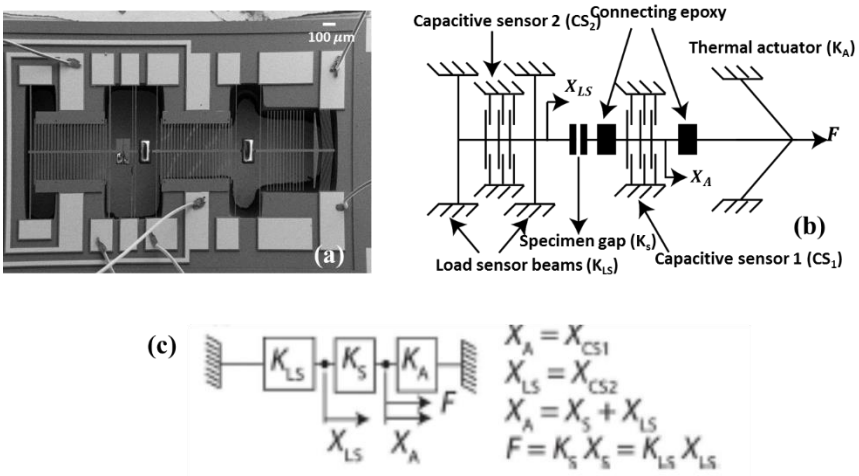

Figure 2.1 (a) SEM image of a wirebonded device, (b) Schematic showing different components of the MEMS device and the associated displacements and (c) Lump model of the MEMS device with corresponding governing equations.

2.2.2. Capacitive sensing of displacements

As mentioned above, the load and displacement of the specimen are electronically measured using the two capacitive sensors. Each of the capacitive sensors consist of a set of beams attached to the device (fixed beams) and a set of beams attached to the moving central shuttle of the device (moving beams). Every single fixed beam forms a capacitive pair with a corresponding moving beam comprising a total of 21 pairs of combs on each side of the MEMS device symmetry axis. During a test, the moving beams are displaced with respect to the fixed beams and this displacement causes a change in capacitance of the sensors. Therefore, the change in capacitance in each of the capacitive sensors is measured and the associated displacement is analytically calculated. When an input voltage V_{in} is applied to the thermal actuator, the resulting displacement of the thermal actuator, X_A, produces a corresponding displacement in the beams of both capacitive sensors CS_1 and CS_2 if a specimen is present in the specimen

gap (only the CS_1 beams move if there is no specimen). The displacement, X, of the capacitive sensors can be related to their capacitance C using:

$$C = \alpha\kappa\varepsilon_0 nA\left(\frac{1}{d_1 - X} + \frac{1}{d_2 + X}\right) \tag{2-3}$$

where α is the calibration constant, κ is the relative permittivity of air ($\kappa \approx 1$), $\varepsilon_0 = 8.854 \times 10^{-12}$ Fm^{-1} is the permittivity of free space, $n(= 42)$ is the number of comb structures, A is the overlapping area of the comb structure, d_1(nominal value: 2.5 μm) and d_2(nominal value: 10.5 μm) are the initial gaps between the comb structures which are actually measured using SEM images of the device typically after or before the test. The change in capacitance, ΔC, between $X = 0(V_{in} = 0)$ and $X(V_{in})$ is given by:

$$\Delta C = \alpha\kappa\varepsilon_0 nA\left[\left(\frac{1}{d_1 - X} + \frac{1}{d_2 + X}\right) - \left(\frac{1}{d_1} + \frac{1}{d_2}\right)\right] \tag{2-4}$$

The capacitance changes are measured using a commercially available capacitive readout sensor MS3110, manufactured by Microsensors Inc. MS3110 is an ultra-low noise CMOS IC capable of sensing capacitance changes down to 4 aF/rtHz [221]. MS3110 senses the difference in capacitance between two capacitors whose capacitances are to be measured (say, $C_{1,ex}$ and $C_{2,ex}$) and provides an output voltage proportional to that difference. Two internal capacitances $C_{1,in}$ and $C_{2,in}$ are provided to form a balanced pair with the external capacitances ($C_{1,ex}$ and $C_{2,ex}$) as shown in Figure 2.2. The output voltage V_{out} is a linear function of the difference between sensing capacitances $C_{2,t}$ and $C_{1,t}$ according to Eq. (2-5):

$$\begin{aligned} V_{out} &= \lambda\left(C_{2,t} - C_{1,t}\right) + V_{ref} \\ C_{2,t} &= C_{2,in} + C_{2,\mathrm{ex}} \end{aligned} \tag{2-5}$$

$$C_{1,t} = C_{1,in} + C_{1,\text{ex}}$$

$$\lambda = GAIN * V2P25 * 1.14/CF \quad \text{(2-6)}$$

where, λ is constant for a particular test and is determined by Eq. (2-6) using the parameter values selected for the chip as shown in Figure 2.3. $V2P25$ is equal to 2.25 V, $GAIN$ can be either 2 or 4 V/V (always kept at 2) and CF is usually kept at 2.014 pF. V_{ref} is an output offset voltage which be set to 0.5 V or 2.25 V (always kept at 2.25 V) using SOff in Figure 2.3 and it also remains constant during a test.

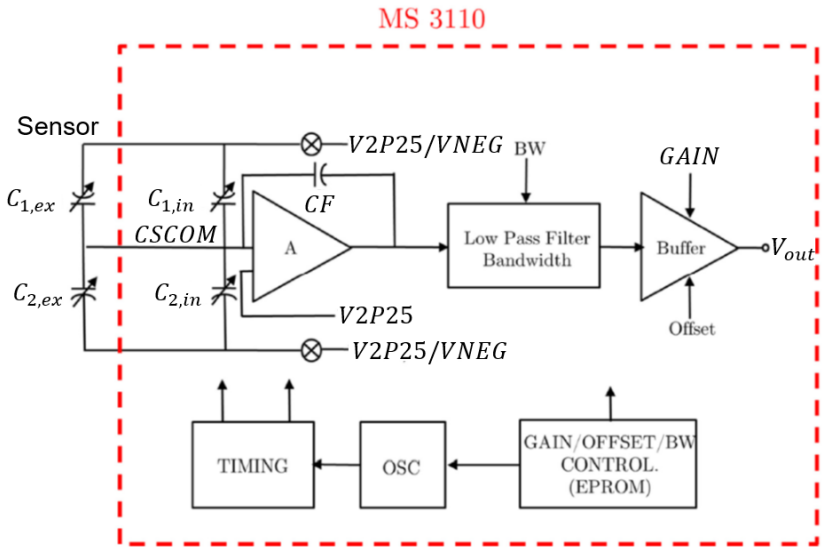

Figure 2.2 Functional block diagram of a MS3110 chip [221].

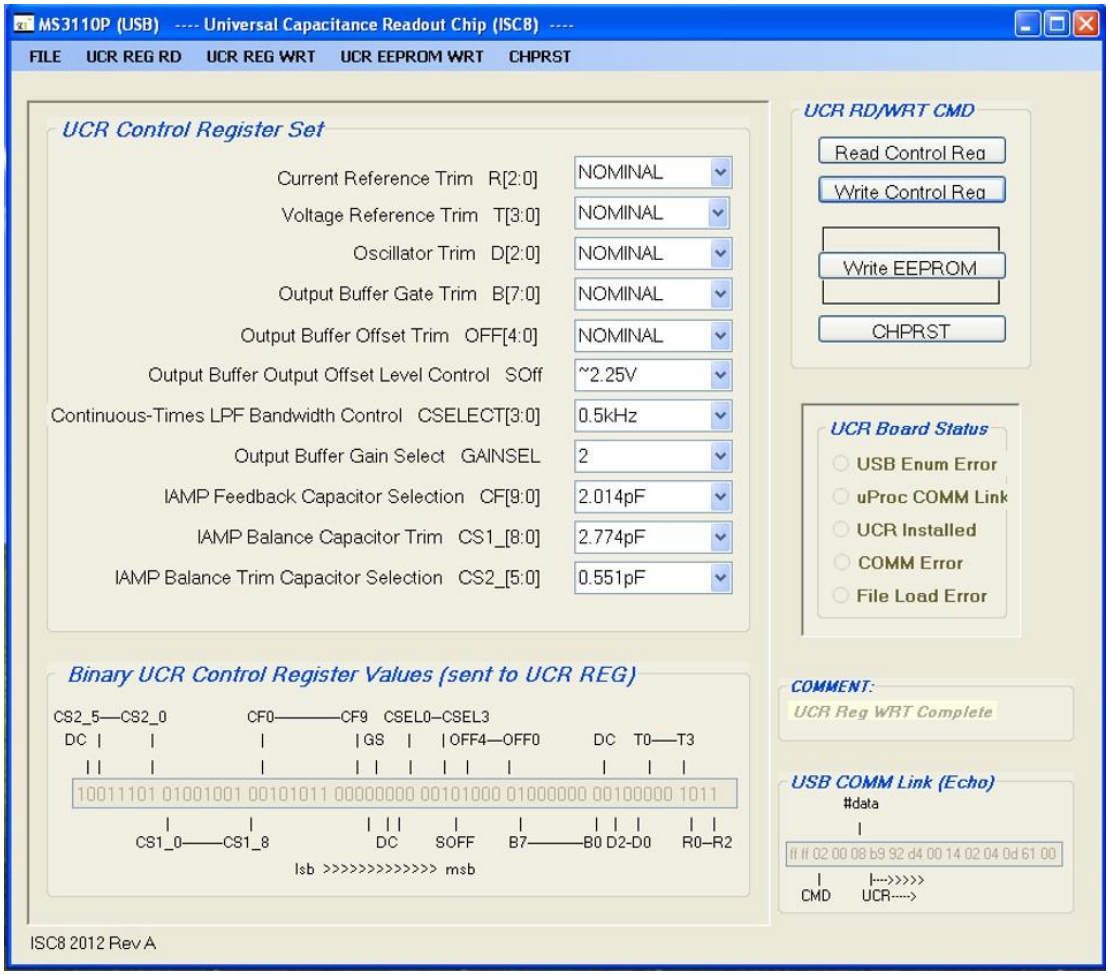

ISC8 2012 Rev A

Figure 2.3 MS3110 chip parameters used in a particular test. It should be noted that the CSELECT value should always be kept at 0.5 kHz to minimize noise. All other parameters except for CS1 and CS2 (which correspond to the values of the internal capacitances $C_{1,\text{in}}$ and $C_{2,\text{in}}$) are usually never changed.

Since the MS3110 chip measures the difference between two input capacitances, in order to measure the value of just one capacitive sensor (say CS_1 or CS_2), one can measure the difference between CS_1 (or CS_2) and a constant capacitor as shown in Figure 2.7 (b). Since the capacitances of CS_1 and CS_2 are of the order of pF, an error in the value of the constant capacitor will significantly affect the stress and strain calculations. However, the constant capacitor can be eliminated from the equation by taking the difference between V_{out} at a particular V_{in} (at which the displacement is to be measured) and $V_{out}(V_{in} = 0)$. This procedure provides us with ΔCS_1 (or ΔCS_2) as a function of V_{in} as given by:

$$\Delta CS_1 = \left[\overline{V_{out}^a}(V_{in} = 0) - \overline{V_{out}^a}(V_{in})\right]/\lambda^a \quad (2\text{-}7)$$

$$\Delta CS_2 = \left[\overline{V_{out}^b}(V_{in} = 0) - \overline{V_{out}^b}(V_{in})\right]/\lambda^b \quad (2\text{-}8)$$

where the superscripts a and b refer to the two MS3110s respectively, λ^a and λ^b are the proportionality constants of the two MS3110s. $\overline{V_{out}}$ represents the average of the samples of V_{out} collected by the data acquisition unit as shown in Figure 2.4.

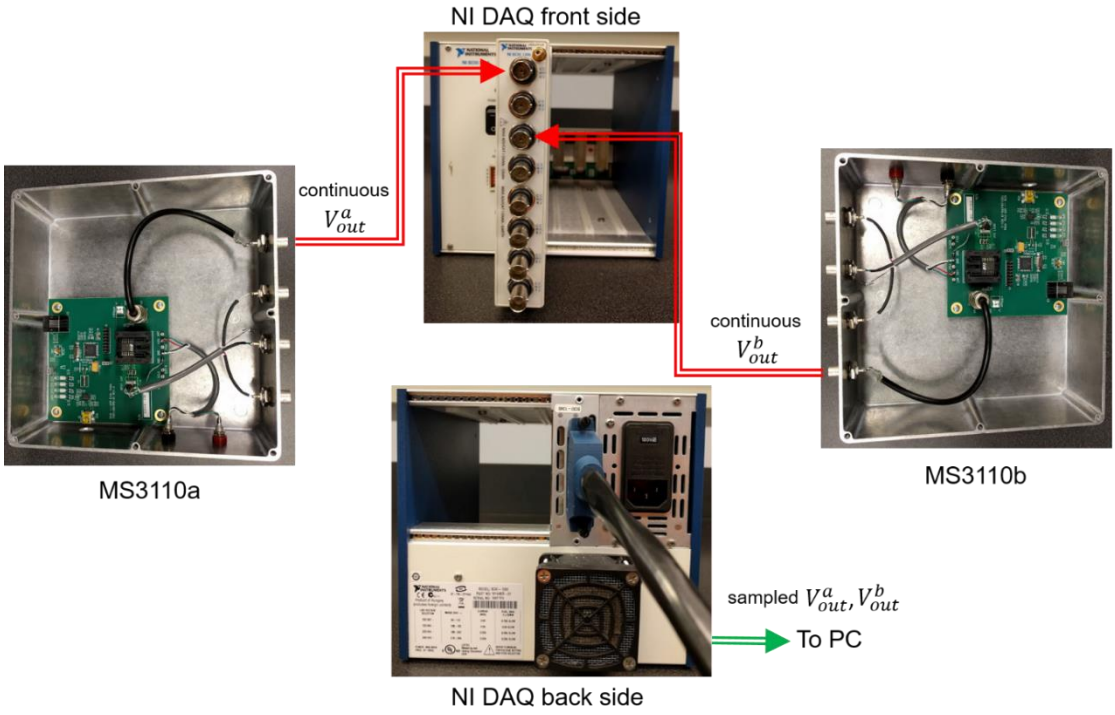

Figure 2.4 National Instruments Data Acquisition system (NI-DAQ) to sample V_{out} collected from the two MS3110 chips

The sampled V_{out} collected from the DAQ system is divided into blocks of 10000 measurements and the average value of each block is calculated to give $\overline{V_{out}}$. The size of these blocks and the sampling frequency can be controlled. It should be noted however, choosing a high sampling frequency slows down the data acquisition rate and therefore the speed of the test. Choosing too large a

block size can prevent one from capturing the transient response since the transient response would be averaged out. Sometimes the sampled V_{out} can be very noisy due to external parasitic capacitances which vary depending on the set-up. An example is shown in Figure 2.5 (a) where the noise in the sampled V_{out} data corresponds to 1 μm of displacement in the capacitive fingers. This level of noise is obviously unrealistic and cannot correspond to physical mechanical motion of the fingers since the fingers move by only 1.6 μm of displacement at the application of 4V to the thermal actuator. If this sampled data were divided into blocks and then each block was averaged then the $\overline{V_{out}}$ obtained would result in a very large noise of the order of 1 fF in the capacitive signals. This noise-to-signal ratio is unacceptable for our experiments because the capacitive signal changes by only a few femtofarads during stress relaxations. Therefore, in order to be able to capture stress relaxation, noise levels of 0.1 fF are required in the capacitive data measurement. Figure 2.5 (b) shows the histogram of the samples of V_{out} from one block of 10000 measurements (this block corresponds to the first 1 second of samples in Figure 2.5 (a)). As shown, most the samples of V_{out} are scattered around the mean of the block of data. Therefore, in order to reduce the noise in the data the following strategy is proposed. A noise reduction band of a certain amplitude is used to filter out the samples of V_{out} that lie above below this band. This band is placed around the mean of a block of the sampled data and then the filtered data in the block is averaged to obtain $\overline{V_{out}}$. By choosing the amplitude of the band appropriately, usually around 20-40 mV, the noise in the data can be reduced as shown in Figure 2.5 (c). As shown in Figure 2.5 (d) the filtering allows us to capture stress relaxations on the order of 7 MPa very

accurately. It should be noted the noise in the sampled V_{out} does not actually affect the average $\overline{V_{out}}$ obtained by averaging the samples in the individual block. This is because as shown in Figure 2.6 the DC component of the FFT of the sampled V_{out} has a very large amplitude compared to the higher frequencies. Therefore, removing the higher frequency components from a block of the sampled V_{out} will not affect the average of the block which will be equal to the amplitude of the DC component of the FFT. Thus, filtering out the higher frequencies of the sampled V_{out} will not reduce the noise in the capacitive data. Therefore, the elaborate noise reduction method, described in this section, by filtering out the V_{out} samples in the real domain using a noise reduction band was developed.

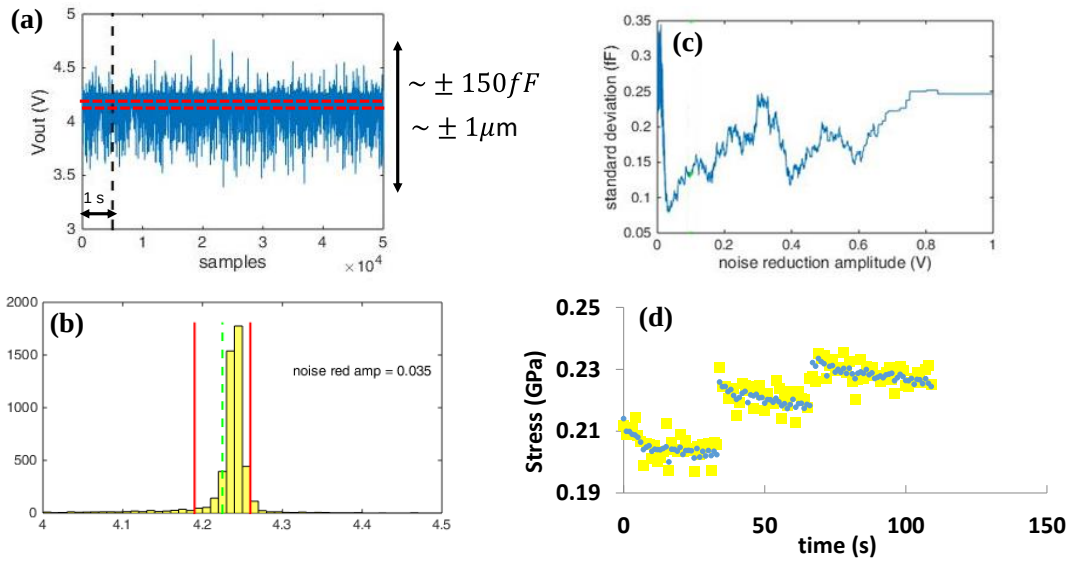

Figure 2.5 (a) Sampled V_{out} with a large noise-to-signal ratio. The band for reducing noise (noise reduction amplitude = 35 mV) is shown and a block from which $\overline{V_{out}}$ is calculated is indicated on the chart. (b) Histogram of the V_{out} from one block of the sampled data (~1s) shows a very narrow distribution of the samples around the mean. The band for removing the noise is also shown. (c) The effect of changing the amplitude of the noise reduction band on the noise showing that there is an optimum amplitude for obtaining minimum

noise. (d) Filtering can reduce the noise levels from 1 fF to 0.1 fF which corresponds to a reduction of noise in the stress from ±5 MPa to ±0.5 MPa.

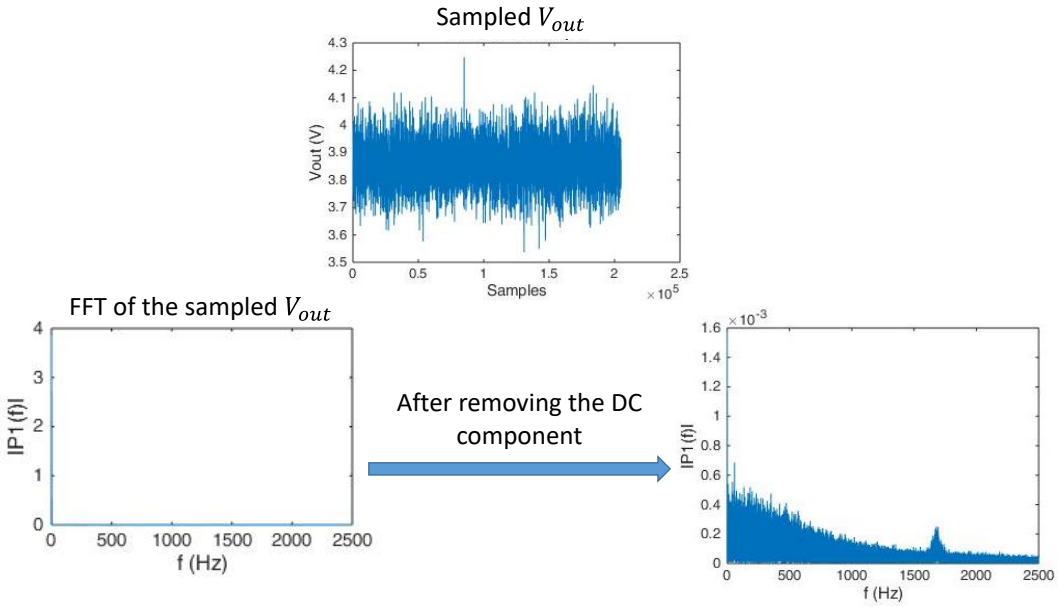

Figure 2.6 FFT of the sampled V_{out} showing that the DC component has a very large amplitude compared to the higher frequencies so therefore filtering out the higher frequency components will have no effect on the $\overline{V_{out}}$.

2.2.2.1. Sensing calibration

The calibration constant, α in Eqs. (2-3) & (2-4) accounts for the deviation of the capacitances measured by the capacitive sensors from the analytical equation and is assumed to be a constant for the entire duration of a test. It has to be obtained separately for each of the two MS3110s used to measure ΔCS_1 and ΔCS_2. To calculate α_{CS_1}(α associated with the MS3110 chip measuring ΔCS_1), X_A is measured optically at a particular V_{in} (say 3V) and the corresponding $(\Delta CS_1)_{exp}$ is measured via the MS3110 chip. Assuming, $\alpha = 1$ in Eq. (2-3), the difference between $C(X_A) - C(X = 0)$ is calculated as $(\Delta CS_1)_{\alpha=1}$. The ratio of $(\Delta CS_1)_{exp}$ to $(\Delta CS_1)_{\alpha=1}$ is equal to the calibration constant α_{CS_1}. Technically, α_{CS_2} can be

calculated in a similar manner, i.e., by measuring X_{LS} and the corresponding $(\Delta CS_2)_{exp}$, but the values of X_{LS} are typically around 100 nm which makes it difficult to measure optically. Therefore, to measure α_{CS2} the two MS3110s were switched after the specimen had failed so that the MS3110 measuring ΔCS_2 during the test now measures ΔCS_1 and hence can be calibrated in a similar manner to CS_1. The ratio of $(\Delta CS_1)_{exp}$ (measured after switching the MS3110s) to $(\Delta CS_1)_{\alpha=1}$ is equal to the calibration constant α_{CS_2}. It should be noted however that in an in-situ test where X_A and X_{LS} can be measured at high magnifications down to a resolution of 10 nm via electron beam, there is no need to make such assumptions and $\alpha_{CS_1}$and α_{CS_2} are calculated independently. The difference between the ex-situ and in-situ methods of obtaining the calibration constants is summarized in Table 2.1.

Table 2.1 Methods for obtaining calibration constants α for CS_1 and CS_2

		ΔCS_{exp}	X	α
Ex-situ	CS_1	Measured with MS3110 for CS_1	X_A measured optically	$(\Delta CS_1)_{exp}/(\Delta CS_1)_{\alpha=}$
	CS_2	Switch MS3110 after test	X_A measured optically	$(\Delta CS_1)_{exp}/(\Delta CS_1)_{\alpha=}$
In-situ	CS_1	Measured with MS3110 for CS_1	X_A measured by TEM	$(\Delta CS_1)_{exp}/(\Delta CS_1)_{\alpha=}$
	CS_2	Measured with MS3110 for CS_2	X_{LS} measured by TEM	$(\Delta CS_2)_{exp}/(\Delta CS_2)_{\alpha=}$

2.2.2.2. Differential vs single sensing

The capacitive technique (single capacitive sensing) presented in this thesis is a significant improvement over the differential sensing technique used earlier [169, 170]. In a differential capacitive sensing technique only one MS3110 chip is used, to measure $\Delta CS_2 - \Delta CS_1$ as shown in Figure 2.7 (a) and Eq. (2-9). By assuming the material being tested to behave in a linear elastic manner, ΔCS_1 and ΔCS_2 are then obtained from the difference $\Delta CS_2 - \Delta CS_1$ using an iterative procedure starting with an initial value of the unknown Young's modulus of the material and running the procedure until the solution converges (see [169] for details). As it can be clearly seen, unlike the single sensing, differential sensing does not provide independent measurements of ΔCS_1 and ΔCS_2, which means that ΔCS_2 could not be measured in real-time with differential sensing used in earlier works [169]. With independent sensing, ΔCS_2 can be measured in real time and hence by Eqs. (2-2) & (2-4) (see Section 2.2.4) stress can be measured in real time which significantly expands the envelope of this technique and enables performing transient mechanical tests such as repeated stress relaxations.

$$\Delta CS_2 - \Delta CS_1 = \left[\overline{V_{out}}(V_{in} = 0) - \overline{V_{out}}(V_{in})\right]/\lambda \tag{2-9}$$

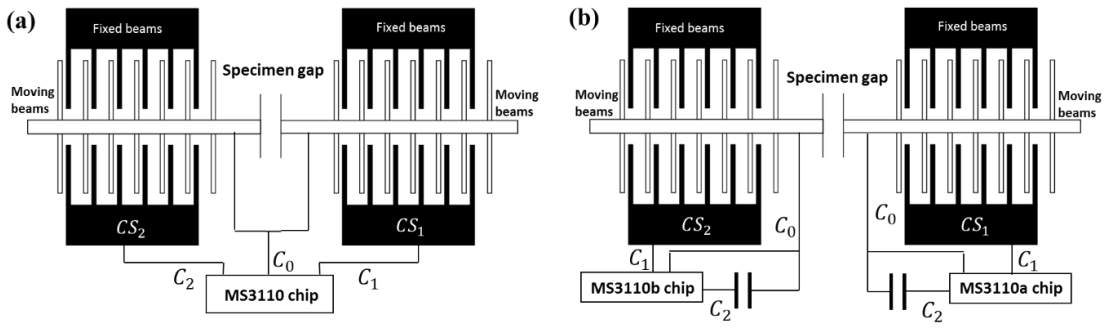

Figure 2.7 (a) Differential capacitive sensing used in previous works [169, 170] and (b) Single capacitive sensing with two MS3110 chips (a and b) and constant capacitors [222, 223].

2.2.3. Specimen fabrication and handling

Nanomechanical testing usually involves handling and manipulation of small scale specimens. Several issues arise with poor manipulation of specimens including misalignment of the specimen with respect to the loading axis, which is significant especially in a tensile test [224]. The microstructure of the thin film could be affected and the film itself can be damaged during manipulation. Clamping of these specimens also presents a great challenge in terms of keeping the stiffness of the clamps large as compared to the specimen being tested. Perhaps the best solution to circumvent these issues is to co-fabricate the specimens with the MEMS device, which can be done with ultrathin films [8, 174, 225]. However, this limits the use of a MEMS device to only one specimen, and restricts the choice of materials and structures (mainly thin films) to be tested. Omniprobes in combination with focused ion beam (FIB) microscopes can be used to pick and place specimens and clamp them with electron-beam induced Pt deposition [226, 227]. However it has been observed that the ion beam damages the specimen because of deposition of Ga ions [228] and that the

stiffness of the Pt clamps may not necessarily be large enough to prevent their deformation. Recent improvements in FIB microscopes, such as Helium ion microscope [229] may provide a pathway to efficient pick-and-place approaches. It should also be noted that clamps compliance is not necessarily an issue if an independent technique for strain measurements (based on digital image correlation) is employed [227, 230].

The specimens used in this study were fabricated independent of the device. using a process involving optical lithography, electron-beam evaporation, a lift-off technique, and XeF_2 etching of the Si substrate with a thin native oxide [169]. At the end of the process, the specimens are free-standing cantilevers, connected on one side to a large island as a support. In order to test these free-standing specimens, we have developed a FIB-less procedure for manipulating microspecimens made of ultrathin film materials under an optical microscope using a micromanipulator. The main idea is to fabricate "dog-bone" shaped specimens (see Figure 2.8 (a)) with large ends (~30 by 20 μm) with respect to the gauge section (a nanobeam that is ~25 μm long, ~1.8 μm wide and ~100 nm thick) to facilitate the process of manipulation and effective clamping of the specimens on our MEMS devices. The free-standing specimen is broken off from the large islands (see Figure 2.8 (a)) using a very fine tungsten tip such that one end of the dog-bone structure gets attached to the tip because of surface tension. Once the specimen has been 'picked' this way, it can be 'placed' on the sample gap in the MEMS device shown in Figure 2.8 (b). The large ends of the dog-bone structure can then be clamped by placing the ends over epoxy (typical modulus 3-4 GPa) pre-dispersed on the Si bridges as shown in Figure 2.8 (b), which should

result in stiff clamps given the large area of the ends. The advantage of the dog-bone shape can be appreciated in the pick and place step. Since only the ends of the structure come in contact with the tungsten tip the gauge length remains free of any physical damage and also the damage caused to the ends is immaterial since they are used only for clamping. The gauge length is chosen as the freestanding length of the gauge section which does not have any glue underneath it. This is explained further in the Section 3.3.6.

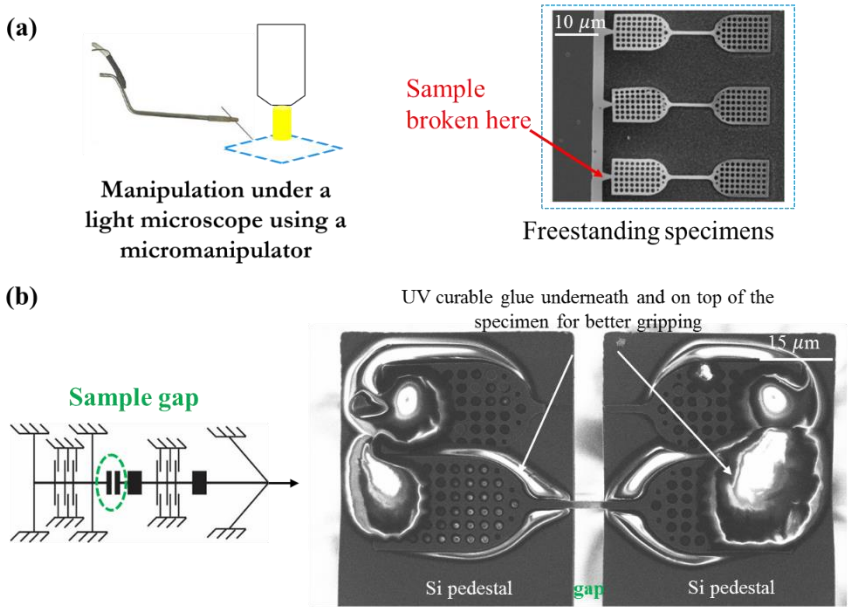

Figure 2.8 Steps to FIB-less manipulation. (a) A micromanipulator is used to break freestanding specimens from an island and "pick" them. (b) The "picked" specimens are "placed" on the sample gap and clamped using UV-curable glue. There is no FIB damage to the gauge length using this procedure.

2.2.4. Calculation of stress and strain

Figure 2.9 shows the calculation of stress and strain from the raw data (ΔCS_1 & ΔCS_2) obtained using the MS3110 chips. X_{LS} is calculated from ΔCS_2 using Eq. (2-4) and the force F in the sample is obtained from X_{LS} using Eq. (2-

2). The stress in the sample, σ, is calculated by dividing F by the nominal cross-sectional area A of the sample. Similarly, X_A is calculated from ΔCS_1 using Eq. (2-4) and the displacement in the sample is obtained using Eq. (2-1). The strain in the sample is calculated by dividing the displacement by the gauge length, l.

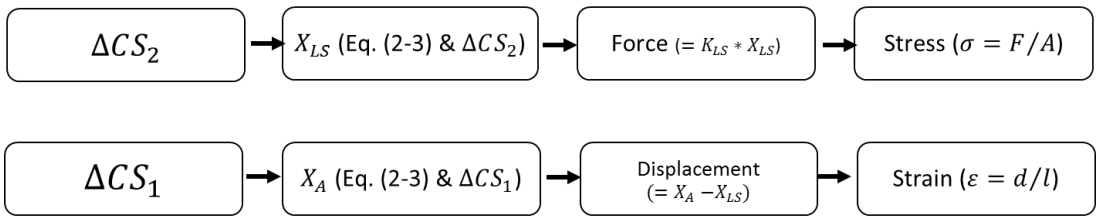

Figure 2.9 Methodology to obtain stress and strain from the measured raw data, ΔCS_1 and ΔCS_2.

2.2.5. Ex-situ and in-situ TEM set-up

Figure 2.10 shows the ex-situ and the in-situ TEM set-ups for these experiments. The in-situ experiments were performed in FEI Tecnai F30 TEM. A 16-lead electrical biasing holder by Nanofactory shown in Figure 2.10 (c) was used to perform the in-situ experiments. The MEMS device was glued to the chip carrier using silver paint and wirebonded to the gold pads.

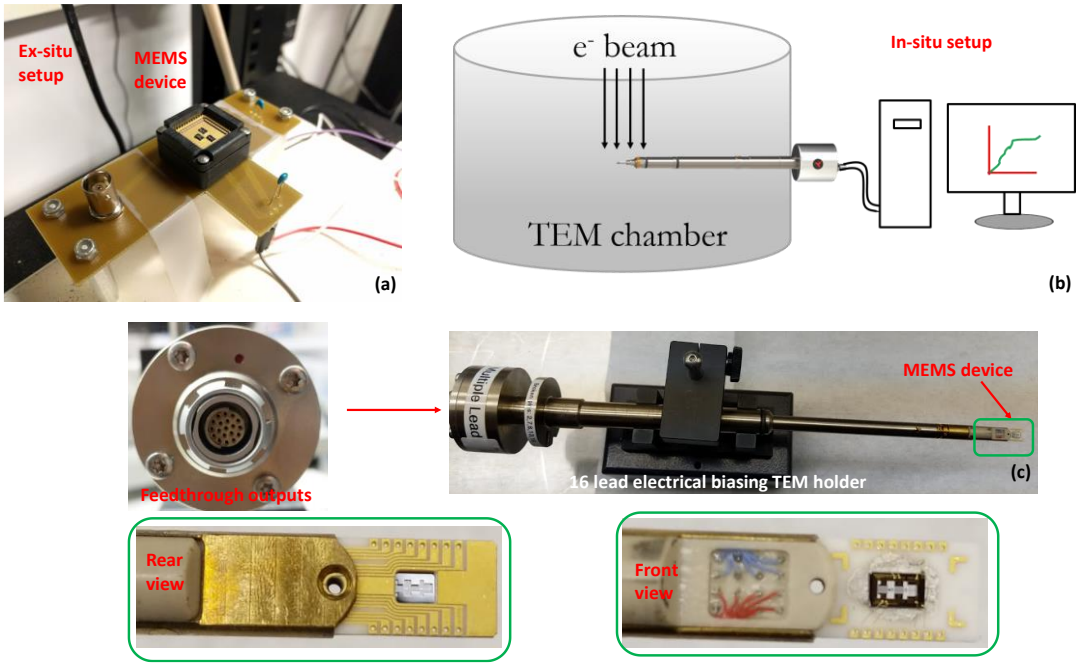

Figure 2.10 Ex-situ and in-situ TEM set-ups.

2.2.6. FEM modeling

To study the effect of the compliance of the glue on the modulus, a 3D finite element model of the specimen and glue was developed using ANSYS 16.1. Figure 2.11 shows the geometry of the model, consisting of half the Au specimen (100-nm-thick) and the epoxy glue (thickness t_g = 1 and 10 μm) underneath one clamp. The overlap between the glue and the specimen varies in the model, in order to study cases where glue is present underneath part of the specimen's nominal gauge length (~20 μm). Linear elastic material properties were assumed and are listed in Table 2.2. The bottom of the glue was fixed and a normal stress (of 300 MPa) was applied onto the other end of the specimen, in order to mimic the boundary conditions of the clamps during a test.

Table 2.2 Material properties used in the FEM model

Material	E (GPa)	ν
Gold	80	0.43
Glue (Epoxy)	3	0.3

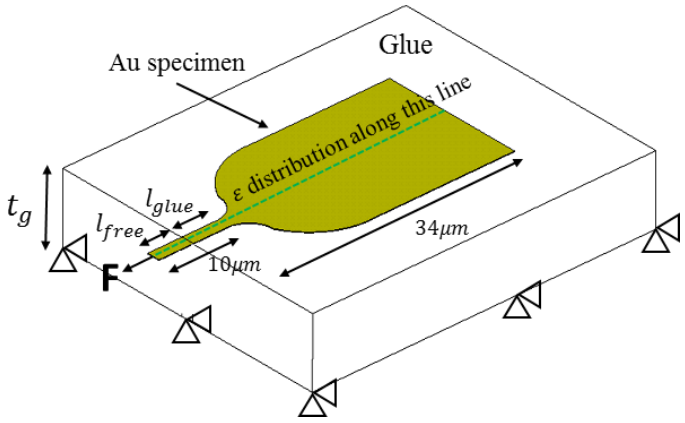

Figure 2.11 Schematic showing the geometry, loads and boundary conditions used in the FEM model to study the effect of compliance of the glue on the effective modulus of the microspecimen [222].

2.3. Push-to-pull (PTP) device for in-situ TEM tensile testing

A commercial technique to realize in-situ tensile testing is by a TEM nanoindentation device (PI 95 PicoIndenter from Hysitron, Inc., Minneapolis, MN, USA) [142, 231-233] coupled with a push-to-pull (PTP) device developed by Hysitron, Inc [151, 158]. The PTP device is microfabricated on a silicon-on-insulator wafer and consists of a semicircular end and specifically designed cutouts, as shown in Figure 2.12 (a). When a diamond punch is driven into the semicircular end, the gap in the middle of the device is elongated and a sample

spanning this gap is pulled uniaxially in tension, attenuated by the spring constant of the PTP device. The gauge section of the sample stays within the field of view of the TEM while the sample is being pulled, and a real-time video of the sample across the gap is taken. The force and displacement of the nanoindentation punch are also recorded simultaneously by the nanoindentation device. This in situ tensile testing setup allows for the investigation of the strain-induced microstructural evolution and mechanical properties in NWs and other electron-transparent samples. The force-displacement curve of an empty PTP device (i.e., without an attached test specimen) is shown in Figure 2.12 (b). As designed, the force loaded on the PTP device is linearly proportional to the motion distance of the nanoindentation punch, which represents the device stiffness along the tensile axis. The linear response of the PTP device facilitates the extraction of the contribution of a sample when attached to the device, because the sample and the PTP device springs are mechanically in parallel. It should be pointed out here that the stiffness of the PTP device can be tuned by changing the dimensions of the springs and that the lateral stiffness of the PTP device is much larger than that along the tensile axis to ensure a predominantly uniaxial loading condition. Additionally, by adjustment of the stiffness or mass of the movable portion of the device, the device's resonant frequency can be improved to protect the sample from undesired sample failure during handling.

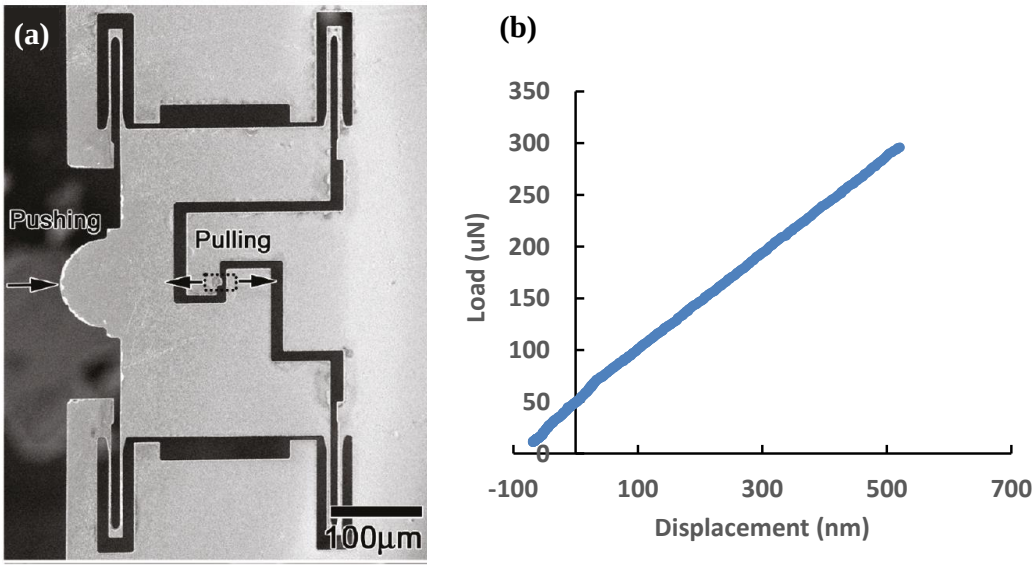

Figure 2.12 (a) SEM image of the microfabricated push-to-pull (PTP) device [151]. When the device is pushed on the semicircle end (arrow at left), the specimen gap (dashed rectangle) expands while staying in the field of view of the electron microscope. (b) The linear force vs displacement response of the PTP device without a sample spanning the specimen gap, showing the inherent stiffness of the device.

2.4. MEMS microresonators for fatigue bending

2.4.1. Specimen geometry and material properties

The specimens were fabricated with the MetalMUMPs® process from MEMSCAP. MetalMUMPs is an electroplated nickel micromachining process, which includes the patterning of a thick layer of photoresist that forms a patterned stencil for the electroplated Ni. The electroplating process is at 30 °C, with a current density of 20mA/cm^2 and a pH level of 4 [234]. The Ni bath consists of nickel sulfamate, nickel bromide, nickel, and boric acid, with a concentration of Ni in the bath of 99.9%. A 20-μm-thick structural layer of Ni is electroplated on top of a 0.55-μm-thick Cu base layer, and the top of the Ni layer is covered with a 0.5-μm-thick Au layer. The fabrication process allows an optional coating of the metallic layer with a 0.85 μm-thick electroplated layer of Au deposited on the top surface and side walls in selected regions [235]. Figure 2.13 shows the geometry of the Au-coated fatigue specimens which are on-chip microresonators (shown in Figure 2.13 (a)), consisting of a large fan-shaped mass connected to a Au-coated Ni microbeam (see Figure 2.13 (b) for the location of the Au coating, covering the entire microbeam). The microbeam is ~60μm long and the width of the narrowest Ni section is ~11.5μm which produces a normalized stress gradient under bending: $\eta = \frac{1}{\sigma_{max}}\frac{d\sigma}{dx} = 17\%\ \mu m^{-1}$. The cross-section SEM image (see Figure 2.13 (c)) shows the 0.85-μm-thick Au coating along the sidewalls, and the 1.35-μm-thick Au coating at the top. The fan shaped

mass has two sets of interdigitated fingers (two "combs"), one for electrostatic actuation and one for capacitive sensing.

The Ni layer has a strong ⟨001⟩ crystallographic out-of-plane texture and a columnar microstructure, with columnar grains that are ~5-10 μm in height [207]. The average grain size (diameter) is 1.2 μm, based on SEM images of FIB cross-sections. The tensile properties were measured using microtensile testing of dog-bone shaped specimens [207]: yield stress of 656 $\pm$ 70 MPa, tensile strength of 873 $\pm$ 26 MPa, and plastic strain at failure of 7.4 $\pm$ 2.8%. The high strength of this electroplated Ni is consistent with previous reports, knowing that the strength is affected by grain size (Hall-Petch effect) and the amount of impurities (likely resulting in solid solution strengthening), which both depend on the Ni bath composition and deposition conditions [236, 237]. The stress-strain curve was fitted with the following Ramberg-Osgood equation:

$$\varepsilon = \frac{\sigma}{E_{Ni}} + \left(\frac{\sigma}{K}\right)^{\frac{1}{n}} \tag{2-10}$$

with E_{Ni} = 172 GPa (a value consistent with the texture [207]), K = 1451 MPa, and n = 0.136.

The average grain size of the Au coating is 650 nm based on SEM images of the FIB cross-sections. The tensile properties of the Au coating could not be measured directly. Instead, the elastic modulus of Au, E_{Au}, was calculated using finite element modeling to match the measured effect of the Au coating on the microresonator's resonance frequency (f_0); see sections 2.3. A value of 71 GPa was obtained for E_{Au} (see section 3.1). Nanoindentation was also performed on the top surface of the Au coating to determine its hardness. The top surface was first

polished using FIB milling and then indentation was performed using a Cube corner 3-sided pyramid tip made of Diamond and having a tip radius of ~100nm (half angle = 35.26°, included angle = 90°). The resulting hardness was 3.02±1.1 GPa obtained from 7 measurements taken at locations 2 μm apart with maximum indentation depth of 120 nm. The large hardness value and therefore high strength seems consistent with the small grain size and possible strengthening due to impurities.

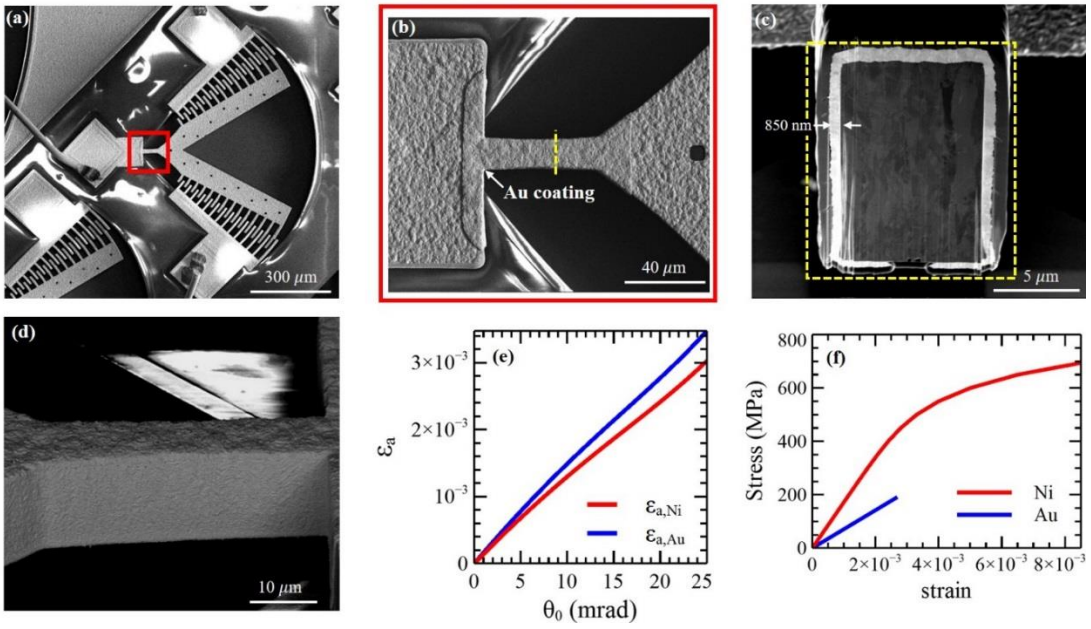

Figure 2.13 (a) & (b) SEM images of the microresonators with Au coated microbeams; (c) Cross section of a coated microbeam; (d) SEM image of the Au side wall prior to fatigue testing, (e) ε_a and θ_0 relationship; (f) stress-strain curves for Ni and Au [238].

2.4.2. Fatigue testing set-up

The microresonators are micro-scale equivalent of bulk ultrasonic fatigue testers: they are driven at resonance, which lead to fully-reversed cyclic bending

of microbeams and fatigue failure under large enough amplitudes of rotation [206, 216]. A fatigue test consists of driving a microresonator at resonance (f_0 ~ 9.5 kHz for the coated devices) and periodically measuring the evolution of f_0 throughout the test. Fatigue failure is defined as the number of cycles required to reach a 10% reduction in f_0 , which was shown to correspond to a crack size of approximately 2 μm on each side of the microbeam [206]. Unlike bulk ultrasonic fatigue testing, the large surface-to-volume ratio associated with the small specimen size prevents any significant heating of the microbeam at resonance: a 50°C increase in temperature would lead to a reversible decrease in f_0 of ~1%. Therefore, no significant increase in temperature occurs since the measured decreases in f_0 during the fatigue tests are irreversible.

The electrically grounded microbeam is actuated via electrostatic forces by applying an AC signal (with no offset) to one comb structure (using a combination of an Agilent 33220A 20 MHz waveform generator and an AVTECH-1l0G high voltage amplifier). A DC bias voltage of 100 V is applied to the second, sensing comb structure, resulting in induced currents generated during cyclic motion, which are amplified and converted to a voltage with a custom-made, off-chip, current-to-voltage amplifier circuit. This output voltage is measured with an SR830 DSP lock-in amplifier, and is proportional to the amplitude of rotation (θ_0). The second comb structure is therefore used to measure f_0 by performing frequency sweeps around the expected f_0 value [207, 239]. The amplitude of rotation θ_0 is also measured at the beginning of each fatigue test using optical images and a technique described in [206], with a precision of ~ ±1 mrad. The high cycle fatigue setup is shown in Figure 2.14.

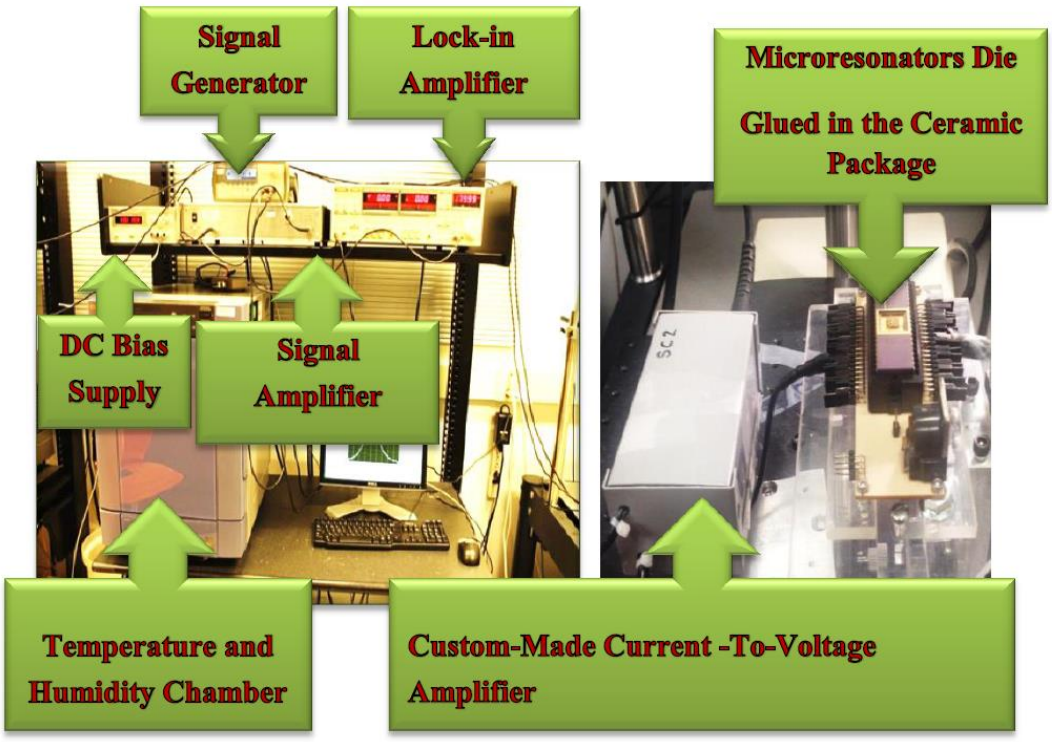

Figure 2.14 High cycle fatigue testing setup used for tracking the changes in resonant frequency during the test [240].

2.4.3. Numerical modelling

A three-dimensional (3-D) finite element model (see Figure 2.15) was created in ANSYS 16.1 to calculate E_{Au}, and to assess the effect of cracks in the Au coating. Modal analyses were done using Block-Lancos method to evaluate the microresonators' f_0 with and without the Au coating (f_0^{coated} and $f_0^{uncoated}$, respectively). The model consisted of 17136 SOLID 186 elements and mesh convergence was ensured. Linear elastic material properties were used for Au and elastic-plastic material properties were used for Ni, as shown in Figure 2.13 (f). All displacements at the base of the beam were set to zero and the analysis was limited to small displacements.

The FEM model was also further modified to include cracks in the Au coating (see Figure 2.15 (c)) in order to capture the effect of cracking of the Au coating on f_0. The cracks extend through the entire coating and the crack opening at the outer surface is kept at 300 nm.

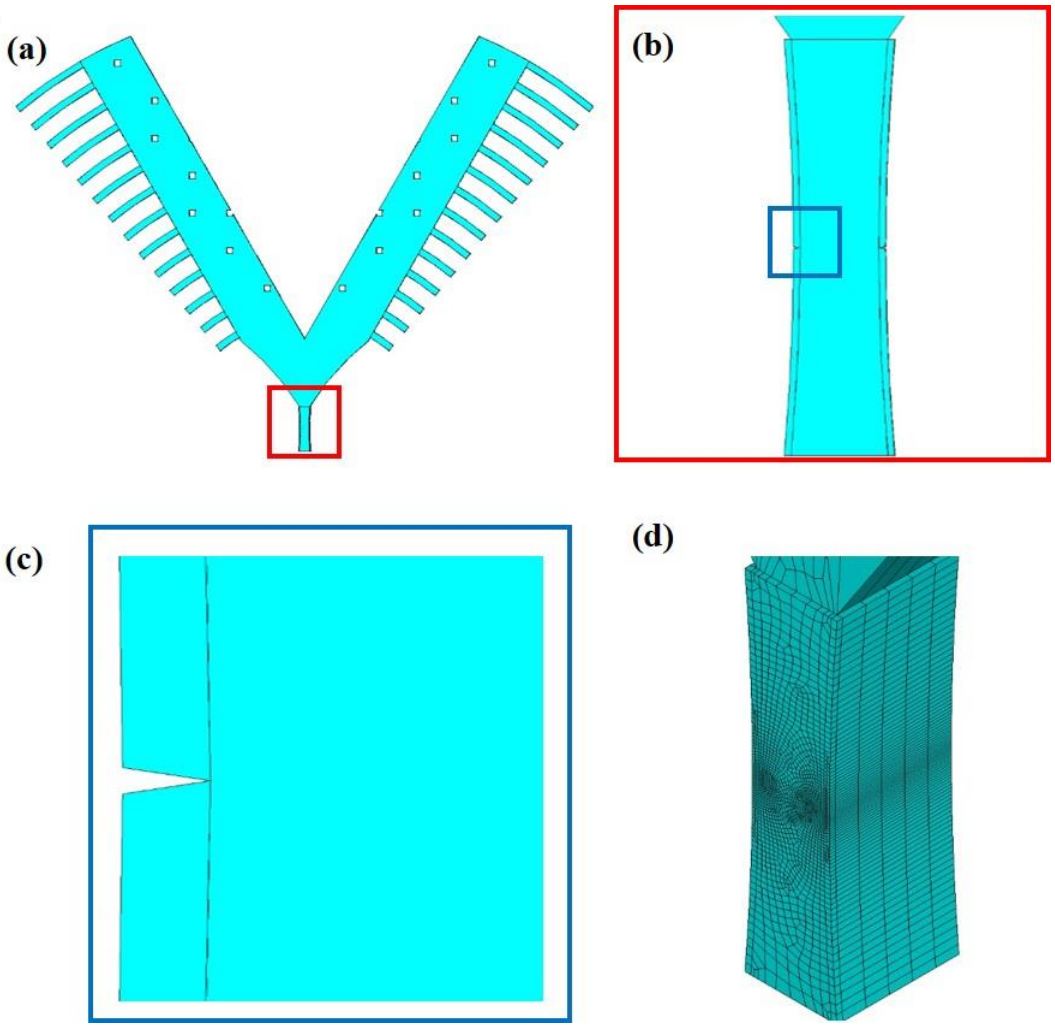

Figure 2.15 (a)-(c) Geometries of the cracked Au coated microbeams used in FEM; (d) Mesh of a coated microbeam without cracks [238].

2.4.4. Calculation of stress and strain amplitudes

The strain amplitude at the outer edges of the Ni beam, $\varepsilon_{a,Ni}$, is calculated from the measured θ_0 at the beginning of each fatigue test, using a finite element model of the microresonator described in [239], whose results are shown in Figure 2.13 (e). Conventional beam bending theory was used to calculate the corresponding strain amplitude at the outer edge of the Au coating, $\varepsilon_{a,Au}$. Based on the half-width of the microbeam (5.75 μm) and the coating thickness (0.85 μm), the maximum strain in Au, $\varepsilon_{a,Au}$, is about 15% larger than $\varepsilon_{a,Ni}$:

$$\varepsilon_{a,Au} = \frac{6.6}{5.75} \times \varepsilon_{a,Ni} = 1.148 \times \varepsilon_{a,Ni} \quad (2\text{-}11)$$

These strain amplitude values are used to estimate the corresponding stress amplitudes in Ni ($\sigma_{a,Ni}$) and Au ($\sigma_{a,Au}$), based on the following assumptions. First, any transient cyclic behavior is ignored since it cannot be accurately measured with the current technique that does not include a force transducer. Instead, the monotonic properties are employed for both Ni and Au, using the measured stress-strain curve for Ni (see Eq. (2-10) and Figure 2.13 (f)), and assuming a nominally elastic behavior for Au (see Figure 2.13 (f)). The assumption for Au is justified by the fact that the maximum strain amplitude in Au is low (0.25%) and that the fatigue life of the Au is large (see CHAPTER 5).

2.4.5. Fractography methods

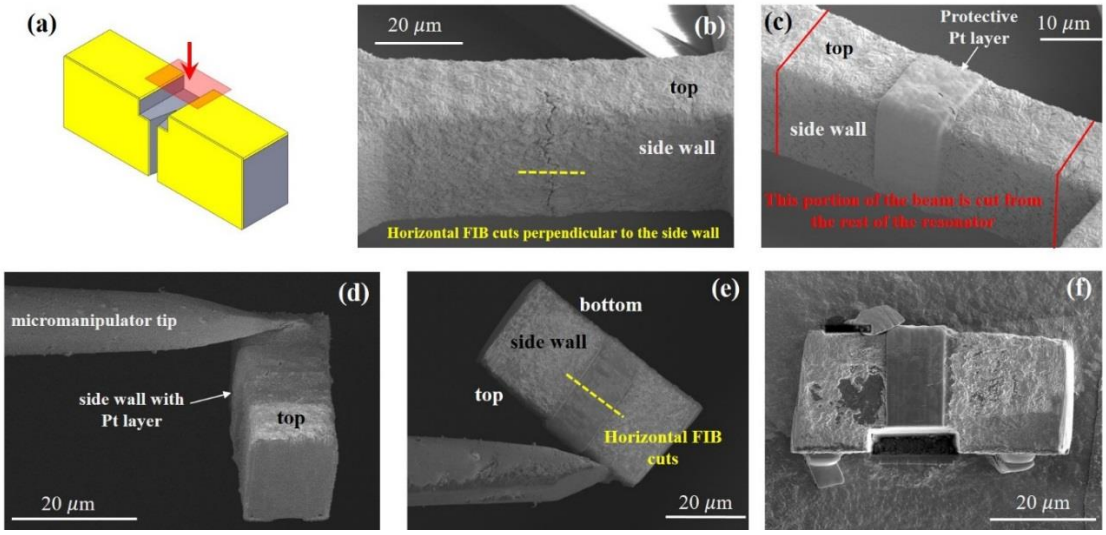

Figure 2.16 (a) Schematic of a horizontal cross-section of a microbeam. (b)-(f) Steps involved in the processing of a horizontal FIB cut (see text for details) [238].

A combination of SEM and FIB milling was used to observe the fatigue damage in the tested microbeams. FIB cuts were made using Ga ions in the FEI Nova Nanolab 200 FIB/SEM tool. The regions around the cracks were protected by depositing a ~2-μm-thick layer of platinum (Pt) as shown in Figure 2.16 (c) prior to the FIB milling to prevent any damage to the crack morphology. The Pt deposition was done at 30 kV and at a current of 0.3 nA. Three kinds of FIB cuts were made: transverse, vertical and horizontal cuts. Transverse and vertical cuts were made perpendicular to the top surface of the coated beam, the cutting plane being perpendicular to the neutral plane for the transverse cuts while the cutting plane was parallel to the neutral plane for the vertical cuts as shown in Figure 5.5 (b)-(d) (see Figure 5.5). The transverse and vertical cuts were made at 30 kV and 1 nA current. Horizontal cuts were made perpendicular to the side wall of the beam as shown in Figure 2.16. To do the horizontal FIB cuts, the microbeam has

to be rotated by 90° and therefore is cut from the rest of the microresonator at high currents of 5 nA at 30 kV (see Figure 2.16 (c)-(f)). A tip mounted on a Kleindiek MM3A-EM micromanipulator is attached to the top of the microbeam, which is rotated by 90° so that the side walls are horizontal. The microbeam is mounted on a substrate using Pt clamps. FIB cuts are then made perpendicular to the side walls at a beam current of 1 nA at 30 kV.

2.5. Conclusions

Three nanomechanical testing techniques, two in-house MEMS-based techniques and one commercial technique using a Push-to-Pull device, were described. The two MEMS techniques shown here covered two different realms of nanomechanical testing: one was developed for *in-situ* tensile testing and the other for very high cycle bending fatigue. The development of the MEMS-based *in-situ* TEM nanomechanical tensile testing technique involved improvements in the existing electronic sensing scheme. The VHCF bending fatigue was realized by using kilohertz microresonators and actuating them under resonance and tracking the evolution of their natural resonant frequency. It was shown that coating these microbeams can be an effective way of studying the influence of metallic coatings such as Au on the VHCF behavior of small scale materials.

CHAPTER 3

RESULTS – IN SITU TRUE ACTIVATION VOLUME CALCULATIONS

3.1. Overview

The methodology to perform transient relaxation tests using the MEMS and the accuracy of the signature parameters obtained from such tests is presented in this chapter. Three different microspecimens were tested *in-situ* to calculate their V^*: 100-nm-thick Au, 200-nm-thick as-deposited Al and 200-nm-thick annealed Al. The details of the microstructure of the three microspecimens are described in the Section 3.2. Section 3.3 analyzes the σ-ε response obtained through ex-situ characterization using the MEMS device and describes the various corrections that need to be made to the raw data. Section 3.4 then describes the *in-situ* monotonic response of all the three microspecimens. Section 3.5 describes the methodology to perform transient relaxation tests *in-situ* and presents the results from the *in-situ* repeated stress relaxation experiments on the three microspecimens. Section 3.6 talks about the practical considerations while performing an *in-situ* experiment. Section 3.7 presents some preliminary TEM observations during relaxation of 100-nm-thick Au microspecimens and the V^* associated with those relaxation segments. Finally, the accuracy of the values of V^* obtained in these *in-situ* tests is discussed in Section 3.8 and guidelines to obtain a reliable V^* are presented.

3.2. Microstructure of Au and Al ultrathin microspecimens

As mentioned earlier, the free-standing ultrathin microspecimens were fabricated independent of the MEMS device, using a process involving optical lithography, electron-beam evaporation, a lift-off technique, and XeF_2 etching of the Si substrate with a thin native oxide. The details of the fabrication of these microspecimens can be found in [169, 185].

The SEM images of the free-standing Au microspecimens are shown in Figure 3.1 (a) & (b). The nominal gauge length of these specimens is 20 μm, width is 1.8 μm and thickness is 100 nm. It can be seen in Figure 3.1 (b) that there are a few large grains ~ 300-400 nm in size among a lot of small grains < 100nm in size. This can be better seen from the grain size distribution shown in Figure 3.1 (e). Figure 3.1 (c) shows a TEM image of the ultrathin microspecimen. Twins and dislocations can be seen within some of the grains and the diffraction patter in the inset shows no in-plane texture. Figure 3.1 (d) shows a TKD (Transmission Kikuchi Diffraction) [241] map of the microspecimen which clearly reveals a <111> out-of-plane texture, as in common observed in deposited Au films [10, 11]. The grain size distribution shown in Figure 3.1 (e) was obtained from this TKD map with average grain size of ~150 nm. The AFM map of the surface roughness of these microspecimens shown in Figure 3.1 (f) reveals that the average surface roughness of these microspecimens is 1.5 nm (~1.5% of the thickness). However, there are some very large grooves ~5 nm deep which can influence the mechanical properties of these ultrathin microspecimens.

The SEM images of the free-standing as-deposited microspecimens are shown in Figure 3.2 (a) & (b). The nominal gauge length of these specimens is 20 μm, width is 1.6 μm and thickness is 200 nm. It can be seen in Figure 3.2 (b) that the grains are roughly the same size, which is also better seen from the narrow grain size distribution shown in Figure 3.2 (e). Figure 3.2 (c) shows a TEM image of the ultrathin microspecimen and no dislocations could be observed in the as-deposited state. Figure 3.2 (d) shows a TKD map of the microspecimen which clearly reveals a random texture. The diffraction contrast was not very clear for the Al microspecimens, therefore the dictionary approach was used to obtain the TKD map [242]. The grain size distribution shown in Figure 3.2 (e) was obtained from this TKD map with average grain size of ~90 nm and a very narrow grain size distribution. The lack of fringes in the TEM image in Figure 3.2 (c) means that there is only one grain per thickness which would mean the grains are columnar since the average grain size is less than the thickness of the microspecimen, although thickness contours could be seen in several grains indicating that the size of the grains is not uniform through the thickness. The AFM map of the surface roughness of these microspecimens shown in Figure 3.2 (f) reveals that the average surface roughness of these microspecimens is 2.7 nm (~1.4% of the thickness).

The as-deposited Al samples were annealed at 450^0C under high vacuum conditions (less than 10^{-7} Torr) with the purpose of increasing the grain size of the microspecimens, however not much increase in grain size was observed after annealing. Figure 3.4 shows the microstructural characterization of the annealed Al microspecimens and the microstructure is very similar to the as-deposited Al

microspecimens. The grain size distribution obtained from the PED (Precession-Enhanced Diffraction) [243] map of the annealed Al microspecimens shown in Figure 3.4 (e) gives the average grain size as 50 nm. Although it is almost half of the average grain size of the as-deposited Al specimens obtained from the TKD map, the PED map of the as-deposited specimens gives an average grain size of 50 nm as well. Therefore, it was concluded that there was not much increase in grain size during the annealing of the Al microspecimens. The reason for the discrepancy between the PED and TKD maps is not known. The geometry of the annealed microspecimens is exactly the same as that of the as-deposited specimens except for one difference. As shown in Figure 3.3 the as-deposited microspecimens have a very thin boundary layer on the sides which is not present in annealed microspecimens. The nature of this layer is amorphous as can be seen from the TEM images. The boundary layer could be the result of the deposition process and might evaporate during annealing. The PED map shown in Figure 3.4 (d) shows a random texture just like the as-deposited specimens. The AFM map of the surface roughness shown in Figure 3.4 (f) reveals that the average surface roughness of these specimens is also 2.7 nm.

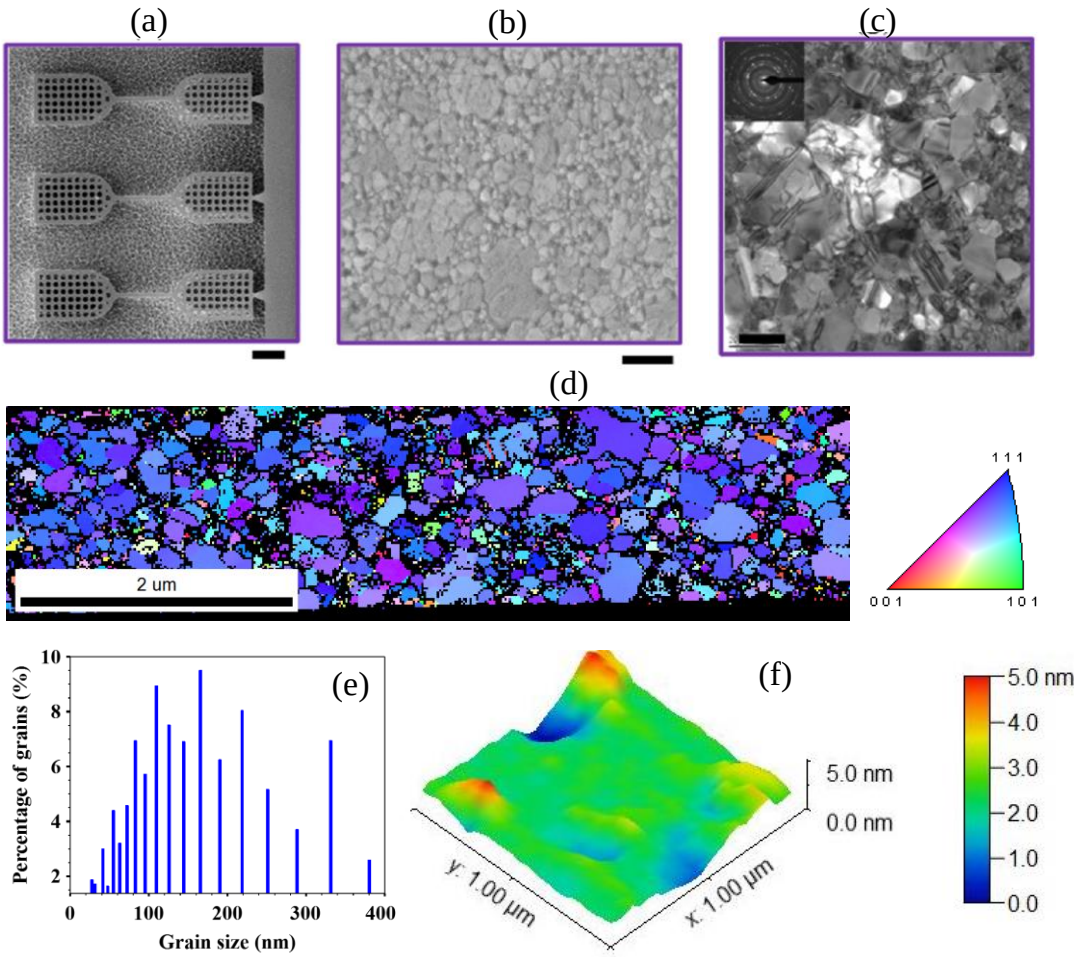

Figure 3.1 Microstructural characterization of 100-nm-thick Au ultrathin microspecimens. (a) & (b) SEM images of the free-standing microspecimens (Scale bar: 1 μm and 2 μm). (c) TEM image of the film showing twins and dislocations within the grains (Scale bar: 100nm). (d) TKD map of the gauge length showing <111> out-of-plane texture. (e) Grain size distribution. (f) AFM map of the surface roughness.

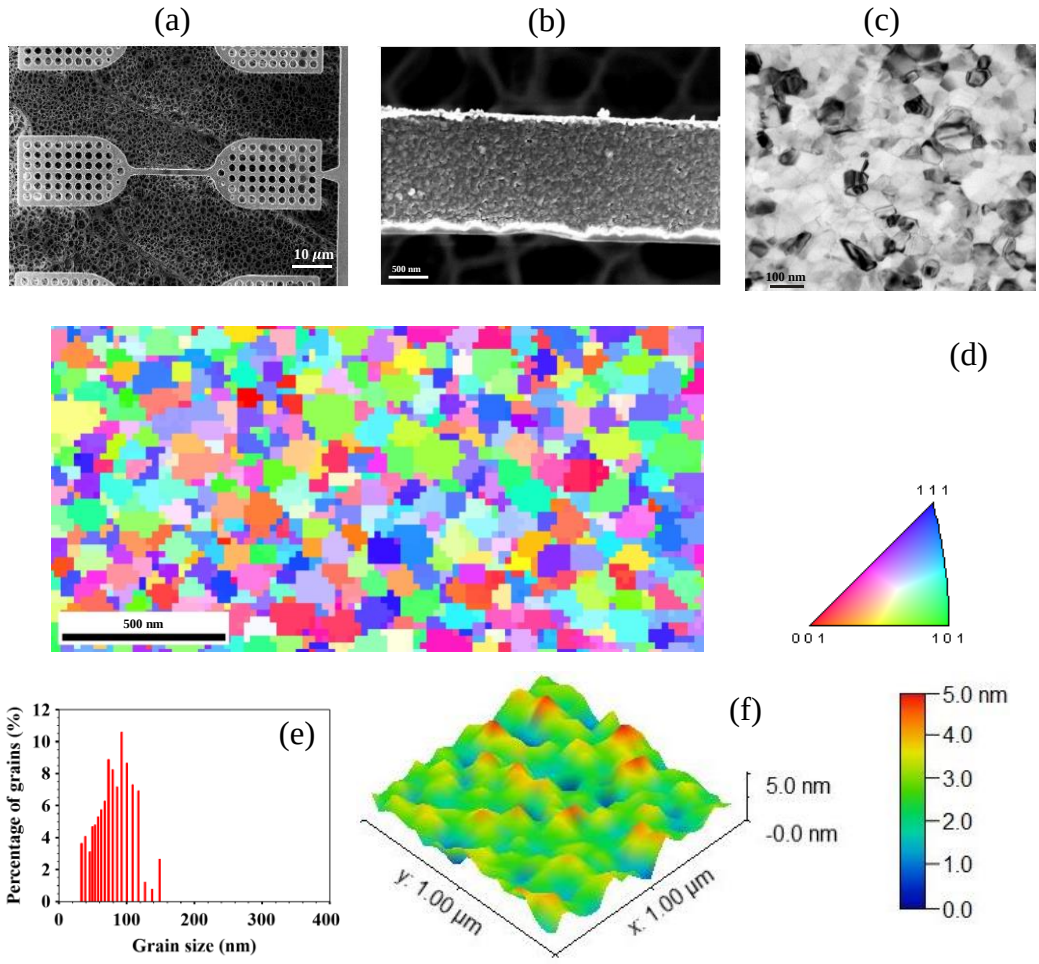

Figure 3.2 Microstructural characterization of 200-nm-thick as-deposited Al ultrathin microspecimens. (a) & (b) SEM images of the free-standing microspecimens. (c) TEM image of the microspecimen. (d) TKD map of the gauge length showing random texture. (e) Grain size distribution. (f) AFM map of the surface roughness.

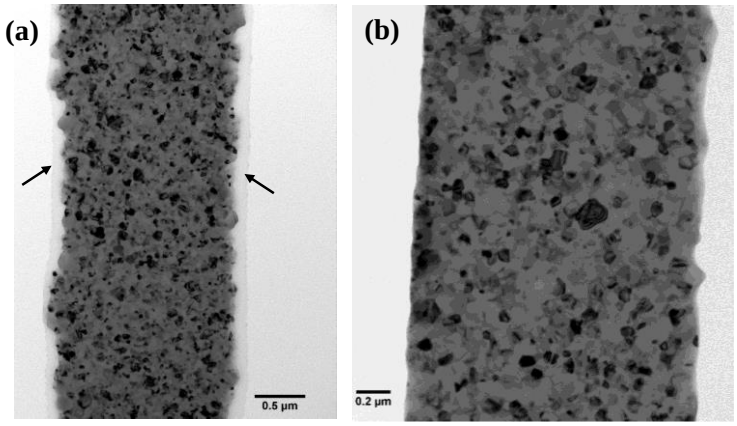

Figure 3.3 Images showing the boundary layer in (a) as-deposited Al microspecimens. No such layer in (b) annealed Al.

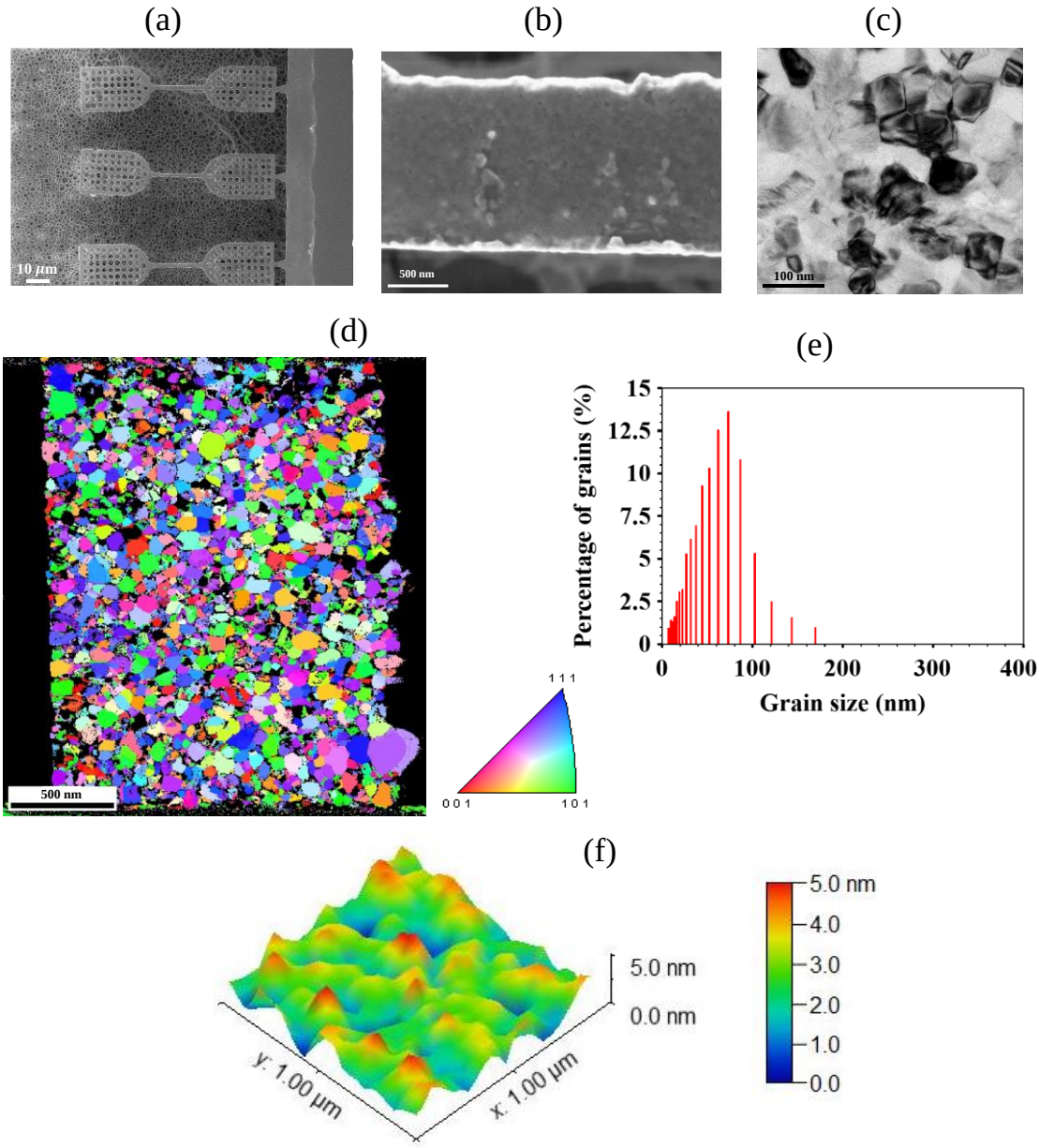

Figure 3.4 Microstructural characterization of 200-nm-thick annealed Al ultrathin microspecimens. (a) & (b) SEM images of the free-standing microspecimens. (c) TEM image of the microspecimen. (d) PED map of the gauge length showing random texture. (e) Grain size distribution. (f) AFM map of the surface roughness.

3.3. Ex-situ testing: Correcting and rationalizing the σ-ε curve

Figure 3.5 shows data obtained from the capacitive sensors CS_1 and CS_2 during a monotonic ex-situ test of 100-nm-thick Au microspecimens and the resulting $\sigma-\varepsilon$ curve. Figure 3.5 (a) shows ΔCS_1 vs the voltage applied to the thermal actuator V_{in} during the test and once the specimen fractures. The value of ΔCS_1 (for a given V_{in}) is expected to decrease in the presence of a specimen because the displacement of the thermal actuator, X_A (measured by ΔCS_1), in the presence of a force (due to the specimen) is less compared to when there is no force (or no specimen). Although as shown in Figure 3.5 (a) the difference is not significant. Figure 3.5 (b) shows ΔCS_2 vs the voltage applied to the thermal actuator V_{in} during the test and once the specimen fractures. It can be seen that the value of ΔCS_2 does not go to zero when the specimen fails. This is anomalous behavior since ΔCS_2 measures the force in the specimen and the force should go to zero when the specimen fails. Figure 3.5 (c) shows the resulting $\sigma-\varepsilon$ curve from this capacitive data and it can be seen that the σ goes to -180 MPa instead of zero once the specimen fractures as is expected because of the anomalous behavior of ΔCS_2. Also, once V_{in} begins to unload after the specimen has fractured, the σ does not remain at -180 MPa but starts to increase as V_{in} reduces (again corresponding to the anomalous behavior of CS_2 in Figure 3.5 (b)). Ultimately, when V_{in} has completely unloaded to zero σ still shows a negative value of -90 MPa. Finally, the elastic modulus obtained from the $\sigma-\varepsilon$ curve is 36 GPa which is only 45% of the bulk value of 80 GPa for Au [244].

Figure 3.6 shows more examples of σ–ε curves obtained with this MEMS device. It can be seen from Figure 3.6 (a), (b) & (c) that sometimes during initial loading the microspecimen does not come under stress even when there is an applied V_{in} and the sample gap X_S is increasing (as indicated by the increasing ε). This is due to the initial buckling of the specimen either because of previously accumulated plastic strain or due to improper manipulation. When the microspecimen is initially buckled and a V_{in} is applied it only comes under stress once the microspecimen becomes taut. Figure 3.6 (c) & (e) show examples of buckling of the specimen (post-test) due to the elongated gauge length because of accumulated plastic strain during the test. Figure 3.7 (a) shows a SEM image of an unfractured buckled Al microspecimen. Figure 3.7 (c), (d) & (e) show examples of plastic overlap obtained after fracture of a microspecimen due to elongation in gauge length because of plastic deformation. Figure 3.7 (b) shows that a fractured Au microspecimen buckled instead of showing the plastic overlap. Figure 3.7 (c) shows a fractured Au microspecimen which exhibits buckling and has plastic overlap. The buckling (to accommodate plastic strain) or the plastic overlap is a direct consequence of the geometry of the microspecimens. Since the microspecimens are so thin, the stiffness of these specimens is not sufficient to change the specimen gap to accommodate the extra length acquired by these microspecimens once they elongate during a test and hence they either buckle or show plastic overlap.

Negative σ values are obtained not only when a microspecimen fails as shown in Figure 3.5 (c) and Figure 3.6 (b) but also upon unloading V_{in} (as shown in Figure 3.6 (d) & (e)). However, when negative σ values are obtained with the

microspecimen not fractured, the ε does not go to zero (see Figure 3.6 (d) & (e)) unlike when the microspecimen fractures (see Figure 3.5 (c) and Figure 3.6 (b)). In fact it is expected that the ε shows a positive value upon complete unloading when σ is negative (and the specimen is not fractured). Assuming X_A is completely reversible upon complete unloading of the sample (i.e., V_{in}= 0), if σ is negative upon complete unloading (which means ΔCS_2 or X_{LS} is negative), Eq. (2-1) implies that X_S should be positive or ε should be positive. Lastly, negative σ values are not always obtained when the microspecimen fails or completely unloads as shown in Figure 3.6 (a) & (c). It should be noted that in Figure 3.6 (c) ε also goes to zero upon complete unloading.

It is pretty clear by now from the σ–ε curves shown in Figure 3.5 and Figure 3.6 that there are several unresolved issues in fully understanding the σ–ε curves obtained with this MEMS technique. It will be shown in this section that the accuracy of stress and strain measurement (and therefore elastic modulus) depends on six factors:

(a) The error induced by not correcting the raw ΔCS_2 data. This is especially important for the accuracy of σ.

(b) The accuracy of the calibration constants α_{CS1} and α_{CS2}.

(c) Pre-stress in the microspecimen. This can easily be measured and accounted for.

(d) Drift in the capacitive signals. This is the most significant source of error since it is very difficult to quantify and nearly impossible to control. The drift in the capacitive signals makes it difficult to control the other sources of error such as (a) and (b).

(e) Compliance of the epoxy glue. This affects the elastic modulus directly.

(f) Uncertainty in the gauge length. This induces errors in the strain measurement.

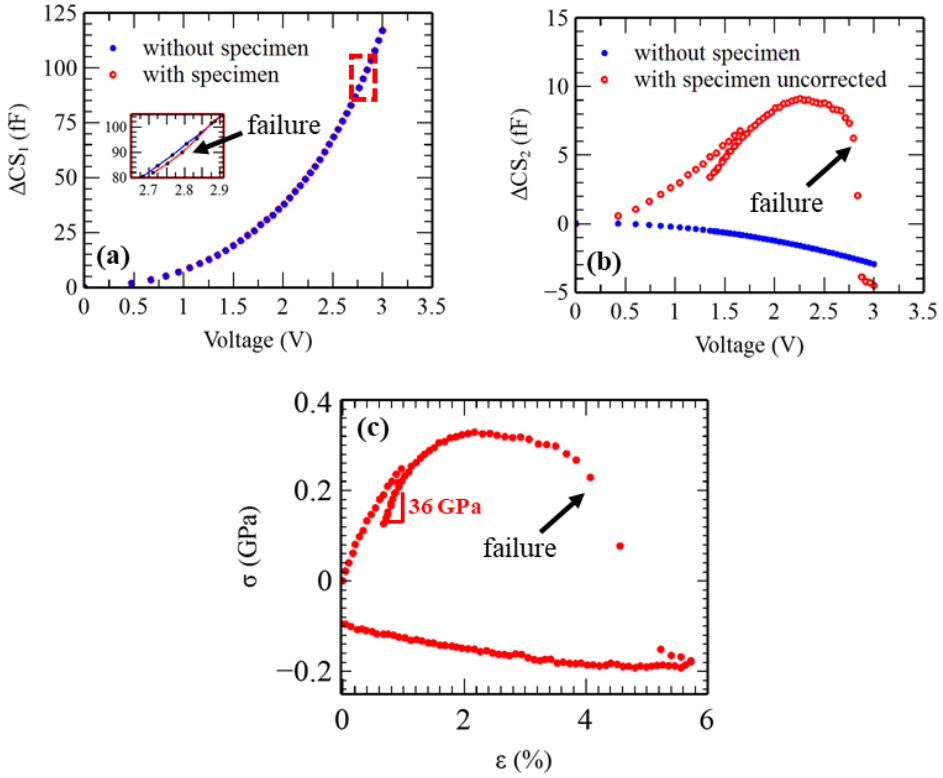

Figure 3.5 (a) Raw capacitive measurement of ΔCS_1 showing little difference between the data with and without the microspecimen, (b) Raw capacitive measurements of ΔCS_2 with and without the microspecimen. (c) Resulting σ–ε curve.

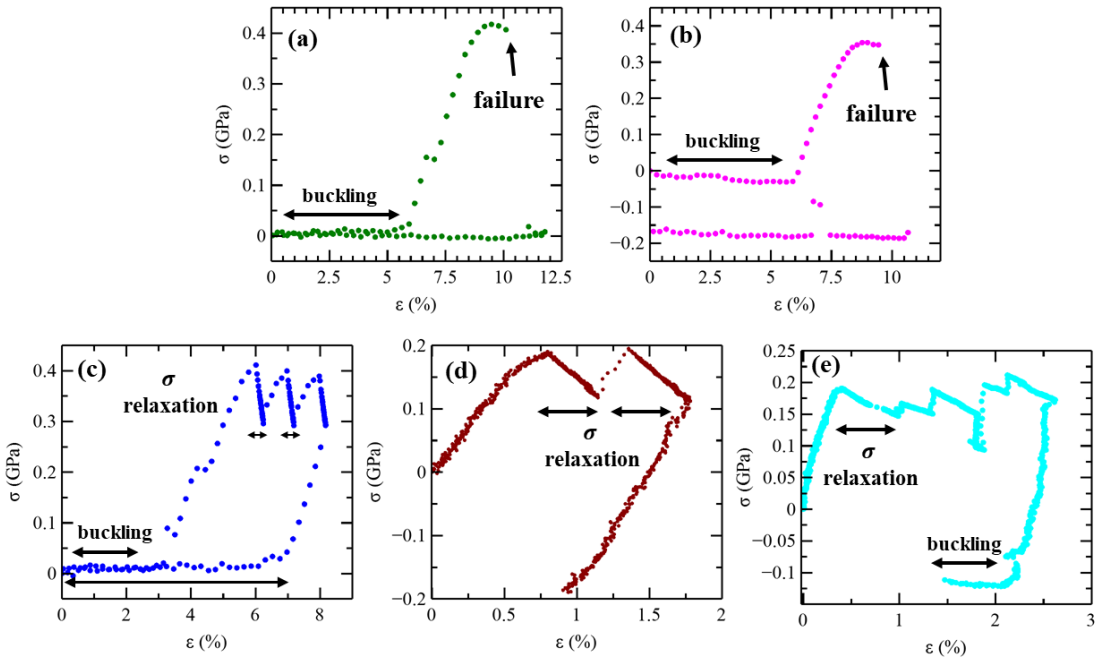

Figure 3.6 Different types of σ–ε curves obtained during testing with the MEMS device. (a) 100-nm-thick Au. (b) 200-nm-thick annealed Al. (c) 100-nm-thick Au. (d) 200-nm-thick annealed Al. (e) 100-nm-thick Au.

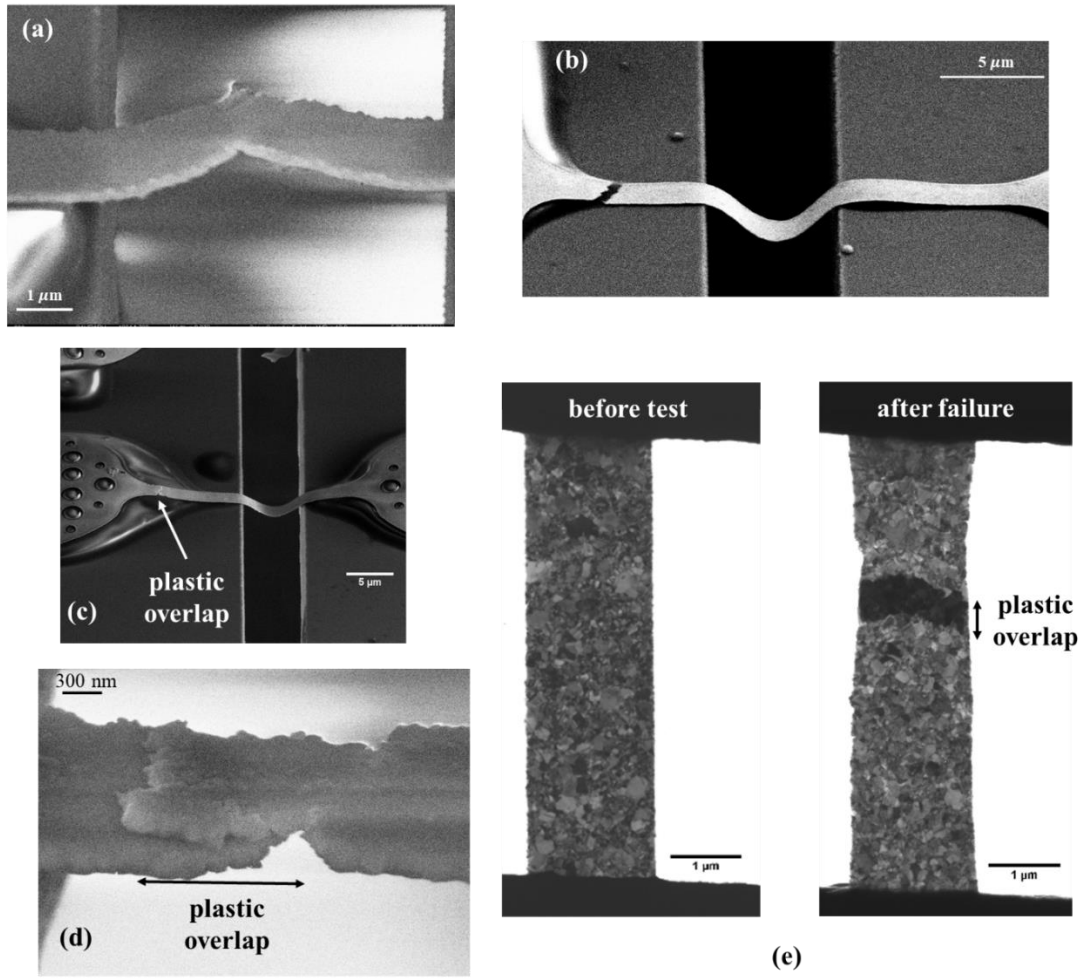

Figure 3.7 (a) Inclined SEM image showing buckling caused by plastic deformation in an unfractured microspecimen. (b) Inclined SEM image showing buckling caused by plastic deformation in a failed microspecimen. (c) SEM image showing buckling and plastic overlap in a fractured Au microspecimen. (d) SEM image showing plastic overlap after fracture. (e) TEM images showing plastic overlap caused by tensile elongation in a fractured microspecimen.

3.3.1. Correction of the raw CS_2 data

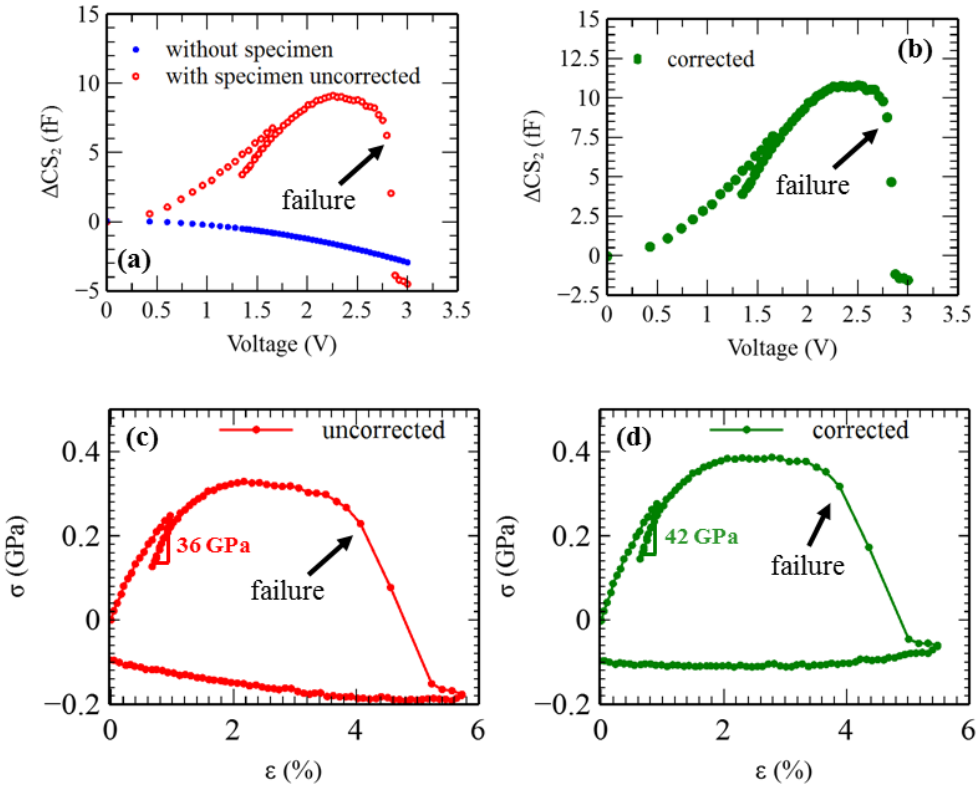

Figure 3.8 Monotonic testing of 100-nm-thick Au. (a) Raw capacitive measurement of ΔCS_2 with and without the specimen. (b) Corrected capacitive measurements of ΔCS_2. (c) Uncorrected and (d) Corrected σ–ε curve.

As shown earlier and in Figure 3.8 (a) ΔCS_2 does not go to zero when the specimen fails. In situ SEM examination shows that CS_2 does not move in the absence of a specimen (based on SEM images providing a precision of 5 nm) for V_{in}= 3 V, whereas the corresponding measured ΔCS_2 value of –2 fF would be equivalent to a displacement of 80 nm [222]. Therefore, it can be concluded that the non-zero values of CS_2 in the absence of a specimen are not related to mechanical motion but instead electrical parasitic coupling [223]. This requires that the raw ΔCS_2 measurement be corrected for this behavior. A polynomial is fit between ΔCS_2 and V_{in} (obtained in the absence of a sample) shown in Figure 3.8 (a) and using this fit the appropriate correction corresponding to the applied

voltage is added to ΔCS_2 obtained from a test. The corrected curves for ΔCS_2 are shown in Figure 3.8 (b). It can be readily seen that ΔCS_2 goes to zero when the sample fractures. It can also be seen from Figure 3.8 (c) & (d) that the apparent elastic modulus increases by ~17% from 36 GPa to 42 GPa upon correcting the anomalous ΔCS_2 behavior. Also, σ more or less stays flat upon unloading after the correction as shown in Figure 3.8 (d). σ upon failure is however still has a negative value of -90 MPa even after correction. This could be due to pre-stress in the microspecimen or the drift in the capacitive signals.

It is important to note that the magnitude and direction of the anomalous behavior of CS_2 can be very different. Figure 3.9 shows several examples. But no matter what this behavior is completely an electrical effect and not a physical one. This behavior is also seen in CS_1 sensor but the magnitude of CS_1 signals are of the order of 100 fF (see Figure 3.5 (a)) and therefore this anomalous behavior whose magnitude is typically of the order of 5 fF is negligible for ΔCS_1. It is however very critical for ΔCS_2 as has been shown here.

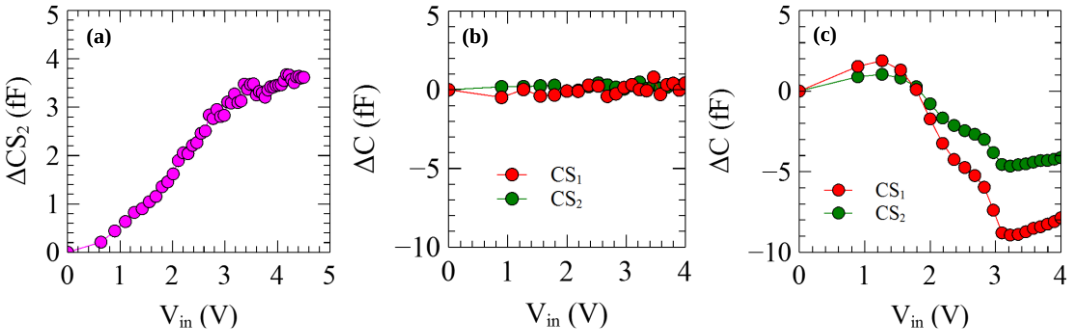

Figure 3.9 Different kinds of anomalous behavior of the capacitive sensors. (a) Positive values. (b) Negligible anomalous behavior. (c) Negative values. It should be noted that in (c) anomalous behavior of CS_1 is also shown when the CS_1 gap is not glued and thus CS_1 beams do not move upon applying a voltage to thermal actuator and therefore ideally ΔCS_1 should be zero. It is interesting that the behavior is absent in both CS_1 and CS_2 in (b).

3.3.2. Error in calibration constant

Figure 3.10 shows the effect of changing α_{CS_2} while keeping α_{CS_1} constant on the monotonic response of a 100-nm-thick Au microspecimen. It can be seen that there is an inverse relationship between σ and α_{CS_2}. As α_{CS_2} is doubled σ decreases by a factor of two and vice-versa. However, this relationship is not as linear for all values of ΔCS_2 (see Section 3.8). As α_{CS_2} is increased the apparent Young's modulus decreases more sharply. As α_{CS_2} was doubled, the apparent Young's modulus reduced by one-third. This is because increasing α_{CS_2} decreases σ and therefore X_{LS} and so X_s increases leading to increase in ε and the combination of the two factors leads to a sharper decrease in the apparent Young's modulus.

Figure 3.11 shows the effect of changing α_{CS_1} while keeping α_{CS_2} constant on the same monotonic response. As expected σ values are not affected however ε decreases as α_{CS_1} is increased. This two studies show the importance of determining α accurately and therefore doing calibration in-situ using TEM is absolutely essential.

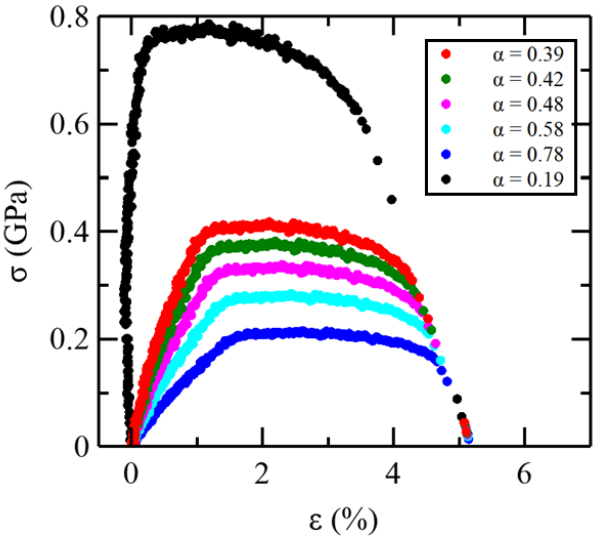

Figure 3.10 Effect of changing α_{CS_2} on the σ–ε curve. α_{CS_2} is increased from an initial value of 0.39 by 10%, 25%, 50%, 100% and -50%. The apparent Young's modulus (in GPa) obtained from the slope initial linear portion of the curves are 39.5, 33.29, 26.93, 20.42, 13.75 and 190.84 respectively. (K_{LS} = 480 N/m, d_{CS_2} = 2.68 μm).

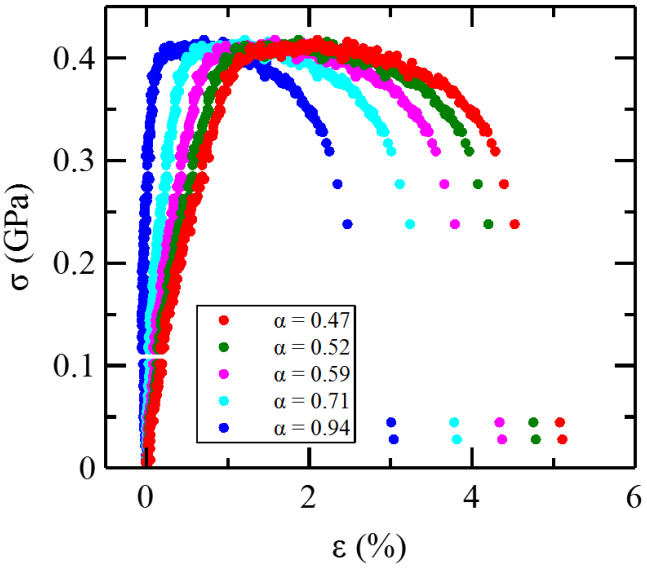

Figure 3.11 Effect of changing α_{CS_1} on the σ–ε curve. α_{CS_1} is increased from an initial value of 0.47 by 10%, 25%, 50% and 100%. The apparent Young's modulus (in GPa) obtained from the slope initial linear portion of the curves are 39.5, 47.08, 61.44, 98.51 and 192.54 respectively. (d_{CS_1} = 2.40 μm).

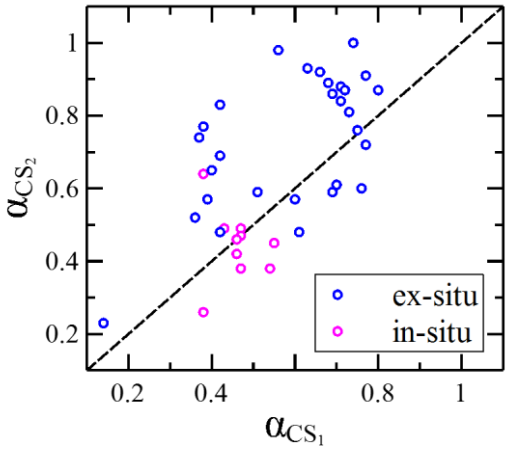

Figure 3.12 Values of α for various in-situ and ex-situ tests.

Figure 3.12 shows the different calibration constants for the in-situ and ex-situ tests done by the MEMS device. It can be clearly seen that the assumption used to calculate α_{CS_2} for an ex-situ test does not give the same results as the

independent in-situ calibration for CS_1 and CS_2. It is important however to highlight that any drift in the capacitive signals can completely throw the calibration off.

3.3.3. Pre-stress in the microspecimens

Figure 3.13 shows the monotonic behavior of an Au sample tested in –situ. The σ value after the microspecimen fails is -150 MPa. It was measured from TEM images of CS_2 gap before and after test that the gap increases by 25 nm. The initial gap (with unfractured specimen at V_{in} = 0) was 2.68 μm and the gap increased to 2.885 μm after the microspecimen failed. This means CS_2 was under a positive stress equivalent to 25 nm of X_{LS} which corresponds to σ equal to 55 MPa. However, the pre-stress doesn't match the -150 MPa. Further, there is no physical change in the CS_2 gap during the drop in σ shown within the dotted circle in Figure 3.13. The reason for this drop could not be drift or anomalous behavior of CS_2 because of the instantaneous nature of the drop once the specimen completely fails. This drop could however explain the negative σ observed when microspecimens fail such as in Figure 3.6 (b) and Figure 3.8 (d).

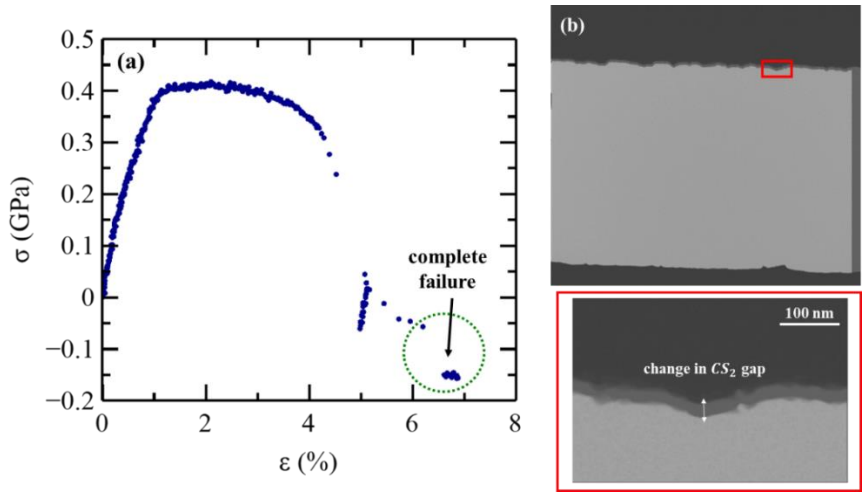

Figure 3.13 Pre-stress calculation. (a) Monotonic σ-ε curve of 100-nm-thick Au microspecimen showing a negative stress of -150 MPa after failure instead of zero. (b) Overlay of the TEM images of the CS_2 gap before test and after microspecimen failure showing a difference of 25 nm in the gap indicating the existing of a tensile pre-stress of 55 MPa (see text) in the microspecimen.

3.3.4. Drift in the capacitive signals

Figure 3.14 shows ΔCS_1 signal during a stress relaxation segment. Ideally, since X_A remains constant during a stress relaxation ΔCS_1 should also remain constant. This has been verified with *in-situ* SEM experiments that CS_1 gap does not change even at high applied voltages when the temperature near the CS_1 gap is high and can cause the epoxy to creep. However, as shown in Figure 3.14 ΔCS_1 drifts with time and so does ΔCS_2. The reason for this kind of drift has to be purely electrical as physically there is no motion. It is therefore to quantify and predict this kind of drift and therefore very difficult to control. This can cause issues with calibration. Figure 3.6 (d) shows that σ after complete unloading is -170 MPa however from TEM images before and the end of the test the change in CS_2 gap corresponds to -60 MPa of change in σ. The negative value of σ is therefore only partially explained by the pre-stress in the microspecimen. The value of α_{CS_2} used for this test was 0.54 and if the value of the negative σ of -60 MPa were to be matched by the capacitive data then the value of α_{CS_2} that needs to be used is 0.90. This is almost a 50% change in α_{CS_2} or 50% error in calibration. Figure 3.14 shows that this much error in α_{CS_2} is not likely to occur because of the drift in capacitive signals.

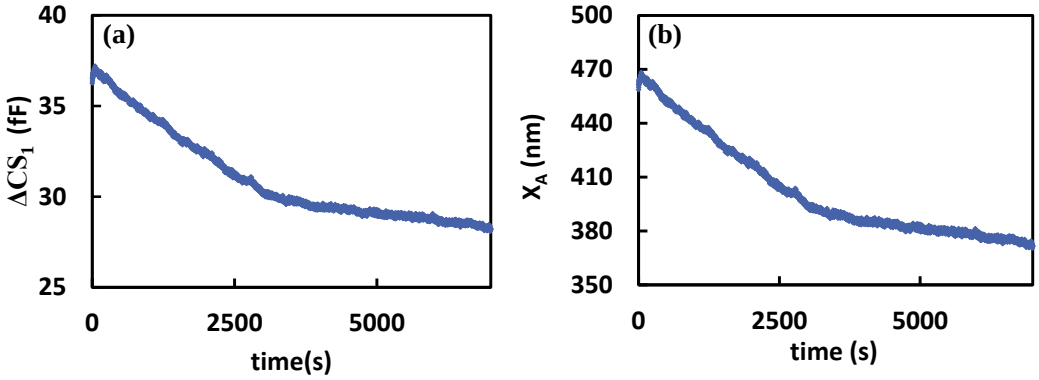

Figure 3.14 Drift in ΔCS_1 signal (a) and correspondingly X_A (b) during a stress relaxation segment during which X_A and ΔCS_1 should ideally be constant.

3.3.5. Deformation of the epoxy glue

Figure 3.8 (c) shows that the modulus of the 100-nm-thick Au microspecimen is about 53% of the bulk value of 80 GPa. This low value of elastic modulus is partially the result of deformation of the sample outside of the "gauge length" due to compliance of the epoxy glue underneath it.

Figure 3.15 (a) & (b) show the normal strain distribution obtained for a stress of 300 MPa in the specimen's gauge section for two thicknesses of the glue (t_g = 10 μm and 1 μm respectively), corresponding to two free-standing half gauge lengths (5 and 10 μm). The strain maps clearly illustrate non-negligible local deformation of the specimen in the fillet region and gauge section where glue is underneath, while the deformation in the widest part of the pad is negligible (as predicted in [223]). The strain distribution as a function of distance from the specimen's half point is shown in Figure 3.15 (c) & (d); as a reference, the ideal case (rigid glue) is shown as well. In each case, an effective E value, E_{eff}, is calculated by including the finite deformation of the section of the specimen that has glue underneath. The local deformation results in E_{eff} = 64.2 GPa (19.75%

lower than E_{Au} = 80 GPa) in the case of the entire gauge section being free-standing. The 19.75% decrease in E results from the local deformation in the fillet region. If the glue is present underneath 5 μm of the gauge section, the model predicts E_{eff} = 45.7 GPa (42.9% lower than E_{Au} = 80 GPa). The model predicts little effect of the thickness of the glue (see Figure 3.15 (c) and (d)). This model therefore shows that the accuracy in elastic strain measurement from the MEMS device is poor, in part due to the local deformation of part of the specimen that is glued. Another important reason for the poor accuracy is that the value of elastic strain in these specimens itself is very small due to the very small gauge lengths. A gauge length of 10 μm would accommodate an elastic strain of 20 nm (0.2%) and an error of only 6 nm in the measurement can produce 30% error in the elastic strain. However, such a small error will not produce a significant inaccuracy in the measurements of plastic strain (typically 200-400 nm), as is shown next.

Figure 3.15 (c) & (d) show that the stress in the specimen drops quickly in the section where glue is underneath. Hence it is reasonable to assume that most of the plastic deformation of the specimen only occurs within the free-standing part of the gauge section. Therefore, in the plastic regime, the increase in X_S corresponds to the increase in plastic elongation of the specimen's free-standing gauge section, implying that plastic strains can be measured accurately (the free-standing gauge length can be measured accurately from SEM images). This is only true if the glue underneath the specimen does not deform plastically or viscoelastically. This was confirmed with *in situ* SEM measurements. Figure 3.16 (a) shows a clamped specimen that underwent a series a loading-unloading at

increasing V_{in} values, including three holds at large V_{in} values during which the specimen deforms viscoplastically [177]. The specimen was then loaded to failure, which occurred at V_{in} = 2.89 V. The plastic overlap at the failure location (see Figure 3.16 (b)) after the test is ~370-400 nm. The distance d between the tip of the specimen and one edge of the Si MEMS (see Figure 3.16 (a)) was measured during most of the load-unloads and holds, and no significant change could be measured (within the resolution of the SEM images ~ 6.2 nm; for example see Figure 3.16 (c)). Any change in d would be related to plastic deformation of the glue (the predicted change in d due to elastic deformation of the glue is ~0.2 nm). Hence, a constant d is a clear indication that no plastic or viscoelastic deformation of the glue occurred during the test which resulted in 370-400 nm of plastic elongation (2.8% of plastic strain).

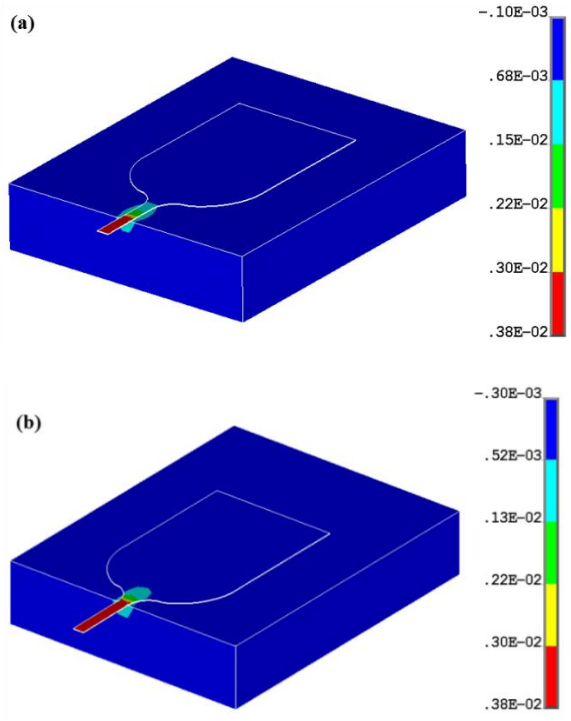

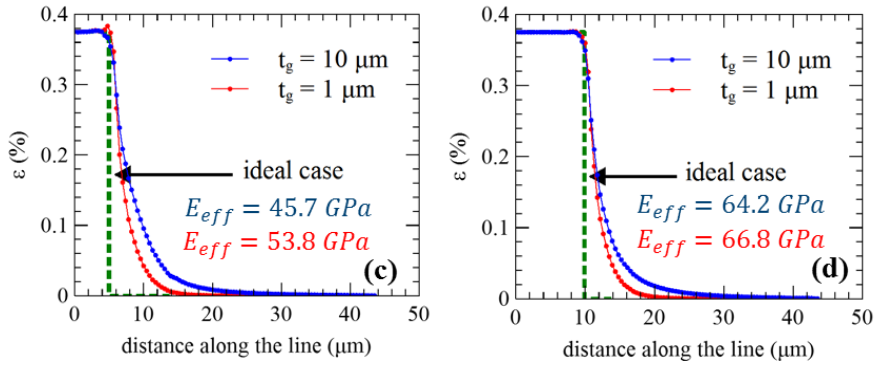

Figure 3.15 (a) & (b) Strain maps for glue thickness (t_g) of 10 μm and free standing lengths of the specimen (l_{free}) equal to 5 μm and 9.9 μm respectively, (c) & (d) Strain distribution along the length of the specimen and in the clamps for free standing lengths of the specimen (l_{free}) equal to 5 μm and 9.9 μm respectively.

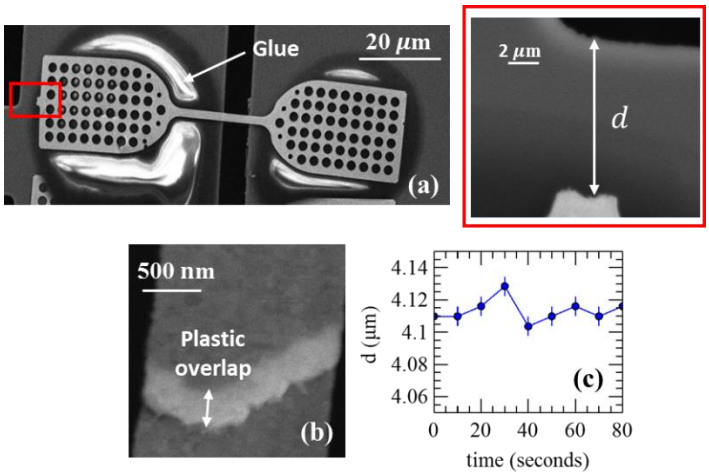

Figure 3.16 (a) Clamped specimen before any tests, (b) Plastic overlap after several relaxations and (c) the variation in '*d*' measured during one of the relaxation segments.

3.3.6. Uncertainty in gauge length

As the FEM model discussed in Section 3.3.5 predicts that most of the elastic strain and therefore stress is taken by the free-standing part of the specimen where there is no glue underneath it. Therefore, since failure and plastic deformation is expected to occur in the region where stresses are the highest, nominal gauge length for a test is chosen to be the free-standing length of the microspecimen as shown in Figure 3.17 (a). However there are certain

issues with this assumption. In practice it is difficult to say whether a part of the specimen that has glue underneath it is actually attached to the glue. For example, as shown in Figure 3.17 (b) fracture was observed in the region that had glue underneath it. This creates uncertainty in determining the gauge length.

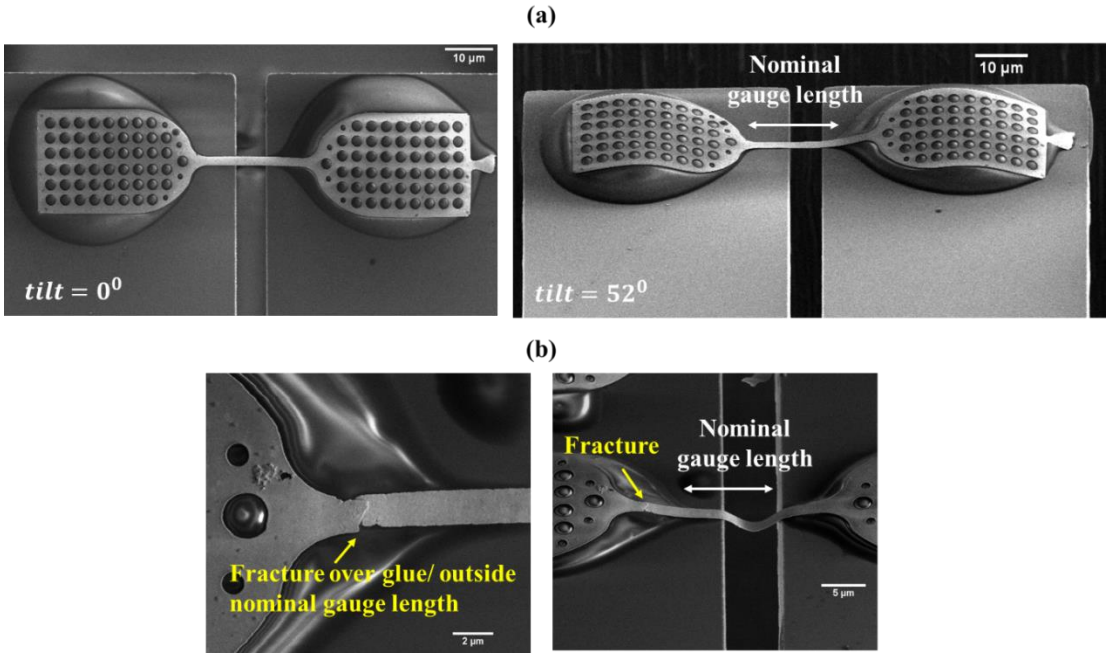

Figure 3.17 (a) Before test SEM images to identify nominal gauge length. (b) After test SEM images showing fracture outside nominal gauge length.

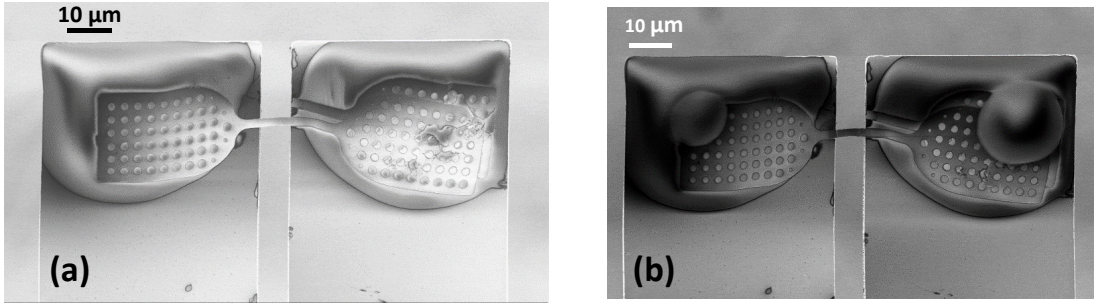

Figure 3.18 (a) Specimen with no glue on top completely slips over the glue underneath under worst case scenario, (b) Addition of two small drops of glue on top on the same specimen improves the clamping substantially.

Further, it was observed that, for the specimen shown in Figure 3.18 (a), for which there was glue only underneath the specimen, the force sensor did not

even move upon testing the specimen after curing the glue. The specimen was loaded to 2.71 V corresponding to X_A of 0.82 μm, yielding $X_{LS} = 0$ instead of an expected value of 350 nm assuming the modulus of the specimen is 70 GPa. Therefore, the end of the specimen pulling CS_2 was not clamped well enough to pull the load sensor and the specimen was just slipping over the glue underneath to accommodate X_A of 0.82 μm. However, when the additional two drops of glue were dispersed as shown in Figure 3.18 (b), and the specimen was loaded to 2.71 V, a X_S of 340 nm and X_{LS} of 450 nm were recorded giving a modulus value of 16 GPa. The two small drops were clearly not large enough to provide good clamping for the specimen but large size of the drops should improve the clamping significantly. This might be due to the glue underneath the specimen not getting cured under UV light, which is possible since the specimen is not transparent. This type of behavior adds to the uncertainty in choosing the nominal gauge length.

3.4. In-situ monotonic testing

The in-situ TEM monotonic response of 100-nm-thick Au films is shown in Figure 3.19 (a). The test was conducted in a strain rate regime of ~1-2x10^{-4} s^{-1}. The apparent elastic modulus obtained from the linear portion of the stress-strain curve was 40 GPa. The tensile strength was obtained as 460 MPa after accounting for the pre-stress. The ductility was around 4%. The curve shows very little work hardening and plateaus around 1.5% strain showing virtually no work hardening. The failure occurred at 45^0 to the tensile axis as shown in Figure 3.20

(a) and Figure 3.21 (f). Figure 3.21 shows snapshots from an in-situ TEM monotonic test of the 100-nm-thick Au microspecimens. It was observed that below 1% strain there is not much dislocation activity but it rapidly increases in several grains as the strain increases. The strain remains almost uniformly distributed until 3% strain as can be seen from the local strain distribution in the microspecimen in Figure 3.21 (a)-(c), (g) & (h). But the strain rapidly localizes (see Figure 3.21 (d), (g) & (h)) and voids start to form as the strain further localizes (see Figure 3.21 (e)) and eventually the sample fails by the coalescence of the voids along a plane at 45^0 to the tensile axis (see Figure 3.21 (f)).

The yield stress of the 100-nm-thick Au microspecimens was obtained as 450 MPa at a strain rate of ~1-2 x $10^{-4}\ s^{-1}$. Wang and Prorok [11] obtained yield stress yield stress values around 390 MPa for 250-nm-thick Au films with average grain size of 40nm tested at a strain rate of 2 x $10^{-4}\ s^{-1}$. Emery and Povirk [245] obtained yield stress in the range of 380-470 MPa for Au films with thickness ranging from 200-550 nm (thicker films having lower yield stresses) tested in the 10^{-5} – $10^{-4}\ s^{-1}$ strain rate range. Chasiotis et al. [246] obtained yield and saturation stress as 220 MPa and 280 MPa respectively for 500-nm-thick Au films tested at $10^{-4}\ s^{-1}$. Jonnalagadda et al. [10] measured the yield stress of 850-nm-thick Au films with average grain size of 40 nm as 700 MPa tested at $10^{-4}\ s^{-1}$.

The in-situ TEM monotonic response of 200-nm-thick as-deposited Al films is shown in Figure 3.19 (b). The test was conducted in a strain rate regime of ~1-2x$10^{-4}\ s^{-1}$. The apparent elastic modulus obtained from the linear portion of the stress-strain curve was 17 GPa. The tensile strength was obtained as 235

MPa and the ductility was around 4%. The curve becomes non-linear showing some work hardening after just 1% of strain and ultimately plateaus around 3% strain. The in-situ TEM monotonic response of 200-nm-thick annealed Al films is shown in Figure 3.19 (c). The test was conducted in a strain rate regime of ~1-2x$10^{-4}\,s^{-1}$. The apparent elastic modulus obtained from the linear portion of the stress-strain curve was 20 GPa. The tensile strength was obtained as 280 MPa after accounting for the pre-stress and the ductility was around 2.5%.

The yield stress of the 200-nm-thick Al microspecimens was obtained as 220 MPa at a strain rate of ~1-2 x $10^{-4}\,s^{-1}$. Haque and Saif [8, 247] measured the yield stress of 50-nm-thick Al films with average grain size of 22 nm as 350 MPa. Haque and Saif [8] also tested 100-nm-thick Al films with 50 nm grain size which failed in a brittle manner at stress of 680 MPa. They also tested films with thickness 150 nm and 480 nm with grain sizes 65 nm and 212 nm respectively and obtained yield stresses of 420 MPa and 280 MPa respectively. Gianola et al. [133] measured the yield stress of 150-nm-thick Al films with mean grain size of 62 nm as 200 MPa tested at $10^{-5}\,s^{-1}$.

The thickness of the films could be responsible for higher strength of the Au microspecimens compared to the Al films even though Al has lower grain size. Due to the Hall-Petch relationship, the yield stress of Al was expected to be higher than Au. During a test when the as-deposited Al sample was not exposed to electron beam the stress at failure was 360 MPa as compared to 250 MPa when the sample was exposed to the TEM while testing. Stress relaxation upon exposure to high energy electron beam has been observed in Al films by Haque and Saif [247]. Several researchers have reported artifacts introduced by the

electron beam during in-situ TEM testing of nanostructured metals [248]. So, the yield stress of Al could be lowered because of the electron beam effects.

The comparison between the in-situ and ex-situ monotonic behavior of the three microspecimens is shown in Figure 3.19. It should be noted that the ex-situ stress values may not be accurate since the capacitive sensor CS_2 cannot be calibrated ex-situ. The in-situ and ex-situ monotonic σ-ε curve is similar for Au and annealed Al films except for the magnitude of σ however differs significantly for the annealed Al film but the discrepancy can be explained in terms of the error in the calibration of CS_2 as shown in Section 3.3.2. The responses are qualitatively similar suggesting that the response does not change between ex-situ and in-situ testing. The monotonic response of the as-deposited Al microspecimens however is significantly different when the microspecimen is tested in air (ex-situ) vs when it is tested in vacuum (in-situ). As shown in Figure 3.19 (b), ex-situ the σ-ε curve has a strain softening behavior after the peak σ is reached similar to that of annealed Al behavior but in vacuum the microspecimen fails right after necking without showing the strain softening behavior.

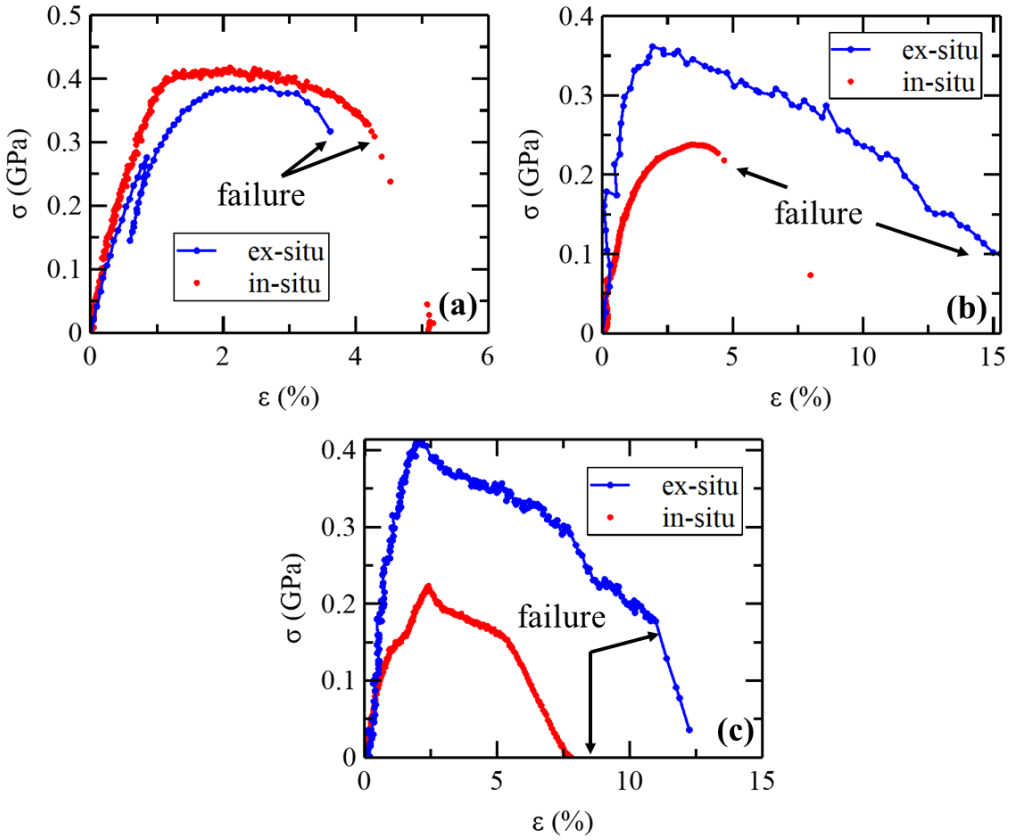

Figure 3.19 Comparison of ex-situ and in-situ monotonic test data of the three microspecimens: (a) 100-nm-thick Au, (b) 200-nm-thick as-deposited and (c) 200-nm-thick annealed Al.

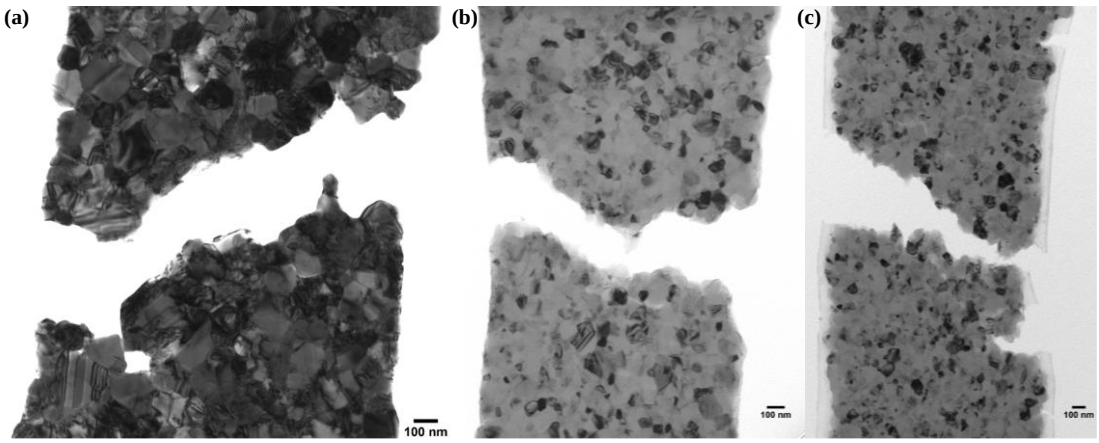

Figure 3.20 Fracture surfaces of (a) 100-nm-thick Au microspecimens, (b) 200-nm-thick annealed Al microspecimens and (c) 200-nm-thick as-deposited microspecimens.

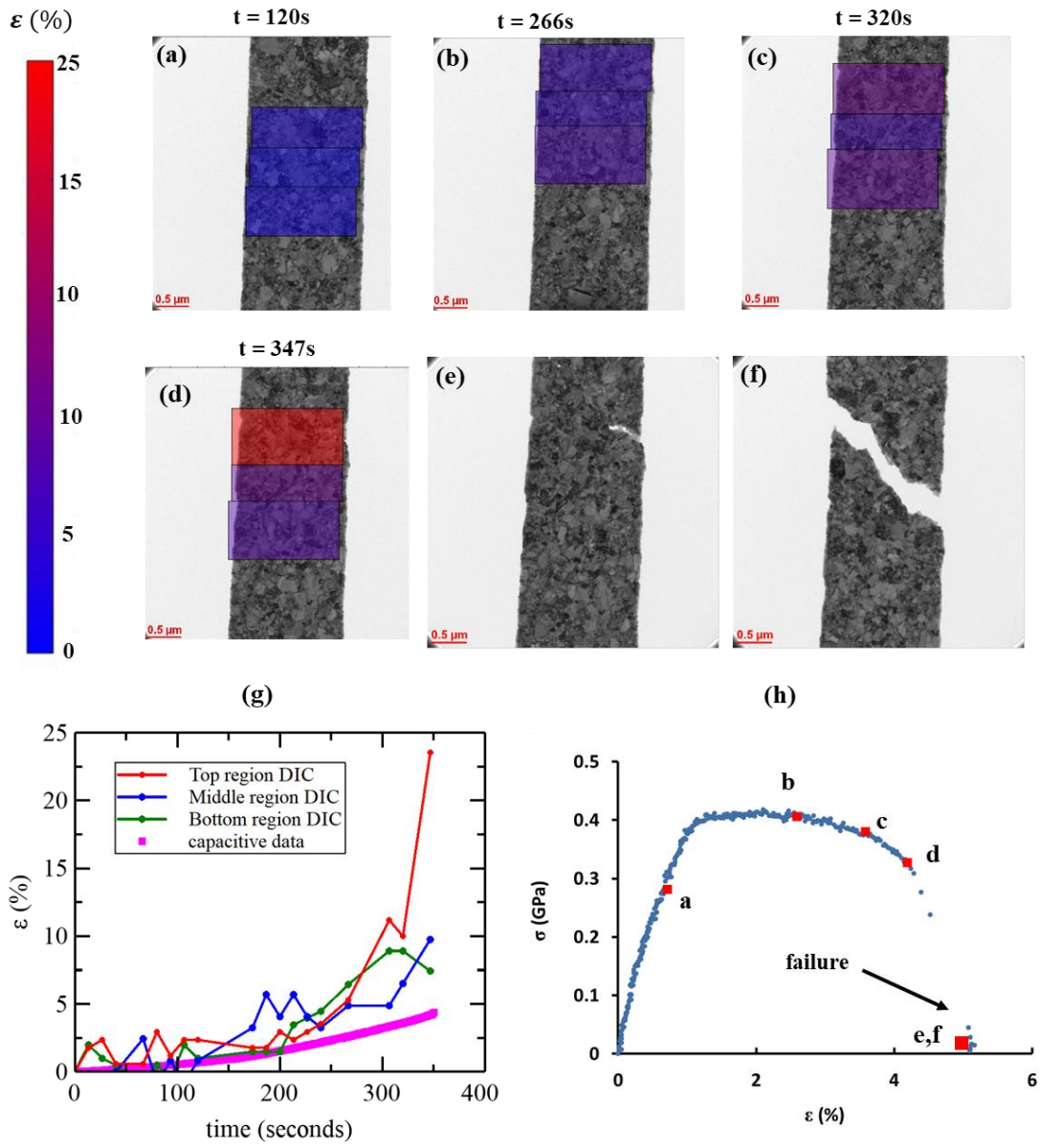

Figure 3.21 In-situ TEM monotonic testing of 100-nm-thick Au microspecimens. Local strain distributions in three regions namely top, middle and bottom are shown in (a)–(d) computed by DIC at instances indicated on the stress-strain curve in (h). (e) & (f) TEM snapshots very close to failure of the microspecimen. (g) Evolution of the strains computed by DIC in the three regions compared to overall strain calculated by capacitive data.

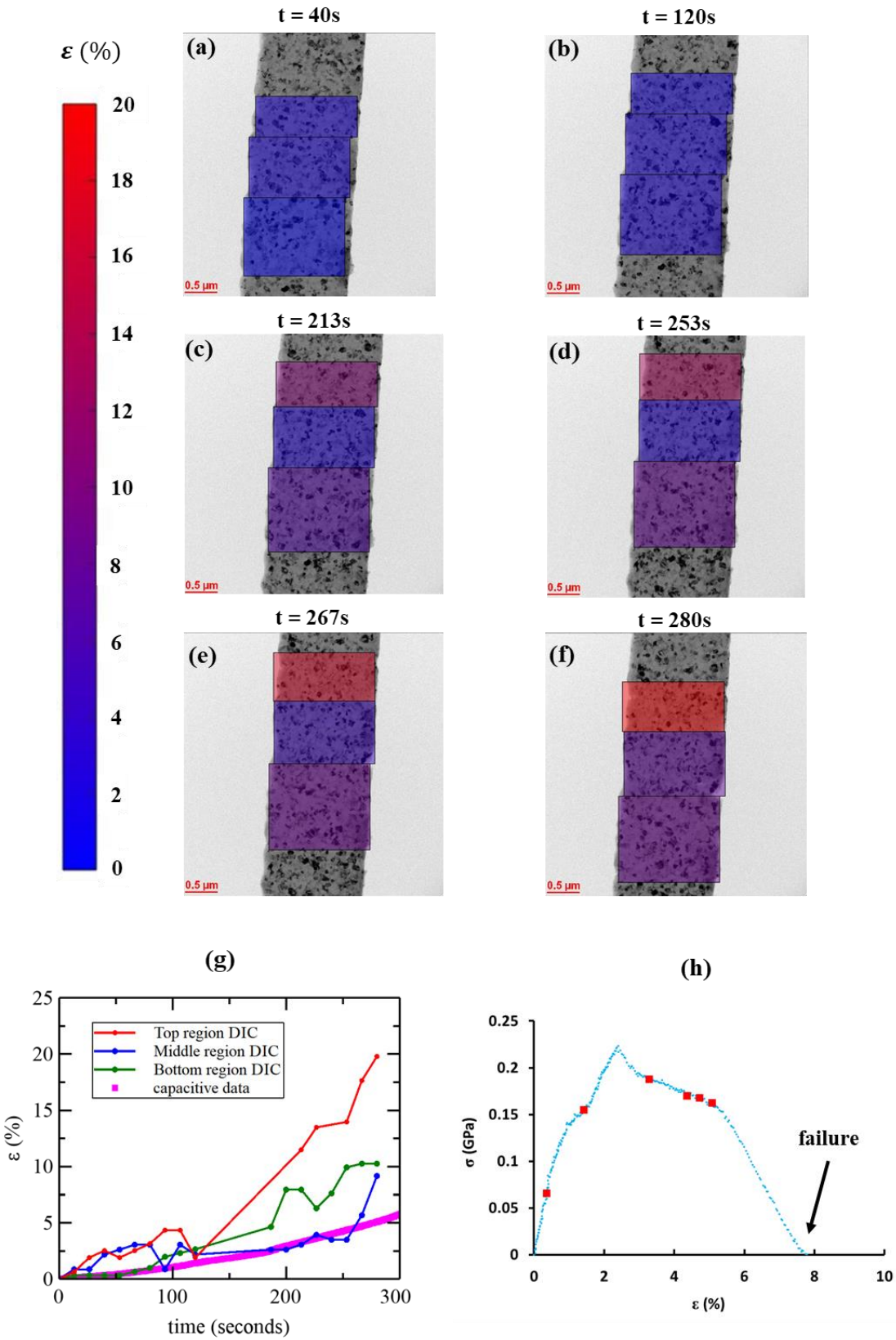

Figure 3.22 In-situ TEM monotonic testing of 200-nm-thick annealed Al microspecimens. Local strain distributions in three are shown in (a)–(f) computed by DIC at instances indicated on the stress-strain curve in (h). (g) Evolution of the strains computed by DIC in the three regions compared to overall strain calculated by capacitive data.

3.5. Transient testing

3.5.1. Methodology for calculating activation volumes

A material undergoes stress relaxation when the total strain in the sample is held constant. In this MEMS device this is achieved by maintaining a constant voltage to the thermal actuator V_{in} which leads to the applied displacement X_A being held constant. Therefore by Eq. (2-9), the sum of the displacement of the sample and the load sensor remains a constant during a relaxation experiment:

$$X_A = X_S + X_{LS} = constant \tag{3-1}$$

The load sensor is assumed to undergo only elastic deformation and the machine-specimen modulus M is given by:

$$M = \left(\frac{K_{LS} * K_S}{K_{LS} + K_S}\right) * \left(\frac{l}{\mathrm{w} * \mathrm{t}}\right) \tag{3-2}$$

The plastic strain rate in the sample can be related to the rate of decrease in the stress in the sample using M [122]:

$$\dot{\varepsilon}_p = -\dot{\sigma}/M \tag{3-3}$$

Repeated stress relaxation experiments consist of several consecutive relaxation segments, with each relaxation segment beginning at the same stress level and each relaxation lasting for the same amount of time [126]. The loading between consecutive relaxation segments must be e*lastic* in order to prevent any substructure changes and to ensure that all the relaxations begin with nominally the same substructure and stress. The stress at the beginning of each relaxation can be the same by making sure that all relaxation segments begin at a similar value of ΔCS_2, which is monitored in real-time during reloading with our

independent sensing scheme of CS_1 and CS_2. As explained in Section 1.2.2, V^* is calculated using Eq. (2-14) which does not require the stress at the end of the reloading to be equal to the initial stress. Hence, there is some flexibility in determining the amount of reloading (i.e. increasing V_{in}), as long as the reloading is elastic (an assumption that can be verified with in situ TEM experiments).

As shown in the previous section the elastic strain calculations are not accurate because of the local, non-negligible elastic deformation of part of the specimen's clamp that is glued. As a result, this technique cannot determine accurately the elastic modulus. Additional measurements would be necessary to calculate accurately E, such as digital image correlation to keep track of the elongation of the gauge length. However, it is important to note that this deficiency of the technique does not affect the accurate calculation of V^*. As explained in this section, these parameters are only extracted from stress and plastic strain measurement, which are accurately measured as shown above.

3.5.2. MEMS stability during transient mechanical tests

Figure 3.23 (a) shows the raw data ΔCS_2 as a function of time during a series of four repeated stress relaxation experiments. To confirm that the observed decreases in ΔCS_2 are solely the result of plastic deformation of the specimen, a MEMS device with the glued specimen gap was used to measure the evolution of ΔCS_2 for the same V_{in} loading series. In this case ΔCS_2 is much larger since $X_{LS} = X_A$. Importantly enough, the signal is fairly constant in the case of

the glued MEMS, confirming the stability of the MEMS device to perform these measurements. This is further shown in Figure 3.23 (b) where the MEMS device behavior is shown without any glue in the gaps.

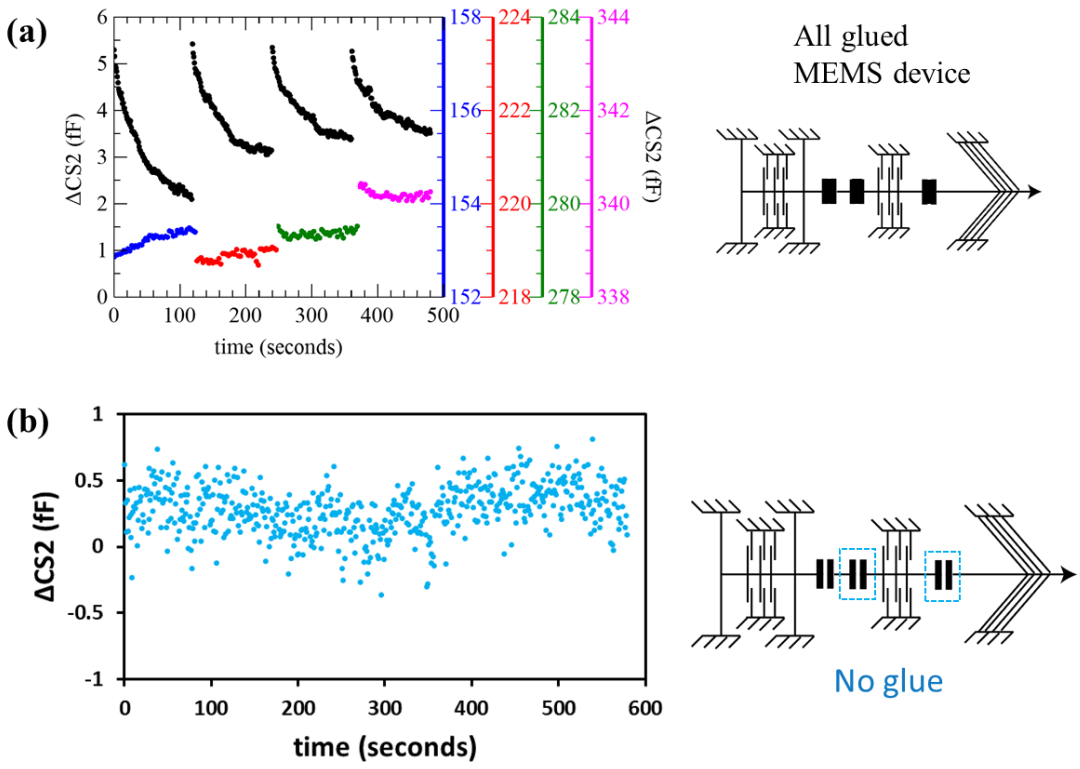

Figure 3.23 (a) Raw data ΔCS_2 as a function of time during a series of four repeated stress relaxation experiments of an Au specimen (black data), along with baseline behavior of an all-glued MEMS (see text for details) [222]. (b) MEMS baseline behavior without any glue in the gaps.

3.5.3. Extraction of signature parameters

As described in Section 3.5.1 the MEMS device can used to study stress relaxation behavior of the thin films. The stress relaxation data can then be used to calculate an apparent activation volume V_a using Eq. (2-13). Figure 3.24 shows the raw data ΔCS_1 and ΔCS_2 as a function of time for one particular relaxation segment for an Au microspecimen. The decrease in ΔCS_2 indicates relaxation of

the stress, whose evolution with time is shown in Figure 3.24 (a). Figure 3.24 (a) shows the logarithmic nature of the stress relaxation, with the fit corresponding to Eq. (2-13). From this fit the apparent activation volume was calculated as ~12 b^3. V_a can also be calculated using the derivative form of Eq. (2-11) [124]:

$$V_a = \sqrt{3}kT\frac{\partial ln\dot{\varepsilon}_p}{\partial\sigma} = \sqrt{3}kT\frac{\partial \ln(-\dot{\sigma}/M)}{\partial\sigma} = \sqrt{3}kT\frac{\partial \ln(-\dot{\sigma})}{\partial\sigma} \tag{3-4}$$

In this equation, $\dot{\varepsilon}_p$ was calculated using Eq. (3-3). As mentioned in the previous section, this equation reveals that the accuracy of V_a only depends on the accuracy of stress measurements, and can be accurately determined from measuring the slope in Figure 3.24 (b). Alternatively, $\dot{\varepsilon}_p$ can be calculated from the slope of the plastic strain vs time curves. For the latter, the plastic strain is calculated as follows:

$$\varepsilon_p = \varepsilon - \sigma/E \tag{3-5}$$

where ε is the total strain (obtained as shown in Figure 2.9)and E is the Young's modulus (calculated from the actual stress-strain curve). Both methods of plastic strain rate calculation are consistent (see Figure 3.24 (d)), showing that the lump model of the setup (Eqs. (2-1), (2-2), (3-1), (3-2) & (3-3)) is accurate. Likewise, the V_a values calculated from Eqs. (2-13 & 3-4) are in very close agreement (~12 b^3), again showing the logarithmic nature of the relaxation.

Corresponding to the apparent activation volume, strain rate sensitivity m can be calculated for each relaxation using Eq. (3-6) or equivalently from the slope in Figure 3.24 (c) [124, 136], which gives a m value of ~0.08 for the relaxation curve shown in Figure 3.24 (a).

$$m = \partial \ln\sigma/\partial \ln\dot{\varepsilon} \approx \partial \ln\sigma/\partial \ln\dot{\varepsilon}_p = \partial \ln\sigma/\partial \ln(-\dot{\sigma}) = \sqrt{3}kT/\sigma V_a \tag{3-6}$$

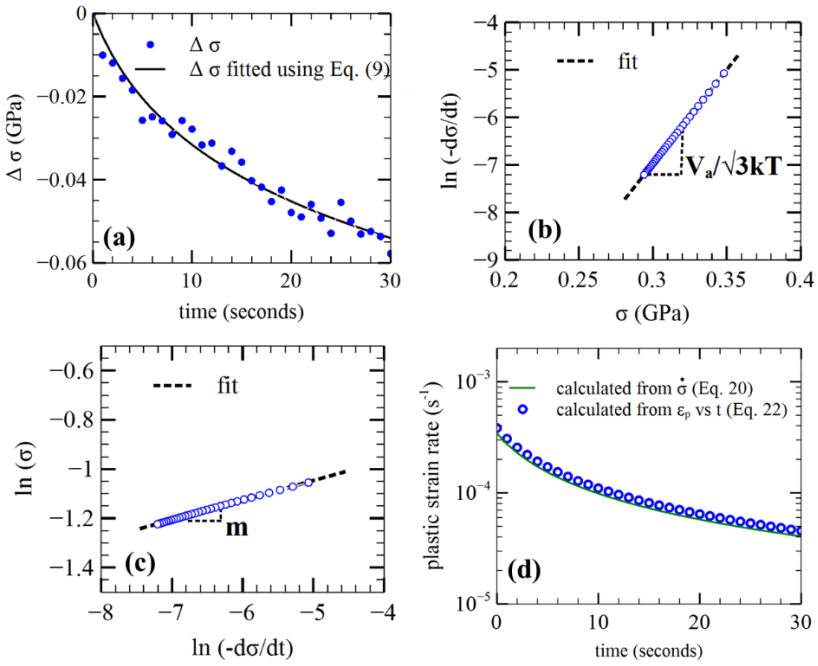

Figure 3.24 (a) Evolution of stress during a relaxation segment, and fit based on Eq. (2-13), showing the logarithmic nature of the stress relaxation. (b) Linear fit of $\ln(-d\sigma/dt)$ vs σ, whose slope is proportional to V_a. (c) Linear fit of $\ln\sigma$ *vs* $\ln(-d\sigma/dt)$, whose slope is proportional to m. (d) Two equivalent methods of calculating plastic strain rate from the relaxation data

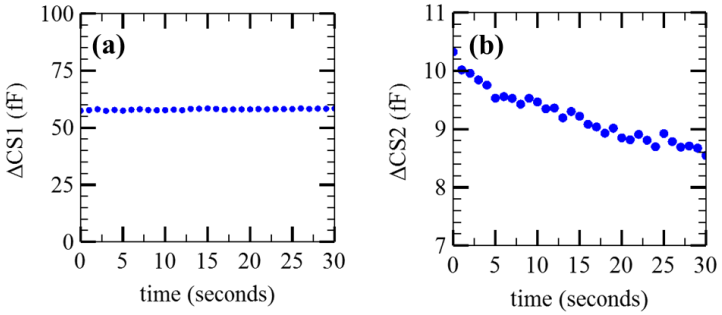

Figure 3.25 Raw data during a stress relaxation: (a) ΔCS_1 vs time, (b) ΔCS_2 vs time.

3.5.4. In-situ repeated stress relaxation: Proof-of-concept experiments

Repeated stress relaxation experiments were performed *in-situ*, on the three microspecimens, consisting of consecutive 30-60 seconds long stress relaxation segments, each relaxation segment starting at approximately at the same stress. Although the length of the relaxation segments was nominally around 30 seconds for most ex-situ experiments, this duration was increased to 60-120 seconds for in-situ experiments to increase the accuracy of the measurements. Apart from these short transients longer transients up to 20 minutes long were needed to make TEM observations.

Figure 3.27 shows transient repeated stress relaxations of 100-nm-thick Au microspecimens done in-situ. Figure 3.27 (a) shows the stress-strain curve corresponding to the complete test including these stress transients. The stress transients are seen as straight lines with a negative slope on the graph. Figure 3.27 (b) shows the individual relaxation segments which are each 60 seconds long and it can be easily seen that the amount of stress relaxation $\Delta\sigma$ depends on the initial stress levels σ_i. When σ_i is around 250-300 MPa $\Delta\sigma$ in 60 seconds is approximately 20 MPa. At higher stress levels σ_i around 450 MPa the $\Delta\sigma$ is around 100 MPa ($\sim$ 25% of σ_i). This is extremely large amount of stress relaxation compared to coarse-grained metals. As shown in Figure 3.27 (c) & (d), the true activation volume V^* is $\sim 3\ b^3$ for these transients. The strain rate sensitivity m $\sim$ 0.1 and the apparent activation volume V_a is between 5-30 b^3 as seen in Figure 3.27 (e) & (f) respectively.

Figure 3.28 shows transient repeated stress relaxations of 200-nm-thick as-deposited Al microspecimens done in-situ. Figure 3.28 (a) shows the stress-strain curve corresponding to the complete test including these stress transients. The microspecimen failed during the last relaxation stress transient. Figure 3.28 (b) shows the individual relaxation segments most of which are 60 seconds long and it can be easily seen gain in this case that the amount of stress relaxation $\Delta\sigma$ depends on the initial stress levels σ_i. When σ_i is around 200 MPa, $\Delta\sigma$ in 60 seconds is almost negligible approximately 5 MPa. At higher stress levels σ_i around 250 MPa the $\Delta\sigma$ is around 30 MPa. As shown in Figure 3.28 (c) & (d), the true activation volume V^* is between 5-40 b^3 for these transients. Similarly, the strain rate sensitivity m is anywhere between 0.05 to 0.1 and the apparent activation volume V_a is between 10-150 b^3 as shown in Figure 3.28 (e) & (f) respectively. This large scatter in the data suggests that there could be issues with the accuracy with the calculation of true activation volume when the $\Delta\sigma$ is very small.

Figure 3.29 shows transient repeated stress relaxations of 200-nm-thick annealed Al microspecimens done in-situ. Figure 3.29 (a) shows the stress-strain curve corresponding to the complete test including these stress transients. The microspecimen failed during the last relaxation stress transient. Figure 3.29 (b) shows the individual relaxation segments each 60 seconds long and it can be easily seen gain in this case that the amount of stress relaxation $\Delta\sigma$ depends on the initial stress levels σ_i. When σ_i is around 170 MPa, $\Delta\sigma$ is almost negligible approximately. At higher stress levels σ_i around 230 MPa the $\Delta\sigma$ is around 15-20 MPa. As shown in Figure 3.29 (c) & (d), the true activation volume V^* is around

10 b^3 for these transients. Similarly, the strain rate sensitivity m is between 0.05-0.1 and the apparent activation volume V_a is between 5-25 b^3 as shown in Figure 3.29 (e) & (f) respectively.

Figure 3.26 shows the comparison between the measurements of true activation volume in-situ vs ex-situ for both Au and Al microspecimens. For this comparison no distinction was made between annealed and as-deposited Al microspecimens. It can be seen in Figure 3.26 (a) that true activation volume for Au microspecimens does not show a discernible difference between in-situ and ex-situ measurements. V^* for Au microspecimens lies between 3-15 b^3 with the modal value being ~5 b^3. It also appears that at as σ increases, V^* decreases. In the case of Al also as shown in Figure 3.26 (b) the in-situ and ex-situ measurements of V^* are similar except for a few data points which show a very high value. The ex-situ measurements of V^*~ 10 b^3 and the in-situ measurements lie between 5-10 b^3 except for a few data points which show V^*between 30-40 b^3. It was found that these high values correspond to cases where the reloading stress values were relatively small around ~ 5 MPa. The reliability of these activation volumes especially for the ex-situ case will be discussed in Section 3.8.

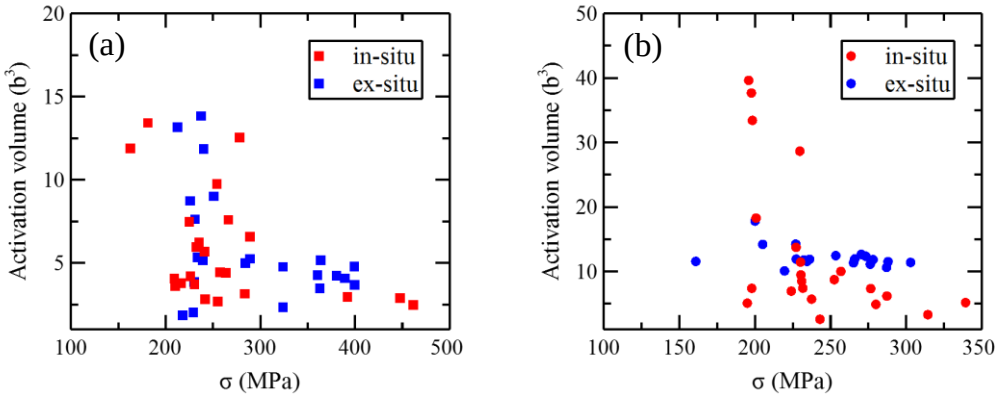

Figure 3.26 Comparison of ex-situ vs in-situ measurements of true activation volume. (a) 100-nm-thick Au. (b) 200-nm-thick Al.

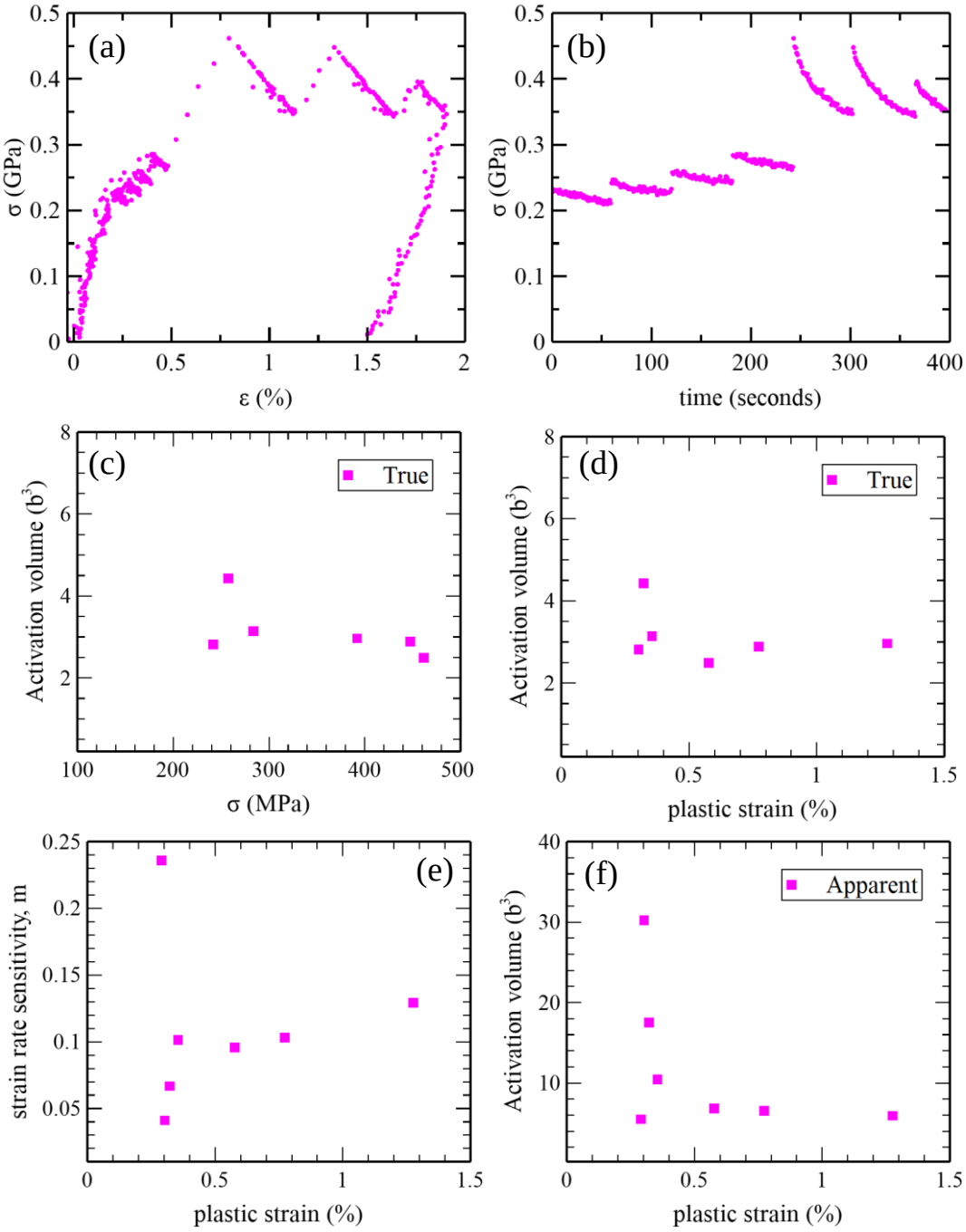

Figure 3.27 In-situ repeated stress relaxations in 100-nm-thick Au microspecimens.

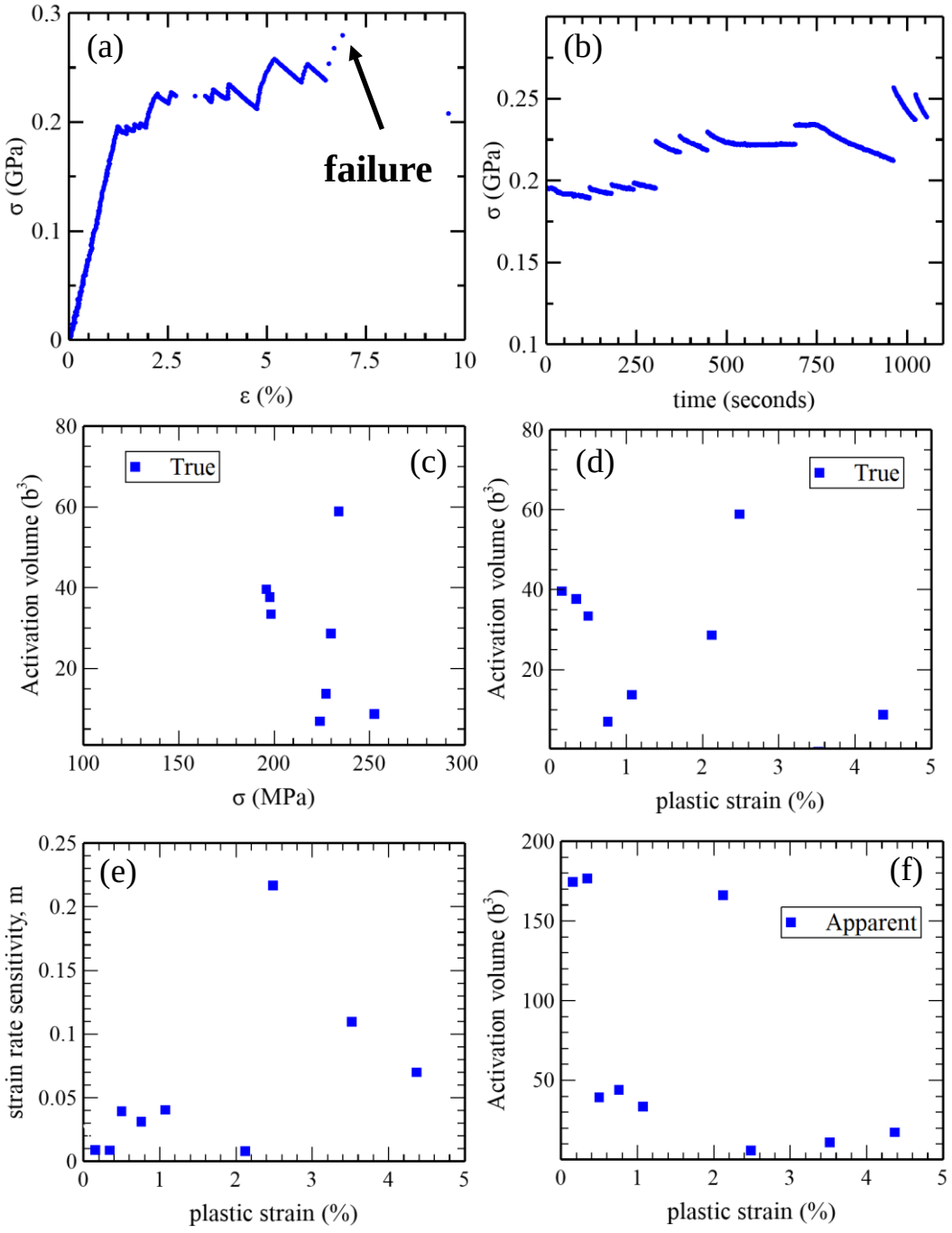

Figure 3.28 In-situ repeated stress relaxations in 200-nm-thick as-deposited Al microspecimens.

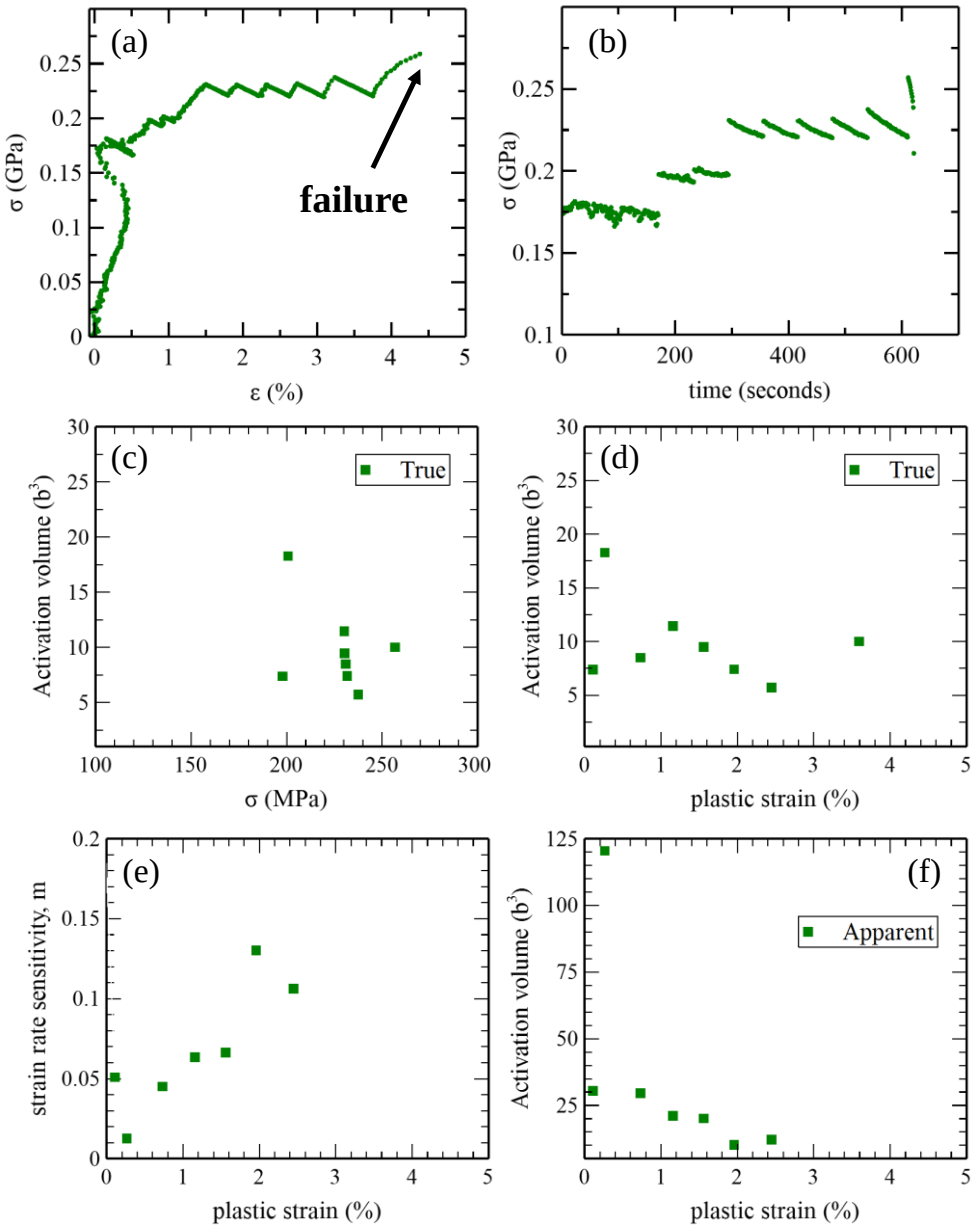

Figure 3.29 In-situ repeated stress relaxations in 200-nm-thick annealed Al microspecimens.

3.6. Practical considerations for in-situ experiments

Figure 3.31 shows the drift issues in the TEM when a voltage was applied to the MEMS device. The TEM image was seen to drift rapidly whenever the voltage was ramped up and eventually stabilize when the voltage was held

constant for a period of time as shown in Figure 3.31. When the voltage was removed the drifted image came back to its original position after a long period of time. The drift was observed irrespective of which part of the MEMS device was imaged. The electrical sensing worked reliably despite of this drift. If this drift were actually real, i.e., the device actually heated up and physically moved in the TEM when a voltage was applied, the MEMS substrate temperature would have to increase by 200^0C in order to account for the ~ 2 μm of drift. To prove that the drift was not the physical motion of the device, an experiment was performed by sticking a Au wire on the rear of the TEM holder as shown in Figure 3.32 so that both the MEMS and the Au wire can be observed through the TEM window. If the drift were due to the physical motion of the MEMS device then the Au wire would not drift. But as shown in Figure 3.32 both the Au wire and the MEMS device were observed to drift very similar to each other. This further points to that the fact that the MEMS device cannot be physically moving and the most likely cause of the drift can be either the heat generated when a voltage is applied or some distortion of the magnetic field of the TEM. A further experiment was done by applying a voltage to the CS2 beams instead of the thermal actuator. This would heat the beams but the beams would not move unlike the thermal actuator. As shown in Figure 3.32 very minimal drift was observed proving that the cause of the drift is the motion of the thermal actuator beams.

As shown in Figure 3.30, a good practice while wirebonding the MEMS device to the chip carrier is to have spider-shaped wirebonds. This helps in reducing the parasitic noise sometimes and it easier to manipulate specimens on

to the MEMS device if the wires are not crossing each other over the MEMS device.

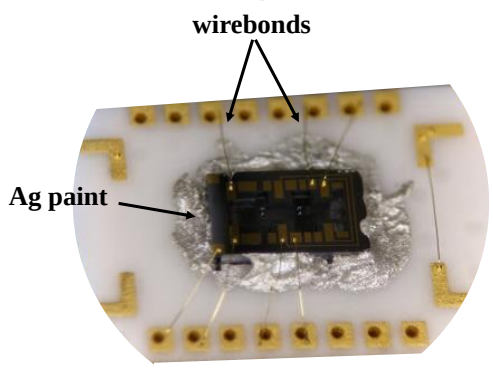

Figure 3.30 Best practice for wirebonding is to bond the wires in "spider-like" fashion such that no two wires are crossing each other and no wire goes across the MEMS device.

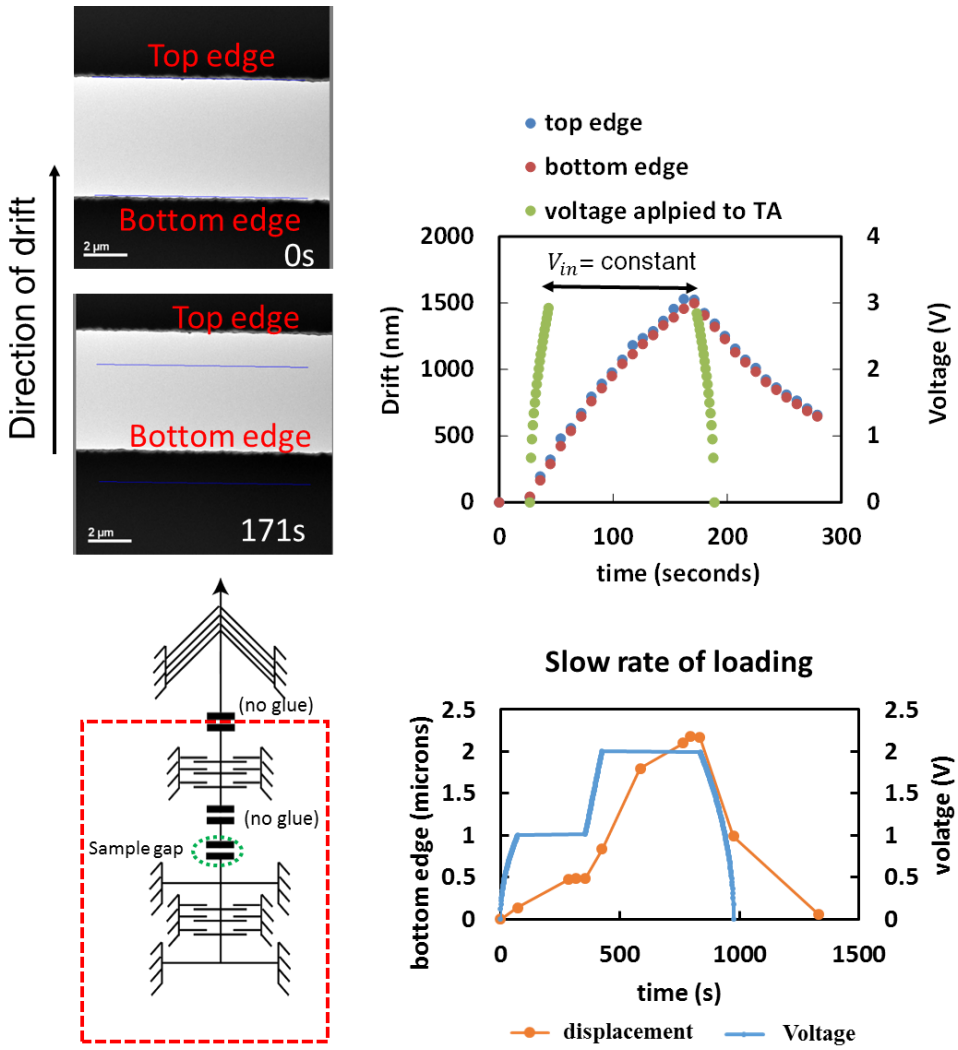

Figure 3.31 Drift issues in the TEM when a voltage is applied to the MEMS.

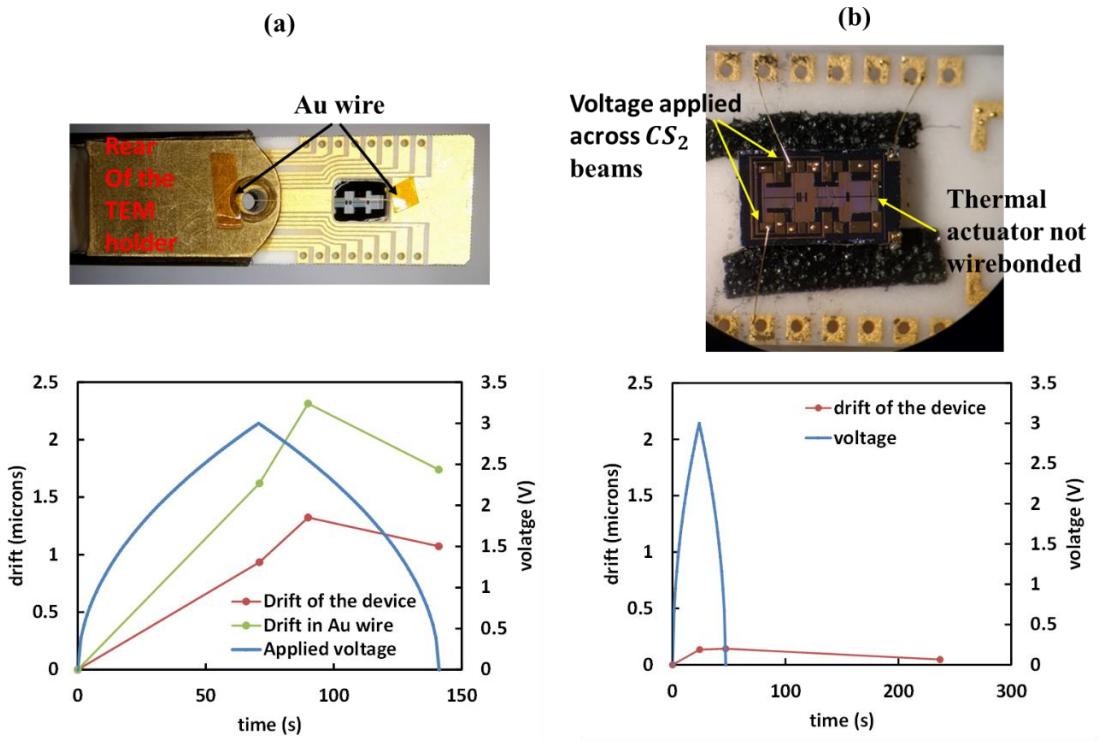

Figure 3.32 Experiments proving the cause of the drift observed in the TEM to be the motion of thermal actuator beams.

3.7. TEM observations during stress relaxation

Figure 3.33 shows TEM snapshots during two consecutive stress relaxation segments starting at $\sigma = 230$ MPa. Figure 3.33 (a) shows a dislocation loop originating at a triple junction in the middle of the first relaxation at $\sigma \sim 215$ MPa. Over the next four and half minutes this dislocation loop grows in size and traverses through the grain (shown by white arrows) and ultimately exists the crystal (see Figure 3.33 (b)-(g)). There are two important features of the growth of this dislocation loop: (i) The size of the dislocation loop does not seem to increase much during the reloading segment as shown in Figure 3.33 (d) & (e). (ii) The pinning points of the dislocation loop are always at the grain boundaries.

This could reflect the fact that the density of dislocation interlocks is not as high as in conventional CG metals and the grain boundaries therefore act as the major pinning points. The true activation volume V^* obtained from the reloading segment was 6 b^3.

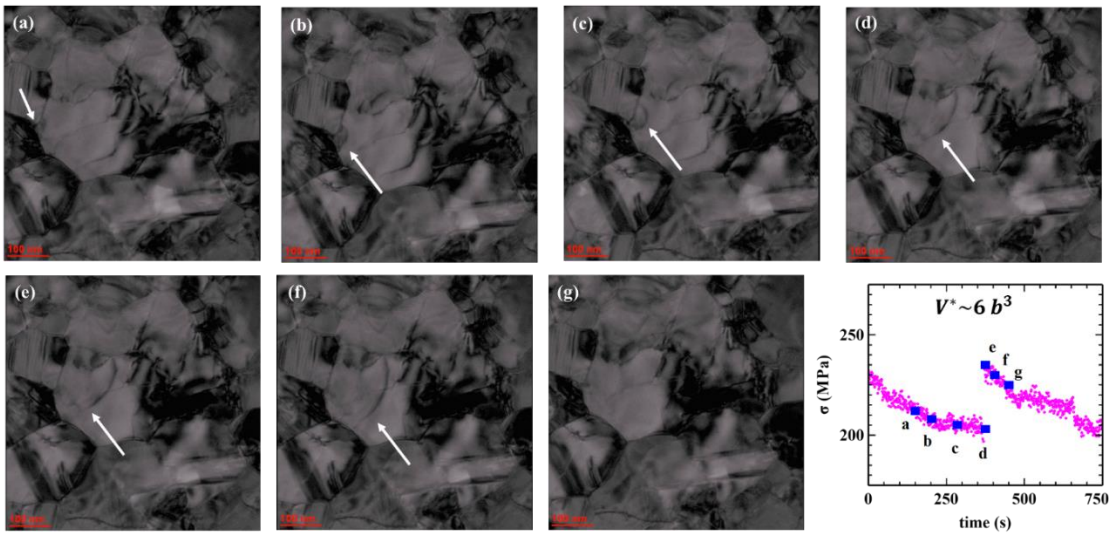

Figure 3.33 A dislocation loop originating from a triple junction, traversing through a grain and exiting the crystal.

Figure 3.34 shows TEM snapshots during a stress relaxation segment on a different Au microspecimen. As shown in Figure 3.34 (a) & (b), a dislocation (pointed by red arrows) is seen to traverse through a grain (highlighted in dotted line) and absorbed by a grain boundary as shown in Figure 3.34 (c) & (d). It should be noted that even in this case the ends of the dislocation were pinned by the grain boundaries. The abrupt decrease in stress during the relaxation between the points $'c'$ and $'d'$ is most likely a result of noise in the data and not due to a physical process. The true activation volume V^* obtained from the reloading segment was 8 b^3.

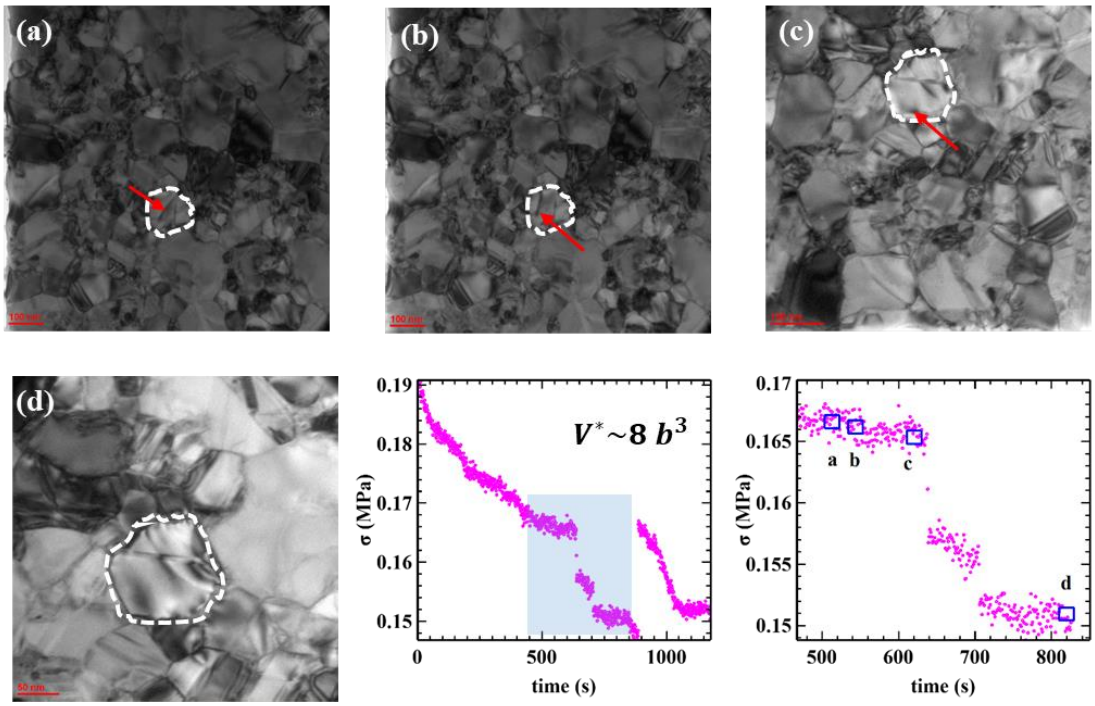

Figure 3.34 A single dislocation moving through a grain during stress relaxation and getting absorbed by a grain boundary.

Figure 3.35 shows TEM snapshots during a relaxation segment during which the microspecimen failed. The most important aspect of the crack growth is that it is completely intergranular. As seen in Figure 3.35 (e) - (g), the crack growth is a result of shearing of the grain boundaries. Figure 3.35 (a) – (d) show the slow growth of the void as the stress decreased at a constant pace. Dislocations were seen to be emitted from the crack tips into the grain interiors. A large amount of dislocation transgranular dislocation activity was observed during the rapid void growth in Figure 3.35 (f) & (g) during which the stress rapidly decreased. The microspecimen ultimately fails because of coalescence of two cracks as shown in Figure 3.35 (g).

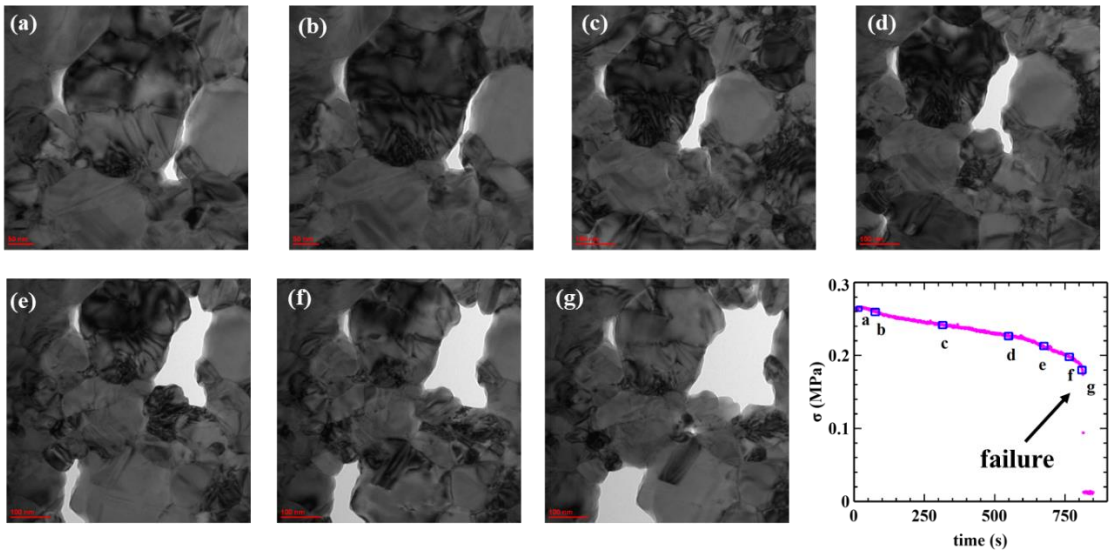

Figure 3.35 Growth and coalescence of voids during stress relaxation.

3.8. Discussion

Using Eq. (3-3), Eq. (1-14) can be re-written as follows:

$$V^* = \sqrt{3}kT\frac{ln\left(\dot{\varepsilon}_{i2}/\dot{\varepsilon}_{f1}\right)}{\Delta\sigma_{12}} = \sqrt{3}kT\frac{ln\left(\dot{\sigma}_{i2}/\dot{\sigma}_{f1}\right)}{\Delta\sigma_{12}} \tag{3-7}$$

Eq. (3-7) shows that the true activation volume does not depend on the gauge length or the absolute value of σ or ε. The accuracy of the true activation volume depends only on the accuracy of the plastic strain rates $\dot{\varepsilon}$ or the rates of stress decrease $\dot{\sigma}$ and the accuracy of the measurement of $\Delta\sigma$. The accuracy in the determination of the rates depends largely on the goodness of the logarithmic fit to the data and therefore it is affected significantly by the noise-to-signal ratio (NSR) of the measurement.

In order to calculate NSR for a relaxation segment, the amount of stress relaxation $\Delta\sigma$ and the noise $\delta\sigma$ needs to be calculated. NSR is then given by:

$$\text{NSR} = |\delta\sigma|/\Delta\sigma \tag{3-8}$$

To calculate $\Delta\sigma$ and $\delta\sigma$ for a relaxation segment, first the best logarithmic fit to relaxation segment needs to be determined. This is the same logarithmic function used to calculate V_a given by Eq. (1-13). Then the $\Delta\sigma$ is given by the difference between the initial and final values of σ during the relaxation. $|\delta\sigma|$ is given by twice the standard deviation of the difference between the actual data and the fit.

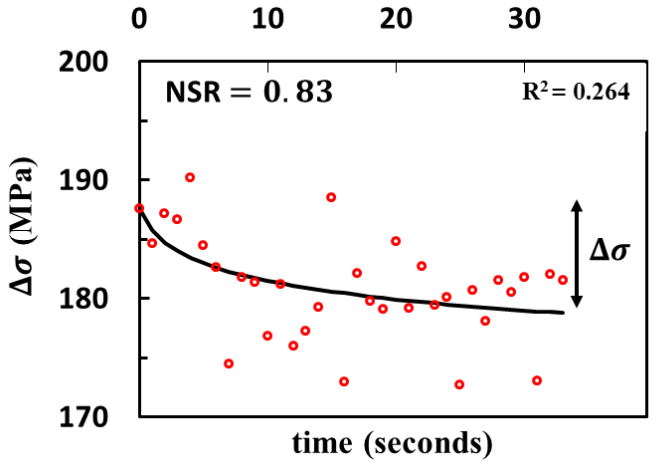

Figure 3.36 A relaxation segment with a high noise-to-signal ratio NSR fitted with a logarithmic function. $\Delta\sigma$ for the relaxation segment is also shown.

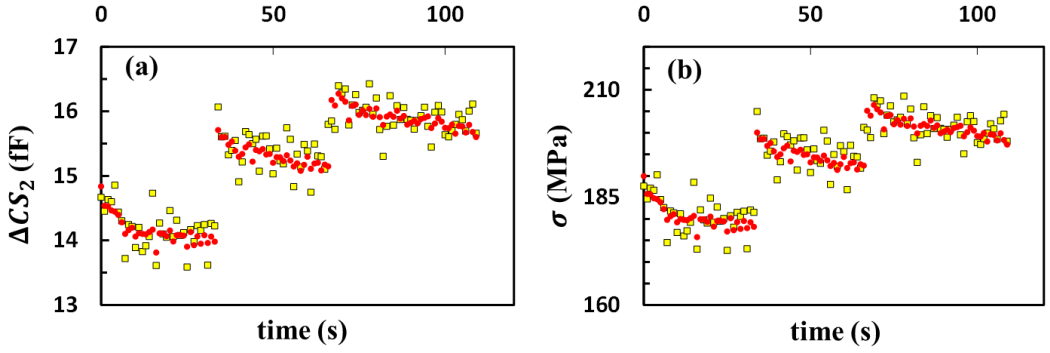

Figure 3.37 Comparing a low NSR (0.19) measurement (in red) to a high NSR (0.83) measurement (in yellow) for a small $\Delta\sigma$ (10 MPa). (a) Noise in ΔCS_2: $\pm$0.08 fF vs $\pm$0.25 fF and (b) $\delta\sigma$: $\pm$1 MPa vs $\pm$3.5 MPa.

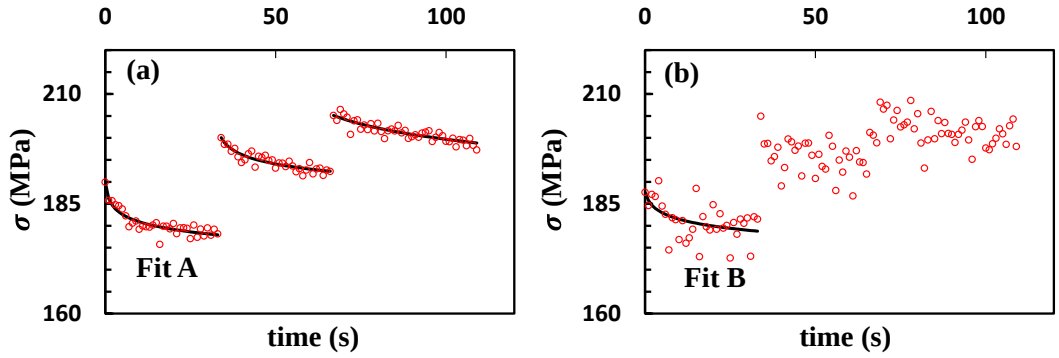

Figure 3.38 (a) Logarithmic fits for the data with low NSR. (b) Only one relaxation segment of the data with high NSR could be fitted with a logarithmic fit.

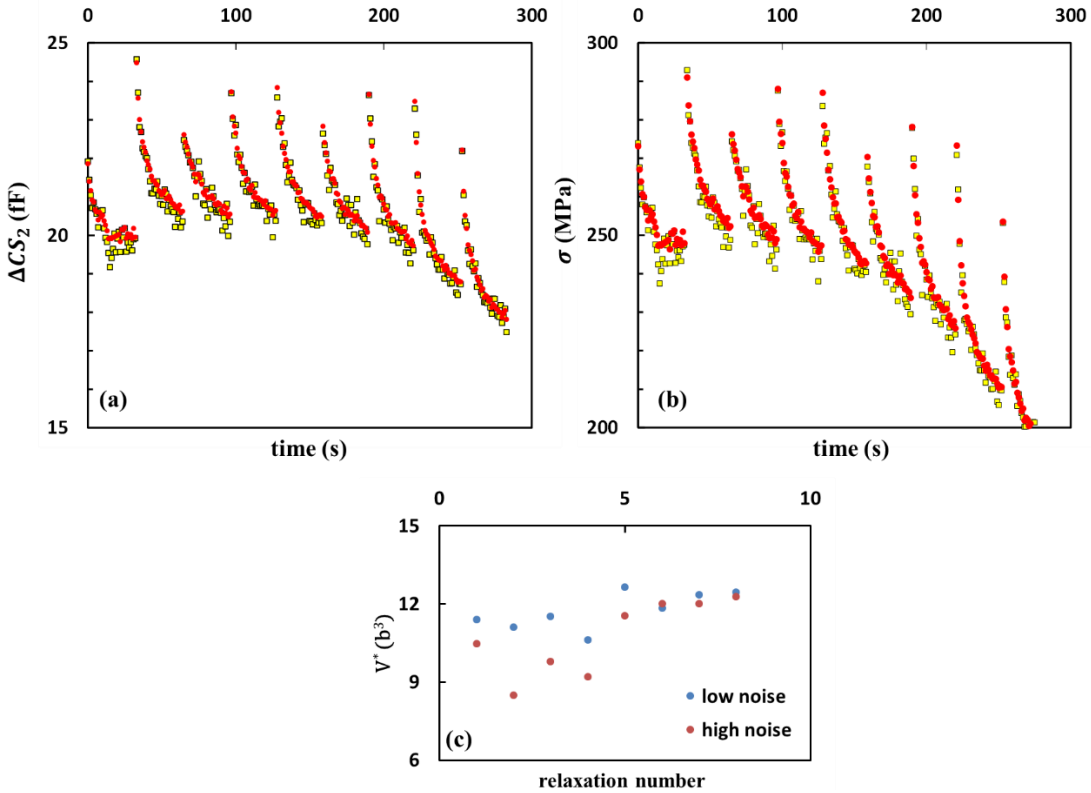

Figure 3.39 Comparing a low $\delta\sigma$ (NSR = 0.075) measurement (in red) to a high $\delta\sigma$ (NSR = 0.12) measurement (in yellow) for a large $\Delta\sigma$ (50 MPa). (a) Noise in ΔCS_2: $\pm$0.05 fF vs $\pm$0.2 fF and (b) $\delta\sigma$: $\pm$1 MPa vs $\pm$3 MPa. (c) Comparison of the V^* obtained from the two measurements.

Figure 3.37 shows a comparison between two measurements, one with a $\pm$0.08 fF noise level in ΔCS_2 which corresponds to $\delta\sigma$ of $\pm$1 MPa (NSR = 0.19), second with $\pm$0.25 fF noise level in ΔCS_2 which corresponds to $\delta\sigma$ of $\pm$3.5 MPa (NSR = 0.83). As can be seen from Figure 3.38 that for relaxation segments having small $\Delta\sigma \sim$ 10 MPa, the low NSR measurements can be easily fitted with logarithmic fits however it was not possible to fit all the relaxation segments with the high NSR. As the $\Delta\sigma$ itself is only ~10 MPa, a $\delta\sigma$ of $\pm$3.5 MPa would cause a lot of scatter in the data making it unsuitable for any kind of fitting. However for a large $\Delta\sigma \sim$ 50 MPa, a $\delta\sigma$ of $\pm$3 MPa would still give a low NSR (0.12) and would not cause too much scatter in the data as shown in Figure 3.39. This has huge implications for true activation volume calculations from the logarithmic data fitting. As can be seen from Figure 3.39 (c) that for the large $\Delta\sigma$ both low and high $\delta\sigma$ measurements yield similar values of V^*. But for small $\Delta\sigma$, $\delta\sigma$ is a lot more significant as the high $\delta\sigma$ yields a considerably bad NSR. Consider the fits Fit A (low noise measurement) and Fit B (high noise measurement) shown in Figure 3.38. The R^2 value for Fit A is 0.827 and for Fit B is 0.264. For Fit A the ratio of the rates at the beginning of the relaxation to the end of the relaxation is 115 while that for Fit B is 40. This difference in ratio of the rates leads to difference of ~ 25% in the activation volume according to Eq. (3-7). Moreover, for the 2nd and the 3rd relaxation segments, the data with the high NSR could not even be fitted and therefore no activation volume could be calculated from such data.

It can be seen from Figure 3.39 (c) that even when $\Delta\sigma$ is large there can be up to 20% variation in the values of V^* between high and low $\delta\sigma$ measurements. This is because $\dot{\sigma}$ is very sensitive to the fit used. This is especially

true when the NSR is large. The NSR can be large either because $\Delta\sigma$ is small or because the $\delta\sigma$ is large and $\Delta\sigma$ is moderately large (see Figure 3.41). Therefore, it is important to associate the fit used for calculating V^* with a R^2 value such that by choosing fits with a reasonable R^2 value the error associated with fitting can be minimized. Table 3.1, Table 3.2 and Table 3.3 show the three components used in calculating V^* namely $\dot{\varepsilon}_{i2}$, $\dot{\varepsilon_{f1}}$ and $\Delta\sigma$ and the corresponding NSR and R^2 values of each relaxation segment (~60 seconds long) for 100-nm-thick Au, 200-nm-thick as-deposited Al and 200-nm-thick annealed Al microspecimens respectively. It is not trivial to choose a R^2 value which can be used to distinguish between reliable and unreliable fits, but most fits with NSR less than 0.2 have been found to have R^2 values greater than 0.90 as seen from Table 3.1, Table 3.2 and Table 3.3. Figure 3.40 shows the fits used to calculate V^* with a R^2 value greater than 0.90. Note that the NSR is very low for both the fits. Figure 3.41 shows examples of fits with a R^2 value less than 0.90. In both cases the NSR is greater than 0.2. A NSR of 0.2 means that if $\Delta\sigma$ is 10 MPa then $\delta\sigma$ of $\pm$1 MPa would be desirable (see Figure 3.40 (b)). However, if the noise level is $\pm$3 MPa then the NSR would be 0.6 and the fit will result in a poor R^2 (see Figure 3.41 (a)). Figure 3.42 shows the effect of choosing fits with similar R^2 values for high noise to $\Delta\sigma$ ratio relaxation segment. As can be seen from Table 3.4 V^* can vary from 1 to 18 b^3 for the same reloading segment depending on the fit chosen. A data can be fitted with different fits only when the NSR is large or the R^2 is small (in this case ~0.75). When R^2 is in the vicinity of 0.99, it is not possible to have completely different fits have the same R^2 and therefore V^* calculated from fits with high R^2 can be relied upon. Also, although it is generally true that the

transient relaxations follow a logarithmic function but sometimes when the NSR is high other functions like linear or quadratic fits can also work as shown in Figure 3.42 and can result in very different V^* values.

Table 3.1 Components of V^* for 100-nm-thick Au

$\dot{\varepsilon}_{i2}$ (s^{-1})	$\dot{\varepsilon_{f1}}$ (s^{-1})	$\dot{\varepsilon}_{i2}/\dot{\varepsilon}_{f1}$	$\Delta\sigma$ (MPa)	V^* (b^3)	NSR	R^2
-	-	-	-	-	0.21	0.877
2.1 E-05	1.1 E-05	1.91	30	2.8	0.37	0.746
1.3 E-05	4.8 E-06	2.79	30	4.4	0.38	0.734
1.6 E-05	6.0 E-06	2.63	40	3.1	0.28	0.826
3.5 E-04	8.5 E-05	41.73	196	2.5	0.05	0.990
2.4 E-04	2.6 E-05	9.29	101	2.9	0.04	0.993
7.6 E-05	2.5 E-05	3.03	49	3.0	0.12	0.963

Table 3.2 Components of V^* for 200-nm-thick as-deposited Al

$\dot{\varepsilon}_{i2}$ (s^{-1})	$\dot{\varepsilon_{f1}}$ (s^{-1})	$\dot{\varepsilon}_{i2}/\dot{\varepsilon}_{f1}$	$\Delta\sigma$ (MPa)	V^* (b^3)	NSR	R^2
-	-	-	-	-	0.16	0.934
7.3 E-05	1.2 E-05	6.35	6	39.6	0.12	0.944
4.2 E-05	8.9 E-06	4.75	6	37.7	0.15	0.924
2.0 E-05	8.1 E-06	2.42	4	33.4	0.17	0.934
6.0 E-05	1.4 E-05	4.41	29	6.9	0.05	0.993
6.4 E-05	2.3 E-05	2.79	10	13.7	0.07	0.984

Table 3.2 continued

7.9 E-05	2.6 E-05	3.10	11	13.8	-	0.989
-	-	-	-	-	0.02	0.999
2.3 E-04	8.3 E-05	2.78	16	8.7	0.03	0.998

Table 3.3 Components of V^* for 200-nm-thick annealed Al

$\dot{\varepsilon}_{i2}$ (s^{-1})	$\dot{\varepsilon_{f1}}$ (s^{-1})	$\dot{\varepsilon}_{i2}/\dot{\varepsilon}_{f1}$	$\Delta\sigma$ (MPa)	V^* (b^3)	NSR	R^2
-	-	-	-	-	-	0.229
2.5 E-05	6.5 E-06	3.87	24	7.4	0.38	0.744
4.3 E-05	1.7 E-05	2.46	7	18.3	0.31	0.783
9.3 E-05	1.1 E-05	8.48	34	8.5	0.05	0.991
7.9 E-05	3.7 E-05	2.16	9	11.5	0.06	0.989
8.2 E-04	4.1 E-05	2.01	10	9.5	0.06	0.990
8.0 E-05	4.3 E-05	1.88	11	7.4	0.05	0.993
1.1 E-04	5.4 E-05	2.10	17	5.7	0.04	0.996

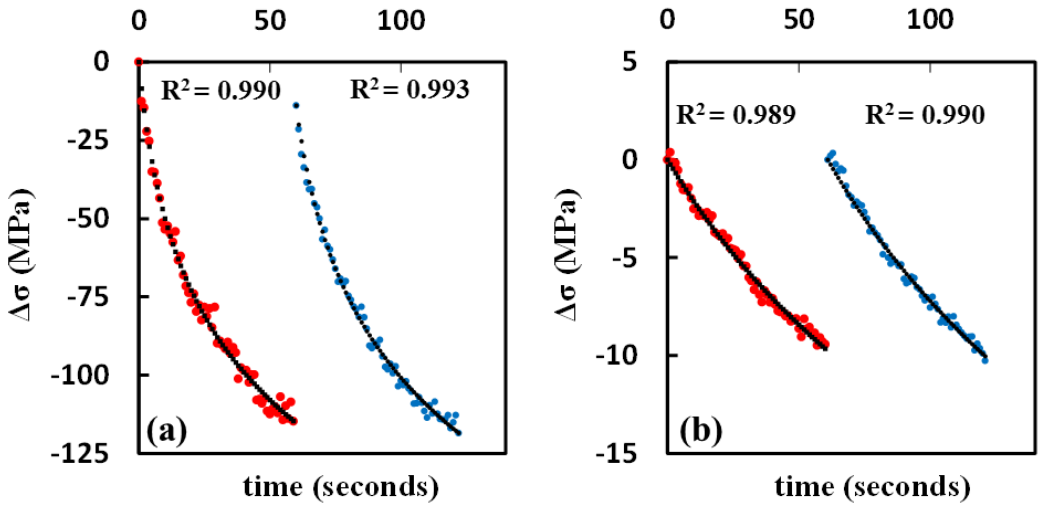

Figure 3.40 Examples of fits with R^2 more than 0.90. (a) NSR = 0.04, corresponds to the reloading segment in 100-nm-thick Au with $V^* = 2.9\ b^3$ shown in Table 3.1 (σ at t = 0s is 460 MPa). (b) NSR = 0.06, corresponds to the reloading segment in 200-nm-thick annealed Al with $V^* = 9.5\ b^3$ shown in Table 3.3 (σ at t = 0s is 230 MPa).

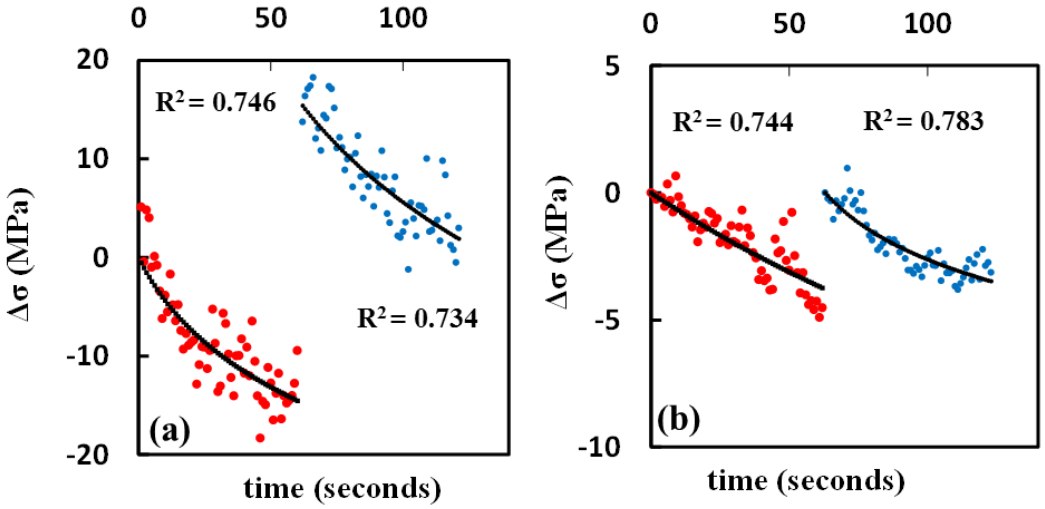

Figure 3.41 Examples of fits with R^2 less than 0.90. (a) High $\delta\sigma$ ($\pm$2.6 MPa) and moderate $\Delta\sigma$ (~15 MPa), NSR = 0.38. Corresponds to the reloading segment in 100-nm-thick Au with $V^* = 4.4\ b^3$ shown in Table 3.1 (σ at t = 0s is 241 MPa). (b) Low $\delta\sigma$ ($\pm$0.5 MPa) and low $\Delta\sigma$ (~3.5 MPa), NSR = 0.31. Corresponds to the reloading segment in 200-nm-thick annealed Al with $V^* = 18.3\ b^3$ shown in Table 3.3 (σ at t = 0s is 200 MPa).

Table 3.4 Components of V^* for the fits with low R^2 shown in Figure 3.42

	$\dot{\varepsilon}_{i2}$ (s^{-1})	$\dot{\varepsilon_{f1}}$ (s^{-1})	$\dot{\varepsilon}_{i2}/\dot{\varepsilon}_{f1}$	$\Delta\sigma$ (MPa)	V^* (b^3)	R^2
(a)	4.3 E-05	1.7 E-05	2.46	7.0	18.3	0.744, 0.783
(b)	3.3 E-05	2.0 E-05	1.59	7.7	8.0	0.750, 0.781
(c)	2.3 E-05	2.2 E-05	1.05	6.7	1.0	0.759, 0.692
(d)	3.9 E-05	2.2 E-05	1.78	6.7	11.5	0.759, 0.817

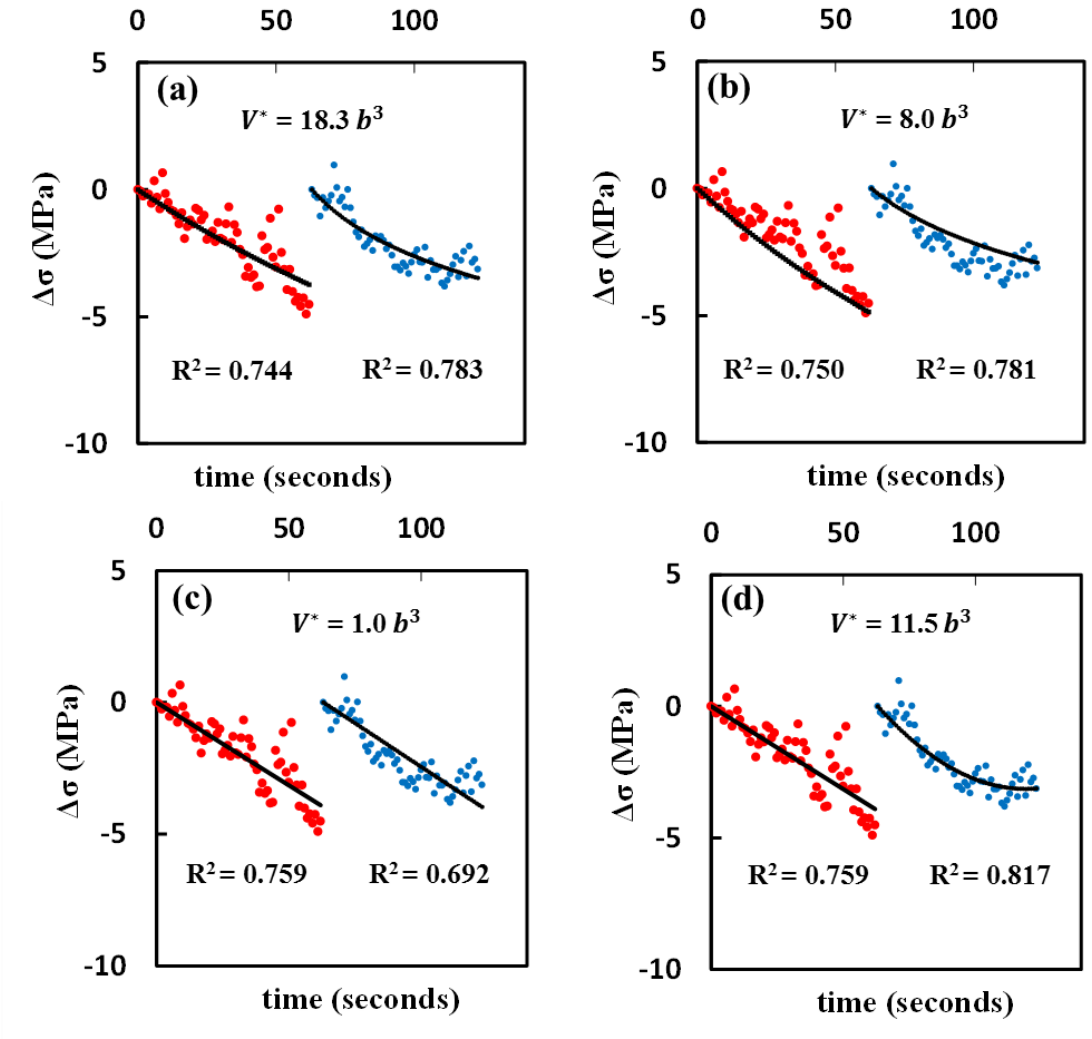

Figure 3.42 Low R^2 fits with similar R^2 can result in very different V^* values. (a) & (b) Logarithmic fits. (c) Linear fits. (d) Linear and quadratic fits. This is due to the high noise-to-signal ratio which allows for several fits with very different initial and final slopes (see Table 3.4) to have similar R^2 values.

The examples of the logarithmic fits shown until now involved short transients (~ 60 seconds long) of relaxation. However, in practice while in order to make in-situ TEM observations generally long periods of stress relaxation interrupted by short transients make the most sense. The rates can be significantly affected by fitting the whole segment compared to the initial or final 60 seconds of the relaxation segment. Figure 3.43 (a) shows a 20 minute long relaxation transient and the corresponding logarithmic fit. The R^2 of the fit is 0.995 which is extremely good but if the first 60 seconds of the data is taken then the fit does not seem as good as seen in Figure 3.43 (b). Compared to Figure 3.43 (d) where a separate fit has been used to fit the first 60 seconds of the data, the fit in Figure 3.43 (b) is poor. The initial strain rate from the fit in Figure 3.43 (b) was 1.4 x $10^{-4}\ s^{-1}$ while the fit in Figure 3.43 (d) gives an initial strain rate of 3.3 x $10^{-4}\ s^{-1}$. This difference in strain rates will cause an error of 15% in V^*. Figure 3.43 (c) shows the last 100 seconds of the data and it can be seen that the fit in Figure 3.43 (a) has a R^2 of only 0.075 for the last 100 seconds which is extremely poor. The strain rate obtained from this fit was 6.0 x $10^{-6}\ s^{-1}$ which is really small. In fact since the $\Delta\sigma$ is almost negligible any line with a slope between 10^{-5} - 10^{-6} s^{-1} can be fitted. This will cause serious errors in V^*. It can be seen from Table 3.1, Table 3.2 and Table 3.3 that strain rates of the order of $10^{-5}\ s^{-1}$ can be measured quite accurately with this technique but when the strain rates decrease to $10^{-6}\ s^{-1}$ the measurements become very uncertain. It is therefore best to perform two short transients in between long transients to get V^* accurately.

Table 3.5 Effect of changing α_{CS_2} on V^* (K_{LS} = 100 N/m)

α_{CS_2}	$\dot{\varepsilon}_{i2}$ (s^{-1})	$\dot{\varepsilon_{f1}}$ (s^{-1})	$\dot{\varepsilon}_{i2}/\dot{\varepsilon}_{f1}$	$\Delta\sigma$ (MPa)	V^* (b^3)	R^2
0.42	1.1 E-04	5.4 E-05	2.10	17	5.7	0.993, 0.996
0.46	1.1 E-04	5.2 E-05	2.10	17	6.0	0.993, 0.996
0.53	1.0 E-04	4.8 E-05	2.15	16	6.5	0.993, 0.996
0.63	9.4 E-05	4.4 E-05	2.16	14	7.3	0.993, 0.996
0.84	8.0 E-05	3.7 E-05	2.18	12	8.7	0.993, 0.996
0.21	1.3 E-04	6.7 E-05	2.02	21	4.5	0.993, 0.996

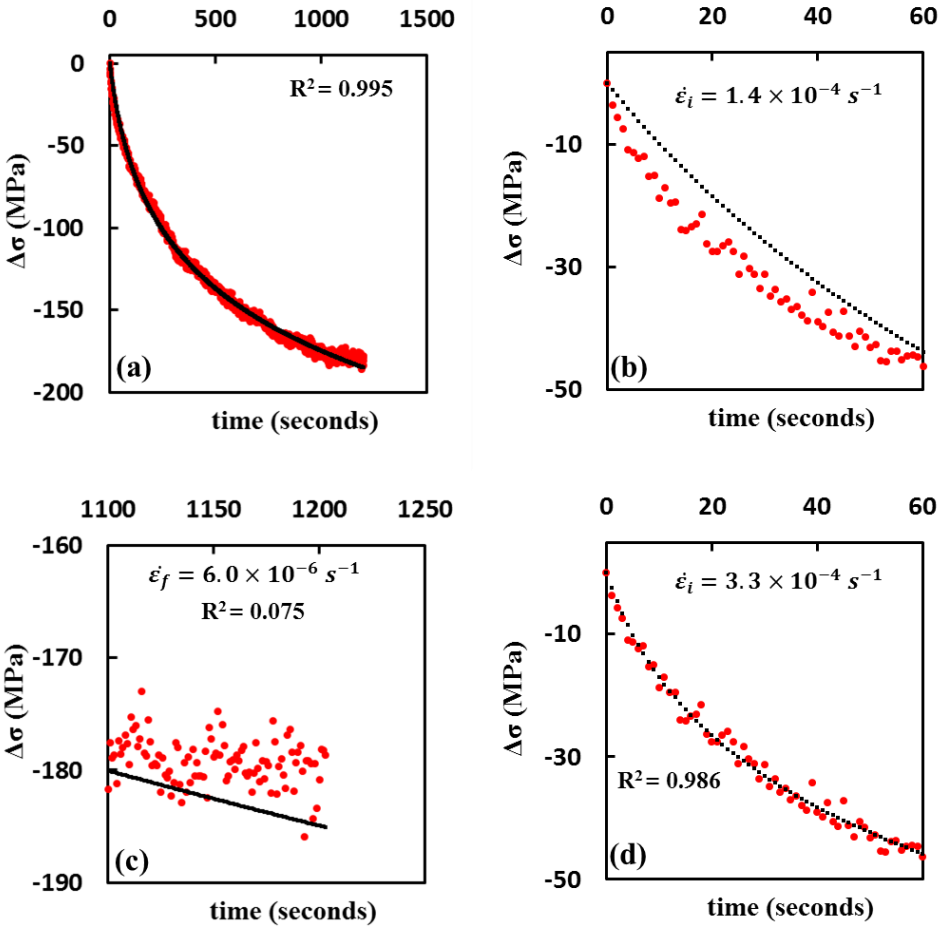

Figure 3.43 (a) A long transient relaxation with the logarithmic fit. (a) First 60 seconds of the data are not as well fit. (c) Last 100 seconds of data also are not well fitted. (d) Separate fit for the first 60 seconds of data.

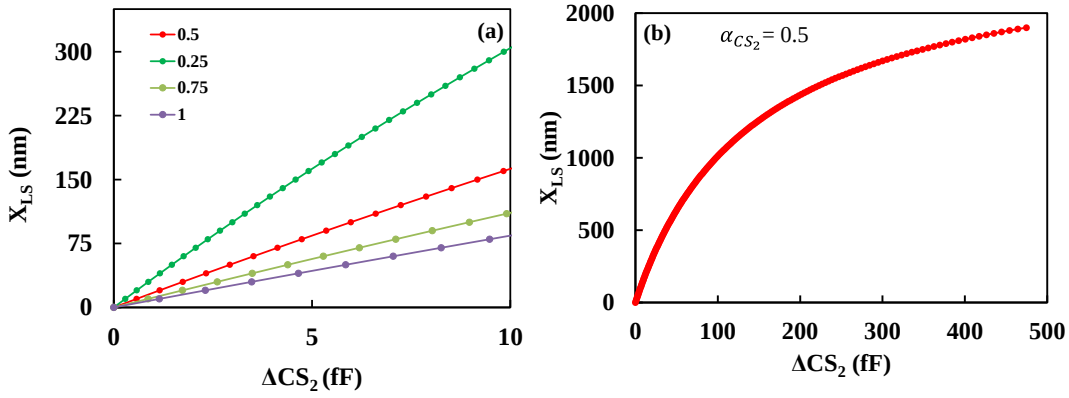

Figure 3.44 Effect of changing α_{CS_2} on X_{LS}. $d_{CS_2} = 2.5\ \mu m$.

It has been shown that there are several issues with obtaining the rates accurately using a good fit but even when a good fit has been determined there

can be errors in V^* induced by errors in $\Delta\sigma$. σ is affected mostly by errors in α_{CS_2} as shown in Section 3.3.2. To analyze the error induced in $\Delta\sigma$ by α_{CS_2} it is sufficient to analyze the change in X_{LS} with α_{CS_2}. Figure 3.44 shows the change in the value of X_{Ls} with changes in α_{CS_2} for several values of ΔCS_2. The curve follows a log type function so the slope at smaller values of ΔCS_2 is larger than the slope at higher values (seen in Figure 3.44 (b)) therefore the maximum change in X_{LS} upon changing α_{CS_2} will occur at small values of ΔCS_2 (typical values of ΔCS_2 during a test are ~5-50 fF). It can be seen from Figure 3.44 (a) that for values of ΔCS_2 ~10 fF, when α_{CS_2} is halved/doubled, X_{LS} (and therefore σ or $\Delta\sigma$) double/halve respectively. From Table 3.5 it can be seen that the major effect on V^* when α_{CS_2} is changed comes from $\Delta\sigma$ and from Eq. (3-7) V^* is inversely proportional to $\Delta\sigma$, therefore the change in V^* is directly proportional to the change in α_{CS_2}. It is important to note that this is the worst case scenario because as it can be seen from Table 3.5 that when α_{CS_2} is changed by $\pm$50% V^* changes only by $\pm$30%.

The α_{CS_2} is pretty accurately calculated during in-situ testing but however in ex-situ testing there can be a lot of errors in the values of α_{CS_2} (see Section 2.2.2.1). The average value of α_{CS_2} from ex-situ tests is 0.73$\pm$0.18 and that of α_{CS_2} from in-situ tests is 0.44$\pm$0.10 (see Figure 3.12). The lower and upper negative error bounds on α_{CS_2} from ex-situ tests are therefore 13% and 65% respectively. So, it can be assumed that the average negative error in α_{CS_2} is the average of the upper and lower bounds which is ~40%. The positive error in α_{CS_2} can be assumed as the standard deviation in α_{CS_2} from the ex-situ tests which is

about 20%. Figure 3.45 shows the values of V^* obtained from ex-situ and in-situ tests with good R^2 values and including the error bars of +20%/-40% for the ex-situ values (to account for the error in α_{CS_2}).

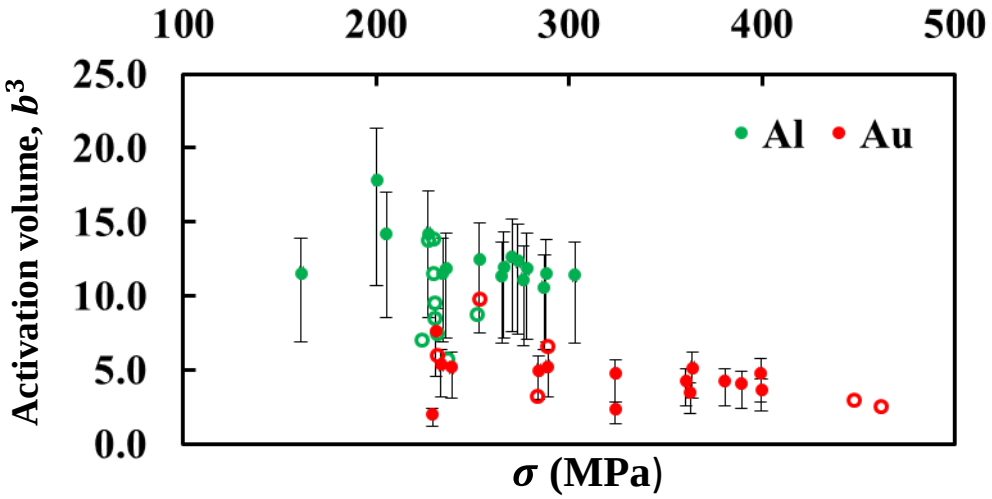

Figure 3.45 V^* of Au and Al microspecimens obtained from fits with R^2 greater than 0.9. The solid circles represent ex-situ data and the open circles represent in-situ data. Error bars have been added to the ex-situ data to account for the errors in α_{CS_2}.

3.9. Conclusions

It was shown that this MEMS device can be used to reliably extract signature parameters of plastic deformation such as true activation volume *in-situ*. True activation volume calculations were performed *in-situ* on 100-nm-thick Au and 200-nm-thick Al microspecimens. It was observed that for Au V^* values between 2-10 b^3were obtained while for Al V^*between 5-20 b^3 was obtained. It was found that the care should be taken while calculating the rates for calculation of V^* and Table 3.6 shows the important bounds for different parameters required to obtain a reliable V^* value.

Table 3.6 Limits on different parameters required to obtain a reliable V^*

Parameter	Value
R^2 for the fits	> 0.9
NSR for the relaxation segment	< 0.2
Noise in ΔCS_2	< 0.1 fF
decrease in ΔCS_2 during a relaxation segment	> 0.5 fF

The following are some of the best practices while performing *in-situ* transient experiments:

- Doing short transients when a TEM observation is made in between long transients.
- Use MEMS devices with low K_{LS} to reduce $\delta\sigma$.
- The rate of loading the thermal actuator should be kept low to about 0.01 V/s to minimize drift in the TEM imaging.

CHAPTER 4

RESULTS - IN SITU EXPERIMENTS WITH PTP

4.1. Overview

This chapter describes results from in-situ TEM testing of 200-nm-thick Al microspecimens using the PTP device. PED maps of the gauge length were collected during various stages of deformation. Section 4.2 describes the tests done on both annealed and as-deposited Al microspecimens and the analysis of the PED maps. Only one specimen of each type was tested. Section 4.3 discusses various studies that have reported grain growth in Al and compares the results obtained in this study to the literature. Finally, in Section 4.4 a comparison is made between the in-house MEMS technique described in Chapters 2 and 3 and the PTP technique.

4.2. Mechanical tests using the PTP device and PED maps

The 200-nm-thick as-deposited and annealed Al microspecimens were tested under monotonic loading using the PTP device. These in-situ tests were conducted in the JEOL 200 KeV TEM. The reasoning behind conducting these tests was to (i) compare the mechanical behavior of the microspecimens obtained using the MEMS and the PTP device, (ii) the JEOL TEM was equipped with additional capability of collecting Precession enhanced diffraction (PED) maps. PED maps were obtained for both microspecimens to investigate whether the Al microspecimens showed any signs of grain growth. The microspecimens

were manipulated in a FIB-less manner but clamped using Pt instead of glue as shown in Figure 4.2 (d). This was done again to compare the elastic compliance between the glue and the Pt clamps.

The annealed microspecimens were tested in a displacement controlled manner. Figure 4.2 (a) & (b) show the PED maps of the entire gauge length obtained before testing the annealed films and after they failed, respectively. As can be clearly seen from the PED maps that there is significant amount of grain growth in certain grains of the annealed Al microspecimens. This is better seen through the grain size distributions plotted in Figure 4.2 (c). The plot clearly shows that there was negligible fraction of grains above 150 nm grain size before testing while after failure 10% of the grains have sizes between 150-200 nm. The grain growth is actually even more severe since the PED assumes the sample to be in-plane however it can be clearly seen from Figure 4.2 (e) that the sample was in fact severely bent out-of-plane after failure. This out-of-plane bending is the direct result of the extra length acquired by the microspecimen during plastic deformation. Due to this the actual grain sizes of the grains after the failure is underestimated by the PED map.

The as-deposited samples were notched before testing as shown in Figure 4.6 (a) by condensing the electron beam in Tecnai F30 TEM to a point. The purpose of the notch was to observe grain growth in the vicinity of the notch. The as-deposited Al microspecimens were tested in a load controlled manner. PED map of the region local to the e-beam notch was obtained before testing the as-deposited microspecimen shown in Figure 4.3 (a). The sample was loaded and unloaded three times, each load-unload cycle was followed by a PED scan of the

notch area, leading to a total of four PED scans in the area, as shown in Figure 4.3. The failure of the sample however did not occur at the notch but elsewhere as shown in Figure 4.6 (a). It was observed that right from the first loading cycle a crack developed near the top edge of the microspecimen which ultimately led to the failure of the microspecimen. Two PED maps were obtained in this area after the first and second loading-unloading cycles as shown in Figure 4.4. PED maps could not be obtained after the microspecimen failed because of the plastic overlap as shown in Figure 4.6 (a). The grain size distributions obtained from the PED scans near the notched area shown in Figure 4.3 (e) do not shown much grain growth in the first three scans i.e., until the end of second loading-unloading cycle or the test 2. However, after the failure of the specimen during the third load-unload cycle there is some amount of grain growth. Similarly, PED maps from the region where failure occurred do not shown grain growth during test 2 as seen in Figure 4.4 (c). But it can be seen from Figure 4.4 (d) that the grain size distribution near the non-notch region after test 2 is similar to the grain size distribution in the notched region after failure. So, if we assume that the grain size distribution before testing is nominally the same throughout the entire gauge length then there is evidence of grain growth in the non-notch region.

To verify where the differences in the amount of grain growth between the as-deposited and annealed microspecimens could be associated with the distribution of plastic strains in the gauge length, the local strains were measured using DIC in both specimens as shown in Figure 4.5 and Figure 4.6. It can be clearly seen that the deformation was more uniform in the case of annealed

microspecimens as shown in Figure 4.5 and also where large amounts of grain growth was observed. However, there was almost no strain in the notched region of the as-deposited microspecimen until the test 3 (see Figure 4.6 (b) & (c)) and correspondingly there was not much grain growth as seen in Figure 4.3 (e). The fact that the notched region was not strained can also be seen from the fact that there is no blunting of the notch as seen from Figure 4.6 (b) & (c) after test 1 and test 2. However as can be seen from the blunting of the notch in Figure 4.6 (a) after the failure of the specimen, there must have been plastic deformation during test 3 near the notch region and correspondingly there is small amount of grain growth as seen in Figure 4.3 (e). In conclusion, there seems to be a correlation between accumulation of plastic deformation and grain growth in the Al microspecimens.

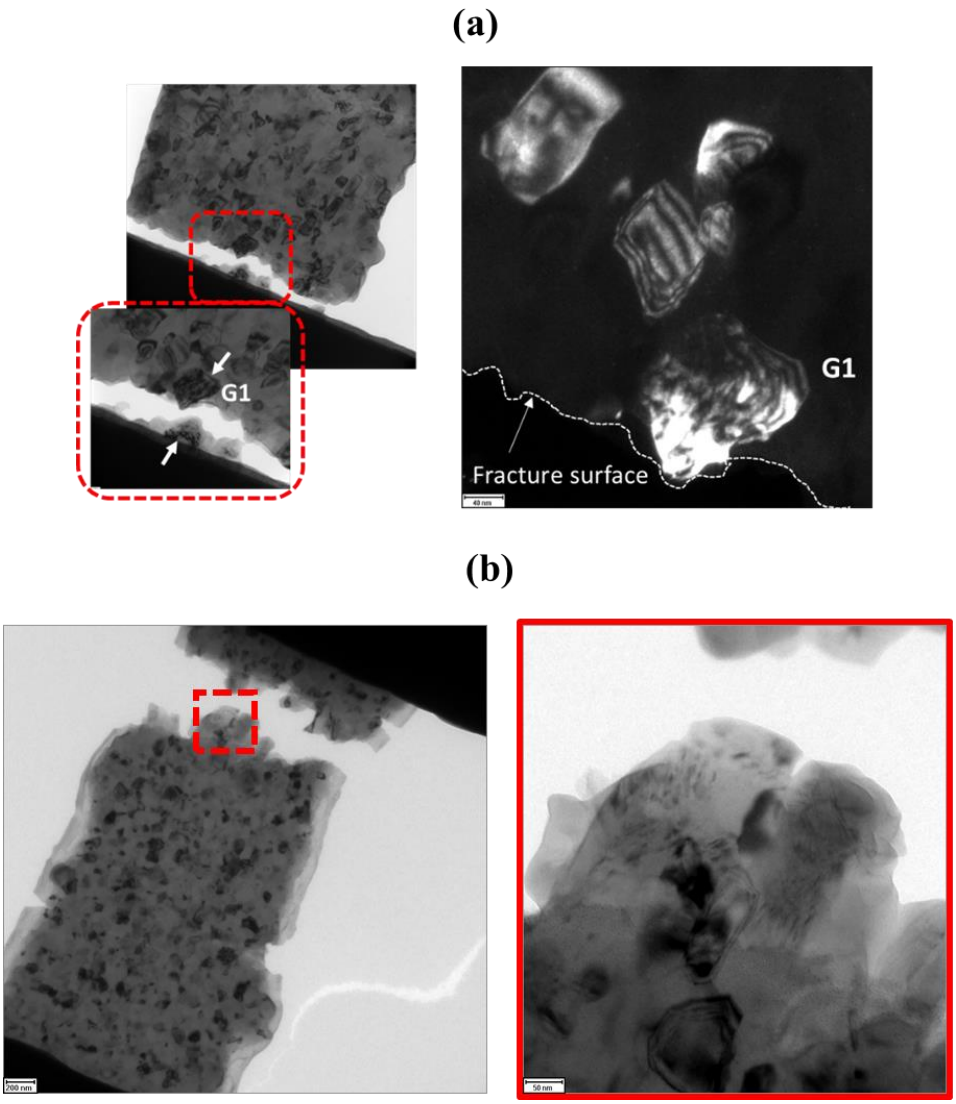

Figure 4.1 Bright field and dark field TEM images of (a) annealed and (b) as-deposited Al microspecimen showing dislocations in grains near the fracture surface.

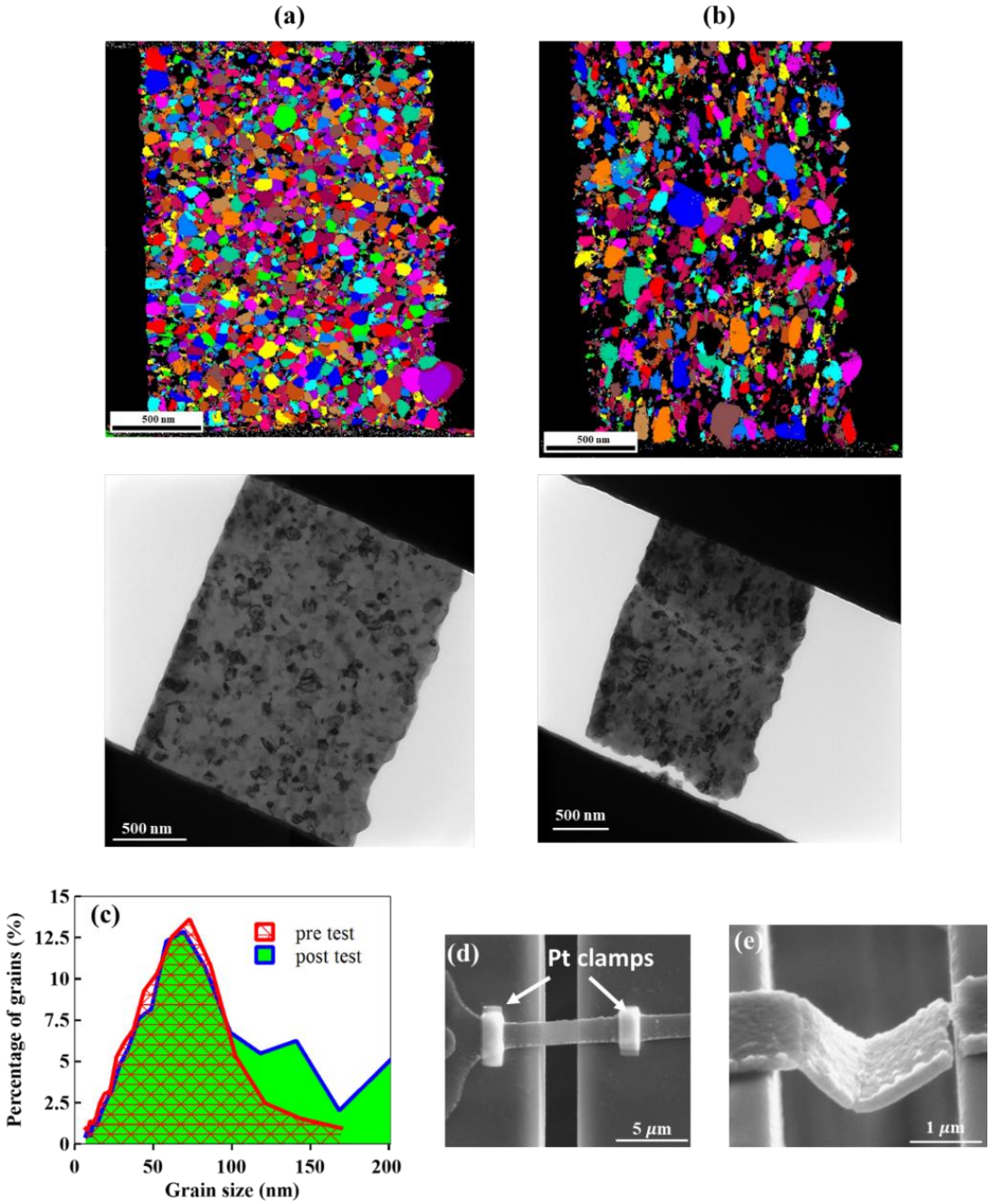

Figure 4.2 Testing of as-deposited 200-nm-thick Al microspecimen using PTP device. (a) PED map and TEM image before testing. (b) PED map and TEM image after failure. (c) Comparison of grain size distributions obtained from the PED maps. (d) SEM image pre-test showing the Pt clamps. (e) SEM image after failure showing extensive plastic deformation.

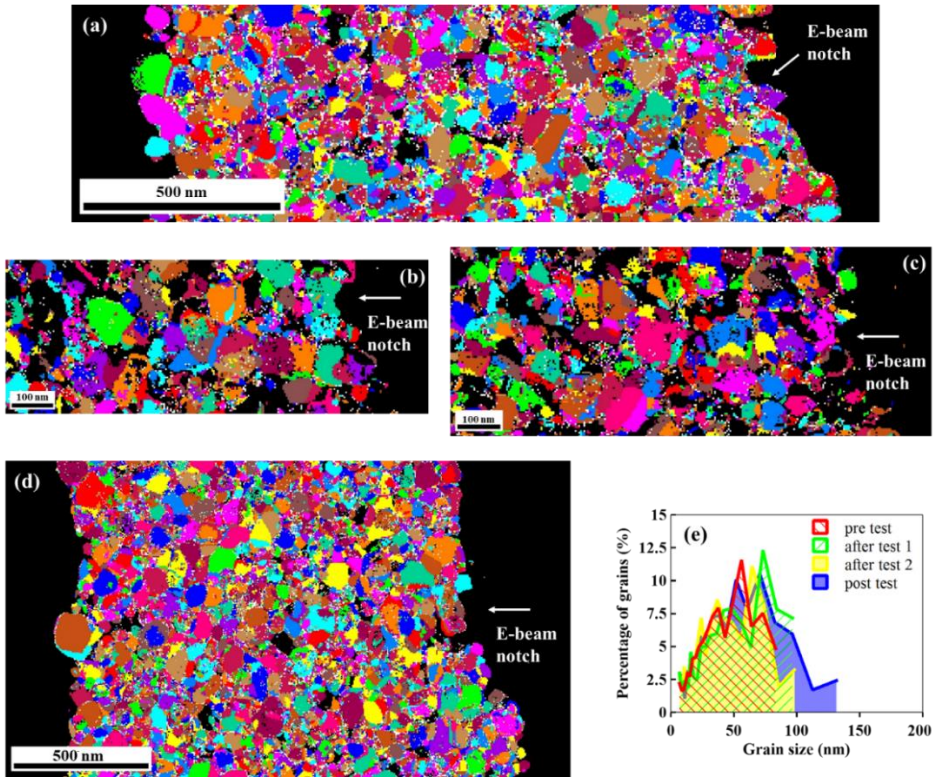

Figure 4.3 PED maps near the E-beam notch. (a) before test. (b) after test 1. (c) after test 2. (d) after failure.

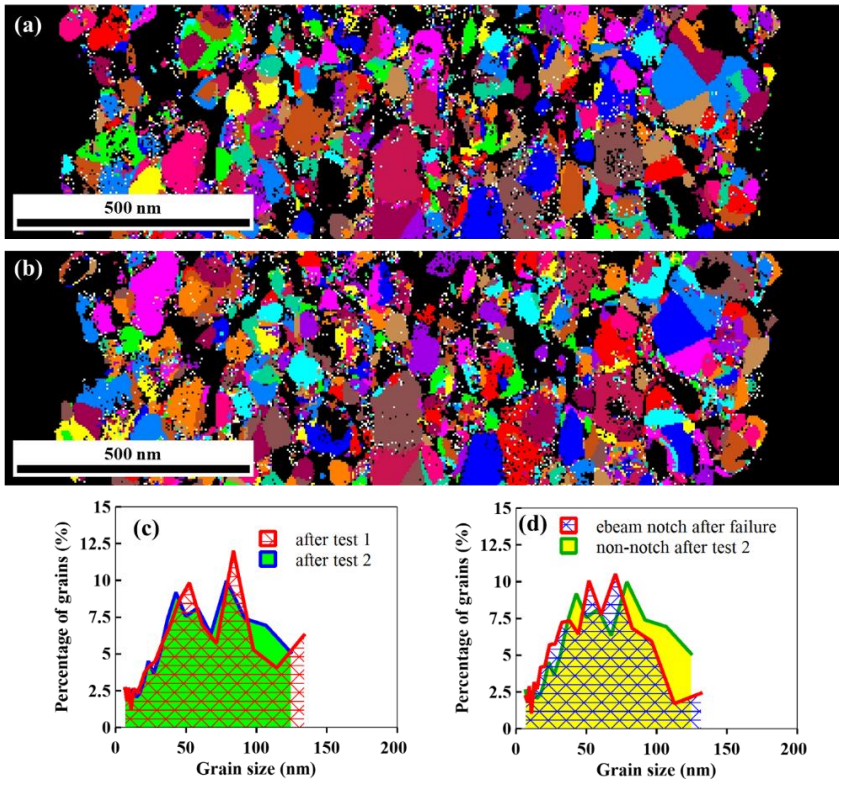

Figure 4.4 (a) & (b) PED maps near the region where failure occurred (non-notch). (a) after test 1. (b) after test 2. (c) and (d) Grain size distributions.

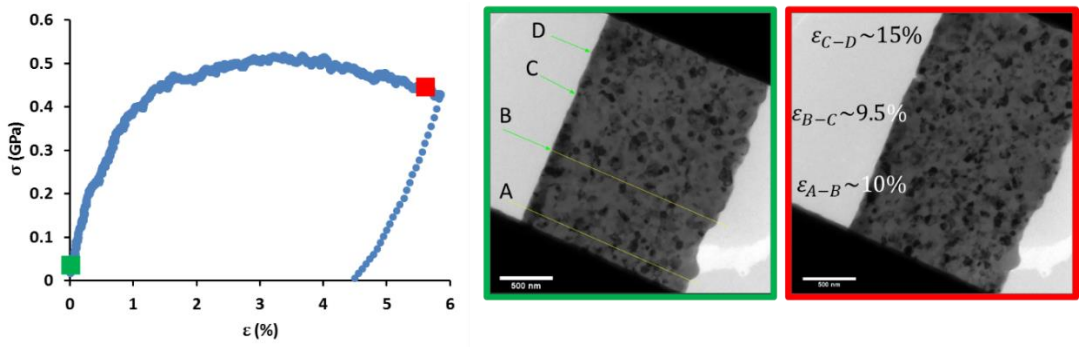

Figure 4.5 Regions used for obtaining the strain distribution along the length of the annealed microspecimen.

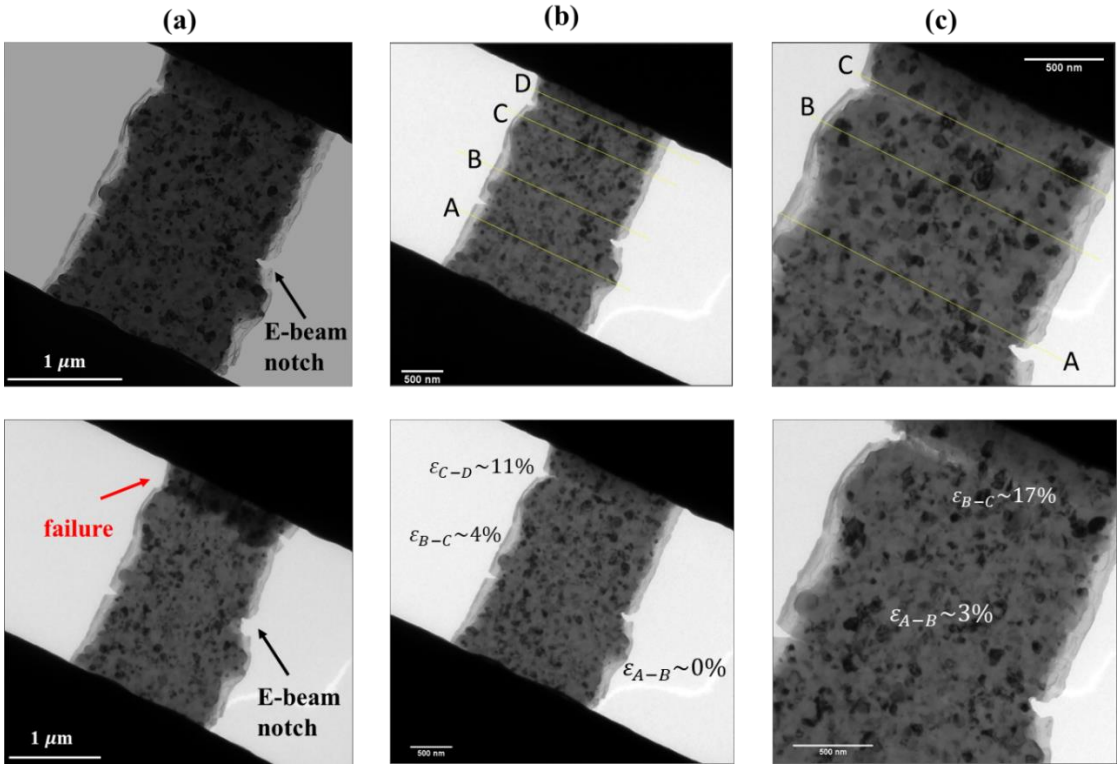

Figure 4.6 TEM images of the as-deposited Al microspecimen with a pre-notch created via electron beam. (a) Images before testing (top) and after sample failure (bottom). (b) Images before and at the maximum load during test 1. (b) Images before and at the maximum load during test 2. Also, the strain distributions obtained by DIC during test 1 and test 2 are shown in (b) and (c) respectively.

4.3. Discussion

The topic of grain growth in nanostructured metals has attracted a lot of attention. Several researchers have reported grain growth in NC/UFG metals [105, 106, 108, 133, 249-252]. In contrast, there are several others who do not report any grain growth in NC/UFG metals [124, 134, 253, 254]. The studies which report grain growth cite various reasons associated to grain growth. Jin et al. [105] observed deformation-induced grain growth resulting from grain boundary migration, grain rotation and grain coalescence during indentation on UFG Al films deposited on a Si substrate. Gianola et al. [133] reported stress-assisted grain growth in 150-nm-thick and 300 nm-thick Al films with mean grain sizes 62 nm and 104 nm respectively due to grain boundary processes such as migration, sliding, and dislocation nucleation. Legros et al. [106] showed clear evidence of stress-coupled grain boundary migration through in-situ straining of UFG Al films in the TEM. Grain growth has been associated with plastic deformation as well. Gianola et al. [108] have established grain growth as an active deformation mode in abnormally ductile NC Al thin films at room temperature. Legros at. al [106] observed grin growth only near crack tips in 380-nm-thick and 180-nm-thick Al films with mean grain sizes 90 nm and 40 nm respectively. Mompiou and Legros [249] provide quantitative measurements of both grain growth and grain rotation in notched areas of a 250-nm-thick Au film with grain size of 250 nm. They also provide evidence that grain rotation results from the motion of intergranular dislocations. The results presented in this section on the Al microspecimens tested using the PTP are aligned with the observations made by

other studies. The grain growth observed in both as-deposited and annealed specimens was associated with plastic deformation. In the case of as-deposited Al microspecimen grain growth was observed in the notched region only when there was plastic deformation in the notched region. Dislocation activity was seen in the grains near the fracture surface in the post-mortem TEM images of both microspecimens, as shown in Figure 4.1. It can be seen from Figure 4.2 (b) that the grains near the fracture surface of the annealed microspecimen show significantly larger sizes compared to the grains in Figure 4.2 (a). The grains in Figure 4.2 (b) also seem to be elongated in the tensile direction probably suggesting a preference in the direction of grain boundary migration. It was difficult to study grain rotations because of the complications arising due to out-of-plane bending of the microspecimen after fracture as shown in Figure 4.2 (e).

The apparent elastic modulus obtained from the σ-ε curve for annealed Al microspecimens shown in Figure 4.5 was 25 GPa. The bulk value of the elastic modulus for Al is 70 GPa [244]. This shows that even Pt clamps suffer from the same compliance issues as the epoxy glue for specimen manipulation. With the MEMS technique, the apparent elastic modulus for Al microspecimen is between 15-20 GPa. The reason for compliance with the Pt clamps probably is the poor adhesion between the deposited Pt and the Si of the PTP device which allows to microspecimen to pull the clamps along with it.

4.4. Comparison between the MEMS technique and the PTP device

As can be seen in Figure 4.7, the force in the sample is measured directly in the MEMS technique. However, to measure the force with the PTP device the stiffness of the device needs to be subtracted and that introduces error in force measurement. Therefore, after proper calibration MEMS is a more reliable technique for force measurement.

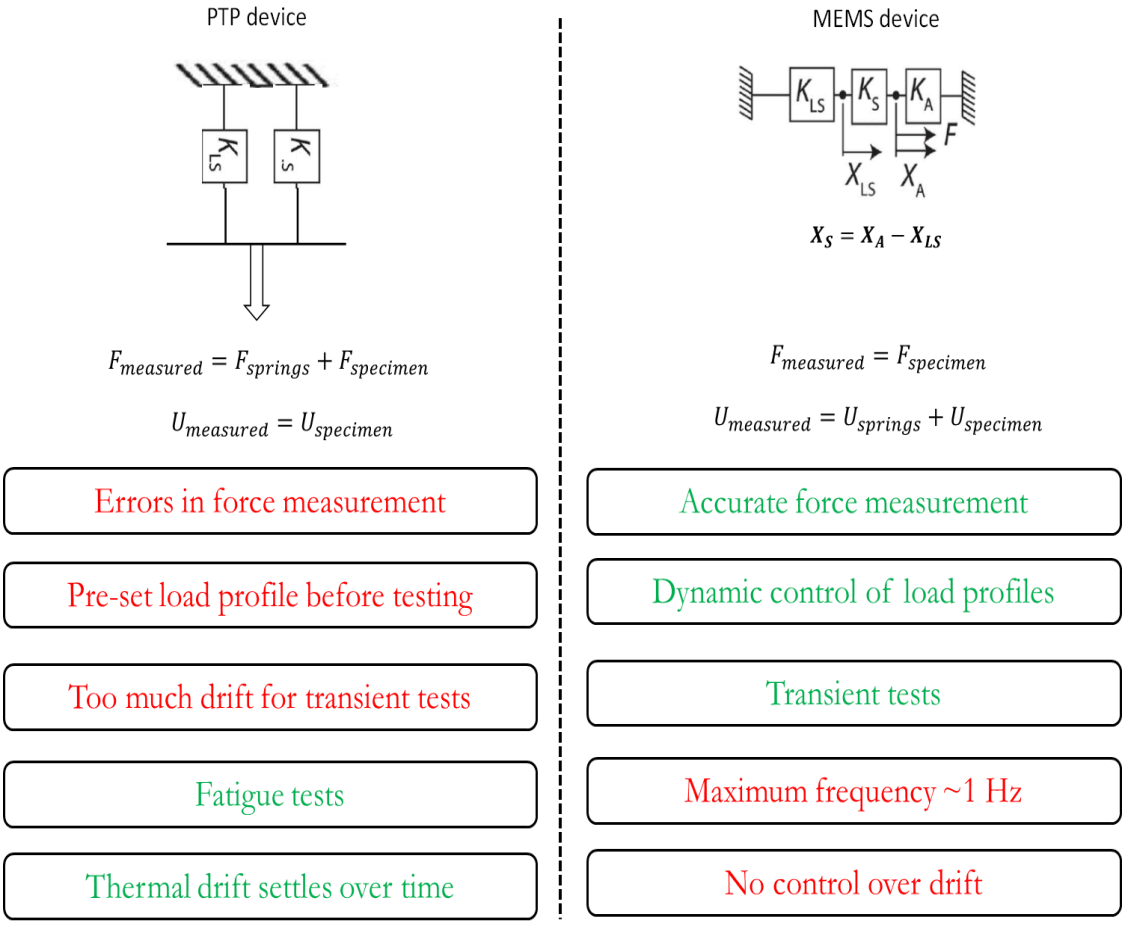

Figure 4.7 Comparison of PTP device and MEMS technique.

MEMS also has a better capability to perform transient tests than PTP because of the use of capacitive sensors which are very sensitive to displacements

and have very high displacement resolution (<0.1 nm). Further, the noise in the MEMS capacitive data is only due to parasitic capacitances and not any physical reasons while the PTP has drift issues due to the physical contact between the picoIndenter and the PTP device which makes it unreliable for doing transient mechanical tests which are only a few seconds long. Also, the MEMS technique is more customizable compared to PTP since PTP is a commercial technique. One of the great flexibilities that MEMS offers is the dynamic control of the load profile which is not possible with a PTP device. The reason for this flexibility is that the LabView program for controlling the MEMS is totally customizable while the use of PTP is limited by the software capabilities provided by Hysitron. The biggest disadvantage of using the MEMS technique is that the long term stability in the MEMS is completely dominated by electrical drift which cannot be controlled however the PTP has the advantage of the drift settling over time. The PTP can be used to perform fatigue tests with frequencies as high as 200 Hz however the maximum frequency of a fatigue test with the MEMS is limited by the speed of data collection in MEMS which is about ~1Hz.

4.5. Conclusions

Grain growth was observed in 200-nm-thick Al microspecimens using PED in combination with PTP testing. The grain growth occurred in conjunction with plastic deformation suggesting it could be the rate controlling mechanism in these Al microspecimens. The amount of grain growth found in the annealed microspecimens was found to be significantly higher than the as-deposited

microspecimens. This discrepancy was attributed to the strain localization seen in as-deposited microspecimens due to cracking of the microspecimen. The Pt clamps were found to be as compliant as the epoxy glue clamps.

CHAPTER 5

RESULTS - FATIGUE BENDING OF MICROBEAMS

5.1. Overview

Section 5.2 discusses the FEM results to calculate the E_{Au} and predict the percent decrease in f_0 due to cracking in the Au coating. Section 5.3 presents the difference in the S-N curves for the coated and uncoated microbeams. Section 5.4 discusses the evolution of f_0 in the Au coated microbeams up to failure. Section 5.5 presents the analysis of the cross-sections by FIB of the cracked microbeams. Section 5.6 discusses the mechanisms of cracking during VHCF under extreme stress gradients based on the results presented.

5.2. FEM results

The change in f_0 of the Au-coated microresonators as a function of E_{Au} was evaluated using the modal analysis described in Section 2.4.3. Figure 5.1 shows the $f_0^{uncoated}$ / f_0^{coated} ratio as a function of E_{Au}. The average experimental value of $f_0^{uncoated}$ is 8630±210 Hz based on the initial values of 22 uncoated microbeams [205], and the average value of f_0^{coated} is 9512±169 Hz, based on 11 Au-coated microbeams. Therefore, the FEM model predicts a value of E_{Au} = 71 GPa to best match the experimental ratio $f_0^{uncoated}/f_0^{coated}$ = 0.907 (see Figure 5.1).

Further modal analyses were performed to evaluate the effect of cracks in the Au coating on f_0. The cracks were modelled on both Au side walls in a

symmetrical fashion; see two crack configurations in Figure 5.1 (b) & (c). For one crack on each side of the microbeam, f_0 decreases by ~1.3%, due to the associated decrease in stiffness. For three cracks on each side that are spaced 2 μm apart, the decrease in f_0 is larger (2.2%) but to a lesser extent.

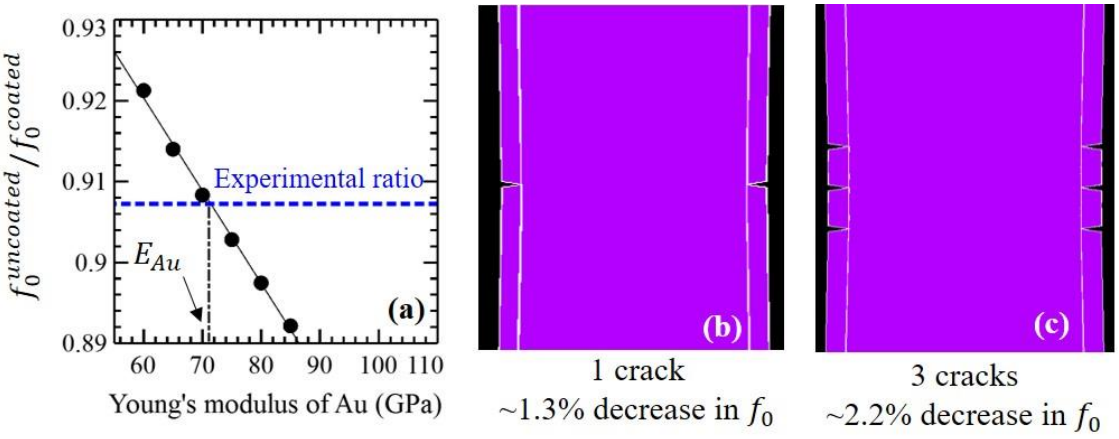

Figure 5.1 (a) Normalized decrease in f_0 due to the Au coating as a function of E_{Au}; (b) & (c) Effect of cracks in Au coating on f_0 [238].

5.3. S-N curves

Eleven Au-coated Ni microbeams were tested in laboratory conditions until failure (defined as the number of cycles required for a 10% reduction in f_0) or a run-out behavior. Figure 5.2 (a) & (b) show the S - N and ε_a - N curves, respectively, for the Au-coated and uncoated Ni microbeams. The graphs show both the stress and strain amplitudes in the Ni at the outer edge of the microbeam (for all specimens) and the amplitudes at the outer edge of the Au coating for the coated specimens. The Au-coated microbeams show an increase in N_f by at least a factor of 5 compared to uncoated ones tested in air at similar stress levels. Therefore, the coating provides a beneficial effect on N_f in air, even though it does not appear to significantly affect the endurance limit

(approximately $\sigma_{a,Ni}$ ~ 300 MPa). As a comparison, however, the fatigue behavior of the Au-coated microbeams in air is not as good as that of the uncoated microbeams tested in vacuum, which exhibit much longer fatigue lives and larger endurance limit (approximately $\sigma_{a,Ni}$ = 440 MPa).

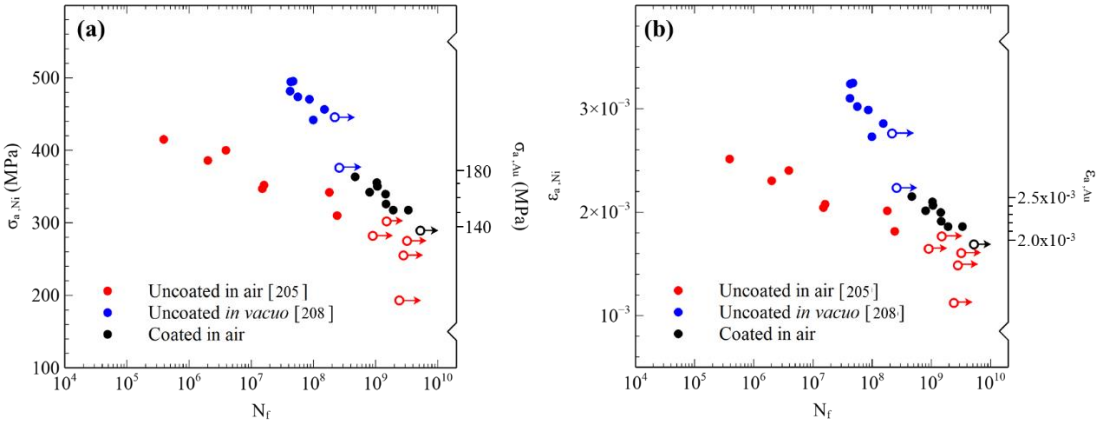

Figure 5.2 (a) S - N and (b) ε_a - N curves for Au-coated microbeams tested in air, compared to uncoated microbeams tested *in vacuo* and in air; open dots represent run-out tests [238].

5.4. Resonant frequency evolution curves

The beneficial effect of the coating on the fatigue behavior in air can also be observed with the f_0 evolution curves which indicate accumulation of damage. Figure 5.3 (a) compares the f_0 evolution curves for a coated microbeam tested at $\sigma_{a,Ni}$ = 290 MPa versus an uncoated microbeam tested at $\sigma_{a,Ni}$ = 305 MPa. Both tests were run-outs (i.e. less than a 10% decrease in f_0). However, Figure 5.3 (a) clearly indicates a different fatigue behavior, with a decrease of 6% after 1.5×10^9 cycles for the uncoated microbeam, whereas the coated microbeam kept its f_0 nearly constant over 5.2×10^9 cycles. As will be shown later, this behavior indicates less fatigue damage along the sidewalls of the Ni microbeam thanks to

the coating. Similarly, Figure 5.3 (b) highlights significantly different characteristics in the f_0 evolution curves of two specimens (coated vs uncoated) for similar $\sigma_{a,Ni}$ values (350 vs 340 MPa). The uncoated specimen fails after 4×10^7 cycles with a steady decrease in f_0. Instead, the coated specimen fails after 1.05×10^9 cycles, with a very slow decrease of ~1% over the first 10^9 cycles, followed by a sharp decrease that is similar in rates with that of the uncoated specimen. The f_0 evolution curves of the microbeams shown in Figure 5.3 (b) are representative of all other fatigue tests in air for $\sigma_{a,Ni} > 300$ MPa, and indicate that the increase in N_f by at least a factor of 5 for the coated microbeams results from the initial slow decrease in f_0 prior to a fast decrease that is similar to that of the uncoated specimens.

Figure 5.3 also shows that the coated microbeams exhibit an initial increase in f_0 (over the first 1 to 5×10^8 cycles) of ~0.5-1%, regardless of the $\sigma_{a,Ni}$ value (based on 11 tests). This initial increase is not observed for the uncoated microbeams and is therefore directly related to the presence of the coatings. One possible explanation is a transient cyclic hardening behavior of the Au that could result in an apparent stiffer coating.

Figure 5.3 (c) and (d) show the f_0 evolution curves for a coated microbeam that was first tested in air for 7×10^8 cycles at $\sigma_{a,Ni} = 375$ MPa, until the specimen reached the transition from a slow decrease to a sharp decrease in f_0. The test was then interrupted and resumed in vacuum (inside the SEM, as done in [208]) at a similar $\sigma_{a,Ni}$ of 385 MPa. At the end of the fatigue test in air, f_0 decreased by about ~2.5% in less than 10^6 cycles while in vacuum, f_0 decreased by less than 0.5% in more than 5×10^6 cycles, a decrease rate almost 25 times lower. Hence

the environment plays a critical role in the fatigue of the coated microbeams for the portion of the test corresponding to the fast decrease in f_0.

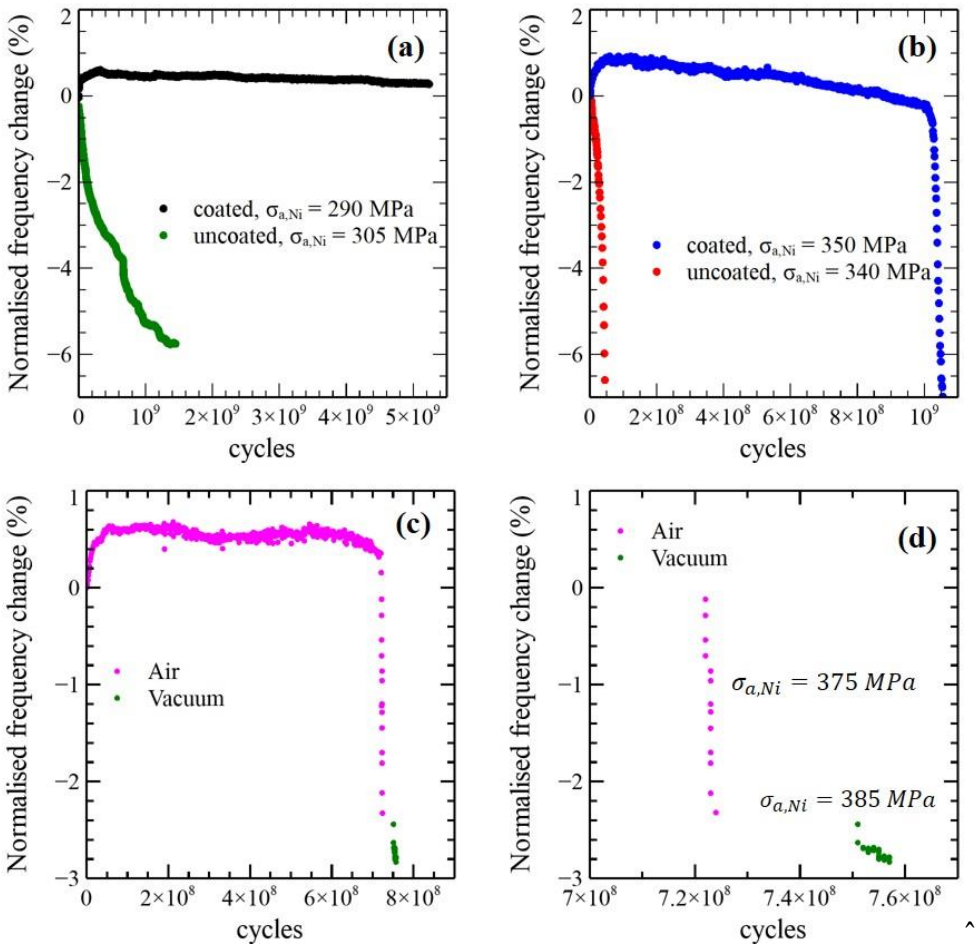

Figure 5.3 . (a) and (b) Comparison of f_0 evolution curves of coated and uncoated fatigue tests in air at similar stress levels. (c) and (d) f_0 evolution curve of a coated specimen tested in air ($\sigma_{a,Ni}$ = 375 MPa) up to 7.2 × 10^8 cycles than tested *in vacuo* ($\sigma_{a,Ni}$ = 385 MPa) inside a SEM [238].

5.5. Fractography

A series of SEM images, including FIB cuts, after completed or interrupted fatigue tests, were taken to determine the extent and location of fatigue damage and correlate it to the f_0 evolution curves shown in the previous section. SEM images of a coated microbeam tested at $\sigma_{a,Ni}$ = 290 MPa for 5.2 × 10^9 cycles did

not reveal any cracks in the Au coating, although fatigue damage in the form of extrusions could be seen. Fatigue extrusions were also observed for a microbeam tested at $\sigma_{a,Ni}$ = 350 MPa for 3×10^7 cycles, corresponding to an increase in f_0 of 0.6%. Figure 5.4 (a)-(f) show SEM images of a Au-coated Ni microbeam tested at $\sigma_{a,Ni}$ = 315 MPa for ~1.9×10^9 cycles, with a corresponding 27% decrease in f_0. In that case, two main cracks grew, one from each sidewall, towards the neutral plane of the beam, extending throughout the microbeam's thickness (see Figure 5.4 (a) & (b)). Extrusions in the Au coating surrounding the fatigue crack can also be observed (see Figure 5.4 (c)). Figure 5.4 (d) shows the cross sectional view of the same fatigued microbeam after rupturing the remaining ligament (corresponding to the middle part of the cross section). The SEM image suggests transgranular fatigue failure. In addition, a large amount of voids are present in both Ni and Au (see Figure 5.4 (e)). EDS map of the cross-section in Figure 5.4 (f) shows a smooth interface between the Au coating and the Ni microbeam, indicating that the presence of the Au coating prevented the formation of large extrusions/intrusions in the Ni that were observed for the uncoated fatigued microbeams [205, 208].

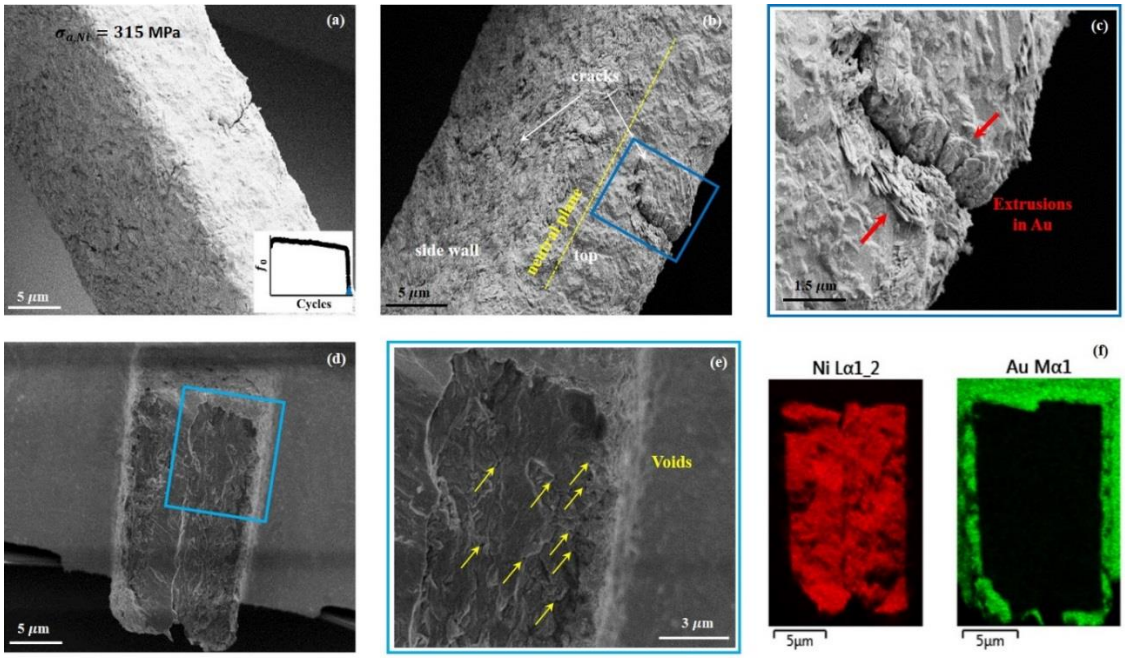

Figure 5.4 . (a)-(c) Fatigued coated microbeam tested at $\sigma_{a,Ni}$ = 315 MPa for 1.9 x 10^9 cycles; (d) & (e) Cross-sectional view of the fatigue surface of the same microbeam, (f) EDS of the cross-section showing absence of any significant extrusions in Ni [238].

Figure 5.5 shows transverse (see Figure 5.5 (b) and (c)) and vertical (see Figure 5.5 (b) and (d)) FIB cuts (see their locations on Figure 5.5 (a),(e), and (i)) that were obtained after an interrupted fatigue test of a coated microbeam (8.5 × 10^8 cycles at $\sigma_{a,Ni}$ = 350 MPa, leading to a decrease of only 1.8% in f_0, i.e. before the test reached the fast decrease portion of the f_0 evolution curve (see schematic in Figure 5.5 (a))). Figure 5.5 (f)-(h) show cracks and voids in the Au coating, along the sidewalls and on top of the sidewall (i.e., at the location of the largest stress amplitudes). In contrast, no cracks or voids can be observed in Ni even in the vicinity of the sidewall where σ_a is maximum. Figure 5.5 (i) shows the location of three vertical cuts made on the same microbeam at increasing distances w from the sidewall (i.e., closer to the neutral plane), w = 1.4, 3.2, and 4.8 μm. Figure 5.5 (j)-(o) show extensive fatigue damage in the top Au layer in

the form of extrusions and voids at distances w = 1.4 μm (σ_a = 335 MPa in Ni, 95% of $\sigma_{a,Ni}$) and 3.2 μm (σ_a = 275 MPa in Ni, 80% of $\sigma_{a,Ni}$). More specifically, Figure 5.5 (n) & (o) (w = 1.4 μm) show a crack through the thickness of the Au coating that appears to be formed by the coalescence of adjacent nanometer scale voids. Figure 5.5 (k) & (l) also show a few voids in Ni. Small extrusions in Ni can also be seen in Figure 5.5 (m) & (o). For w = 4.8 μm (where σ_a = 230 MPa in Ni (~66% of $\sigma_{a,Ni}$)), no extrusions or voids can be seen in the Au coating or in Ni (see Figure 5.5 (p)), providing evidence that the damage observed for w = 3.2 and 1.4 μm is due to fatigue.

Figure 5.6 (d)-(h) show SEM images of horizontal FIB cuts on a coated microbeam fatigued at $\sigma_{a,Ni}$ = 350MPa for ~10^9 cycles that resulted in a decrease in f_0 of 9.3%. As was shown in Figure 5.4 (a), the large decrease in f_0 results from cracking of the Ni microbeam. The fatigue crack in the Ni has similar characteristics than the fatigue cracks observed for the uncoated microbeams tested in air [208]. Specifically, the crack follows a tortuous crack path, and appears to be formed by connection of a large density of voids that only form in its vicinity. As was shown for fatigue tests of uncoated microbeams in air, the voids in Ni are associated with larger oxygen concentration (see EDS maps in Figure 5.6 (i)). As can be seen in Figure 5.6 (d), there is only one fatigue crack in the Au coating (that looks similar to the fatigue crack observed in Figure 5.5 (n) and (o) and consists of a large density of nanoscale voids (<10 nm in size), at the location of the Ni fatigue crack. It is therefore likely that the fatigue crack in the Au coating first reached the Au/Ni interface before propagating in Ni. In fact, Figure 5.6 (e)-(g) clearly show signs of delamination at the Au/Ni interface,

suggesting that interfacial cracking occurred once the fatigue crack in the Au reached the interface and before propagation of the fatigue crack in Ni.

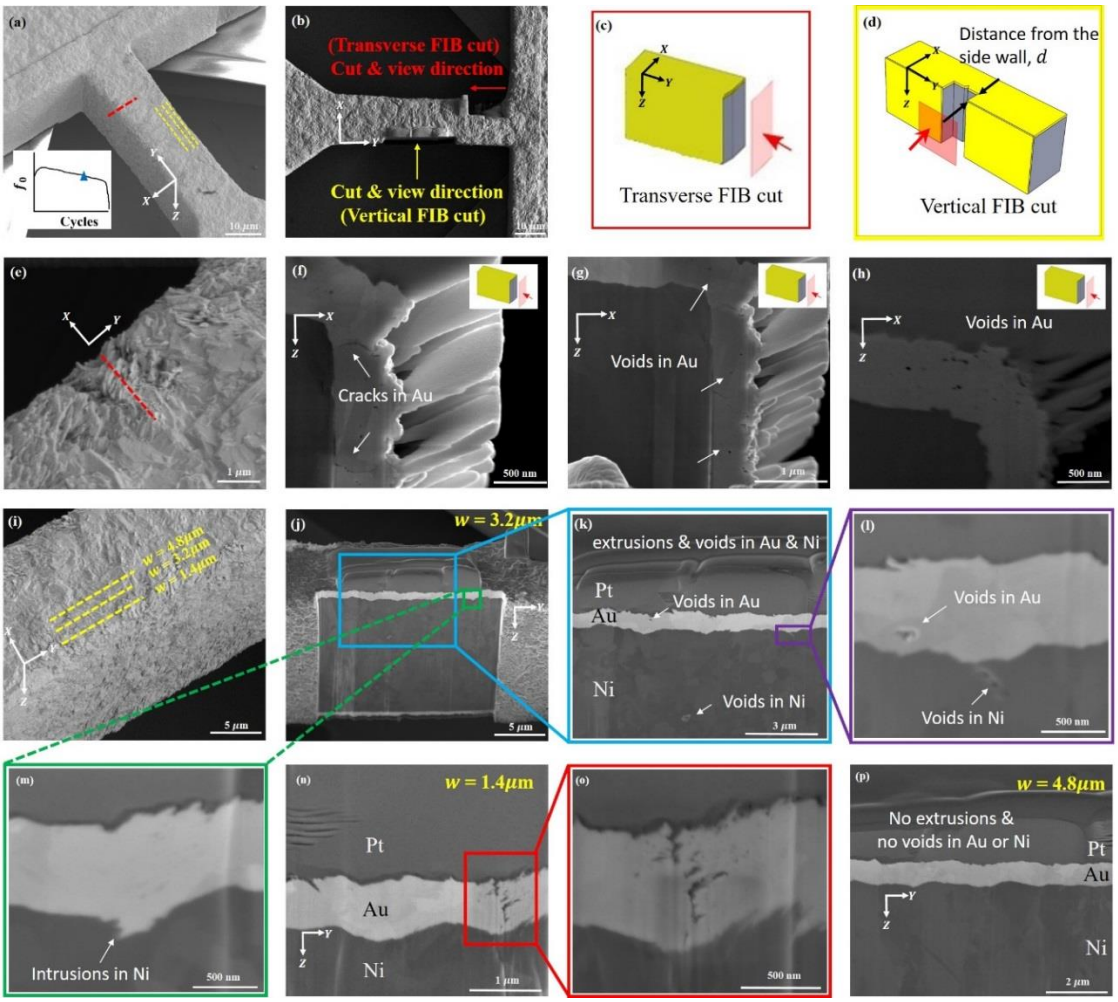

Figure 5.5 (a) Coated microbeam tested at $\sigma_{a,Ni}$ = 350 MPa for 8.5 × 10^8 cycles; (b)-(d) Attributes of the transverse and vertical FIB cuts; (e) Location of the transverse FIB cut; (f)-(h) Cracks and voids in Au top layer and side wall; (i) Locations of the vertical FIB cuts; (j)-(m) Damage in Au and Ni at w = 3.2 μm (σ_a = 275 MPa in Ni, 80% of $\sigma_{a,Ni}$); (n) & (o) Cracking of Au coating by void coalescence at w = 1.4 μm (σ_a = 335 MPa in Ni, 95% of $\sigma_{a,Ni}$); (p) No extrusions or voids in Au or Ni at w = 4.8 μm (σ_a = 230 MPa in Ni, 66% of $\sigma_{a,Ni}$) [238].

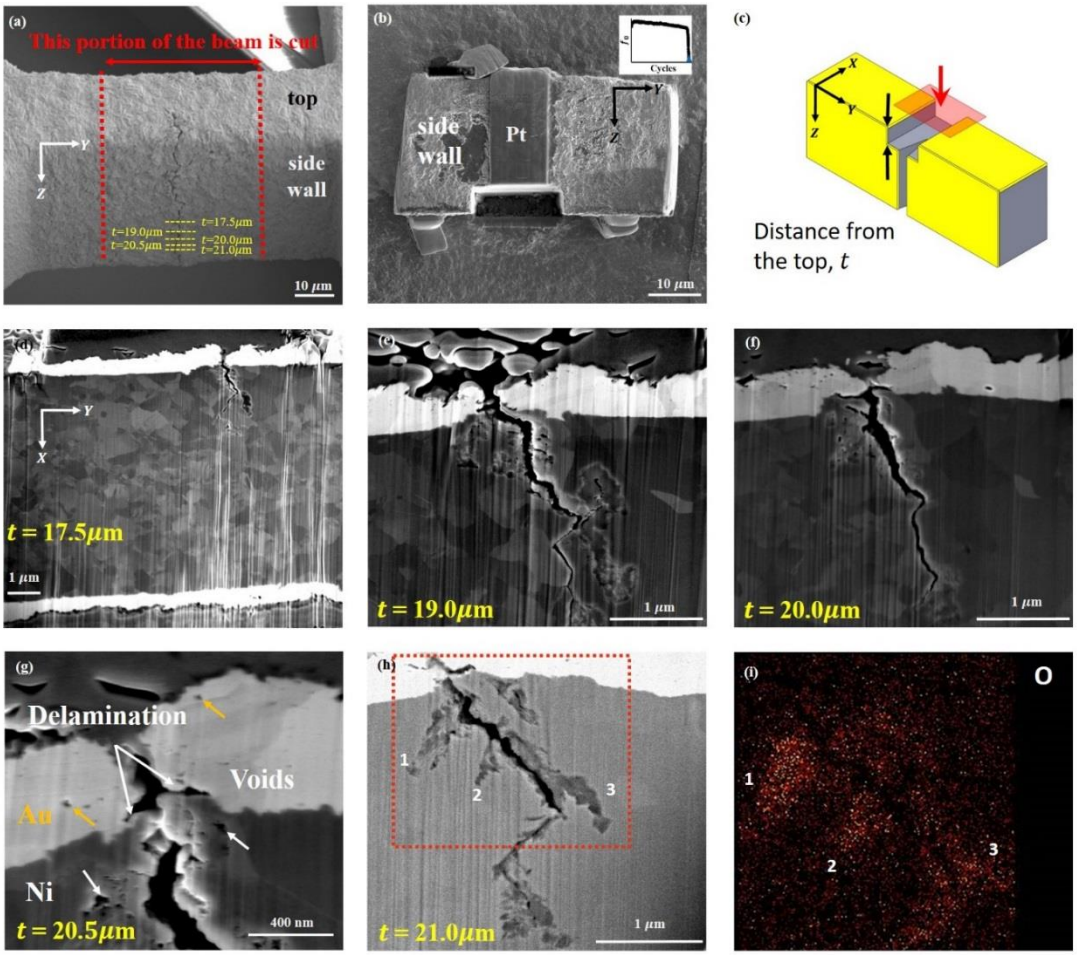

Figure 5.6 (a) Coated microresonator tested at $\sigma_{a,Ni}$ = 350 MPa for 10^9 cycles showing locations of the horizontal FIB cuts; (b) & (c) Attributes of the horizontal FIB cut; (d)-(h) Voids in both Au and Ni all along the crack path, highlighting as well delamination between Au and Ni; (i) EDS images showing larger concentrations of oxygen present at the marked locations (corresponding to voids) along the crack [238].

5.6. Discussion

The results of this study highlight a beneficial effect (i.e. an increase in N_f by at least a factor of 5) of 850-nm-thick Au coatings on the bending HCF / VHCF behavior of 11.5-μm-wide Ni microbeams in air. However, the underlying mechanisms are different from the studies presented in Section 1.3 due to

significant size effects that can govern the fatigue properties of metallic micro-components [204-206, 216, 255-257], the main reason here being the presence of extreme stress gradients in the microbeams [205, 208]. Our results show that, in air, the coated microbeams exhibit longer fatigue lives than the uncoated ones by reducing and delaying void formation in Ni. As shown in Figure 5.5, very few voids could be observed in the Ni underneath the Au coating at σ_a = 350 MPa and after 8.5×10^8 cycles in air. In contrast, the uncoated beams fail in air at N_f ~ 10^7 cycles at σ_a = 350 MPa (see Figure 5.2 (a)), for which FIB cuts have revealed a large concentration of voids (see [208]). Hence, the coating effectively delayed fatigue crack nucleation by preventing void formation. To further confirm that these findings are specific to void-driven fatigue mechanisms, we performed two "manual" low cycle fatigue (LCF) tests of coated and uncoated microbeams. These tests consist of using a micromanipulator placed at the bottom of the fan-shaped mass to cycle back-and-forth the microbeam to the maximum allowable angle of rotation that is dictated by the comb drive design (80 mrad; see Figure 2.13 (a)). This angle of rotation corresponds to σ_a = 720 MPa, ε_a = 1% and ε_{pa} = 0.6% for Ni. The fatigue life of the uncoated microbeam was 1000. Interruption of the fatigue test revealed fatigue cracks after only 500 cycles, and average crack growth rates of 6 nm/ cycle between 500 and 700 cycles (compare Figure 5.7 (a) and (b)). These crack growth rates are more than 3 orders of magnitude faster rates compared to that measured in the HCF regime in air (~10^{-12} m/cycle). The fracture surfaces did not reveal any void formation (see Figure 5.7 (d)). This result clearly highlights different fatigue mechanisms between LCF and HCF/VHCF regimes. In the LCF regime, the measured crack growth rates and

lack of void formation suggest that the classical fatigue mechanisms, based on sufficient crack tip plasticity for fatigue crack growth, are dominant. As such, the effect of the Au coating on LCF properties should be different from what we observe in the HCF/VHCF regimes. In fact, the fatigue life of the coated microbeam for ε_{pa} = 0.6% is 1900, which represents a much smaller increase in N_f (less than a factor of 2). Figure 5.7 (h) shows a fracture surface of the Ni similar to that of the uncoated LCF test, with no voids. In that case, the increase in N_f is likely due to the extra cycling required to induce fatigue failure of the Au coating. After only 500 cycles, only extrusions in the Au coating could be observed (Figure 5.7 (e)) whereas clear fatigue cracks were already formed in the uncoated Ni (Figure 5.7 (a)). After 700 cycles, the extrusions in the coating were more developed and some fatigue crack embryos were present in the coating (see Figure 5.7 (f)), whereas the fatigue cracks had already propagated towards the neutral axis for the uncoated microbeam (Figure 5.7 (b)). As shown in Figure 5.7 (g), only after 1000 cycles could well developed fatigue cracks be observed. Presumably between 1000 and 1900 cycles, these cracks propagated into the Ni until fatigue failure.

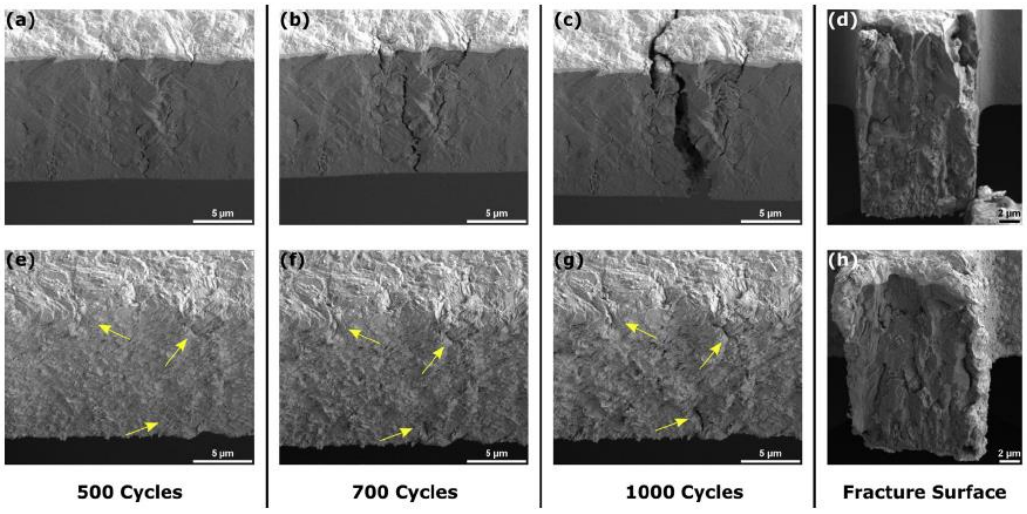

Figure 5.7 Comparison of evolution of fatigue damage for two LCF tests ($\varepsilon_{a,Ni}$ = 1%, $\varepsilon_{pa,Ni}$ = 0.6%) of (a)-(c) uncoated and (e)-(g) coated microbeams. Fracture surface after fatigue failure occurring after (d) 1000 cycles for uncoated microbeam and (h) 1900 cycles for coated microbeam [238].

Even though the Au coating delays fatigue crack formation in Ni in air, our results show that it eventually undergoes fatigue failure, as evidenced by the extrusions formation in Au (see Figure 5.4 (c,(f) and (i)) as well as Figure 5.5 (e)) and the fatigue cracks observed in Figure 5.5 (n) and Figure 5.6. In addition, our FEM results showed that a crack in the Au coating through the thickness of the microbeam represent a 1% decrease in f_0. Hence the observed decrease of ~1-2% decrease in f_0 over the first 10^9 cycles (see Figure 5.3 (a) and (b)) is consistent with the notion of a few fatigue cracks developing inside the coating and reaching the Au/Ni interface (as observed for example is Figure 5.5 (n)). Figure 5.6 (d)-(h) show a fatigue crack in Ni, based on interconnected voids, at the location of a fatigue crack in the Au coating, as well as delamination between the coating and Ni. Once a fatigue crack in the coating reaches the interface, Ni becomes exposed to the environment, especially if delamination occurs. As such, the fatigue process in the exposed Ni is expected to be similar to that of the uncoated microbeams fatigued in air. This is consistent with the same fatigue damage observed in Ni for both uncoated and coated microbeams tested in air, and the similarity in f_0 evolution curves (see Figure 5.3 (b); the last portion of the f_0 evolution curve for the coated microbeam, corresponding to the cracking in Ni, is similar to the curve for the uncoated microbeam). This is also consistent with the results shown in Figure 5.3 (c) and (d), showing that the last portion of

the f_0 evolution curve for the coated microbeam is also very sensitive to the environment, as is for uncoated microbeams [208].

Figure 5.8 summarizes the overall HCF/VHCF fatigue behavior of the coated and uncoated microbeams in air discussed above, by plotting two representative f_0 evolution curves and highlighting the corresponding nature and location of fatigue damage throughout the fatigue test. In contrast to the five desired coating properties listed in the introduction to prevent/delay PSB-induced fatigue damage and to the known coating effects for bulk alloys undergoing classical fatigue mechanisms [188-195], the main reason for the delay in fatigue crack nucleation for the coated microbeams is the Au coating acting as an oxygen barrier. However, the fatigue life of the coated microbeams in air is less than that of the uncoated microbeam tested *in vacuo* (see Figure 5.2), because the improvement in the fatigue behavior is limited by the fatigue behavior of the Au coating. Hence, the coating needs to have a good fatigue resistance (better than that of the Ni) to be effective. As explained above, the fatigue damage in the Au coating is, similarly to Ni, associated with void formation. There are two possible explanations for its good fatigue resistance. First, its small grain size likely results in a large enough yield stress that minimizes the plastic strain amplitude, thereby preventing the development of PSB-induced extrusion. Second, as a noble metal, the void formation in Au is unlikely to be assisted by a chemisorption process of oxygen on the void surface, which could explain why only small voids were formed in the coating in comparison to Ni (see Figure 5.6 (g)).

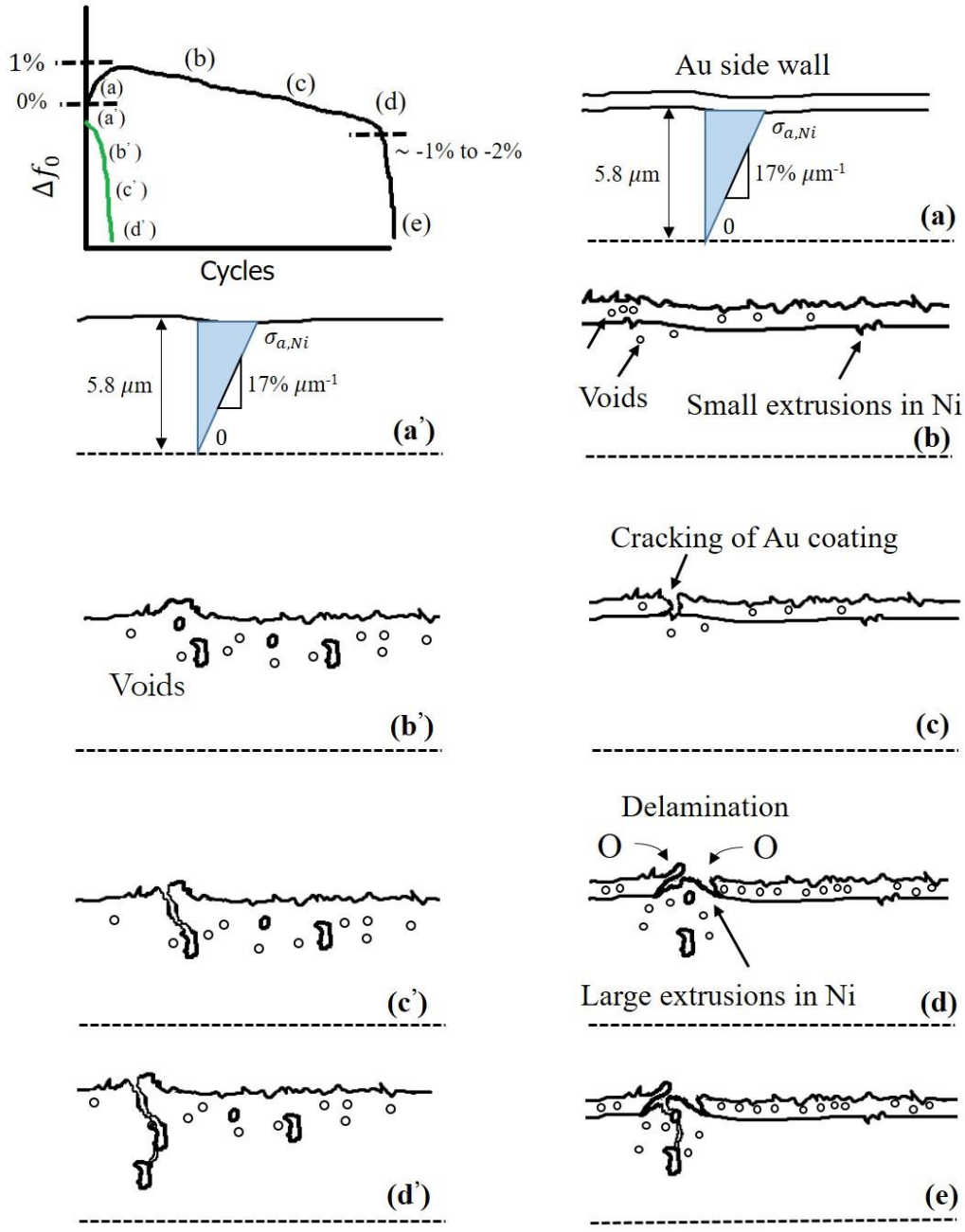

Figure 5.8 Schematics summarizing the overall fatigue behavior of the coated and uncoated microbeams in air, with the corresponding representative f_0 evolution curves [238].

5.7. Conclusions

The effect of an 850-nm-thick electroplated Au coating on the very high cycle bending fatigue behavior of electroplated Ni microbeams tested under resonance in air at high frequencies (~9 kHz) was investigated. The S-N curves show longer fatigue lives for the coated microbeams by at least a factor of 5 compared to the uncoated ones. This beneficial effect was demonstrated to be related to the delay in oxygen-assisted void formation, and therefore in void-assisted fatigue crack nucleation and growth in Ni. The improvement in fatigue life was limited by the fatigue degradation of the Au coating, which was also controlled by the formation of nanosized voids. Once a fatigue crack in the coating reached the interface, delamination occurred, leading to exposure of the underlying Ni to air and fast, "uncoated-like", fatigue degradation thereafter. This study highlighted that thin, noble metallic coatings can significantly improve the fatigue lives of metallic microbeams whose very high cycle fatigue behavior is sensitive to the environment and controlled by void formation.

CHAPTER 6

SIGNIFICANCE

Novel MEMS-based nanomechanical testing methods were presented in this dissertation aimed at providing a fundamental understanding of plasticity in ultrafine-grained FCC microspecimens. This understanding provides useful guidelines for increasing the safety and mechanical reliability of thin films and coatings, frequently used in MEMS technology.

The significant contributions are:

1. Advanced an existing novel MEMS-based *in-situ* nanomechanical testing technique proposed by Pierron and co-workers [169, 170, 175]. The capacitive sensing scheme was modified to get independent measurements of stresses and strains which expanded the envelope of the technique to perform transient mechanical tests such as repeated relaxation. Methods to control the noise-to-signal ratio were developed to maintain noise levels of ~0.1 fF required for measuring relaxation behavior during short transient mechanical tests. These advancements make this technique uniquely capable for performing *in-situ* repeated stress relaxation tests in the TEM and make microstructural observations simultaneously. As shown in Figure 1.17, this advancement of the MEMS-based nanomechanical technique is a very important step towards understanding the rate-controlling mechanisms in NC/UFG metals. The unit cubic micrometer sized volumes investigated with the microspecimens allow for direct comparisons with atomistic simulations by taking the advantage of the *quantitative* nature of the technique.

2. True activation volume calculation for nanograined metals were performed *in-situ* for the first time. 100-nm-thick Au microspecimens were tested in-situ and ex-situ and true activation volumes of the order of 2-10 b^3 were obtained. The environment (vacuum vs air) was seen to have no effect on these values. GB mediated dislocation plasticity was observed in the TEM in these Au microspecimens. This provides a very clear evidence of a correlation between GB mediated mechanisms and low activation volumes observed in NC/UFG metals. 200-nm-thick Al microspecimens were also tested in-situ and ex-situ. True activation volumes of the order of 5-20 b^3 were obtained but in these microspecimens grain growth was observed. These microspecimens were also tested with a PTP device in combination with PED mapping techniques to show grain growth. The addition of the PED is a very powerful tool when combined with either the MEMS or PTP techniques.

3. It was demonstrated that a thin Au coating can improve the fatigue life of electroplated Ni microbeams in the HCF / VHCF regime by at least a factor of 5. Previous work already highlighted the beneficial effect of coatings for HCF [195], including for thin film fatigue [202], mainly by preventing the development of PSB-induced surface morphology that results in fatigue crack initiation. In contrast, the novelty of this work is to demonstrate an effective coating strategy against fatigue degradation involving void-assisted fatigue crack nucleation and propagation, which characterizes the HCF/VHCF behavior of the uncoated Ni microbeams [208]. Specifically, the coating needs to prevent exposure of the underlying Ni to air, given that the fatigue lives of the uncoated

microbeams in vacuum conditions are three orders of magnitude longer than in air. Here, the combination of a noble metal with small grain size resulted in a coating that is more fatigue resistant than Ni, even though the underlying fatigue mechanism is similar.

CHAPTER 7

RECOMMENDATIONS FOR THE FUTURE WORK

The MEMS device has great capabilities but there are several areas of improvements. The capacitive sensor design can be modified to accommodate differential sensing in both capacitive sensors which will greatly reduce the parasitic noise and increase the simplicity of the circuitry. Conductive epoxy should be sought after for clamping and bridging the gaps between the thermal actuator, CS_1 and sample gaps for reducing charging in the TEM.

It is highly recommended the existing *in-situ* technique be combined with other techniques like the PED to provide more guided TEM observations to increase the likelihood of observing a mechanism and increasing the statistical understanding of the entire gauge length. Because of the modular nature of the technique this can be easily achieved.

Many researchers have noted the effect of texture on the mechanical properties of thin films [258-260], therefore it is recommended to compare films with different textures preferably by keeping the grain size distribution similar. Single crystal or bi-crystal nanowires can also provide great insight into the plastic mechanisms. To exploit the full potential of the technique *in-situ* experiments in an environmental TEM such as TITAN are highly recommended.

To further increase the understanding of the void controlled fatigue crack initiation and propagation low cycle fatigue tests should be studied in detail to prove that the void controlled mechanisms are indeed activated during HCF/VHCF. Also, Ni microbeams coated with different materials such as Cu or

Pd which are not noble metals should be tested to confirm the effects of the Au coatings observed in this study. Further TEM observations on lamellas of the microbeams should be made to study the dislocation structures. EBSD can be used to study the orientations of the grains during fatigue. It is highly recommended to combine all this experimental observations with crystal plasticity simulations to develop a model for predicting fatigue life in microscale structures.

REFERENCES

1. Nix, W.D. (1989). Mechanical-Properties of Thin-Films. *Metallurgical Transactions a-Physical Metallurgy and Materials Science*, *20, 2217-2245*.

2. Thompson, C.V. (2000). Structure Evolution During Processing of Polycrystalline Films. *Annual Review of Materials Science*, *30, 159-190*.

3. Prorok, B.C., Zhu, Y., Espinosa, H.D., Guo, Z., Bazant, Z.P., Zhao, Y., & Yakobson, B.I. (2004). Micro- and Nanomechanics. In H.S. Nalwa (Eds.), *Encyclopedia of Nanoscience and Nanotechnology*. (555-600).

4. Beck, P.A., Kremer, J.C., Demer, L.J., & Holzworth, M.L. (1948). Grain growth in high-purity aluminum and in an aluminum-magnesium alloy. *Trans. Am. Inst. Min. Metall. Eng.*, *175, 372-400*.

5. Mullins, W.W. (1958). The effect of thermal grooving on grain boundary motion. *Acta Metallurgica*, *6, 414-427*.

6. Espinosa, H.D., Prorok, B.C., & Peng, B. (2004). Plasticity size effects in free-standing submicron polycrystalline FCC films subjected to pure tension. *Journal of the Mechanics and Physics of Solids*, *52, 667-689*.

7. Espinosa, H.D., & Prorok, B.C. (2003). Size effects on the mechanical behavior of gold thin films. *Journal of Materials Science*, *38, 4125-4128*.

8. Haque, M.A., & Saif, M.T.A. (2004). Deformation mechanisms in free-standing nanoscale thin films: A quantitative in situ transmission electron microscope study. *Proceedings of the National Academy of Sciences of the United States of America*, *101, 6335-6340*.

9. Salvadori, M.C., Brown, I.G., Vaz, A.R., Melo, L.L., & Cattani, M. (2003). Measurement of the elastic modulus of nanostructured gold and platinum thin films. *Physical Review B*, *67*.

10. Jonnalagadda, K., Karanjgaokar, N., Chasiotis, I., Chee, J., & Peroulis, D. (2010). Strain rate sensitivity of nanocrystalline Au films at room temperature. *Acta Materialia*, *58, 4674-4684*.

11. Wang, L., & Prorok, B.C. (2008). Characterization of the strain rate dependent behavior of nanocrystalline gold films. *Journal of Materials Research*, *23, 55-65*.

12. Yilmaz, M., & Kysar, J.W. (2013). Monolithic integration of nanoscale tensile specimens and MEMS structures. *Nanotechnology*, *24, 165502*.

13. Chokshi, A.H., Rosen, A., Karch, J., & Gleiter, H. (1989). On the validity of the hall-petch relationship in nanocrystalline materials. *Scripta Metallurgica*, *23, 1679-1683*.

14. Nieman, G.W., Weertman, J.R., & Siegel, R.W. (1989). Microhardness of nanocrystalline palladium and copper produced by inert-gas condensation. *Scripta Metallurgica*, *23, 2013-2018*.

15. Hansen, N., & Ralph, B. (1982). The strain and grain size dependence of the flow stress of copper. *Acta Metallurgica*, *30, 411-417*.

16. Gertsman, V.Y., Hoffmann, M., Gleiter, H., & Birringer, R. (1994). The study of grain size dependence of yield stress of copper for a wide grain size range. *Acta Metallurgica et Materialia*, *42, 3539-3544*.

17. Youngdahl, C.J., Sanders, P.G., Eastman, J.A., & Weertman, J.R. (1997). Compressive yield strengths of nanocrystalline Cu and Pd. *Scripta Materialia*, *37, 809-813*.

18. Ma, E. (2003). Instabilities and ductility of nanocrystalline and ultrafine-grained metals. *Scripta Materialia*, *49, 663-668*.

19. Zhang, X., Wang, H., Scattergood, R.O., Narayan, J., Koch, C.C., Sergueeva, A.V., & Mukherjee, A.K. (2002). Studies of deformation mechanisms in ultra-fine-grained and nanostructured Zn. *Acta Materialia*, *50, 4823-4830*.

20. Suryanarayana, C. (1995). Nanocrystalline materials. *International Materials Reviews*, *40, 41-64*.

21. Suryanarayana, C., & Koch, C.C. (2000). Nanocrystalline materials – Current research and future directions. *Hyperfine Interactions*, *130, 5-44*.

22. Suryanarayana, C. (2005). Cover Picture: Recent Developments in Nanostructured Materials (Adv. Eng. Mater. 11/2005). *Advanced Engineering Materials*, *7, NA-NA*.

23. Wang, N., Wang, Z.R., Aust, K.T., & Erb, U. (1997). Room temperature creep behavior of nanocrystalline nickel produced by an electrodeposition technique. *Materials Science And Engineering A-Structural Materials Properties Microstructure And Processing*, *237, 150-158*.

24. Tanimoto, H., Sakai, S., & Mizubayashi, H. (1999). Mechanical property of high density nanocrystalline gold prepared by gas deposition method. *Nanostructured Materials*, *12, 751-756*.

25. Cai, B., Kong, Q.P., Lu, L., & Lu, K. (1999). Interface controlled diffusional creep of nanocrystalline pure copper. *Scripta Materialia*, *41, 755-759*.

26. Wei, Q., Cheng, S., Ramesh, K.T., & Ma, E. (2004). Effect of nanocrystalline and ultrafine grain sizes on the strain rate sensitivity and activation volume: fcc versus bcc metals. *Materials Science and Engineering a-Structural Materials Properties Microstructure and Processing*, *381, 71-79*.

27. Wang, Y.M., & Ma, E. (2003). Strain Hardening and Strain Rate Sensitivity of Ultrafine-Grained Metals. *Journal of Metastable and Nanocrystalline Materials*, *17, 55-64*.

28. Hall, E.O. (1951). The Deformation and Ageing of Mild Steel: III Discussion of Results. *Proceedings of the Physical Society. Section B*, *64, 747-753*.

29. Petch, N.J. (1953). The Cleavage Strength of Polycrystals. *Journal of the Iron and Steel Institute*, *174, 25-28*.

30. Valiev, R.Z., Islamgaliev, R.K., & Alexandrov, I.V. (2000). Bulk nanostructured materials from severe plastic deformation. *Progress in Materials Science*, *45, 103-189*.

31. Schiotz, J., Di Tolla, F.D., & Jacobsen, K.W. (1998). Softening of nanocrystalline metals at very small grain sizes. *Nature*, *391, 561-563*.

32. Conrad, H., & Narayan, J. (2000). On the grain size softening in nanocrystalline materials. *Scripta Materialia*, *42, 1025-1030*.

33. Koch, C.C. (2003). Optimization of strength and ductility in nanocrystalline and ultrafine grained metals. *Scripta Materialia*, *49, 657-662*.

34. Pande, C.S., Masumura, R.A., & Armstrong, R.W. (1993). Pile-up based hall-petch relation for nanoscale materials. *Nanostructured Materials*, *2, 323-331*.

35. Hughes, G.D., Smith, S.D., Pande, C.S., Johnson, H.R., & Armstrong, R.W. (1986). Hall-petch strengthening for the microhardness of twelve nanometer grain diameter electrodeposited nickel. *Scripta Metallurgica*, *20, 93-97*.

36. Meyers, M.A., Mishra, A., & Benson, D.J. (2006). Mechanical properties of nanocrystalline materials. *Progress In Materials Science*, *51, 427-556*.

37. Koch, C.C., Morris, D.G., Lu, K., & Inoue, A. (1999). Ductility of Nanostructured Materials. *MRS Bulletin*, *24, 54-58*.

38. Koch, C.C. (2003). Ductility in Nanostructured and Ultra Fine-Grained Materials: Recent Evidence for Optimism. *Journal of Metastable and Nanocrystalline Materials*, *18, 9-20*.

39. VanSwygenhoven, H., & Caro, A. (1997). Molecular dynamics computer simulation of nanophase Ni: Structure and mechanical properties. *Nanostructured Materials*, *9, 669-672*.

40. Carsley, J.E., Fisher, A., Milligan, W.W., & Aifantis, E.C. (1998). Mechanical behavior of a bulk nanostructured iron alloy. *Metallurgical and Materials Transactions A*, *29, 2261-2271*.

41. Jia, D., Wang, Y.M., Ramesh, K.T., Ma, E., Zhu, Y.T., & Valiev, R.Z. (2001). Deformation behavior and plastic instabilities of ultrafine-grained titanium. *Applied Physics Letters*, *79, 611-613*.

42. Youssef, K.M., Scattergood, R.O., Murty, K.L., Horton, J.A., & Koch, C.C. (2005). Ultrahigh strength and high ductility of bulk nanocrystalline copper. *Applied Physics Letters*, *87, 091904*.

43. Asgari, S., El-Danaf, E., Kalidindi, S.R., & Doherty, R.D. (1997). Strain hardening regimes and microstructural evolution during large strain compression of low stacking fault energy fcc alloys that form deformation twins. *Metallurgical and Materials Transactions A*, *28, 1781-1795*.

44. Wang, Y.M., Ma, E., & Chen, M.W. (2002). Enhanced tensile ductility and toughness in nanostructured Cu. *Applied Physics Letters*, *80, 2395-2397*.

45. Kocks, U.F. (1976). Laws for Work-Hardening and Low-Temperature Creep. *Journal of Engineering Materials and Technology*, *98, 76*.

46. Weertman, J.R., Farkas, D., Hemker, K., Kung, H., Mayo, M., Mitra, R., & Swygenhoven, H.V. (1999). Structure and Mechanical Behavior of Bulk Nanocrystalline Materials. *MRS Bulletin*, *24, 44-53*.

47. Valiev, R.Z., Kozlov, E.V., Ivanov, Y.F., Lian, J., Nazarov, A.A., & Baudelet, B. (1994). Deformation behaviour of ultra-fine-grained copper. *Acta Metallurgica et Materialia*, *42, 2467-2475*.

48. Gertsman, V.Y., Valiev, R.Z., Akhmadeev, N.A., & Mishin, O.V. (1996). Deformation Behaviour of Ultrafine-Grained Materials. *Materials Science Forum*, *225-227, 739-744*.

49. Wang, Y.M., & Ma, E. (2004). Strain hardening, strain rate sensitivity, and ductility of nanostructured metals. *Materials Science and Engineering: A*, *375-377, 46-52*.

50. Arzt, E. (1998). Size effects in materials due to microstructural and dimensional constraints: a comparative review. *Acta Materialia*, *46, 5611-5626*.

51. Conrad, H. (1965). In V.F. Zackey (Eds.), *High-Strength Materials.* Wiley.

52. Yu, Q., Legros, M., & Minor, A.M. (2015). In situ TEM nanomechanics. *Mrs Bulletin*, *40, 62-68*.

53. Kumar, K.S., Suresh, S., Chisholm, M.F., Horton, J.A., & Wang, P. (2003). Deformation of electrodeposited nanocrystalline nickel. *Acta Materialia*, *51, 387-405*.

54. Ke, M., Hackney, S.A., Milligan, W.W., & Aifantis, E.C. (1995). Observation and measurement of grain rotation and plastic strain in nanostructured metal thin films. *Nanostructured Materials*, *5, 689-697*.

55. Mompiou, F., Legros, M., Boe, A., Coulombier, M., Raskin, J.P., & Pardoen, T. (2013). Inter- and intragranular plasticity mechanisms in ultrafine-grained Al thin films: An in situ TEM study. *Acta Materialia*, *61, 205-216*.

56. Milligan, W.W., Hackney, S.A., Ke, M., & Aifantis, E.C. (1993). In situ studies of deformation and fracture in nanophase materials. *Nanostructured Materials*, *2, 267-276*.

57. Cheng, S., Spencer, J.A., & Milligan, W.W. (2003). Strength and tension/compression asymmetry in nanostructured and ultrafine-grain metals. *Acta Materialia*, *51, 4505-4518*.

58. Hirth, J.P., & Lothe, J. (1992). *Theory of Dislocations*. Malabar, FL: Krieger Publishing Company.

59. Morris, J.W. (2001). Dislocation-controlled Plasticity of Crystalline Materials: Overview. *Encyclopedia of Materials: Science and Technology*. (2245-2255).

60. Weissmuller, J., & Markmann, J. (2005). Deforming nanocrystalline metals: New insights, new puzzles. *Advanced Engineering Materials*, *7, 202-207*.

61. Murr, L.E. (2016). Dislocation Ledge Sources: Dispelling the Myth of Frank–Read Source Importance. *Metallurgical and Materials Transactions A*, *47, 5811-5826*.

62. Shan, Z., Stach, E.A., Wiezorek, J.M., Knapp, J.A., Follstaedt, D.M., & Mao, S.X. (2004). Grain boundary-mediated plasticity in nanocrystalline nickel. *Science*, *305, 654-7*.

63. Zhu, Y.T., Huang, J.Y., Gubicza, J., Ungar, T., Wang, Y.M., Ma, E., & Valiev, R.Z. (2003). Nanostructures in Ti processed by severe plastic deformation. *Journal of Materials Research*, *18, 1908-1917*.

64. Zhu, Y.T., Liao, X.Z., & Wu, X.L. (2012). Deformation twinning in nanocrystalline materials. *Progress in Materials Science*, *57, 1-62*.

65. Yamakov, V., Wolf, D., Phillpot, S.R., Mukherjee, A.K., & Gleiter, H. (2002). Dislocation processes in the deformation of nanocrystalline aluminium by molecular-dynamics simulation. *Nat Mater, 1, 45-8*.

66. Bobylev, S.V., Gutkin, M.Y., & Ovid'ko, I.A. (2004). Transformations of grain boundaries in deformed nanocrystalline materials. *Acta Materialia, 52, 3793-3805*.

67. Mukherjee, A.K. (2002). An examination of the constitutive equation for elevated temperature plasticity. *Materials Science and Engineering a-Structural Materials Properties Microstructure and Processing, 322, 1-22*.

68. Yamakov, V., Wolf, D., Phillpot, S.R., & Gleiter, H. (2002). Deformation twinning in nanocrystalline Al by molecular dynamics simulation. *Acta Materialia, 50, 5005-5020*.

69. Schiotz, J., Vegge, T., Di Tolla, F.D., & Jacobsen, K.W. (1999). Atomic-scale simulations of the mechanical deformation of nanocrystalline metals. *Physical Review B, 60, 11971-11983*.

70. Van Swygenhoven, H., Farkas, D., & Caro, A. (2000). Grain-boundary structures in polycrystalline metals at the nanoscale. *Physical Review B, 62, 831-838*.

71. Liao, X.Z., Zhou, F., Lavernia, E.J., Srinivasan, S.G., Baskes, M.I., He, D.W., & Zhu, Y.T. (2003). Deformation mechanism in nanocrystalline Al: Partial dislocation slip. *Applied Physics Letters, 83, 632-634*.

72. Liao, X.Z., Zhao, Y.H., Srinivasan, S.G., Zhu, Y.T., Valiev, R.Z., & Gunderov, D.V. (2004). Deformation twinning in nanocrystalline copper at room temperature and low strain rate. *Applied Physics Letters, 84, 592-594*.

73. Liao, X.Z., Srinivasan, S.G., Zhao, Y.H., Baskes, M.I., Zhu, Y.T., Zhou, F., Lavernia, E.J., & Xu, H.F. (2004). Formation mechanism of wide stacking faults in nanocrystalline Al. *Applied Physics Letters, 84, 3564-3566*.

74. Zhu, Y.T., Liao, X.Z., Srinivasan, S.G., & Lavernia, E.J. (2005). Nucleation of deformation twins in nanocrystalline face-centered-cubic metals processed by severe plastic deformation. *Journal of Applied Physics, 98*.

75. Wu, X.L., & Zhu, Y.T. (2006). Partial-dislocation-mediated processes in nanocrystalline Ni with nonequilibrium grain boundaries. *Applied Physics Letters, 89*.

76. Zhu, Y.T., Liao, X.Z., Srinivasan, S.G., Zhao, Y.H., Baskes, M.I., Zhou, F., & Lavernia, E.J. (2004). Nucleation and growth of deformation twins in nanocrystalline aluminum. *Applied Physics Letters, 85, 5049-5051*.

77. El-Danaf, E., Kalidindi, S.R., & Doherty, R.D. (1999). Influence of grain size and stacking-fault energy on deformation twinning in fcc metals. *Metallurgical and Materials Transactions a-Physical Metallurgy and Materials Science, 30, 1223-1233*.

78. Chen, M., Ma, E., Hemker, K.J., Sheng, H., Wang, Y., & Cheng, X. (2003). Deformation twinning in nanocrystalline aluminum. *Science, 300, 1275-7*.

79. Liao, X.Z., Zhou, F., Lavernia, E.J., He, D.W., & Zhu, Y.T. (2003). Deformation twins in nanocrystalline Al. *Applied Physics Letters, 83, 5062-5064*.

80. Wu, X.L., & Zhu, Y.T. (2008). Inverse grain-size effect on twinning in nanocrystalline Ni. *Phys Rev Lett, 101, 025503*.

81. Ookawa, A. (1957). On the Mechanism of Deformation Twin in fcc Crystal. *Journal of the Physical Society of Japan, 12, 825-825*.

82. Venables, J.A. (1961). Deformation twinning in face-centred cubic metals. *Philosophical Magazine, 6, 379-396*.

83. Niewczas, M., & Saada, G. (2002). Twinning nucleation in Cu-8 at. % Al single crystals. *Philosophical Magazine A, 82, 167-191*.

84. Mahajan, S., & Chin, G.Y. (1973). Twin-slip, twin-twin and slip-twin interactions in Co-8 wt.% Fe alloy single crystals. *Acta Metallurgica, 21, 173-179*.

85. Mahajan, S., Green, M.L., & Brasen, D. (1977). A model for the FCC→HCP transformation, its applications, and experimental evidence. *Metallurgical Transactions A, 8, 283-293*.

86. Wang, Y.B., Sui, M.L., & Ma, E. (2007). In situ observation of twin boundary migration in copper with nanoscale twins during tensile deformation. *Philosophical Magazine Letters, 87, 935-942*.

87. Zhu, Y.T., Narayan, J., Hirth, J.P., Mahajan, S., Wu, X.L., & Liao, X.Z. (2009). Formation of single and multiple deformation twins in nanocrystalline fcc metals. *Acta Materialia, 57, 3763-3770*.

88. Narayan, J., & Zhu, Y.T. (2008). Self-thickening, cross-slip deformation twinning model. *Applied Physics Letters, 92*.

89. Dregia, S.A., & Hirth, J.P. (1991). A Rebound Mechanism for Lomer Dislocation Formation in Strained Layer Structures. *Journal of Applied Physics, 69, 2169-2175*.

90. Zhu, Y.T., Wu, X.L., Liao, X.Z., Narayan, J., Mathaudhu, S.N., & Kecskes, L.J. (2009). Twinning partial multiplication at grain boundary in nanocrystalline fcc metals. *Applied Physics Letters*, *95*.

91. Langdon, T.G. (2006). Grain boundary sliding revisited: Developments in sliding over four decades. *Journal of Materials Science, 41, 597-609*.

92. Lifshitz, I.M. (1963). On the Theory of Diffusion-Viscous Flow of Polycrystalline Bodies. *Soviet Physics Jetp-Ussr*, *17, 909-920*.

93. Kumar, P., Kawasaki, M., & Langdon, T.G. (2015). Review: Overcoming the paradox of strength and ductility in ultrafine-grained materials at low temperatures. *Journal of Materials Science*, *51, 7-18*.

94. Ivanov, K.V., & Naydenkin, E.V. (2012). Grain boundary sliding in ultrafine grained aluminum under tension at room temperature. *Scripta Materialia*, *66, 511-514*.

95. Valiev, R.Z., Murashkin, M.Y., Kilmametov, A., Straumal, B., Chinh, N.Q., & Langdon, T.G. (2010). Unusual super-ductility at room temperature in an ultrafine-grained aluminum alloy. *Journal of Materials Science*, *45, 4718-4724*.

96. Schiotz, J., & Jacobsen, K.W. (2003). A maximum in the strength of nanocrystalline copper. *Science*, *301, 1357-1359*.

97. Van Swygenhoven, H., & Derlet, P.A. (2001). Grain-boundary sliding in nanocrystalline fcc metals. *Physical Review B*, *64*.

98. Suzuki, A., & Mishin, Y. (2005). Atomic mechanisms of grain boundary diffusion: Low versus high temperatures. *Journal of Materials Science, 40, 3155-3161*.

99. Ovid'ko, I.A., Valiev, R.Z., & Zhu, Y.T. (2018). Review on superior strength and enhanced ductility of metallic nanomaterials. *Progress in Materials Science, 94, 462-540*.

100. Ovid'ko, I.A. (2002). Materials science. Deformation of nanostructures. *Science, 295, 2386*.

101. Izadi, E., Darbal, A., Sarkar, R., & Rajagopalan, J. (2017). Grain rotations in ultrafine-grained aluminum films studied using in situ TEM straining with automated crystal orientation mapping. *Materials & Design*, *113, 186-194*.

102. Wang, L., Teng, J., Liu, P., Hirata, A., Ma, E., Zhang, Z., Chen, M., & Han, X. (2014). Grain rotation mediated by grain boundary dislocations in nanocrystalline platinum. *Nat Commun*, *5, 4402*.

103. Murayama, M., Howe, J.M., Hidaka, H., & Takaki, S. (2002). Atomic-level observation of disclination dipoles in mechanically milled, nanocrystalline Fe. *Science, 295, 2433-5*.

104. Gutkin, M.Y., & Ovid'ko, I.A. (2005). Grain boundary migration as rotational deformation mode in nanocrystalline materials. *Applied Physics Letters, 87*.

105. Jin, M., Minor, A.M., Stach, E.A., & Morris, J.W. (2004). Direct observation of deformation-induced grain growth during the nanoindentation of ultrafine-grained Al at room temperature. *Acta Materialia, 52, 5381-5387*.

106. Legros, M., Gianola, D.S., & Hemker, K.J. (2008). In situ TEM observations of fast grain-boundary motion in stressed nanocrystalline aluminum films. *Acta Materialia, 56, 3380-3393*.

107. Mompiou, F., Caillard, D., & Legros, M. (2009). Grain boundary shear–migration coupling—I. In situ TEM straining experiments in Al polycrystals. *Acta Materialia, 57, 2198-2209*.

108. Gianola, D.S., Van Petegem, S., Legros, M., Brandstetter, S., Van Swygenhoven, H., & Hemker, K.J. (2006). Stress-assisted discontinuous grain growth and its effect on the deformation behavior of nanocrystalline aluminum thin films. *Acta Materialia, 54, 2253-2263*.

109. Winning, M., Gottstein, G., & Shvindlerman, L.S. (2001). Stress induced grain boundary motion. *Acta Materialia, 49, 211-219*.

110. Molodov, D.A., Ivanov, V.A., & Gottstein, G. (2007). Low angle tilt boundary migration coupled to shear deformation. *Acta Materialia, 55, 1843-1848*.

111. Rupert, T.J., Gianola, D.S., Gan, Y., & Hemker, K.J. (2009). Experimental Observations of Stress-Driven Grain Boundary Migration. *Science, 326, 1686-1690*.

112. Sansoz, F., & Dupont, V. (2006). Grain growth behavior at absolute zero during nanocrystalline metal indentation. *Applied Physics Letters, 89*.

113. Farkas, D., Froseth, A., & Van Swygenhoven, H. (2006). Grain boundary migration during room temperature deformation of nanocrystalline Ni. *Scripta Materialia, 55, 695-698*.

114. Soer, W.A., Hosson, J.T.M.D., Minor, A.M., Morris, J.W., & Stach, E.A. (2004). Effects of solute Mg on grain boundary and dislocation dynamics during nanoindentation of Al–Mg thin films. *Acta Materialia, 52, 5783-5790*.

115. Ovid'ko, I.A. (2005). Deformation and diffusion modes in nanocrystalline materials. *International Materials Reviews*, *50, 65-82*.

116. Markmann, J., Bunzel, P., Rosner, H., Liu, K.W., Padmanabhan, K.A., Birringer, R., Gleiter, H., & Weissmuller, J. (2003). Microstructure evolution during rolling of inert-gas condensed palladium. *Scripta Materialia*, *49, 637-644*.

117. Kottada, R.S., & Chokshi, A.H. (2005). Low temperature compressive creep in electrodeposited nanocrystalline nickel. *Scripta Materialia*, *53, 887-892*.

118. Bobylev, S.V., Morozov, N.F., & Ovid'ko, I.A. (2010). Cooperative grain boundary sliding and migration process in nanocrystalline solids. *Phys Rev Lett*, *105, 055504*.

119. Sergueeva, A.V., Mara, N.A., Krasilnikov, N.A., Valiev, R.Z., & Mukherjee, A.K. (2006). Cooperative grain boundary sliding in nanocrystalline materials. *Philosophical Magazine*, *86, 5797-5804*.

120. Mara, N.A., Sergueeva, A.V., Mara, T.D., McFadden, S.X., & Mukherjee, A.K. (2007). Superplasticity and cooperative grain boundary sliding in nanocrystalline Ni3Al. *Materials Science and Engineering a-Structural Materials Properties Microstructure and Processing*, *463, 238-244*.

121. Wang, L.H., Xin, T.J., Kong, D.L., Shu, X.Y., Chen, Y.H., Zhou, H., Teng, J., Zhang, Z., Zou, J., & Han, X.D. (2017). In situ observation of stress induced grain boundary migration in nanocrystalline gold. *Scripta Materialia*, *134, 95-99*.

122. Caillard, D. (2003). *Thermally activated mechanisms in crystal plasticity*. Pergamon: Amsterdam ;.

123. Argon, A.S. (2008). *Strengthening mechanisms in crystal plasticity*. USA: Oxford University Press.

124. Wang, Y.M., Hamza, A.V., & Ma, E. (2006). Temperature-dependent strain rate sensitivity and activation volume of nanocrystalline Ni. *Acta Materialia*, *54, 2715-2726*.

125. Mohanty, G., Wehrs, J., Boyce, B.L., Taylor, A., Hasegawa, M., Philippe, L., & Michler, J. (2016). Room temperature stress relaxation in nanocrystalline Ni measured by micropillar compression and miniature tension. *Journal of Materials Research*, *31, 1085-1095*.

126. Spätig, P., Bonneville, J., & Martin, J.L. (1993). A new method for activation volume measurements: application to Ni3(Al,Hf). *Materials Science and Engineering: A*, *167, 73-79*.

127. Martin, J.L., Lo Piccolo, B., Kruml, T., & Bonneville, J. (2002). Characterization of thermally activated dislocation mechanisms using transient tests. *Materials Science and Engineering: A, 322, 118-125*.

128. Zhu, T., & Li, J. (2010). Ultra-strength materials. *Progress in Materials Science, 55, 710-757*.

129. Hull, D., & Bacon, D.J. (2001). *Introduction to Dislocations* Butterworth–Heinemann.

130. Bonneville, J., Escaig, B., & Martin, J.L. (1988). A study of cross-slip activation parameters in pure copper. *Acta Metallurgica, 36, 1989-2002*.

131. Escaig, B. (1968). L'activation thermique des déviations sous faibles contraintes dans les structures h.c. et c.c. Par. *Physica Status Solidi (b), 28, 463-474*.

132. Karanjgaokar, N.J., Oh, C.S., Lambros, J., & Chasiotis, I. (2012). Inelastic deformation of nanocrystalline Au thin films as a function of temperature and strain rate. *Acta Materialia, 60, 5352-5361*.

133. Gianola, D.S., Warner, D.H., Molinari, J.F., & Hemker, K.J. (2006). Increased strain rate sensitivity due to stress-coupled grain growth in nanocrystalline Al. *Scripta Materialia, 55, 649-652*.

134. Wang, Y.M., Hamza, A.V., & Ma, E. (2005). Activation volume and density of mobile dislocations in plastically deforming nanocrystalline Ni. *Applied Physics Letters, 86*.

135. Conrad, H. (2003). Grain size dependence of the plastic deformation kinetics in Cu. *Materials Science and Engineering: A, 341, 216-228*.

136. Duhamel, C., Brechet, Y., & Champion, Y. (2010). Activation volume and deviation from Cottrell-Stokes law at small grain size. *International Journal of Plasticity, 26, 747-757*.

137. Zhu, T., Li, J., & Yip, S. (2013). Atomistic Reaction Pathway Sampling: The Nudged Elastic Band Method and Nanomechanics Applications. In H.D. Espinosa, & G. Bao (Eds.), *Nano and Cell Mechanics: Fundamentals and Frontiers.* (313-338). John Wiley & Sons, Ltd.

138. Dehm, G., Jaya, B.N., Raghavan, R., & Kirchlechner, C. (2018). Overview on micro- and nanomechanical testing: New insights in interface plasticity and fracture at small length scales. *Acta Materialia, 142, 248-282*.

139. Vinci, R.P., & Vlassak, J.J. (1996). Mechanical behavior of thin films. *Annual Review of Materials Science, 26, 431-462*.

140. Nix, W.D. (1997). Elastic and plastic properties of thin films on substrates: nanoindentation techniques. *Materials Science and Engineering a-Structural Materials Properties Microstructure and Processing*, *234, 37-44*.

141. Oliver, W.C., & Pharr, G.M. (1992). An improved technique for determining hardness and elastic modulus using load and displacement sensing indentation experiments. *Journal of Materials Research*, *7, 1564-1583*.

142. Warren, O.L., Shan, Z., Asif, S.A.S., Stach, E.A., Morris, J.W., & Minor, A.M. (2007). In situ nanoindentation in the TEM. *Materials Today*, *10, 59-60*.

143. Uchic, M.D., Dimiduk, D.M., Florando, J.N., & Nix, W.D. (2004). Sample dimensions influence strength and crystal plasticity. *Science*, *305, 986-9*.

144. Ziebart, V., Paul, O., Munch, U., Schwizer, J., & Baltes, H. (1998). Mechanical properties of thin films from the load deflection of long clamped plates. *Journal of Microelectromechanical Systems*, *7, 320-328*.

145. Nicola, L., Xiang, Y., Vlassak, J.J., Van der Giessen, E., & Needleman, A. (2006). Plastic deformation of freestanding thin films: Experiments and modeling. *Journal of the Mechanics and Physics of Solids*, *54, 2089-2110*.

146. Haque, M.A., & Saif, M.T.A. (2003). A review of MEMS-based microscale and nanoscale tensile and bending testing. *Experimental Mechanics*, *43, 248-255*.

147. Zhu, Y., & Chang, T.-H. (2015). A review of microelectromechanical systems for nanoscale mechanical characterization. *Journal of Micromechanics and Microengineering*, *25, 093001*.

148. Rajagopalan, J. (2018). Microelectromechanical Systems (MEMS)-Based Testing of Materials. In C. Hsueh (Eds.), *Handbook of Mechanics of Materials*. (1-26). Singapore: Springer.

149. Kang, W., Rajagopalan, J., & A. Saif, M.T. (2010). In Situ Uniaxial Mechanical Testing of Small Scale Materials—A Review. *Nanoscience and Nanotechnology Letters*, *2, 282-287*.

150. Lu, Y., Ganesan, Y., & Lou, J. (2010). A Multi-step Method for In Situ Mechanical Characterization of 1-D Nanostructures Using a Novel Micromechanical Device. *Experimental Mechanics*, *50, 47-54*.

151. Guo, H., Chen, K., Oh, Y., Wang, K., Dejoie, C., Asif, S.A.S., Warren, O.L., Shan, Z.W., Wu, J., & Minor, A.M. (2011). Mechanics and Dynamics of the Strain-Induced M1-M2 Structural Phase Transition in Individual VO2 Nanowires. *Nano Letters*, *11, 3207-3213*.

152. Begley, M.R., & Hutchinson, J.W. (1998). The mechanics of size-dependent indentation. *Journal of the Mechanics and Physics of Solids, 46, 2049-2068*.

153. Nix, W.D., & Gao, H.J. (1998). Indentation size effects in crystalline materials: A law for strain gradient plasticity. *Journal of the Mechanics and Physics of Solids, 46, 411-425*.

154. Saha, R., & Nix, W.D. (2002). Effects of the substrate on the determination of thin film mechanical properties by nanoindentation. *Acta Materialia, 50, 23-38*.

155. Chen, X., & Vlassak, J.J. (2001). Numerical study on the measurement of thin film mechanical properties by means of nanoindentation. *Journal of Materials Research, 16, 2974-2982*.

156. Volinsky, A.A., Moody, N.R., & Gerberich, W.W. (2002). Interfacial toughness measurements for thin films on substrates. *Acta Materialia, 50, 441-466*.

157. Van Swygenhoven, H., Schmitt, B., Derlet, P.M., Van Petegem, S., Cervellino, A., Budrovic, Z., Brandstetter, S., Bollhalder, A., & Schild, M. (2006). Following peak profiles during elastic and plastic deformation: A synchrotron-based technique. *Review of Scientific Instruments, 77, 013902*.

158. Chisholm, C., Bei, H., Lowry, M.B., Oh, J., Syed Asif, S.A., Warren, O.L., Shan, Z.W., George, E.P., & Minor, A.M. (2012). Dislocation starvation and exhaustion hardening in Mo alloy nanofibers. *Acta Materialia, 60, 2258-2264*.

159. Lu, Y., Peng, C., Ganesan, Y., Huang, J.Y., & Lou, J. (2011). Quantitative in situ TEM tensile testing of an individual nickel nanowire. *Nanotechnology, 22*.

160. Ganesan, Y., Lu, Y., Peng, C., Lu, H., Ballarini, R., & Lou, J. (2010). Development and Application of a Novel Microfabricated Device for the In Situ Tensile Testing of 1-D Nanomaterials. *Journal of Microelectromechanical Systems, 19, 675-682*.

161. Haque, M.A., Espinosa, H.D., & Lee, H.J. (2010). MEMS for In Situ Testing-Handling, Actuation, Loading, and Displacement Measurements. *MRS Bulletin, 35, 375-381*.

162. Espinosa, H.D., Bernal, R.A., & Filleter, T. (2012). In situ TEM electromechanical testing of nanowires and nanotubes. *Small, 8, 3233-52*.

163. Ramachandramoorthy, R., Bernal, R., & Espinosa, H.D. (2015). Pushing the envelope of in situ transmission electron microscopy. *ACS Nano, 9, 4675-85*.

164. Legros, M. (2014). In situ mechanical TEM: Seeing and measuring under stress with electrons. *Comptes Rendus Physique, 15, 224-240*.

165. Haque, M.A., & Saif, M.T.A. (2001). Microscale materials testing using MEMS actuators. *Journal of Microelectromechanical Systems, 10, 146-152*.

166. Zhu, Y., Ke, C., & Espinosa, H.D. (2007). Experimental Techniques for the Mechanical Characterization of One-Dimensional Nanostructures. *Experimental Mechanics, 47, 7-24*.

167. Zhu, Y., & Espinosa, H.D. (2005). An electromechanical material testing system for in situ electron microscopy and applications. *Proc Natl Acad Sci U S A, 102, 14503-8*.

168. Zhu, Y., Moldovan, N., & Espinosa, H.D. (2005). A microelectromechanical load sensor for in situ electron and x-ray microscopy tensile testing of nanostructures. *Applied Physics Letters, 86, 013506*.

169. Hosseinian, E., & Pierron, O.N. (2013). Quantitative in situ TEM tensile fatigue testing on nanocrystalline metallic ultrathin films. *Nanoscale, 5, 12532*.

170. Pant, B., Allen, B.L., Zhu, T., Gall, K., & Pierron, O.N. (2011). A versatile microelectromechanical system for nanomechanical testing. *Applied Physics Letters, 98, 053506*.

171. Haque, M.A., & Saif, M.T.A. (2002). In-situ tensile testing of nano-scale specimens in SEM and TEM. *Experimental Mechanics, 42, 123-128*.

172. Haque, M.A., & Saif, M.T.A. (2002). Application of MEMS force sensors for in situ mechanical characterization of nano-scale thin films in SEM and TEM. *Sensors and Actuators A: Physical, 97-98, 239-245*.

173. Espinosa, H.D., Yong, Z., & Moldovan, N. (2007). Design and Operation of a MEMS-Based Material Testing System for Nanomechanical Characterization. *Journal of Microelectromechanical Systems, 16, 1219-1231*.

174. Gravier, S., Coulombier, M., Safi, A., Andre, N., Boe, A., Raskin, J.P., & Pardoen, T. (2009). New On-Chip Nanomechanical Testing Laboratory - Applications to Aluminum and Polysilicon Thin Films. *Journal of Microelectromechanical Systems, 18, 555-569*.

175. Pant, B., Choi, S., Baumert, E., Allen, B., Graham, S., Gall, K., & Pierron, O. (2012). MEMS-Based Nanomechanics: Influence of MEMS Design on Test Temperature. *Experimental Mechanics*, *52, 607-617*.

176. Samaee, V., Gatti, R., Devincre, B., Pardoen, T., Schryvers, D., & Idrissi, H. (2018). Dislocation driven nanosample plasticity: new insights from quantitative in-situ TEM tensile testing. *Sci Rep*, *8, 12012*.

177. Hosseinian, E., Legros, M., & Pierron, O.N. (2016). Quantifying and observing viscoplasticity at the nanoscale: highly localized deformation mechanisms in ultrathin nanocrystalline gold films. *Nanoscale*, *8, 9234-44*.

178. Basinski, Z.S., Pascual, R., & Basinski, S.J. (1983). Low amplitude fatigue of copper single crystals—I. The role of the surface in fatigue failure. *Acta Metallurgica*, *31, 591-602*.

179. Thompson, N., Wadsworth, N., & Louat, N. (1956). Xi. The origin of fatigue fracture in copper. *Philosophical Magazine*, *1, 113-126*.

180. Mughrabi, H. (2015). Microstructural mechanisms of cyclic deformation, fatigue crack initiation and early crack growth. *Philos Trans A Math Phys Eng Sci*, *373*.

181. Repetto, E. (1997). A micromechanical model of cyclic deformation and fatigue-crack nucleation in f.c.c. single crystals. *Acta Materialia*, *45, 2577-2595*.

182. Forsyth, P.J.E. (1953). Exudation of Material from Slip Bands at the Surface of Fatigued Crystals of an Aluminium–Copper Alloy. *Nature*, *171, 172-173*.

183. Bao-Tong, M., & Laird, C. (1989). Overview of fatigue behavior in copper single crystals—I. Surface morphology and stage I crack initiation sites for tests at constant strain amplitude. *Acta Metallurgica*, *37, 325-336*.

184. Polák, J., & Liškutían, P. (1990). NUCLEATION AND SHORT CRACK GROWTH IN FATIGUED POLYCRYSTALLINE COPPER. *Fatigue & Fracture of Engineering Materials & Structures*, *13, 119-133*.

185. Hosseinian, E. (2016). *Failure properties of nanocrystalline FCC metallic ultrathin films* (Doctoral). Georgia Institue of Technology, Atlanta, GA.

186. Padture, N.P., Gell, M., & Jordan, E.H. (2002). Materials science - Thermal barrier coatings for gas-turbine engine applications. *Science*, *296, 280-284*.

187. Goward, G.W. (1998). Progress in coatings for gas turbine airfoils. *Surface & Coatings Technology*, *108, 73-79*.

188. Sadananda, K., & Holtz, R.L. (2000). *Review of fatigue of coatings/substrates*. Dordrecht: Springer.

189. McGrann, R.T.R., Greving, D.J., Shadley, J.R., Rybicki, E.F., Kruecke, T.L., & Bodger, B.E. (1998). The effect of coating residual stress on the fatigue life of thermal spray-coated steel and aluminum. *Surface & Coatings Technology, 108, 59-64*.

190. Hockauf, K., Kohler, L., Handel, M., Halle, T., Nickel, D., Alisch, G., & Lampke, T. (2011). The effect of anodic oxide coating on the fatigue behaviour of AA6082 with an ultrafine-grained microstructure. *Materialwissenschaft Und Werkstofftechnik, 42, 624-631*.

191. Rateick, R.G., Binkowski, T.C., & Boray, B.C. (1996). Effect of hard anodize thickness on the fatigue of AA6061 and C355 aluminium. *Journal of Materials Science Letters, 15, 1321-1323*.

192. de Camargo, J.A.M., Cornelis, H.J., Cioffi, V., & Costa, M.Y.P. (2007). Coating residual stress effects on fatigue performance of 7050-T7451 aluminum alloy. *Surface & Coatings Technology, 201, 9448-9455*.

193. Man, J., Obrtlik, K., & Polak, J. (2009). Extrusions and intrusions in fatigued metals. Part 1. State of the art and history. *Philosophical Magazine, 89, 1295-1336*.

194. Grummon, D.S., Morrison, D.J., Jones, J.W., & Was, G.S. (1989). Ion implantation and fatigue crack initiation: Interaction of persistent slip bands with modified surface layers. *Materials Science and Engineering: A, 115, 331-336*.

195. Stoudt, M.R., Ricker, R.E., & Cammarata, R.C. (2001). The influence of a multilayered metallic coating on fatigue crack nucleation. *International Journal of Fatigue, 23, 215-223*.

196. Costa, M.Y.P., Venditti, M.L.R., Voorwald, H.J.C., Cioffi, M.O.H., & Cruz, T.G. (2009). Effect of WC-10%Co-4%Cr coating on the Ti-6Al-4V alloy fatigue strength. *Materials Science and Engineering a-Structural Materials Properties Microstructure and Processing, 507, 29-36*.

197. Saruki, K., Hotta, S., Fujita, H., & Arai, T. (1989). FATIGUE-STRENGTH OF STEELS WITH THIN HARD COATING. *Thin Solid Films, 181, 383-395*.

198. Baragetti, S. (2007). Fatigue resistance of steel and titanium PVD coated spur gears. *International Journal of Fatigue, 29, 1893-1903*.

199. Baragetti, S., La Vecchia, G.M., & Terranova, A. (2005). Variables affecting the fatigue resistance of PVD-coated components. *International Journal of Fatigue, 27, 1541-1550*.

200. Baumert, E.K., Theillet, P.O., & Pierron, O.N. (2011). Fatigue-resistant silicon films coated with nanoscale alumina layers. *Scripta Materialia, 65, 596-599*.

201. Straub, T., Baumert, E.K., Eberl, C., & Pierron, O.N. (2012). A method for probing the effects of conformal nanoscale coatings on fatigue crack initiation in electroplated Ni films. *Thin Solid Films, 526, 176-182*.

202. Wang, D., Gruber, P.A., Volkert, C.A., & Kraft, O. (2014). Influences of Ta passivation layers on the fatigue behavior of thin Cu films. *Materials Science and Engineering: A, 610, 33-38*.

203. Budnitzki, M., & Pierron, O.N. (2009). The influence of nanoscale atomic-layer-deposited alumina coating on the fatigue behavior of polycrystalline silicon thin films. *Applied Physics Letters, 94, 141906*.

204. Zhang, G.P., Volkert, C.A., Schwaiger, R., Wellner, P., Arzt, E., & Kraft, O. (2006). Length-scale-controlled fatigue mechanisms in thin copper films. *Acta Materialia, 54, 3127-3139*.

205. Sadeghi-Tohidi, F., & Pierron, O.N. (2016). Towards prediction of the fatigue life of Ni microbeams under extreme stress gradients. *Extreme Mechanics Letters, 9, 97-107*.

206. Sadeghi-Tohidi, F., & Pierron, O.N. (2016). Extreme stress gradient effects on the fatigue behavior of Ni notched microbeams. *Acta Materialia, 106, 388-400*.

207. Baumert, E.K., & Pierron, O.N. (2013). Fatigue Degradation Properties of LIGA Ni Films Using Kilohertz Microresonators. *Microelectromechanical Systems, Journal of, 22, 16-25*.

208. Barrios, A., Gupta, S., Castelluccio, G.M., & Pierron, O.N. (2018). Quantitative in Situ SEM High Cycle Fatigue: The Critical Role of Oxygen on Nanoscale-Void-Controlled Nucleation and Propagation of Small Cracks in Ni Microbeams. *Nano Lett, 18, 2595-2602*.

209. Zinkle, S.J., & Lee, E.H. (1990). Effect of Oxygen on Vacancy Cluster Morphology in Metals. *Metallurgical Transactions a-Physical Metallurgy and Materials Science, 21, 1037-1051*.

210. Zinkle, S.J., Wolfer, W.G., Kulcinski, G.L., & Seitzman, L.E. (1987). Stability of Vacancy Clusters in Metals .2. Effect of Oxygen and Helium on Void Formation in Metals. *Philosophical Magazine a-Physics of Condensed Matter Structure Defects and Mechanical Properties, 55, 127-140*.

211. Seitzman, L.E., Dodd, R.A., & Kulcinski, G.L. (1990). The Effect of Oxygen on Void Stability in Ion-Irradiated Steel. *Metallurgical Transactions a-Physical Metallurgy and Materials Science*, *21, 1839-1846*.

212. Seitzman, L.E., Wang, L.M., Kulcinski, G.L., & Dodd, R.A. (1986). The effect of oxygen on void stability in nickel and austenitic steel. *Journal of Nuclear Materials*, *141-143, 738-742*.

213. Cawthorne, C., & Fulton, E.J. (1967). Voids in Irradiated Stainless Steel. *Nature*, *216, 576*.

214. Kunz, L., Lukas, P., & Navratilova, L. (2014). Strain localization and fatigue crack initiation in ultrafine-grained copper in high- and giga-cycle region. *International Journal of Fatigue*, *58, 202-208*.

215. Lukas, P., Kunz, L., Navratilova, L., & Bokuvka, O. (2011). Fatigue damage of ultrafine-grain copper in very-high cycle fatigue region. *Materials Science And Engineering A-Structural Materials Properties Microstructure And Processing*, *528, 7036-7040*.

216. Sadeghi-Tohidi, F., & Pierron, O.N. (2015). Extreme stress gradient effects on microstructural fatigue crack propagation rates in Ni microbeams. *Applied Physics Letters*, *106, 201904*.

217. Asaro, R.J., & Suresh, S. (2005). Mechanistic models for the activation volume and rate sensitivity in metals with nanocrystalline grains and nano-scale twins. *Acta Materialia*, *53, 3369-3382*.

218. Yamakov, V.I. (2011). The mechanical behavior of nanostructured metals based on molecular dynamics computer simulations. In S.H. Whang (Eds.), *Woodhead Publishing Series in Metals and Surface Engineering: Nanostructured Metals and Alloys.* (459-480). Woodhead Publishing.

219. Van Swygenhoven, H. (2008). Footprints of plastic deformation in nanocrystalline metals. *Materials Science and Engineering: A*, *483-484, 33-39*.

220. Pantano, M.F., Bernal, R.A., Pagnotta, L., & Espinosa, H.D. (2014). Multiphysics design and implementation of a microsystem for displacement-controlled tensile testing of nanomaterials. *Meccanica*, *50, 549-560*.

221. MicroSensors Inc. (2001). *MS3110 Universal Capacitive Readout™ IC*. Costa Mesa, CA.

222. Gupta, S., & Pierron, O.N. (2017). A MEMS Tensile Testing Technique for Measuring True Activation Volume and Effective Stress in Nanocrystalline Ultrathin Microbeams. *Journal of Microelectromechanical Systems*, *26, 1082-1092*.

223. Gupta, S., & Pierron, O.N. (2016). MEMS based nanomechanical testing method with independent electronic sensing of stress and strain. *Extreme Mechanics Letters*, *8, 167-176*.

224. Kang, W., & Saif, M.T.A. (2010). A Novel Method for In Situ Uniaxial Tests at the Micro/Nano Scale-Part I: Theory. *Journal of Microelectromechanical Systems*, *19, 1309-1321*.

225. Coulombier, M., Guisbiers, G., Colla, M.S., Vayrette, R., Raskin, J.P., & Pardoen, T. (2012). On-chip stress relaxation testing method for freestanding thin film materials. *Review of Scientific Instruments*, *83, 9*.

226. Gianola, D.S., Sedlmayr, A., Monig, R., Volkert, C.A., Major, R.C., Cyrankowski, E., Asif, S.A.S., Warren, O.L., & Kraft, O. (2011). In situ nanomechanical testing in focused ion beam and scanning electron microscopes. *Review of Scientific Instruments*, *82, 12*.

227. Murphy, K.F., Chen, L.Y., & Gianola, D.S. (2013). Effect of organometallic clamp properties on the apparent diversity of tensile response of nanowires. *Nanotechnology*, *24, 235704*.

228. Samayoa, M.J., Haque, M.A., & Cohen, P.H. (2008). Focused ion beam irradiation effects on nanoscale freestanding thin films. *Journal of Micromechanics and Microengineering*, *18, 7*.

229. Ward, B.W., Notte, J.A., & Economou, N.P. (2006). Helium ion microscope: A new tool for nanoscale microscopy and metrology. *Journal of Vacuum Science & Technology B*, *24, 2871-2874*.

230. Gianola, D.S., & Eberl, C. (2009). Micro- and nanoscale tensile testing of materials. *JOM*, *61, 24-35*.

231. Minor, A.M., Asif, S.A., Shan, Z., Stach, E.A., Cyrankowski, E., Wyrobek, T.J., & Warren, O.L. (2006). A new view of the onset of plasticity during the nanoindentation of aluminium. *Nat Mater*, *5, 697-702*.

232. Shan, Z.W., Mishra, R.K., Syed Asif, S.A., Warren, O.L., & Minor, A.M. (2008). Mechanical annealing and source-limited deformation in submicrometre-diameter Ni crystals. *Nat Mater*, *7, 115-9*.

233. Shan, Z.W., Adesso, G., Cabot, A., Sherburne, M.P., Asif, S.A., Warren, O.L., Chrzan, D.C., Minor, A.M., & Alivisatos, A.P. (2008). Ultrahigh stress and strain in hierarchically structured hollow nanoparticles. *Nat Mater*, *7, 947-52*.

234. He, S.Y., Chang, J.S., Li, L.H., & Ho, H. (2009). Characterization of Young's modulus and residual stress gradient of MetalMUMPs electroplated nickel film. *Sensors and Actuators a-Physical*, *154, 149-156*.

235. A. Cowen, R.M., S. Johnson, B. Hardy. (2002). *MetalMUMPs Design Handbook, Revision 4.0, MEMSCAP Inc.*

236. Borca-Tasciuc, T., Borca-Tasciuc, D.A., Graham, S., Goods, S.H., Kelly, J.J., & Yang, N.Y.C. (2006). Annealing effects on mechanical and transport properties of Ni and Ni-alloy electrodeposits. *Journal of Microelectromechanical Systems*, *15, 1051-1059*.

237. Tang, J., Wang, H., Guo, X.Q., Liu, R., Dai, X.H., Ding, G.F., & Yang, C.S. (2010). An investigation of microstructure and mechanical properties of UV-LIGA nickel thin films electroplated in different electrolytes. *Journal of Micromechanics and Microengineering*, *20, 9*.

238. Gupta, S., Barrios, A., England, N., & Pierron, O.N. (2018). Improved very high cycle bending fatigue behavior of Ni microbeams with Au coatings. *Acta Materialia*, *161, 444-455*.

239. Baumert, E.K., Sadeghi-Tohidi, F., Hosseinian, E., & Pierron, O.N. (2014). Fatigue-induced thick oxide formation and its role on fatigue crack initiation in Ni thin films at low temperatures. *Acta Materialia*, *67, 156-167*.

240. Tohidi, F. (2016). *Investigation of the effects of extreme stress gradients on fatigue behavior of nickel microbeams* (Doctoral). Georgia Institute of Technology, Atlanta, GA.

241. Mortazavi, N., Esmaily, M., & Halvarsson, M. (2015). The capability of Transmission Kikuchi Diffraction technique for characterizing nano-grained oxide scales formed on a FeCrAl stainless steel. *Materials Letters*, *147, 42-45*.

242. Chen, Y.H., Park, S.U., Wei, D., Newstadt, G., Jackson, M.A., Simmons, J.P., De Graef, M., & Hero, A.O. (2015). A Dictionary Approach to Electron Backscatter Diffraction Indexing. *Microsc Microanal*, *21, 739-52*.

243. Midgley, P.A., & Eggeman, A.S. (2015). Precession electron diffraction - a topical review. *IUCrJ*, *2, 126-36*.

244. Lampman, S. (1990). *ASM Handbook*. ASM International.

245. Emery, R.D., & Povirk, G.L. (2003). Tensile behavior of free-standing gold films. Part II. Fine-grained films. *Acta Materialia*, *51, 2079-2087*.

246. Chasiotis, I., Bateson, C., Timpano, K., McCarty, A.S., Barker, N.S., & Stanec, J.R. (2007). Strain rate effects on the mechanical behavior of nanocrystalline Au films. *Thin Solid Films*, *515, 3183-3189*.

247. Haque, M.A., & A Saif, M.T. (2002). Mechanical behavior of 30–50 nm thick aluminum films under uniaxial tension. *Scripta Materialia, 47, 863-867*.

248. Sarkar, R., Rentenberger, C., & Rajagopalan, J. (2015). Electron Beam Induced Artifacts During in situ TEM Deformation of Nanostructured Metals. *Sci Rep, 5, 16345*.

249. Mompiou, F., & Legros, M. (2015). Quantitative grain growth and rotation probed by in-situ TEM straining and orientation mapping in small grained Al thin films. *Scripta Materialia, 99, 5-8*.

250. Wang, Y.B., Li, B.Q., Sui, M.L., & Mao, S.X. (2008). Deformation-induced grain rotation and growth in nanocrystalline Ni. *Applied Physics Letters, 92*.

251. Zhang, K., Weertman, J.R., & Eastman, J.A. (2005). Rapid stress-driven grain coarsening in nanocrystalline Cu at ambient and cryogenic temperatures. *Applied Physics Letters, 87*.

252. Wang, Y., Fu, R., Li, Y., Sang, D., & Jing, L. (2019). Microstructural stability during long-term natural storage and tensile deformation of nanograined FCC pure copper and HCP pure zirconium. *Materials Science and Engineering: A, 744, 171-181*.

253. Rottmann, P.F., & Hemker, K.J. (2017). Experimental quantification of mechanically induced boundary migration in nanocrystalline copper films. *Acta Materialia, 140, 46-55*.

254. Zhang, P., Zhang, J.Y., Li, J., Liu, G., Wu, K., Wang, Y.Q., & Sun, J. (2014). Microstructural evolution, mechanical properties and deformation mechanisms of nanocrystalline Cu thin films alloyed with Zr. *Acta Materialia, 76, 221-237*.

255. Eberl, C., Spolenak, R., Kraft, O., Ruile, W., & Arzt, E. (2007). Fatigue damage in thin film Al interconnects at ultra high frequency: A finite element analysis approach. *Thin Solid Films, 515, 3291*.

256. Kraft, O., Schwaiger, R., & Wellner, P. (2001). Fatigue in thin films: lifetime and damage formation. *Materials Science And Engineering A-Structural Materials Properties Microstructure And Processing, 319, 919-923*.

257. Schwaiger, R., & Kraft, O. (2003). Size effects in the fatigue behavior of thin Ag films. *Acta Materialia, 51, 195-206*.

258. Kacher, J., Hattar, K., & Robertson, I.M. (2016). Initial texture effects on the thermal stability and grain growth behavior of nanocrystalline Ni thin

films. *Materials Science and Engineering a-Structural Materials Properties Microstructure and Processing*, *675*, *110-119*.

259. Wang, B., Idrissi, H., Shi, H., Colla, M.S., Michotte, S., Raskin, J.P., Pardoen, T., & Schryvers, D. (2012). Texture-dependent twin formation in nanocrystalline thin Pd films. *Scripta Materialia*, *66*, *866-871*.

260. Izadi, E., & Rajagopalan, J. (2016). Texture dependent strain rate sensitivity of ultrafine-grained aluminum films. *Scripta Materialia*, *114*, *65-69*.